Stability, Composition and Function of Palladium Surfaces in Oxidizing Environments:

A First-Principles Statistical Mechanics Approach

von
Diplom-Chemikerin
Jutta Rogal

im Fachbereich Physik der Freien Universität Berlin eingereichte
Dissertation zur Erlangung des akademischen Grades

DOCTOR RERUM NATURALIUM

Berlin 2006

Diese Arbeit wurde in der Zeit von Juli 2002 bis Mai 2006 unter der Aufsicht von Herrn PD Dr. K. Reuter am Fritz-Haber-Institut der Max-Planck-Gesellschaft durchgeführt.

Erstgutachter: PD Dr. K. Reuter
Zweitgutachter: Prof. E.K.U. Gross
Disputationstermin: 19. Juli 2006

Abstract

The catalytic oxidation using transition metals (TM) as the active material is an important technological process, which is still not fully understood. Recently, there has been an increasing awareness that the surface of the TM catalysts employed might be oxidized under the oxygen-rich conditions of the catalytic reaction (ambient pressures of O_2 and other reactant gases). The resulting changes in the composition and structure of the surface can then also strongly influence the catalytic activity of the material.

In the present work the catalytic CO oxidation over the Pd(100) surface is studied as a model system. Recent experimental results for this system suggest that the Pd(100) surface might actually be oxidized under conditions as applied in industrial oxidation catalysis. However, it is still being discussed, if the observed oxidic phase is already a thick, bulk-like oxide film or a nanometer thin surface oxide layer, and if the actual active state of the catalyst under reaction conditions is then mainly dominated by a metallic or an oxidic phase.

To address this topic from a theoretical point of view a multiscale modeling approach has been employed in this work. To describe the system quantitatively on an atomic (microscopic) level density-functional theory (DFT) has been used. The results of the DFT calculations have then been combined with concepts from thermodynamics and statistical mechanics to transfer the information obtained in the microscopic regime to meso- and macroscopic length and time scales.

In a first step the atomistic thermodynamics approach is used to obtain a large scale picture about the thermodynamic stability of different phases in a *constrained* thermodynamic equilibrium with an O_2 and CO gas phase (i.e. the formation of CO_2 is not considered). Focussing on temperature and pressure conditions representative of technological oxidation catalysis it is found that a thin surface oxide structure or a CO covered metal surface are the relevant system states under these conditions. In a second refining step the stability of the surface oxide structure under steady-state conditions is then investigated using kinetic Monte Carlo (kMC) simulations, now explicitly taking into account the on-going CO_2 formation. The result is that despite the catalytic CO oxidation reaction the surface oxide on Pd(100) is still stable under stoichiometric p_{O_2}/p_{CO} ratios in the gas phase at elevated temperatures. This indicates the importance of this surface oxide and calls for detailed studies evaluating its contribution to the overall catalytic activity.

Contents

1 Introduction **1**

I Theoretical Background **5**

2 Density-Functional Theory **7**
- 2.1 The Many-Body Problem . . . 7
- 2.2 The Thomas-Fermi Model . . . 9
- 2.3 The Hohenberg-Kohn Theorems . . . 10
- 2.4 The Kohn-Sham Equations . . . 11
- 2.5 Exchange-Correlation Functionals . . . 12

3 The (L)APW+lo Method **15**
- 3.1 Choosing A Basis Set . . . 15
- 3.2 The APW Method . . . 16
- 3.3 The LAPW Method . . . 18
  - 3.3.1 Semi-Core States . . . 18
- 3.4 The APW+lo Method . . . 19
  - 3.4.1 Semi-Core States . . . 20
- 3.5 Mixed Augmentation . . . 20
- 3.6 The Full Potential (L)APW+lo Method . . . 20
- 3.7 Application To Solids And Surfaces . . . 21
  - 3.7.1 Integration Over The Brillouin Zone . . . 21
  - 3.7.2 The Supercell Approach . . . 22
  - 3.7.3 Surface Core-Level Shifts . . . 22
- 3.8 The WIEN2k Code . . . 24

4 DFT And Thermodynamics **27**
- 4.1 Ab Initio Atomistic Thermodynamics . . . 28
- 4.2 Surface Free Energy . . . 29
- 4.3 The Gibbs Free Energy Of Adsorption . . . 36
  - 4.3.1 One-Component Gas Phase . . . 36
  - 4.3.2 Two-Component Gas Phases . . . 39

4.4 Gas Phase Chemical Potential 41
4.5 Summary 42

5 DFT And Statistical Mechanics 45
5.1 Monte Carlo Simulations 45
    5.1.1 Kinetic Monte Carlo 46
    5.1.2 Lattice Gas Hamiltonian 49
5.2 Determining The Process Rates 50
    5.2.1 Transition State Theory 51
    5.2.2 Adsorption 52
    5.2.3 Desorption 53
    5.2.4 Diffusion 56
    5.2.5 Reaction 56
5.3 Summary 57

II CO Oxidation At Pd(100) 59

6 Palladium In A Pure Oxygen Gas Phase 61
6.1 Oxidation Stages Of Pd(100) 61
6.2 Thermodynamic Stability 65
6.3 PdO Low-Index Surfaces 73
    6.3.1 Structure And Stability 73
    6.3.2 Wulff Construction 81
    6.3.3 Stability vs. Polarity 83
6.4 Conclusions 86

7 Palladium In An Oxygen And CO Gas Phase 89
7.1 CO Adsorption On Pd(100) 89
7.2 Co-Adsorption Of Oxygen And CO 91
7.3 Phase Diagram For Pd(100) In An O_2 And CO Gas Phase 99
7.4 Conclusions 105

8 The Onset Of Surface Oxide Decomposition 107
8.1 The Model 108
8.2 The Rates 113
    8.2.1 Adsorption 113
    8.2.2 Desorption 115
    8.2.3 Diffusion 118
    8.2.4 Reaction 119
8.3 The Simulations 123
    8.3.1 Reproducing The Constrained Equilibrium 123

8.3.2 Onset Of Surface Oxide Decomposition Under Reaction Conditions . . . 125
8.4 Conclusions . . . 130

9 Summary And Outlook 131

III Appendix 135

A Convergence Tests 137
A.1 PdO Surfaces . . . 138
A.2 Adsorption On Pd(100) And $(\sqrt{5}\times\sqrt{5})R27°$ . . . 142
A.3 Molecular Binding Energies . . . 144

B Adsorption Structures Involving The $(\sqrt{5}\times\sqrt{5})R27°$ 149
B.1 O And CO In A $(\sqrt{5}\times\sqrt{5})R27°$ Surface Unit Cell . . . 149
B.2 O And CO In Larger $(\sqrt{5}\times\sqrt{5})R27°$ Surface Unit Cells . . . 162

C Lattice Gas Hamiltonian 165

Bibliography 173

Acknowledgements 181

List of Figures

3.1 The muffin-tin potential approximation 17
3.2 Basis functions in APW and LAPW 19
3.3 The Supercell Approach 23

4.1 Multiscale Modeling 27
4.2 Surface in thermodynamic equilibrium with gas phase and bulk 30
4.3 Surface free energy vs. oxygen chemical potential 32
4.4 Vibrational contribution to the surface free energy 36
4.5 Gibbs free energy of adsorption vs. oxygen chemical potential 38
4.6 Calculated vs. experimental values of the oxygen chemical potential . . 42

5.1 Flowchart for a kinetic Monte Carlo simulation 48
5.2 1D Reaction coordinate 54

6.1 The Pd(100) surface 62
6.2 Adlayers on Pd(100) 63
6.3 $(\sqrt{5} \times \sqrt{5})R27^\circ$ Surface oxide structure 64
6.4 Tetragonal unit cell of PdO 65
6.5 Surface phase diagram for Pd(100) using the PBE E_{xc} 68
6.6 Surface phase diagram for Pd(100) using the PBE, RPBE and LDA E_{xc} 70
6.7 Vibrational contribution to ΔG^{ads} 72
6.8 Schematic illustration of low-index PdO surfaces 74
6.9 Surface free energy of PdO(001) and PdO(100) surfaces vs. $\Delta\mu_{\mathrm{O}}$ 77
6.10 Surface free energy of PdO(101) and PdO(110) surfaces vs. $\Delta\mu_{\mathrm{O}}$ 78
6.11 Surface free energy of PdO(111) surface vs. $\Delta\mu_{\mathrm{O}}$ 79
6.12 Constrained Wulff construction for PdO low-index surfaces 82
6.13 Stoichiometric reconstructions of the PdO(001)-O and PdO(110)-O terminations 84

7.1 CO adlayers on Pd(100) 90
7.2 O/CO adlayers on Pd(100) 92
7.3 Adsorption sites on $(\sqrt{5} \times \sqrt{5})R27^\circ$ 94
7.4 Measured C-1s SCLSs of CO in $(2\sqrt{2}\times\sqrt{2})R45^\circ$ and on the $(\sqrt{5} \times \sqrt{5})R27^\circ$ structure 98

7.5 ΔG^{ads} for Pd(100) vs. $\Delta\mu_{\mathrm{O}}$ and $\Delta\mu_{\mathrm{CO}}$ - PBE 100
7.6 Phase diagram for Pd(100) in an O_2 and CO environment - PBE 102
7.7 Phase diagram for Pd(100) in an O_2 and CO environment - RPBE and LDA 104

8.1 Schematic illustration of the kMC model 109
8.2 Gas phase conditions of the kMC simulations 110
8.3 First nearest neighbor interactions in the $(\sqrt{5} \times \sqrt{5})R27^\circ$ surface unit cell 116
8.4 Diffusion barriers 119
8.5 TS search for the reaction of O+CO→CO_2 on the surface oxide 120
8.6 PES for the reaction of O+CO→CO_2 on the surface oxide 121
8.7 Reaction barriers 122
8.8 Average hollow site occupation by O vs. CO pressure – $T = 300\,\mathrm{K}$ . . . 127
8.9 Average hollow site occupation by O vs. CO pressure – $T = 400\,\mathrm{K}$ . . . 128
8.10 Average hollow site occupation by O vs. CO pressure – $T = 600\,\mathrm{K}$ . . . 129

A.1 Planewave cutoff test for the PdO low-index surfaces 139
A.2 **K**-point test for the PdO low-index surfaces 140
A.3 Slab-thickness test for the PdO low-index surfaces 141
A.4 Surface phase diagram for $E^{\mathrm{wf}}_{\mathrm{max}} = 20\,\mathrm{Ry}$ and $24\,\mathrm{Ry}$ 143
A.5 O_2 binding energy vs. $E^{\mathrm{wf}}_{\mathrm{max}}$ 145
A.6 CO binding energy vs. $E^{\mathrm{wf}}_{\mathrm{max}}$ 146

List of Tables

6.1 Lattice constant of Palladium 62
6.2 Lattice constants of Palladium oxide 65
6.3 $\widetilde{E}^{\text{bind}}$ and ΔG^{ads} for adlayers and the surface oxide on Pd(100) 68
6.4 Phase boundaries of oxidation stages of Pd(100) 69
6.5 Monkhorst-Pack grids for the low-index PdO surfaces 76
6.6 Surface free energy of all low-index PdO (1 × 1) terminations 80
6.7 Required lowering of the surface free energy to change the Wulff construction 83
6.8 Work function of all low-index PdO surfaces 85
6.9 Binding energies of the topmost oxygen atoms of the low-index PdO surfaces 86

7.1 Binding energies of CO on Pd(100) 91
7.2 Binding energies of O and CO on Pd(100) 92
7.3 Binding energies of CO on $(\sqrt{5} \times \sqrt{5})R27^\circ$ 94
7.4 Pd-3d SCLSs of $(\sqrt{5} \times \sqrt{5})R27^\circ$ and $(\sqrt{5} \times \sqrt{5})R27^\circ$+CO 97
7.5 C-1s SCLSs of $(2\sqrt{2} \times \sqrt{2})R45^\circ$ and $(\sqrt{5} \times \sqrt{5})R27^\circ$+CO 98
7.6 Binding energies of O_2, CO and CO_2 103
7.7 $\Delta G^{\text{ads}}(0,0)$ of all relevant structures of Pd(100) in an O_2 and CO gas phase 104

8.1 Lattice gas hamiltonian parameters 117
8.2 Diffusion barriers 119
8.3 Average occupation of sites for kMC simulations without reactions . . . 124

A.1 Monkhorst-Pack grids applied in the cutoff test of the low-index PdO surfaces 139
A.2 Monkhorst-Pack grids for the low-index PdO surfaces 141
A.3 Number of Pd layers in the $(\sqrt{5} \times \sqrt{5})R27^\circ$ structure 143
A.4 O_2 binding energy and bond length 145
A.5 CO binding energy and bond length 146
A.6 CO_2 binding energy and bond length 147

Chapter 1

Introduction

Most of today's technologically relevant, chemical reactions would not be very efficient or even possible without the use of a catalyst. Some examples for such processes are oil refining, the production of chemicals (e.g. ammonia synthesis) and the cleaning of exhaust gases [1]. The catalyst can be either in the same phase as the reactants (homogeneous catalysis) or in a different phase, e.g. a solid catalyst and gaseous or liquid reactants (heterogeneous catalysis). The latter is usually preferred by industry due to an easier separation of the reactants/products and the catalyst. Here, the discussion will be focused on heterogeneous catalysis with solid catalysts and gaseous reactants. The industrially used, solid catalysts are very complex materials often consisting of a precious transition metal, which is considered as the catalytically active part, dispersed on a cheaper support material (like alumina, silica or carbon). To improve the performance of the catalyst additives like alkali metals or halogens are commonly used. Due to this complexity most of the catalysts used today have been discovered and improved by sophisticated, but in essence *trial-and-error* approaches. Recently, also high-speed screening techniques for searching new heterogeneous catalyst systems have been proposed [2, 3].

A different approach in trying to understand on a microscopic scale, how and why a catalyst works, is the use of model catalysts representing essential properties of the real catalyst. In the field of surface science single crystal surfaces of the catalytically active metals are usually taken as model catalysts and are investigated under the well-defined gas phase conditions of ultra-high vacuum (UHV). Over the last decades much valuable information about the structure and composition of clean and adsorbate covered surfaces could thus be obtained on an atomic scale. However, the transferability of the results to real catalysis is questioned by the so-called *materials gap* between the structurally rather simple model catalysts and the complex real catalysts, and the *pressure gap*, which is many orders of magnitude in pressure between the UHV conditions and conditions applied in industrial heterogeneous catalysis. Under reaction conditions, the entire structure and composition of the catalyst's surface might thus be changed, which might then also influence its catalytic activity.

Focusing on heterogeneous oxidation catalysis, where rather high oxygen partial pressures are applied, the surface of the transition metal catalyst might e.g. be oxidized, so that the actual catalytically active phase under technologically relevant environmental conditions is not the metal, but rather the oxide. A prominent example for such an effect is the CO oxidation reaction over ruthenium. Here it was found, that under UHV conditions the Ru(0001) surface shows almost no catalytic activity [4], whereas under high oxygen pressures the catalytic activity exceeds even the one of the frequently used palladium and platinum catalysts [5]. This increase in the catalytic activity towards CO oxidation was assigned to the formation of RuO_2 under these gas phase conditions [6, 7, 8, 9, 10]. For the ruthenium catalyst there is thus a clear distinction between the active phases, the rather unreactive metal under low oxygen pressures and the highly active oxide under high oxygen pressures. For the more noble metals like palladium, platinum and silver, which are also frequently used as catalysts in oxidation reactions, the situation appears to be somewhat different. Here, already the metal surfaces show a quite good catalytic activity under UHV conditions. In addition, the oxides of the more noble metals are much less stable than in the case of ruthenium, as can be seen from the heat of formation of the different oxides (most apparent, if presented in eV/O: $\Delta H^f_{\mathrm{RuO_2}} = -1.60\,\mathrm{eV/O}$, whereas $\Delta H^f_{\mathrm{PdO}} = -0.88\,\mathrm{eV/O}$, $\Delta H^f_{\mathrm{PtO_2}} = -0.69\,\mathrm{eV/O}$ and $\Delta H^f_{\mathrm{Ag_2O}} = -0.34\,\mathrm{eV/O}$ [11, 12]). Hence, the nature of the active surface under reactive conditions is less clear than in the ruthenium case. In addition, on palladium, platinum and silver the formation of so-called *surface oxides* has been observed under ambient oxygen pressures. In the present context a surface oxide refers to a structure, that is already more complex than a simple ordered oxygen adlayer, but still represents only a nanometer thin oxide-like film on the metal surface. The role of these surface oxide structures in oxidation catalysis is still an open question.

For the surface oxide on Ag(111), which has already been reported in the 1970s [13, 14], not even the atomic structure is fully resolved. A very recent study suggests even that under reaction conditions not one defined structure, but a variety of structures (possibly built by common building blocks) might prevail at the surface [15]. The hitherto observed surface oxide structures on platinum and palladium show a similar complexity. However, here at least so far consistent structural models have been proposed for the surface oxides on Pt(110) [16], Pd(111) [17] and Pd(100) [18].

To obtain a deeper, atomic-scale understanding of the catalytically active state under reaction conditions a growing number of so-called *in-situ* experimental techniques is presently being developed to bridge the pressure gap between UHV and ambient pressure conditions, like e.g. scanning tunneling microscopy (STM) [19, 20, 16], surface x-ray diffraction (SXRD) [21, 22, 23, 24], transmission electron microscopy (TEM) [25] and photoelectron spectroscopy (PES) [26]. Also from a theoretical point of view new methodologies have to be developed to describe a macroscopically observed function like heterogeneous catalysis on the basis of microscopic understanding. The elementary molecular processes, which take place on microscopic time and length scales and which determine the behavior of the system, can be well described by modern electronic structure methods (like density-functional theory, DFT). Their statistical interplay, though, which is decisive for the functionalities of a certain compound, only develops in the meso- and macroscopic regime. Also here, methods from statistical mechanics and/or thermodynamics are well established. It is thus the appropriate linking between the different regimes, which becomes decisive. Such an approach is also referred to as *multiscale modeling* [27, 28].

As a model system for heterogeneous catalysis the present work will focus on the CO oxidation on Pd(100). Experimentally, the Pd(100) surface has been widely studied by a variety of UHV surface science techniques, in contact with both an oxygen and CO gas phase. Recently, also some of the above mentioned *in-situ* methods have been applied to investigate the structure and composition of Pd(100) over an extended temperature and pressure range. Using SXRD measurements a (T, p)-diagram showing the detected phases in an oxygen atmosphere over a temperature range of $T = 600 - 1000\,\mathrm{K}$ and pressures of $p_{\mathrm{O}_2} = 10^{-9} - 1\,\mathrm{atm}$ could be obtained [23]. Here, also the afore mentioned surface oxide has been measured over an extended (T, p)-range, suggesting that this phase might also appear under catalytic reaction conditions. In reactor STM experiments by Hendriksen and Frenken [29, 30, 31] the structure of the Pd(100) surface could directly be monitored during the catalytic oxidation of CO. Here, the surface was exposed to both oxygen and CO at a total pressure of $p_{\mathrm{tot}} \approx 1\,\mathrm{atm}$ and a temperature of $T \approx 400\,\mathrm{K}$. The partial pressures of the reactant gases CO and O_2, as well as the reaction product CO_2, were measured simultaneously with the STM images. Depending on the partial pressures of O_2 and CO Hendriksen and Frenken observed a change in the reaction rate, which was accompanied by a significant change in the morphology of the surface. Starting on a very smooth surface, which was assigned to the clean Pd(100) surface, and decreasing the CO partial pressure, a sudden increase in the reaction rate went together with a roughening of the surface, which was assigned to the formation of some oxidic phase. Increasing the CO pressure led again to a smoothing of the surface and a decrease in the reaction rate. Unfortunately, it has not been possible so far to obtain atomic resolution in the reactor STM experiments, so that the structure of the oxidic phase could not yet be identified.

These experiments clearly indicate, that the formation of an oxidic phase at Pd(100) might well be possible under gas phase conditions applied in industrial CO oxidation catalysis. What remains unknown, is if it is already the bulk oxide or rather a nanometer thin surface oxide structure that forms under these conditions, and if this is then also the actual catalytically active state. In the present work this problem is addressed theoretically by combining DFT calculations (for the microscopic regime) with concepts from thermodynamics and statistical mechanics (for the mesoscopic regime). Applying an *ab initio* atomistic thermodynamics approach, the structure and composition of Pd(100) is investigated in a first step in thermodynamic equilibrium with a pure oxygen gas phase (Chapter 6). It is then possible to compare the stability of the clean metal surface, different oxygen adlayers, the surface oxide and the bulk oxide over a wide range of oxygen gas phase conditions and identify the thermodynamically most stable phase in a respective (T, p)-range. In a second step, also the CO is taken into account. The stability of different phases containing oxygen and/or CO is compared in a *constrained* equilibrium with an oxygen and CO gas phase in Chapter 7. Here, the formation of CO_2 is still neglected in the gas phase, as well as at the surface. To explicitly include the effects of the on-going catalytic reaction, in a last step, kinetic Monte Carlo (kMC) simulations are applied (Chapter 8). Here, a connection between the micro- and mesoscopic regime is established by deriving the input parameters of the kMC simulations on the basis of DFT results, instead of using fitted or empirical parameters.

In short, it is found that a $(\sqrt{5} \times \sqrt{5})R27^\circ$ surface oxide structure on Pd(100) is actually a stable phase over an extended temperature and pressure range in thermodynamic equilibrium with a pure oxygen gas phase, as well as in a constrained thermodynamic equilibrium with an O_2 and CO gas phase. Its stability region does extend to catalytically relevant gas phase conditions of ambient temperatures and pressures. Including the on-going CO_2 formation at the surface leads to a small decrease in the stability region of the surface oxide, such that slightly oxygen-rich gas phase conditions are needed to stabilize the surface oxide structure. These results suggest that the $(\sqrt{5} \times \sqrt{5})R27^\circ$ surface oxide structure might actually form under catalytic reaction conditions and might then also contribute to the active state of the Pd(100) surface in CO oxidation catalysis.

Part I

Theoretical Background

Chapter 2

Density-Functional Theory

2.1 The Many-Body Problem

Since the formulation of the Schrödinger equation in the 1920s the ultimate goal of quantum mechanics has been to find at least approximate solutions of this equation for systems containing more then just two mutually interacting particles (like the one-proton and one-electron structure of the hydrogen atom, for which an exact solution can be derived). The result would be a powerful tool to understand and predict material properties without depending on experimental data. The time-independent, non-relativistic Schrödinger equation can be written as

$$H\Psi(\mathbf{x}_i, \mathbf{R}_A) = E\Psi(\mathbf{x}_i, \mathbf{R}_A) \quad . \tag{2.1}$$

The equation describes an eigenvalue problem of the Hamilton operator H with the total energy E of the system as eigenvalue and the many-body wave function $\Psi(\mathbf{x}_i, \mathbf{R}_A)$ as eigenfunction. Any system is then explicitly characterized by the corresponding wave function $\Psi(\mathbf{x}_i, \mathbf{R}_A)$, which depends on the combined spatial and spin coordinates of the electrons $\mathbf{x}_i = (\mathbf{r}_i, \sigma_i)$ and the spatial coordinates of the nuclei $\mathbf{R}_A$ (for an introduction to quantum mechanics see e.g. Refs. [32, 33]). A dependence on the spin coordinates σ_i is necessary, since in contrast to a relativistic treatment, where the electron spin arises naturally, in the non-relativistic approach the electron spin has to be introduced additionally. In atomic units (i.e. $m_\mathrm{e} = \hbar = \mathrm{e} = 1$) the Hamilton operator for a system containing N electrons and M nuclei is given by

$$H = -\frac{1}{2}\sum_{i=1}^{N}\nabla_i^2 - \frac{1}{2}\sum_{A=1}^{M}\frac{1}{m_A}\nabla_A^2 - \sum_{i=1}^{N}\sum_{A=1}^{M}\frac{Z_A}{\mathbf{r}_{iA}} + \sum_{i=1}^{N}\sum_{j>i}^{N}\frac{1}{\mathbf{r}_{ij}} + \sum_{A=1}^{M}\sum_{B>A}^{M}\frac{Z_A Z_B}{\mathbf{R}_{AB}} \quad . \tag{2.2}$$

Here, the indices i and j run over the N electrons whereas A and B run over the M nuclei. ∇_i^2 is the Laplacian operator acting on particle i, m_A is the mass of the nucleus A and Z_A its nuclear charge. $\mathbf{r}_{ij}$ is the distance between particles i and j, i.e. $\mathbf{r}_{ij} = |\mathbf{r}_i - \mathbf{r}_j|$, resp. $\mathbf{r}_{iA} = |\mathbf{r}_i - \mathbf{R}_A|$. The Hamilton operator consists of five parts:

the kinetic energy operators T_e and T_n for the electrons and the nuclei, the Coulomb interaction between electrons and nuclei V_en and the repulsive interaction between the electrons V_ee resp. between the nuclei V_nn, so that Eq. (2.2) can be shortly written as

$$H = T_\mathrm{e} + T_\mathrm{n} + V_\mathrm{en} + V_\mathrm{ee} + V_\mathrm{nn} \quad . \tag{2.3}$$

Although the Hamilton operator is known, Eq. (2.1) is far too complex to be solved due to the large number of variables the wave function Ψ depends on. In a system containing N electrons and M nuclei there are $4N + 3M$ degrees of freedom resulting from the $3N$ spatial coordinates, $\{\mathbf{r}_i\}$, and N spin coordinates, $\{\sigma_i\}$, of the electrons and the $3M$ spatial coordinates, $\{\mathbf{R}_A\}$, of the nuclei, respectively. A first step in simplifying Eq. (2.1) is the Born-Oppenheimer approximation [34]. Since the nuclei are much heavier than the electrons (already a factor of $\sim$ 1800 for a proton), it is assumed within the Born-Oppenheimer approximation, that the response of the electrons to an external perturbation is much faster than the response of the nuclei. Thus, the electrons would be able follow any movement of the nuclei quasi instantaneously and might then be considered as basically moving in a constant field generated by the nuclei at fixed positions. The kinetic energy term T_n for the nuclei in Eq. (2.3) is set to zero and the repulsion term for the nuclei V_nn enters the total energy as a constant. With this first approximation the *electronic* Schrödinger equation is given by

$$H_\mathrm{e}\Psi_\mathrm{e}(\mathbf{x}_i) = [T_\mathrm{e} + V_\mathrm{en} + V_\mathrm{ee}]\Psi_\mathrm{e}(\mathbf{x}_i) = E_\mathrm{e}\Psi_\mathrm{e}(\mathbf{x}_i) \tag{2.4}$$

with the electronic Hamilton operator H_e, the electronic wave function $\Psi_\mathrm{e}(\mathbf{x}_i, \mathbf{R}_A)$ and the electronic energy $E_\mathrm{e}(\mathbf{R}_A)$. The Born-Oppenheimer potential energy surface can then be obtained by calculating the electronic energy $E_\mathrm{e}(\mathbf{R}_A)$ via Eq. (2.4) and the interaction term between the nuclei V_nn for any given position $\{\mathbf{R}_A\}$ of the nuclei.

Although the Born-Oppenheimer approximation simplifies the original Schrödinger equation considerably, the electronic part in Eq. (2.4) is still only numerically solvable by introducing further approximations. One fundamental approach to solve the electronic Schrödinger equation is the Hartree-Fock approximation [35, 36]. Here the many-body problem is transferred into a single particle problem by approximating the electronic wave function $\Psi_\mathrm{e}(\mathbf{x}_i)$ by a Slater-determinant of single particle wave functions, which ensures the antisymmetry of the wave function. In the Hartree-Fock approach the exchange between electrons as well as the correlated motion of electrons of like spin due to the Pauli principle is taken into account. The correlation resulting from the Coulomb repulsion for all electrons of like and unlike spins is missing. Although Hartree-Fock theory therefore contains a part of the correlation, the so-called Pauli correlation, it is commonly agreed that the term correlation is used for all that is missing in Hartree-Fock. To improve on the original Hartree-Fock approach more involved theories have been developed [32, 33]. Among the most popular are second/fourth order perturbation theory by Møller and Plesset (MP2/MP4) [37], configuration interaction (CI) [32], multiconfiguration self-consistent field (MCSCF) [38] and coupled cluster approaches (CC) [39]. These so-called wave function based methods are mainly used for calculating atoms and molecules (containing up to 50 atoms), since on the one hand they can be quite accurate, but on the other they also become quite demanding with an increasing number of electrons.

An alternative approach is given by density-functional theory (DFT). In DFT the central quantity is not the wave function $\Psi_\mathrm{e}(\mathbf{x}_i)$, but the electron density $n(\mathbf{r})$. Originating mainly from solid state physics DFT has become more and more popular also in quantum chemistry [40, 41, 42].

2.2 The Thomas-Fermi Model

The very first approach to use the electron density $n(\mathbf{r})$ of a system to calculate its total energy was already formulated by Thomas and Fermi in 1927 [43, 44]. The electron density determines the probability of finding any of the N electrons in a volume element $d\mathbf{r}_1$, while the other $N-1$ electrons have arbitrary positions, and is given by

$$n(\mathbf{r}_1) = N \int \cdots \int |\Psi_\mathrm{e}(\mathbf{x}_1, \mathbf{x}_2, \ldots, \mathbf{x}_N)|^2 d\sigma_1 d\mathbf{x}_2 \ldots d\mathbf{x}_N \quad . \tag{2.5}$$

Compared to the wave function the electron density has the advantage, that it only depends on 3 instead of $3N$ spatial coordinates, but still contains all information needed to determine the Hamiltonian, i.e. the number of electrons N, the positions of the nuclei $\mathbf{R}_A$ and the charge of the nuclei Z_A. N is simply given by the integral over $n(\mathbf{r})$

$$\int n(\mathbf{r}) d\mathbf{r} = N \quad . \tag{2.6}$$

Furthermore $n(\mathbf{r})$ exhibits cusps only at the positions $\mathbf{R}_A$ and the properties of each cusp are clearly related to the nuclear charge Z_A. Taking into account these considerations it seems at least plausible that $n(\mathbf{r})$ is sufficient to determine all properties of a system.

In their model Thomas and Fermi formulated the total energy of a system in terms of its electron density by using the uniform electron gas as a model for the kinetic energy and treating the nuclear-electron attraction and electron-electron repulsion classically

$$E_\mathrm{TF}[n(\mathbf{r})] = \frac{3}{10}(3\pi^2)^{2/3} \int n^{5/3}(\mathbf{r}) d\mathbf{r} - Z \int \frac{n(\mathbf{r})}{\mathbf{r}} d\mathbf{r} + \int \int \frac{n(\mathbf{r}_1) n(\mathbf{r}_2)}{\mathbf{r}_{12}} d\mathbf{r}_1 d\mathbf{r}_2 \quad . \tag{2.7}$$

The actual results obtained by the Thomas-Fermi model for atoms are not very accurate, since there is neither exchange nor correlation included and the Thomas-Fermi kinetic energy functional is only a very coarse approximation to the true kinetic energy. For molecules the description is even worse, since no molecular binding is predicted in the method, which caused the Thomas-Fermi model to be considered as of only little importance for giving quantitative results in atomic, molecular or solid state physics.

Nevertheless Eq. (2.7) is the first example of an expression of the total energy as a functional of the electronic density $n(\mathbf{r})$ without any information about the wave function Ψ. The correct density is then calculated by applying the variational principle to Eq. (2.7) under the constraint of Eq. (2.6). At that time it was just assumed that the variational principle holds for Eq. (2.7). Mathematical this assumption was not proven until almost 40 years later by Hohenberg and Kohn [45].

2.3 The Hohenberg-Kohn Theorems

In 1964 Hohenberg and Kohn formulated two theorems, which formally justified the use of the electron density as basic variable in determining the total energy and which became the foundation of modern density-functional theory [45]. The first theorem states that for a non-degenerate ground state of an electron gas in an external potential V_{ext}, there exists a one-to-one mapping between the external potential V_{ext}, the wave function Ψ_{e} and the electron density $n(\mathbf{r})$. The electron density therefore uniquely defines the external potential (to within a constant). The electronic energy of a system E can then be formulated as a functional of the electron density $n(\mathbf{r})$

$$E[n(\mathbf{r})] = \int n(\mathbf{r}) V_{\text{ext}} d\mathbf{r} + F_{\text{HK}}[n(\mathbf{r})] \quad . \tag{2.8}$$

Here, $F_{\text{HK}}[n(\mathbf{r})]$ is the Hohenberg-Kohn functional, which does not depend on the external potential and is therefore universal. $F_{\text{HK}}[n(\mathbf{r})]$ contains the electron-electron interaction $E_{\text{ee}}[n]$ as well as the kinetic energy of the electrons $T_{\text{e}}[n]$

$$F_{\text{HK}}[n] = T_{\text{e}}[n] + E_{\text{ee}}[n] \quad . \tag{2.9}$$

If one could find an explicit expression for this functional, Eq. (2.8) would provide an exact solution to the Schrödinger equation. Unfortunately an explicit form of the two functionals in Eq. (2.9) is unknown.

The electron-electron interaction can further be divided into the Coulomb repulsion $J[n]$ and a non-classical part $E_{\text{ncl}}[n]$

$$E_{\text{ee}}[n] = \frac{1}{2} \int \int \frac{n(\mathbf{r}_1) n(\mathbf{r}_2)}{\mathbf{r}_{12}} d\mathbf{r}_1 d\mathbf{r}_2 + E_{\text{ncl}}[n] = J[n] + E_{\text{ncl}}[n] \quad . \tag{2.10}$$

The non-classical part $E_{\text{ncl}}[n]$ contains all contributions arising from self-interaction, exchange and Coulomb correlation. Finding good approximations for $T_{\text{e}}[n]$ and $E_{\text{ncl}}[n]$ is still one of the main tasks in density-functional theory.

The second theorem of Hohenberg and Kohn proofs that the variational principle holds for the minimization of the energy with respect to the electron density, i.e. for any arbitrary, well behaved electron density $n(\mathbf{r})$

$$n(\mathbf{r}) \geq 0 \quad \text{and} \quad \int n(\mathbf{r}) d\mathbf{r} = N \tag{2.11}$$

the lowest energy E_0 is only given as a functional of the true ground state density $n_0(\mathbf{r})$

$$E_0 = E[n_0(\mathbf{r})] \leq E[n(\mathbf{r})] \quad . \tag{2.12}$$

As mentioned above an exact form of the Hohenberg-Kohn functional $F_{\mathrm{HK}}[n]$ is not known. Concerning the variational principle this means that the ground state energy obtained with an approximate functional $F_{\mathrm{HK}}[n]$ does not necessarily have to be an upper bound for the energy of the true system ground state. The variational principle can then only give the ground state energy of the system specified by the approximate functional. The minimization of the energy is performed under the constraint of a constant number of electrons N (cf. Eq. (2.11)), which results in the Euler-Lagrange equation

$$\mu = \frac{\delta E[n(\mathbf{r})]}{\delta n(\mathbf{r})} = V_{\mathrm{ext}}(\mathbf{r}) + \frac{\delta F_{\mathrm{HK}}[n(\mathbf{r})]}{\delta n(\mathbf{r})} \tag{2.13}$$

Here, the Lagrange multiplier μ corresponds to the chemical potential of the electrons.

2.4 The Kohn-Sham Equations

In 1965, about a year after the Hohenberg-Kohn theorems were published, Kohn and Sham proposed a way to approximate the universal functional $F_{\mathrm{HK}}[n]$ [46]. The basic concept of their approach is to separate the kinetic energy functional T_{e} into the kinetic energy of a non-interacting reference system T_{s} and an unknown part T_{c}, which contains the corrections due to the interaction between the electrons in the real system. For a non-interacting system of electrons the kinetic energy can be computed exactly using one-particle wave functions φ,

$$T_{\mathrm{s}} = \sum_{i=1}^{N} \langle \varphi_i | -\frac{1}{2}\nabla^2 | \varphi_i \rangle \quad . \tag{2.14}$$

The Hohenberg-Kohn functional can then be expressed as

$$F_{\mathrm{HK}}[n] = T_{\mathrm{s}}[n] + J[n] + E_{\mathrm{xc}}[n] \tag{2.15}$$

with the exchange-correlation energy E_{xc} defined as

$$E_{\mathrm{xc}}[n] \equiv T_{\mathrm{e}}[n] - T_{\mathrm{s}}[n] + E_{\mathrm{ee}}[n] - J[n] \quad . \tag{2.16}$$

The exchange-correlation energy contains the difference in the kinetic energy between the real, interacting system and the non-interacting system as well as the non-classical part of the electron-electron repulsion, E_{ncl}. Following this approach the many-body problem is again mapped onto an effective single particle problem and all unknown terms are merged into the exchange-correlation part. The one-particle wave functions can now be determined by effective one-particle equations under the constraint to reproduce the density of the real, interacting system. This yields the so-called Kohn-Sham (KS) equations

$$[-\frac{1}{2}\nabla^2 + V_{\mathrm{eff}}(\mathbf{r})]\varphi_i = \epsilon_i \varphi_i \quad , \tag{2.17}$$

with the effective potential $V_{\mathrm{eff}}(\mathbf{r})$ containing the external potential $V_{\mathrm{ext}}(\mathbf{r})$, the classical Coulomb potential and the exchange-correlation potential $V_{\mathrm{xc}}(\mathbf{r})$

$$V_{\mathrm{eff}}(\mathbf{r}) = V_{\mathrm{ext}}(\mathbf{r}) + \int \frac{n(\mathbf{r}')}{|\mathbf{r} - \mathbf{r}'|} d\mathbf{r}' + V_{\mathrm{xc}}(\mathbf{r}) \quad . \tag{2.18}$$

The density of the real system $n(\mathbf{r})$ can be expressed in terms of the Kohn-Sham orbitals φ_i

$$n(\mathbf{r}) = \sum_i^N |\varphi_i(\mathbf{r})|^2 \quad , \tag{2.19}$$

and the exchange-correlation potential is given by the derivative of the exchange-correlation energy in Eq. (2.16) with respect to the density

$$V_{\mathrm{xc}}(\mathbf{r}) = \frac{\delta E_{\mathrm{xc}}[n(\mathbf{r})]}{\delta n(\mathbf{r})} \quad . \tag{2.20}$$

Since the effective potential V_{eff} already depends on the density itself (cf. Eq. (2.18)) the Kohn-Sham equations have to be solved self-consistently. Once a self-consistent density is calculated, the functional in Eq. (2.15) can be evaluated and thus also the electronic energy of the system (Eq. (2.8)). Within the Kohn-Sham formalism the kinetic energy of the non-interacting system is only described indirectly using N one-particle wave functions, but still exact. Solely the exchange-correlation functional $E_{\mathrm{xc}}[n]$ remains unknown. Finding good approximations for $E_{\mathrm{xc}}[n]$ is still one of the greatest challenges is modern DFT. Some of the basic ideas of constructing exchange-correlation functional are outlined in the next Section.

2.5 Exchange-Correlation Functionals

The local-density approximation (LDA) is the simplest, but also most widely used approximation for the exchange-correlation functional. The LDA is based on the homogeneous electron gas, which describes a system of electrons in an infinite region of space with a uniform positive background charge to preserve overall charge neutrality. For any inhomogeneous system it is then assumed that the exchange-correlation energy can be obtained by approximating the density of the inhomogeneous system locally by the density of the homogeneous electron gas

$$E_{\mathrm{xc}}^{\mathrm{LDA}}[n] = \int n(\mathbf{r})\epsilon_{\mathrm{xc}}(n(\mathbf{r}))d\mathbf{r} \quad , \tag{2.21}$$

with $\epsilon_{\mathrm{xc}}(n(\mathbf{r}))$ being the exchange-correlation energy per particle of the homogeneous electron gas. $\epsilon_{\mathrm{xc}}(n(\mathbf{r}))$ can be written as the sum of exchange and correlation contributions

$$\epsilon_{\mathrm{xc}}(n(\mathbf{r})) = \epsilon_{\mathrm{x}}(n(\mathbf{r})) + \epsilon_{\mathrm{c}}(n(\mathbf{r})) \quad , \tag{2.22}$$

where the exchange part $\epsilon_{\mathrm{x}}(n(\mathbf{r}))$ can be expressed explicitly

$$\epsilon_{\mathrm{x}}(n(\mathbf{r})) = -\frac{3}{4}\sqrt[3]{\frac{3\,n(\mathbf{r})}{\pi}} \quad . \tag{2.23}$$

For the correlation part $\epsilon_{\mathrm{c}}(n(\mathbf{r}))$ there is no such explicit expression, but there are highly accurate quantum Monte Carlo calculations for the homogeneous electron gas [47], which can then be parameterized to be used in DFT [48, 49]. Although the LDA appears to be a crude approximation for any realistic system, it has been widely used (especially in solid state physics) and often gives astonishingly good results. Results obtained within the LDA usually become worse with increasing inhomogeneity of the described system, which is particularly the case for atoms or molecules. Typically, in the LDA binding energies are overestimated and therefore bond lengths underestimated. Nevertheless the LDA forms the base of practically all currently used exchange-correlation functionals.

One of the first extensions to the LDA is the generalized gradient approximation (GGA), where in addition to the density itself, information about the gradient of the density are considered

$$E_{\mathrm{xc}}^{\mathrm{GGA}}[n] = \int n(\mathbf{r})\epsilon_{\mathrm{xc}}(n(\mathbf{r}), \nabla n(\mathbf{r}))d\mathbf{r} \quad . \tag{2.24}$$

Again the functional is usually divided into an exchange $E_{\mathrm{x}}^{\mathrm{GGA}}$ and a correlation part $E_{\mathrm{c}}^{\mathrm{GGA}}$, which are expanded separately. In the development of new functionals some known behavior of the exact, but unknown functional is usually considered as well as empirical parameters. For the description of transition metals, which is the main focus of this work, the many different GGAs provide in most cases better results than the LDA, especially with respect to binding energies.

In this work the functional developed by Perdew, Burke and Ernzerhof (PBE) [50] is used. Since the error introduced by an approximate exchange-correlation functional can not be quantified, some of the calculations in this work have also been repeated using the LDA and the GGA-RPBE [51] functionals. Comparing the different results obtained by using different exchange-correlation functionals is then used to provide a first estimate of the uncertainty arising from the approximate E_{xc}.

Chapter 3

The (L)APW+lo Method

3.1 Choosing A Basis Set

The Kohn-Sham equations (Eq. (2.17)) provide a formulation of how to practically find a solution to the Hohenberg-Kohn functional (Eq. (2.15)). Nevertheless also the Kohn-Sham orbitals φ_i have to be expanded in some way. In principle it would be possible to find a purely numerical solution, but in practice most applications of Kohn-Sham density-functional theory use to date an expansion of the Kohn-Sham orbitals φ_i into basis functions ϕ_μ

$$\varphi_i = \sum_{\mu=1}^{L} c_{\mu i} \phi_\mu \quad . \tag{3.1}$$

For $L \to \infty$ Eq. (3.1) would give an exact expression for φ_i. In reality the expansion has to be truncated and the actually needed number of basis functions ϕ_μ to obtain a good representation of φ_i strongly depends on the choice of the basis set. Whether or not a basis set is a good choice again depends on the given problem. To begin with one has to distinguish between calculations with or without periodic boundary conditions. In this work density-functional theory is mainly applied to the calculation of solids. Since solids are infinite in all three dimensions and therefore contain an infinite number of atoms, periodic boundary conditions are used in most cases. The following discussion is thus concentrated on basis sets that are favorable to periodic boundary conditions.

In a crystalline solid the electrons are moving in a periodic, effective potential V_{eff}, that is created by the periodically arranged nuclei and consequently reflects the symmetry of the crystal

$$V_{\text{eff}}(\mathbf{r} + \mathbf{R}_n) = V_{\text{eff}}(\mathbf{r}) \quad \text{with} \quad \mathbf{R}_n = n_1\mathbf{a}_1 + n_2\mathbf{a}_2 + n_3\mathbf{a}_3 \quad . \tag{3.2}$$

$\mathbf{R}_n$ is the translational lattice vector and $\mathbf{a}_i$ are the unit cell vectors of the crystal. According to Bloch's theorem the eigenfunctions, i.e. the electronic wave functions, resulting from a Schrödinger equation including a periodic potential in the Hamiltonian are described by a product of a planewave and a function, which exhibits the periodicity of the crystal

$$\varphi_{\mathbf{k}}(\mathbf{r}) = e^{i\mathbf{kr}} u_{\mathbf{k}}(\mathbf{r}) \quad \text{with} \quad u_{\mathbf{k}}(\mathbf{r} + \mathbf{R}_n) = u_{\mathbf{k}}(\mathbf{r}) \quad . \tag{3.3}$$

Here, $\mathbf{k}$ is the wave vector within the first Brillouin zone. An obvious choice of basis functions to expand the Kohn-Sham wave functions satisfying Eq. (3.3) are planewaves. Planewaves are periodic and mathematically fairly simple. A disadvantage of an expansion in planewaves is the rather large number of basis functions needed for a proper description of the valence wave functions. In contrast to the core electrons, which are quite strongly bound and essentially confined to the core region, the valence electrons have a much larger spatial distribution and are considered as mainly determining the bonding between atoms. Outside of the atomic core region the valence wave functions are rather smooth, whereas in the vicinity of the atomic core they are strongly oscillating. These strong oscillations are induced by the orthogonalization of the valence wave functions to the wave functions of the inner core electrons.

One approach to overcome this problem, which is widely used in the solid state community, is the pseudopotential method [52]. Here, the inner core electrons are not treated explicitly, but they are merged with the nuclei to form the so-called pseudopotential. The wave functions of the valence electrons moving in such a pseudopotential are then much smoother and can thus be described by a much smaller number of planewaves.

Another approach, which in contrast to the pseudopotential method can include all electrons, is the separation of real space into regions close to the nuclei and in between them. The Kohn-Sham orbitals are then expanded differently in each region. The augmented planewave method (APW) [53], which is used in this work, is such an approach and will be described in more detail in the next sections.

3.2 The APW Method

The augmented planewave (APW) method was formulated by Slater in 1937 [54]. Starting from the so-called muffin-tin approximation he constructed a basis set, which consists of a combination of planewaves in regions of a slowly varying potential and atomic orbital like functions in regions of faster varying wave functions. In the muffin-tin approximation the crystal is divided into the muffin-tin (MT) region and the interstitial (I). The muffin-tin region consists of non-overlapping spheres centered around each atom. The potential can then be defined as

$$V_{\mathrm{MT}}(\mathbf{r}) \equiv \begin{cases} \text{constant} & \mathbf{r} \in \mathrm{I} \\ V(r_\alpha) & \mathbf{r} \in \mathrm{MT}_\alpha \end{cases} \tag{3.4}$$

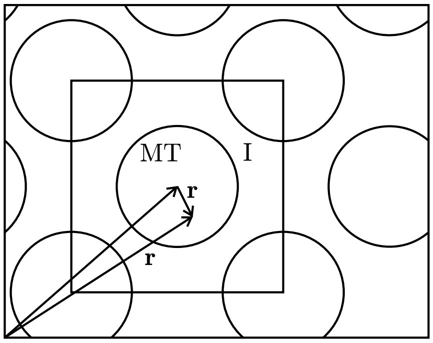

Figure 3.1: Schematic illustration of the muffin-tin potential approximation. Space is divided into muffin-tin spheres (MT_α) centered at each nuclei and the interstitial region (I). (After Ref. [55])

Here α is the index for counting the spheres and r_α is the length of the local position vector $\mathbf{r}_\alpha = \mathbf{r} - \boldsymbol{\tau}_\alpha$ (cf. Fig. (3.1)). The potential $V_{\mathrm{MT}}(\mathbf{r})$ is constant in the interstitial and spherical in the muffin-tin region. The APW basis functions can be written as

$$\phi^{\mathrm{APW}}_{\mathbf{k}+\mathbf{G}}(\mathbf{r},\epsilon) = \begin{cases} \Omega^{-1/2} e^{i(\mathbf{k}+\mathbf{G})\cdot\mathbf{r}} & \mathbf{r} \in \mathrm{I} \\ \sum_{lm} A^{\alpha,\mathbf{k}+\mathbf{G}}_{lm} u_l(r_\alpha,\epsilon) Y_{lm}(\hat{\mathbf{r}}_\alpha) & \mathbf{r} \in \mathrm{MT}_\alpha \end{cases} \tag{3.5}$$

where Ω is the unit cell volume, Y_{lm} is the spherical harmonic function and $\hat{\mathbf{r}}_\alpha$ is the angular part of the local vector $\mathbf{r}_\alpha$. A_{lm} is an expansion coefficient to match the function ϕ at the boundary between the muffin-tin and the interstitial and u_l is the regular solution of the radial Schrödinger equation

$$-\frac{1}{r^2}\frac{d}{dr}\left(r^2\frac{du_l}{dr}\right) + \left[\frac{l(l+1)}{r^2} + V(r) - \epsilon\right] r u_l = 0 \quad , \tag{3.6}$$

with the spherical potential $V(r)$ from Eq. (3.4). Each basis function is connected to a special **k**-point $\mathbf{k}$ and a reciprocal lattice vector $\mathbf{G}$.

In the APW method the augmenting function $u_l(r,\epsilon)$ corresponds to the exact muffin-tin potential eigenstate of eigenenergy ϵ. Because of this energy dependence of the function $u_l(r,\epsilon)$ the eigenvalue problem will be non-linear in energy and has to be solved iteratively. This is, however, computationally very costly. On the other hand, any eigenstate of a different eigenenergy will be poorly described without adapting ϵ. To overcome this problem linearized versions of the APW method have been developed, where the energy ϵ is set to a fixed value ϵ_1 and the basis functions are modified to gain extra flexibility to cover a larger energy region around their linearization energy. The linearized APW method (LAPW) and the APW+ local orbitals (APW+lo) method will be discussed in more detail in the next two sections.

3.3 The LAPW Method

The traditional way of linearizing the APW method is the LAPW method, which was developed in the beginning of the 1970s [56, 53]. In this approach the basis functions are expanded in the same way as in Eq. (3.5) in the interstitial, but inside the muffin-tin the basis functions do not only depend on $u_l(r,\epsilon_1)$, but also on its derivative $\dot{u}_l(r,\epsilon_1) \equiv \partial u_l/\partial\epsilon$,

$$\phi^{\mathrm{LAPW}}_{\mathbf{k+G}}(\mathbf{r},\epsilon_1) = \begin{cases} \Omega^{-1/2} e^{i(\mathbf{k+G})\cdot\mathbf{r}} & \mathbf{r} \in \mathrm{I} \\ \sum_{lm} [A^{\mathbf{k+G}}_{lm}\, u_l(r,\epsilon_1) + B^{\mathbf{k+G}}_{lm}\, \dot{u}_l(r,\epsilon_1)] Y_{lm}(\hat{\mathbf{r}}) & \mathbf{r} \in \mathrm{MT} \end{cases} \quad . \tag{3.7}$$

Here and also in the further equations, the sphere index α has been omitted for clarity. The LAPW's are thus more flexible than the APW's, since for any linearization energy ϵ_1, that differs only slightly from the real eigenenergy ϵ, the radial function $u_l(r,\epsilon)$ can be obtained by a Taylor expansion

$$u_l(r,\epsilon) = u_l(r,\epsilon_1) + (\epsilon-\epsilon_1)\dot{u}_l(r,\epsilon_1) + O((\epsilon-\epsilon_1)^2) \quad . \tag{3.8}$$

The additional term $O((\epsilon-\epsilon_1)^2)$ leads to a second order error in the wave function and a fourth order error in the eigenenergy. However, the two coefficients $A^{\mathbf{k+G}}_{lm}$ and $B^{\mathbf{k+G}}_{lm}$ are not fixed through the Taylor expansion, but by matching both the value and the slope of the augmenting function to a planewave at $\mathbf{R}_{\mathrm{MT}}$. Due to the matching constraints the shape of the function resulting from the linear combination of $u_l(r,\epsilon_1)$ and $\dot{u}_l(r,\epsilon_1)$ will in general not resemble the physical solution u_l. By linearizing the APWs the problem of having energy dependent basis functions is resolved, but the optimal shape of the basis functions inside the muffin-tin sphere is sacrificed (cf. Fig. (3.2)).

3.3.1 Semi-Core States

In the LAPW method there is only one linearization energy ϵ_1 for every l quantum number. This leads to a problem in systems with states having the same l quantum number, but different n quantum number and therefore also clearly different energies. The problem occurs mainly for systems with so-called semi-core states, which do not lie in the valence region, but also not as low in energy as the core states. Semi-core states are treated by introducing local orbitals in the LAPW method. Local orbitals do not depend on **k** and **G**, but only belong to one atom and have a specific l character. They are called *local*, since they are confined to the muffin-tin spheres and thus zero in the interstitial

$$\phi^{\mathrm{LO}} = \begin{cases} 0 & \mathbf{r} \in \mathrm{I} \\ [A_{lm}\, u_l(r,\epsilon_1) + B_{lm}\, \dot{u}_l(r,\epsilon_1) + C_{lm}\, u_l(r,\epsilon_2)] Y_{lm}(\hat{\mathbf{r}}) & \mathbf{r} \in \mathrm{MT} \end{cases} \quad . \tag{3.9}$$

Inside the muffin-tin spheres local orbitals involve an additional radial function evaluated at a new linearization energy ϵ_2. Two of the coefficients are determined by

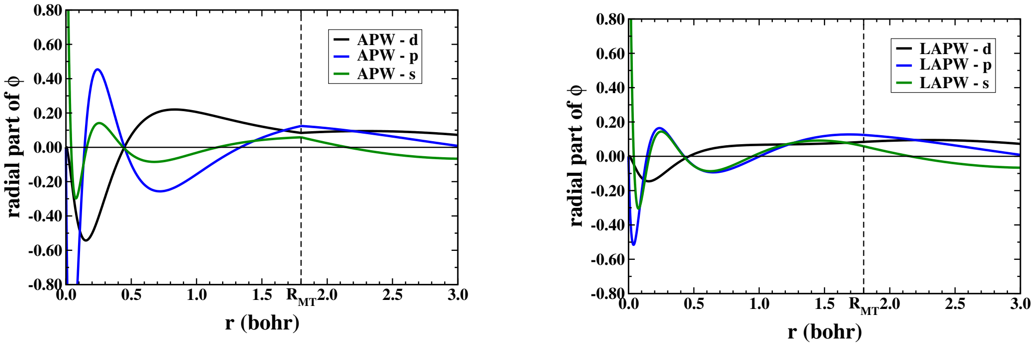

Figure 3.2: Radial part u_l of the l-composition of an APW basis function (left) and the linear combination of u_l and $\dot{u}_l$ of the l-composition of an LAPW basis function (right) for a specific **k**-point. The planewaves are expanded into Bessel functions.

the conditions that the value and first derivative of the local orbitals go to zero at the sphere boundary. The third one can be set to some fixed number, e.g. unity (a modification is used for lattices with inversion symmetry, cf. Section 5.9 in Ref. [53]). The resulting LAPW+LO basis set can be used to describe both the valence region and the already quite localized semi-core states appropriately.

3.4 The APW+lo Method

An alternative method to linearize the APW method is the APW+local orbitals method [57, 58, 55]. Also in this method the eigenvalue problem is linearized by choosing a fixed linearization energy ϵ_1. However, the necessary gain in flexibility is not obtained by adding an additional term to the original APW basis functions, but by a complementary set of local orbitals

$$\phi^{\mathrm{lo}_1} = \begin{cases} 0 & \mathbf{r} \in \mathrm{I} \\ [A_{lm}\, u_l(r, \epsilon_1) + B_{lm}\, \dot{u}_l(r, \epsilon_1)] Y_{lm}(\hat{\mathbf{r}}) & \mathbf{r} \in \mathrm{MT} \end{cases} \quad . \tag{3.10}$$

Each local orbital is matched to zero value at the sphere boundary having no restriction on the derivatives at the muffin-tin boundaries. Thus, a surface term for the kinetic energy has to be taken into account [53]. The complete APW+lo basis set consists therefore of two different types of basis functions, the APWs (Eq. (3.5)) at a fixed linearization energy ϵ_1 and the lo's (Eq. (3.10)), so that the basis set is defined as

$$\phi_i = \begin{cases} \phi_i^{\mathrm{APW}} & i \leq N_{\mathrm{APW}} \\ \phi_i^{\mathrm{lo}_1} & i > N_{\mathrm{APW}} \end{cases} \quad . \tag{3.11}$$

Here, N_{APW} is some integer number, which depends on the total basis set size and the number of included local orbitals. The advantage of this alternative linearization compared to the LAPW method is, that the optimal shape of the basis functions inside the muffin-tin is maintained (cf. Fig. 3.2), which leads to a better description of the eigenstate and therefore to a smaller basis set size to reach the same accuracy.

3.4.1 Semi-Core States

Just as in the LAPW method there is only one linearization energy ϵ_1 per l quantum number, which leads to a problem in the description of semi-core states. In the APW+lo method these semi-core states are treated by a *second* set of local orbitals

$$\phi^{\mathrm{lo}_2} = \begin{cases} 0 & \mathbf{r} \in \mathrm{I} \\ [A_{lm}\, u_l(r, \epsilon_1) + C_{lm}\, u_l(r, \epsilon_2)] Y_{lm}(\hat{\mathbf{r}}) & \mathbf{r} \in \mathrm{MT} \end{cases} \quad . \tag{3.12}$$

Here again the local orbital is introduced with a second linearization energy ϵ_2, which can be chosen to lie in the semi-core region, so that eigenstates with the same l quantum number but different principle quantum number n can be treated properly. Also these local orbitals are matched to zero value at the sphere boundary without any restriction on the first derivative.

3.5 Mixed Augmentation

It has been shown by Madsen *et al.* [58] that the APW+lo method usually converges much faster than the LAPW method. This means that the same accuracy in e.g. the total energy is reached in the APW+lo method already with a smaller basis set compared to the LAPW method. Normally additional lo's are only needed for the expansion up to the *physical* l quantum numbers (i.e. l quantum numbers contained in the electronic configuration of the corresponding element), whereas the higher l quantum numbers are sufficiently treated by pure APW's. However, for some cases also higher l quantum numbers require additional lo's in the complementary basis set, which lessens the gain in basis set size. On the other hand, radial functions of physically not significant l-character do not have a particular advantage of the exact shape of u_l. Therefore a mixed augmentation has been proposed [58], where the physically important l quantum numbers are treated by APW+lo and the higher l quantum numbers are augmented using LAPW, the so-called (L)APW+lo method. All results presented in this work were obtained using the mixed (L)APW+lo scheme.

3.6 The Full Potential (L)APW+lo Method

The accuracy of the (L)APW+lo method can be further improved by using the full potential (FP), i.e. the muffin-tin potential in Eq. (3.4) is replaced by a non-constant potential in the interstitial and a non-spherical part inside the muffin-tin

$$V(\mathbf{r}) = \begin{cases} \sum_{\mathbf{G}} V_{\mathbf{G}}\, e^{i\mathbf{G}\cdot\mathbf{r}} & \mathbf{r} \in \mathrm{I} \\ \sum_{lm} V_{lm}(r) Y_{lm}(\hat{\mathbf{r}}) & \mathbf{r} \in \mathrm{MT} \end{cases} \quad . \tag{3.13}$$

These corrections are also called non-muffin-tin corrections. The choice of basis functions in the interstitial is not effected by the non-muffin-tin corrections, but the radial functions u_l as defined in Eq. (3.6) are no longer the exact solutions inside the muffin-tin sphere. In principle the function u_l would have to be evaluated using the true crystal potential of the muffin-tin region, which is, however, not expected to greatly improve the results, since the non-muffin-tin correction represent only a modest change of the muffin-tin potential. In addition the basis functions in the linearized APW methods should be flexible enough to describe the eigenstates altered by the non-muffin-tin corrections as well as the ones in the muffin-tin potential [59].

3.7 Application To Solids And Surfaces

As already mentioned in Section 3.1 crystalline solids can be best described by exploiting their inherent symmetry and therefore using periodic boundary conditions. Besides an appropriate choice of basis functions the integration over the Brillouin zone is an important factor regarding both the accuracy and the computational cost. A second point, that will be discussed in this Section is the treatment of semi-infinite surfaces in periodic boundary conditions by applying the so-called supercell approach. In the last part of this Section the calculation of surface core-level shifts within the FP-(L)APW+lo method is described.

3.7.1 Integration Over The Brillouin Zone

To evaluate many of the physical quantities of a solid (e.g. electron density, total energy, forces etc.) a summation over all occupied states has to be accomplished. For a crystalline solid this leads to an integration over the Brillouin zone, resp. if the symmetry of the system is considered, to an integration over the *irreducible* part of the Brillouin zone. Numerically this is solved by replacing the integral by a sum over a finite number of **k**-points

$$\int_{\mathrm{BZ}} \frac{1}{\Omega_{\mathrm{BZ}}} d\mathbf{k} \rightarrow \sum_{\mathbf{k}} \omega_{\mathbf{k}} \quad . \tag{3.14}$$

Several methods have been suggested to obtain a most efficient summation over the **k**-points, the two most prominent examples are the tetrahedron method [60] and the special **k**-point method according to Monkhorst and Pack [61]. The results presented in this work were obtained using the Monkhorst-Pack (MP) method. In this method a weighted summation over a grid consisting of representative **k**-points is performed.

These special **k**-points are identified by the following steps: (1) generating a homogeneous grid over the full Brillouin zone, (2) combining symmetry related **k**-points into groups, (3) choosing one representative **k**-point out of every group of equivalent **k**-points and assigning the proper weight $\omega(\mathbf{k})$. $\omega(\mathbf{k})$ is given by the number of **k**-points in a specific group divided by the total number of **k**-points.

In the case of metals one has to cope with an additional problem. Since in metals the bands are crossing the Fermi level ϵ_{F} the occupation and therefore also the integration over the Fermi surface is discontinuous. This can lead to difficulties in the convergence of the self-consistent field cycle. One solution to overcome this problem is the implementation of a Fermi distribution at a finite temperature to artificially broaden the Fermi surface. After the integration the free energy will be extrapolated again to $T = 0\,\mathrm{K}$.

3.7.2 The Supercell Approach

The supercell approach is one possibility to model surfaces using periodic boundary conditions. In principle it would be possible to use only two-dimensional periodicity, but in the (L)APW+lo approach this would require an additional matching constraint to determine the layer for the decay of the planewaves. For systems including e.g. the adsorption of oxygen, as described within this work, such a two-dimensional approach is not necessarily advantageous. In the here applied method the surfaces are modeled with periodic boundary conditions in all three dimensions. The semi-infinite surface is described by slabs, that are infinite in the xy-direction, but only consist of several layers in z-direction. The periodicity in z-direction is artificially maintained by a supercell containing the slab and a vacuum region as shown in Fig. 3.3. To obtain reliable results using a supercell two main parameters have to be considered, the number of layers in the slab and the vacuum thickness. Having two surfaces at the top and the bottom of the slab the number of layers has to be big enough to avoid interactions between these two surface. Atoms in the center of the slab should already exhibit the physical properties of atoms in the bulk. To avoid interactions between the surfaces of consecutive slabs the vacuum region has to be large enough. In planewave based methods, like the (L)APW+lo method, calculations of surfaces can become computational very costly, since also the vacuum region is described by the planewaves, which increases the basis set considerably.

A alternative approach, which is not based on periodic boundary conditions, is the cluster method. Here, the surface is modeled by a large cluster. The decisive parameter in this approach is the cluster size, which strongly influences both the accuracy and the computational cost.

3.7.3 Surface Core-Level Shifts

Evaluating the results of a DFT calculation there are, besides the total energy, also several other quantities available regarding the electronic structure of the investigated

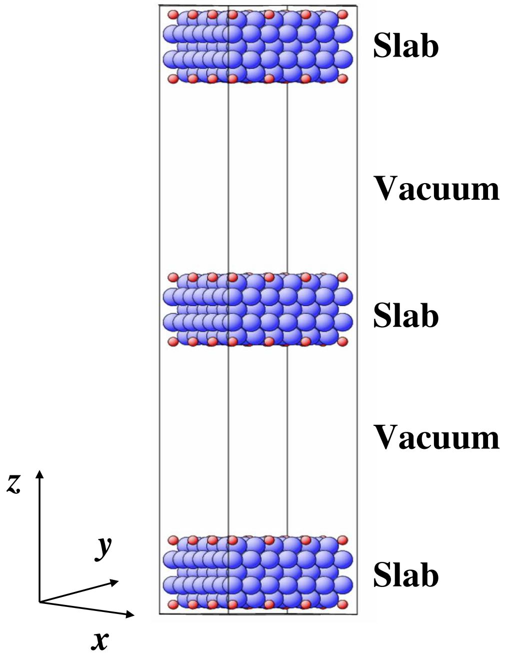

Figure 3.3: Schematic representation of the supercell approach for the calculation of a (100) surface including adsorbate atoms. In the z-direction the supercell consists of a slab (containing several atomic layers) and vacuum. Repeating the supercell periodically in all three dimensions results in the shown figure.

system, which can then be compared to experimental findings. One of these quantities is the surface core-level shift (SCLS), which results from the change in the core-level position of a surface atom compared to the core-level of the corresponding atom in the bulk. The respective SCLS is then given by the difference in energy, that is needed, to remove an electron from the core-level of either a bulk or a surface atom [62, 63]

$$\Delta_{\mathrm{SCLS}} = \left[E^{\mathrm{surf}}(n_c - 1) - E^{\mathrm{surf}}(n_c)\right] - \left[E^{\mathrm{bulk}}(n_c - 1) - E^{\mathrm{bulk}}(n_c)\right] \quad . \tag{3.15}$$

$E^{\mathrm{surf}}(n_c)$ is the total energy of the surface (slab) depending on the number of electrons n_c in the core-level c, $E^{\mathrm{bulk}}(n_c)$ the respective total energy of the bulk system. In the theoretical description it is possible to separate the total SCLS into an initial and a final state contribution. The initial state contribution includes the change in the electronic distribution before the excitation of the core electron and can be approximated by a Taylor expansion of Eq. (3.15)

$$\Delta_{\mathrm{SCLS}}^{\mathrm{initial}} \approx -\left[\epsilon_c^{\mathrm{surf}}(n_c) - \epsilon_c^{\mathrm{bulk}}(n_c)\right] \quad . \tag{3.16}$$

Here, ϵ_c is the Kohn-Sham eigenvalue of the core state c. Since the FP-(L)APW+lo method used in this work is an all electron method it is particularly straightforward to obtain the initial state contribution to the SCLS.

In addition to this initial state contribution the experimentally measured SCLS also contains a final state contribution, which arises from the different screening capabilities of the valence electrons in the core-ionized system at the surface and in the bulk. One possibility to determine the corresponding ionization energy is the calculation of the total energy of an impurity with a core hole in the respective core state. The difference in the total energies of the system with the impurity located at the surface and of the one with the impurity in the bulk gives then the SCLS [64]. This difference can also be approximated within the Slater-Janak transition state approach [65]. Here, total energy differences are evaluated as

$$E(n_c - 1) - E(n_c) = \int_{n_c}^{n_c-1} \frac{\partial E(n')}{\partial n'} dn' = \int_{n_c}^{n_c-1} \epsilon_c(n') dn' \quad , \tag{3.17}$$

and using the mean value theorem of integration

$$\int_{n_c}^{n_c-1} \epsilon_c(n') dn' \approx -\epsilon_c(n_c - 1/2) \quad , \tag{3.18}$$

the total SCLS, including both initial and final state contributions, is then given by combining Eq. (3.15) and Eq. (3.18)

$$\Delta_{\mathrm{SCLS}}^{\mathrm{total}} \approx - \left[\epsilon_c^{\mathrm{surf}}(n_c - 1/2) - \epsilon_c^{\mathrm{bulk}}(n_c - 1/2) \right] \quad . \tag{3.19}$$

In the two described approaches the total SCLS is approximated by the energy difference of two *ground states*, which is only valid, if the screening is perfect, i.e. if the excited electron contains the whole screening energy. For the actual calculation of the total SCLS half an electron is removed from the core level of the respective atom, and for metallic systems having a Fermi reservoir of electrons this half electron is then again added at the Fermi level to simulate the effect of a perfect screening. Within the supercell approach a further complication has to be considered. Here, the ionized atoms can interact with their periodic images, so that the supercell has to be large enough to avoid such an artificial interaction.

Considering these uncertainties, the total SCLS might not always fully agree with the experimental results, but is still more suitable for a direct comparison than the initial SCLS. Additional information can be obtained from the difference between the initial and total SCLS, the screening, which might be related to the electronic hardness and surface chemical activity of the system [66].

3.8 The WIEN2k Code

All DFT calculations presented in this work have been performed using the WIEN2k software package [67]. The WIEN2k code is based on the full potential (L)APW+lo method and was mainly developed for the use in solid state physics. Since calculations are only possible using periodic boundary conditions, all surface calculations are performed within the supercell approach.

The WIEN2k code consists of two parts, the initialization and the main selfconsistent-field cycle. Each part again is composed of several independent programs, that are linked via shell-scripts. In addition many analytical tools are implemented to calculate e.g. band structure, density of states, charge densities etc.

Since the FP-(L)APW+lo method is considered one of the most accurate methods in DFT, results obtained with this method are often taken as benchmark. However, the prize for the high accuracy is the comparable high computational cost. For bulk systems the WIEN2k code performs actually rather well, but for surface calculations using a supercell the calculations become quite time consuming [68]. For this work it was therefore also quite important, that a good parallelization is implemented in the WIEN2k code. There are two kinds of parallelization available, the first one parallelizes over the **k**-points, so that every **k**-point can be calculated separately on a single CPU. This method needs only very little communication between the CPUs and scales quasi linear with the number of CPUs, so that there is almost no loss of resources due to the parallelization. On the other hand, in big systems the number of **k**-points becomes small and therefore also the number of CPUs, that can be used for the parallelization. For big systems with few **k**-points the second parallelization method becomes very attractive. The so-called fine grained parallelization uses different strategies in different parts of the program. The most important part is the parallelization of the setup and diagonalization of the Hamilton and overlap matrices. This parallelization is much more involved and requires a fast communication between the CPUs. The efficiency of the parallelization depends strongly on the number of CPUs and the matrix size [69]. The number of CPUs, N_{CPU}, has to be $N_{\mathrm{CPU}} = 2^{\mathrm{n}}$, where n is an integer number, and a minimum number of four CPUs, $N_{\mathrm{CPU}} \geq 4$, should be used. The matrix size, N_{MAT}, should be $N_{\mathrm{MAT}} \geq 3000$. The scaling $(t_{\mathrm{single}}/(N_{\mathrm{CPU}} \cdot t_{\mathrm{parallel}}))$ can then be as good as ≈ 0.7, which means, that e.g. for a parallelization over 8 CPUs the speed up is ≈ 5.6 compared to a single CPU. For a matrix size of $N_{\mathrm{MAT}} \approx 3000$ the scaling becomes slightly less efficient for $N_{\mathrm{CPU}} \geq 32$ due to the increasing amount of communication compared to gain in computing time. For larger matrices, though, also a larger number of CPUs can be used, for $N_{\mathrm{MAT}} \geq 10000$ the scaling is efficient up to $N_{\mathrm{CPU}} \leq 128$ and for $N_{\mathrm{MAT}} \geq 22000$ even up to $N_{\mathrm{CPU}} \leq 256$.

In the WIEN2k code these two parallelization method can also be combined, so that also quite big supercells can be calculated in a reasonable time provided that the necessary computer resources are available.

Chapter 4

DFT And Thermodynamics

Density-functional theory has nowadays become a standard tool for electronic structure calculations. Using this technique a detailed insight into the microscopic regime can be obtained. On the other hand one would like to understand and describe material science problems, like in this work heterogenous catalysis, which are clearly on a macroscopic time and length scale. To explain macroscopic phenomena on the basis of a microscopic understanding a huge range of time and length scales needs to be covered. To find an appropriate linking between the micro-, meso- and macroscopic regime is referred to as *multiscale modeling* approach [27, 28]. In Fig. 4.1 the time and length scales for the different regimes are schematically shown. Also the different

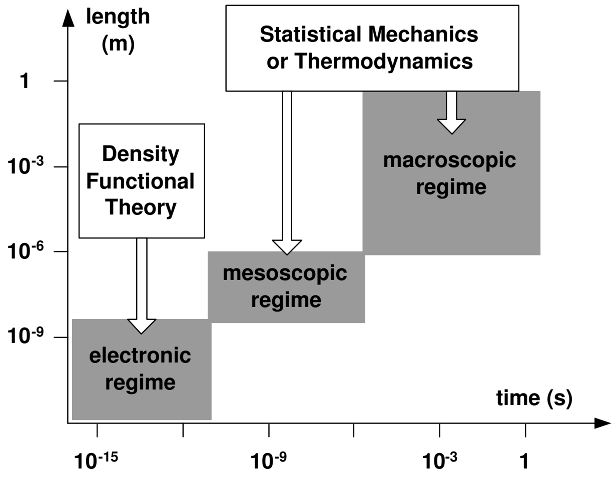
length (m)
1
10^{-3}
10^{-6}
10^{-9}
Statistical Mechanics or Thermodynamics
Density Functional Theory
macroscopic regime
mesoscopic regime
electronic regime
time (s)
10^{-15}
10^{-9}
10^{-3}
1

Figure 4.1: Schematic representation of the time and length scales for the micro-, meso- and macroscopic regime. Several methods have been developed to tackle problems within a certain regime. In the multiscale modeling approach an appropriate linking between the different regimes is developed, so that information obtained in the microscopic regime can, e.g., be transferred into the meso- and macroscopic regime (from Ref. [27]). The present study concentrates on a linking between the electronic and macroscopic regimes.

methods used in this work to describe the different regimes are indicated. As already mentioned DFT is used for the electronic (microscopic) regime. The results from DFT are then combined with concepts from thermodynamics and statistical mechanics to reach the meso- and macroscopic regime. Since the results obtained within DFT do not rely on semi-empirical or fitted parameters they are referred to *first principle* or *ab initio*. Using DFT or other first-principle electronic structure theory results as input to macroscopic theories is similarly classified as first-principle (*ab initio*).

This Chapter focuses on the linking between DFT and thermodynamics, whereas in Chapter 5 a combination of DFT and statistical mechanics is described.

4.1 Ab Initio Atomistic Thermodynamics

In results obtained from electronic structure calculations temperature and pressure effects are not included, i.e. all evaluated physical quantities are strictly only valid at $T = 0\,\mathrm{K}$ and $p = 0\,\mathrm{atm}$. The effect of temperature on the atomic positions can be obtained, though, by evaluating the total energy as a function of the nuclear positions, $\{\mathbf{R}_A\}$, on the Born-Oppenheimer surface (cf. Section 2.1). The resulting Born-Oppenheimer potential energy surface can then be used to extract further information as e.g. vibrational modes. To now actually describe situations of finite temperatures and pressures the results from DFT calculations can be used as an input to thermodynamic considerations [70, 71, 72, 73]. The appropriate thermodynamic functions can then be evaluated over the whole temperature and pressure range.

The key quantity in studying a (T, p)-ensemble is the Gibbs free energy G

$$G(T, p) = E^{\mathrm{tot}} + F^{\mathrm{vib}} - TS^{\mathrm{conf}} + pV \quad . \tag{4.1}$$

The leading term is the total energy E^{tot}, which is directly obtained from the electronic structure calculations. The second term F^{vib} accounts for the vibrational contributions (with $F^{\mathrm{vib}} = E^{\mathrm{ZPE}} - TS^{\mathrm{vib}}$ being the vibrational free energy). The third term TS^{conf} includes configurational entropy and the last one is the pV-term. An evaluation of the different contributions to the Gibbs free energy will be exemplified below for the calculation of the surface free energy and the Gibbs free energy of adsorption.

The combination of DFT and thermodynamics is applicable to systems, that are in thermodynamic equilibrium. This implies another important concept. A system in thermodynamic equilibrium can be divided into smaller subsystems, which again are in thermodynamic equilibrium with each other. In the atomistic thermodynamics approach every subsystem can then be treated separately within DFT. This is especially useful, if infinite but homogeneous subsystems, such as bulk or gas phases acting e.g. as a reservoir, are involved [74, 75, 76, 8, 9, 77].

The general concept of atomistic thermodynamics is exemplified here once for the calculation of the surface free energy and once for the Gibbs free energy of adsorption.

4.2 Surface Free Energy

In equilibrium, a one-component system can be fully described by its internal energy E, which depends on the entropy S, the volume V and the number of particles N in the system

$$E^{\text{bulk}} = TS - pV + N\mu \quad , \tag{4.2}$$

with μ being the chemical potential. If a homogeneous solid is cleaved, two surfaces of size A are being created. Since this process does not occur spontaneously the internal energy of the system has to increase by an amount proportional to A. The constant of proportionality is defined as the surface energy γ [78], so that the internal energy of a cleaved crystal can be written as

$$E^{\text{surf}} = TS - pV + N\mu + \gamma A \quad . \tag{4.3}$$

Introducing again the Gibbs free energy $G = E - TS + pV$ and rearranging Eq. (4.3) the surface free energy for a one-component system is defined as

$$\gamma = \frac{1}{A}[G^{\text{surf}} - N\mu] \quad , \tag{4.4}$$

where G^{surf} is the Gibbs free energy of the cleaved crystal. For a multi-component system being in equilibrium with atomic reservoirs (e.g. a surrounding gas or liquid phase environment, or a macroscopic bulk phase) the expression for the surface free energy can be written more general as

$$\gamma(T, p_i) = \frac{1}{A}\left[G^{\text{surf}} - \sum_i N_i \mu_i(T, p_i)\right] \quad . \tag{4.5}$$

G^{surf} is again the Gibbs free energy of the solid including the surface and $\mu_i(T, p_i)$ is the chemical potential of the various species i present in the system. In the following the application of Eq. (4.5) to *metal oxides* in equilibrium with a surrounding *oxygen gas phase* is discussed (cf. Fig. 4.2). All presented equations can be applied similarly to any other two-component system or easily be extended to multi-component systems. In the case of a metal oxide the surface free energy is a function of the chemical potential of the metal μ_{M} and the oxygen μ_{O}

$$\gamma(T, p) = \frac{1}{A}\left[G^{\text{surf}}(T, p, N_{\text{M}}, N_{\text{O}}) - N_{\text{M}}\mu_{\text{M}}(T, p) - N_{\text{O}}\mu_{\text{O}}(T, p)\right] \tag{4.6}$$

Here, N_{M} and N_{O} are the number of metal and oxygen atoms within the finite part of the total (infinite) system, G^{surf}, that is influenced by the created surface. With increasing distance from the surface the solid as well as the gas phase part of the total system will become equivalent to the homogeneous solid and gas phase systems represented by μ_{M} and μ_{O}. By subtracting the respective amount of the homogeneous

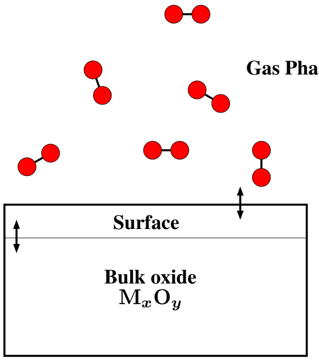

Figure 4.2: Surface in thermodynamic equilibrium with a surrounding gas phase and the underlying bulk phase. If the different phases are in thermodynamic equilibrium, their chemical potentials have to be equal. Thus the system can be divided into three subsystem, bulk oxide, surface and gas phase, the energetics of which can be treated separately within DFT.

systems from the total system these parts are effectively canceled out, so that the surface free energy can sufficiently be determined by the finite part containing N_{M} metal and N_{O} oxygen atoms. Because the surface is in equilibrium with the underlying bulk oxide, the two chemical potentials μ_{M} and μ_{O} can not be varied independently. They connect via the Gibbs free energy of the bulk oxide. In thermodynamic equilibrium this is determined by

$$x\mu_{\mathrm{M}} + y\mu_{\mathrm{O}} = g^{\mathrm{bulk}}_{\mathrm{M}_x\mathrm{O}_y}(T,p) \quad , \tag{4.7}$$

where the small g denotes the Gibbs free energy per formula unit. Substituting Eq. (4.7) into Eq. (4.6) one obtains the surface free energy depending only on the chemical potential of the oxygen μ_{O}

$$\gamma(T,p) = \frac{1}{A}\left[G^{\mathrm{surf}}(T,p,N_{\mathrm{M}},N_{\mathrm{O}}) - \frac{N_{\mathrm{M}}}{x} g^{\mathrm{bulk}}_{\mathrm{M}_x\mathrm{O}_y}(T,p) - (N_{\mathrm{O}} - \frac{y}{x}N_{\mathrm{M}})\mu_{\mathrm{O}}(T,p)\right] \quad . \tag{4.8}$$

The chemical potential is fully determined by the temperature and pressure conditions of the surrounding oxygen gas phase. Using Eq. (4.8) the surface free energy of any given metal oxide surface can be calculated and their thermodynamic stabilities can be compared with respect to the given gas phase conditions.

Range Of Allowed Chemical Potentials

Although the oxygen chemical potential μ_{O} can theoretically be varied from minus to plus infinity, it only makes sense within certain boundaries. For a metal oxide a suitable lower boundary of μ_{O}, which will be called the *O-poor limit*, is defined by the decomposition of the oxide into the pure metal and gas phase oxygen. In terms of thermodynamic quantities this point is reached, if the chemical potential of the metal in the considered oxide system, μ_{M}, becomes larger than its Gibbs free energy in the metal bulk, $g_{\mathrm{M}}^{\mathrm{bulk}}$. This upper bound of μ_{M},

$$\mu_{\mathrm{M}} \leq g_{\mathrm{M}}^{\mathrm{bulk}} \tag{4.9}$$

can be transformed into a lower bound of μ_{O} by utilizing Eq. (4.7)

$$\mu_{\mathrm{O}}(T,p) \geq \frac{1}{y}\left(g_{\mathrm{M}_x\mathrm{O}_y}^{\mathrm{bulk}}(T,p) - x g_{\mathrm{M}}^{\mathrm{bulk}}(T,p)\right) \quad . \tag{4.10}$$

A reasonable upper bound of the chemical potential for a system describing a surface in equilibrium with a gas phase is given by such gas phase conditions, in which the gaseous component is so highly concentrated, that condensation will start on the sample at low enough temperatures. Again, for the example of a metal oxide in equilibrium with an oxygen gas phase this *O-rich limit* will be defined here as

$$\mu_{\mathrm{O}} \leq 1/2 E_{\mathrm{O}_2}^{\mathrm{tot}} \quad , \tag{4.11}$$

with $E_{\mathrm{O}_2}^{\mathrm{tot}}$ being the total energy of the oxygen gas phase. Combining Eq. (4.10) and Eq. (4.11) the range of evaluated oxygen chemical potential is given by

$$\underbrace{\frac{1}{y}\left(g_{\mathrm{M}_x\mathrm{O}_y}^{\mathrm{bulk}}(T,p) - x g_{\mathrm{M}}^{\mathrm{bulk}}(T,p) - \frac{y}{2}E_{\mathrm{O}_2}^{\mathrm{tot}}\right)}_{\simeq \Delta G_{\mathrm{M}_x\mathrm{O}_y}^{f}(0,0)} \leq \underbrace{\mu_{\mathrm{O}}(T,p) - 1/2 E_{\mathrm{O}_2}^{\mathrm{tot}}}_{\Delta\mu_{\mathrm{O}}(T,p)} \leq 0 \quad . \tag{4.12}$$

Here, $\Delta G_{\mathrm{M}_x\mathrm{O}_y}^{f}(0,0)$ is the heat of formation of the corresponding bulk oxide at $T = 0\,\mathrm{K}$. By replacing μ_{O} with $\Delta\mu_{\mathrm{O}}$ the total energy of the oxygen gas phase, $1/2E_{\mathrm{O}_2}^{\mathrm{tot}}$, which marks the upper boundary, is set as a zero reference. This can be done, because the total energy $E_{\mathrm{O}_2}^{\mathrm{tot}}$ does not depend on temperature and pressure. All (T,p)-dependent terms are summarized in $\Delta\mu_{\mathrm{O}}$, cf. Section 4.4. The lower bound is thus approximated by the heat of formation at $T = 0\,\mathrm{K}$. The temperature and pressure dependence of the lower bound introduced by $g_{\mathrm{M}_x\mathrm{O}_y}^{\mathrm{bulk}}(T,p)$ and $g_{\mathrm{M}}^{\mathrm{bulk}}(T,p)$ leads only to small deviations in the here discussed (T,p)-range. An additional advantage of defining the lower bound by $\Delta G_{\mathrm{M}_x\mathrm{O}_y}^{f}(0,0)$ is that the heat of formation is a measurable quantity, which can then also be compared to experimental results.

Surface Free Energy In The O-poor And O-rich Limit

In Eq. (4.8) the dependence of the surface free energy on the chemical potential of the oxygen gas phase is described. To substitute μ_{O} in Eq. (4.8) with the appropriate upper and lower boundaries, Eq. (4.12) is rewritten as

$$\begin{aligned} \frac{1}{y}\left(g_{\mathrm{M}_x\mathrm{O}_y}^{\mathrm{bulk}}(T,p) - x g_{\mathrm{M}}^{\mathrm{bulk}}(T,p)\right) \leq \mu_{\mathrm{O}}(T,p) \leq \\ \leq \frac{1}{y}\left(g_{\mathrm{M}_x\mathrm{O}_y}^{\mathrm{bulk}}(T,p) - x g_{\mathrm{M}}^{\mathrm{bulk}}(T,p)\right) - \frac{1}{y}\Delta G_{\mathrm{M}_x\mathrm{O}_y}^{f}(0,0) \quad . \end{aligned} \tag{4.13}$$

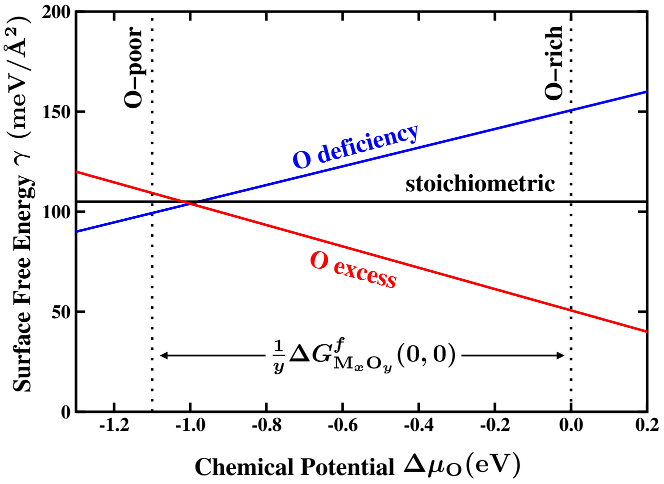

Figure 4.3: Example of plotting the surface free energy γ vs. the chemical potential of the surrounding gas phase $\Delta\mu_\mathrm{O}$. The surface free energy of a stoichiometric surface composition will be independent of the gas phase chemical potential (black line), a surface structure with an oxygen excess (red line) will become more stable and with an oxygen deficiency (blue line) less stable with increasing gas phase chemical potential. The range of allowed oxygen chemical potential is given by the stability of the corresponding bulk oxide, $\frac{1}{y}\Delta G^f_{\mathrm{M}_x\mathrm{O}_y}$.

The surface free energy in the O-poor limit is then obtained by inserting the left part of the inequality (4.13) into the expression for the surface free energy (Eq. (4.8))

$$\begin{aligned}\gamma_{\mathrm{O-poor}}(T,p) =& \frac{1}{A}\Big[G^{\mathrm{surf}}(T,p,N_\mathrm{M},N_\mathrm{O}) - \frac{N_\mathrm{M}}{x} g^{\mathrm{bulk}}_{\mathrm{M}_x\mathrm{O}_y}(T,p) \\ & - \left(\frac{1}{y}N_\mathrm{O} - \frac{1}{x}N_\mathrm{M}\right)\left(g^{\mathrm{bulk}}_{\mathrm{M}_x\mathrm{O}_y}(T,p) - x g^{\mathrm{bulk}}_\mathrm{M}(T,p)\right)\Big] \quad .\end{aligned} \tag{4.14}$$

In the oxygen-rich limit using the right part of Eq. (4.13) yields similarly

$$\gamma_{\mathrm{O-rich}}(T,p) = \gamma_{\mathrm{O-poor}}(T,p) + \frac{1}{A}\left(\frac{1}{y}N_\mathrm{O} - \frac{1}{x}N_\mathrm{M}\right)\Delta G^f_{\mathrm{M}_x\mathrm{O}_y}(0,0) \quad . \tag{4.15}$$

Eq. (4.8) shows a linear dependence of the surface free energy on the chemical potential of the oxygen gas phase. The slope of the resulting line, $-\frac{1}{A}(N_\mathrm{O} - \frac{y}{x}N_\mathrm{M})$, is only determined by the ratio and density of the two components in the system, i.e. in a stoichiometric surface termination, the surface free energy will not depend on the oxygen chemical potential, whereas an oxygen excess will lead to a lowering of γ with increasing μ_O. Respectively, an oxygen deficiency will lead to an increase in the surface free energy with increasing μ_O(cf. Fig. 4.3). The width of the stability range is determined by the stability of the bulk oxide per oxygen atom, i.e. the heat of formation $\frac{1}{y}\Delta G^f_{\mathrm{M}_x\mathrm{O}_y}(0,0)$.

Evaluating The Gibbs Free Energy

To quantitatively calculate the surface free energy in the O-poor and O-rich limit the Gibbs free energies (as defined in Eq. (4.1)) have to be evaluated for the different components. As already mentioned above the leading term is the total energy E^{tot}, which is obtained directly from the electronic structure calculations. In a first approach, an order of magnitude estimate of the remaining terms, the pV-term, the configurational entropy and the vibrational contribution to the surface free energy, is discussed in the following.

The contribution of the last term in Eq. (4.1), the pV-term, can be approximated by a simple dimensional analysis. Since the surface energy is calculated per surface area the pV-term will be roughly $[pV/A] = \text{atm Å}^3/\text{Å}^2 \sim p$ [in atm]$10^{-3}\,\text{meV/Å}^2$. Even for pressures up to $p \sim 100\,\text{atm}$ the pV-contribution will thus still be less than $\sim 0.1\,\text{meV/Å}^2$, which in any case will be insignificant compared to the total energy term. Therefore the contribution of the pV-term to the surface free energy can be safely neglected.

The contribution arising from the configurational entropy is not as easy to estimate and strongly depends on the investigated system. For a complete sampling of the configurational space modern statistical methods, like Monte Carlo simulations, have to be applied, which will be discussed in the following Chapter.

Focusing here on the surface energy of a well-ordered, crystalline metal oxide, nevertheless some approximations can be derived. Here the configurational entropy will mainly result from some disorder, e.g. defects, at the considered surface. From statistical mechanics this configurational entropy is given by

$$S^{\text{conf}} = k_{\text{B}} \ln \frac{(N+n)!}{N!\,n!} \tag{4.16}$$

for a system with N surface sites an a small number of n defects or adsorbate sites, so that $n \ll N$. With A_{site} being the surface area per site, i.e. $A = NA_{\text{site}}$, the energy contribution from the configurational entropy can be written as

$$\frac{TS^{\text{conf}}}{NA_{\text{site}}} = \frac{k_{\text{B}}T}{NA_{\text{site}}} \ln \frac{(N+n)!}{N!\,n!} \quad . \tag{4.17}$$

Applying the Stirling formula ($\ln N! = N \ln N - N$) to Eq. (4.17), for $n, N \gg 1$, yields

$$\frac{TS^{\text{conf}}}{NA_{\text{site}}} = \frac{k_{\text{B}}T}{A_{\text{site}}} \left[\ln\left(1 + \frac{n}{N}\right) + \frac{n}{N} \ln\left(1 + \frac{N}{n}\right) \right] \tag{4.18}$$

Assuming that in a moderately disordered surface the ratio of (n/N) stays within 10%, Eq. (4.18) gives

$$\frac{TS^{\text{conf}}}{A} \leq 0.34 \frac{k_{\text{B}}T}{A_{\text{site}}} \quad . \tag{4.19}$$

For temperatures up to $T = 1000\,\text{K}$ and surface areas per site of about $A_{\text{site}} \approx 10\,\text{Å}^2$ the configurational entropy will thus not contribute more than about $3\,\text{meV/Å}^2$ to the

Gibbs free energy of the surface. To a first approximation this contribution is often also neglected, since in comparing different surface free energies changes in this order of magnitude are often insignificant. It is, however, important to note, that these approximations will not hold for systems having highly disordered surface phases. The atomistic thermodynamics approach as used in this work, on the other hand, is a *direct screening method*, i.e. it can only be used to directly compare the stability of all considered, i.e. of all plausible, structures, but not to sample the configurational space of all, ordered and disordered, structures (as in Monte Carlo simulations). Thus, highly disordered surface phases are usually not considered within this approach.

The remaining vibrational contribution F^{vib} in Eq. (4.1) can in principle be calculated using DFT. In practice this is a very time consuming procedure, since the entire phonon density of states (phonon DOS) $\sigma(\omega)$ at the surface and in the bulk has to be calculated. The free energy F contains an energy E and an entropy S term, which can be calculated via the partition function Z of the system using statistical thermodynamics [79], so that

$$\begin{aligned} F^{\text{vib}}(T,V,N_{\text{M}},N_{\text{O}}) &= E^{\text{vib}} - TS^{\text{vib}} \\ &= -\frac{\partial}{\partial\beta}\ln Z^{\text{vib}} - Tk_{\text{B}}(\ln Z^{\text{vib}} + \beta E^{\text{vib}}) \\ &= -k_{\text{B}}T\ln Z^{\text{vib}} \quad , \end{aligned} \tag{4.20}$$

with $\beta = 1/k_{\text{B}}T$. The vibrational partition function of an N-atomic, solid system is defined as [80]

$$\begin{aligned} Z^{\text{vib}} &= \sum_{i=1}^{3N}\int\frac{d\mathbf{k}}{(2\pi)^3}\sum_{n=0}^{\infty}e^{-[n+(1/2)]\beta\hbar\omega_i(\mathbf{k})} \\ &= \sum_{i=1}^{3N}\int\frac{d\mathbf{k}}{(2\pi)^3}\frac{\exp(-1/2\beta\hbar\omega_i(\mathbf{k}))}{[1-\exp(-\beta\hbar\omega_i(\mathbf{k})]} \end{aligned} \tag{4.21}$$

where $\omega_i(\mathbf{k})$ are the $3N$ vibrational modes. Inserting Eq. (4.21) into Eq. (4.20) and using the phonon DOS $\sigma(\omega)$ the vibrational component of the free energy can then be written as

$$F^{\text{vib}}(T,V,N_{\text{M}},N_{\text{O}}) = \int d\omega F^{\text{vib}}(T,\omega)\sigma(\omega) \quad , \tag{4.22}$$

where the frequency dependent function $F^{\text{vib}}(T,\omega)$ in Eq. (4.22) is then defined as

$$F^{\text{vib}}(T,\omega) = \frac{1}{2}\hbar\omega + k_{\text{B}}T\ln(1-e^{-\beta\hbar\omega}) \quad . \tag{4.23}$$

Instead of calculating the full phonon DOS it might be useful to first obtain an estimate of the magnitude of the phonon contribution to the investigated physical quantity, like in this case to the surface free energy γ. Here, the vibrational contribution, γ^{vib}, only enters as the *difference* in the vibrational energy of atoms in the surface (contributions to $G^{\text{surf}}(T, p, N_{\text{M}}, N_{\text{O}})$) and in the bulk (contributions to $g^{\text{bulk}}_{\text{M}_x\text{O}_y}(T, p)$ and $g^{\text{bulk}}_{\text{M}}(T, p)$). This yield, e.g., in the O-poor limit

$$\begin{aligned} &\gamma^{\text{vib}}_{\text{O-poor}}(T, V) = \\ &= \frac{1}{A}\int d\omega F^{\text{vib}}(T,\omega)\Big[\sigma^{\text{surf}}(\omega) - \frac{N_{\text{O}}}{y}\sigma^{\text{bulk}}_{\text{M}_x\text{O}_y}(\omega) + \Big(\frac{x}{y}N_{\text{O}} - N_{\text{M}}\Big)\sigma^{\text{bulk}}_{\text{M}}(\omega)\Big] \end{aligned} \tag{4.24}$$

As a first estimate of the value of $\gamma^{\text{vib}}_{\text{O-poor}}$ the phonon DOS can be approximated by the Einstein model [80]. In the Einstein model the phonon DOS is simply a delta function at one characteristic frequency $\bar{\omega}$. Here, one characteristic frequency for each atom type is chosen, i.e. for the metal and the oxygen as well as for atoms in the bulk $\bar{\omega}^{\text{bulk}}$ and at the surface $\bar{\omega}^{\text{surf}}$. The vibrational free energy of the surface system can then be expressed as a sum over the different atom types

$$\begin{aligned} \int d\omega F^{\text{vib}}(T,\omega)\sigma^{\text{surf}}(\omega) \approx 3F^{\text{vib,surf}} = \\ = 3\big[(N_{\text{O}} - N^{\text{surf}}_{\text{O}})F^{\text{vib}}(T,\bar{\omega}^{\text{bulk}}_{\text{O}}) + N^{\text{surf}}_{\text{O}}F^{\text{vib}}(T,\bar{\omega}^{\text{surf}}_{\text{O}}) \\ + (N_{\text{M}} - N^{\text{surf}}_{\text{M}})F^{\text{vib}}(T,\bar{\omega}^{\text{bulk}}_{\text{M}}) + N^{\text{surf}}_{\text{M}}F^{\text{vib}}(T,\bar{\omega}^{\text{surf}}_{\text{M}})\big] \quad , \end{aligned} \tag{4.25}$$

where $N^{\text{surf}}_{\text{O}}$ and $N^{\text{surf}}_{\text{M}}$ are the number of oxygen, resp. metal atoms right at the surface. For the other terms the vibrational free energy is similarly

$$F^{\text{vib,bulk}}_{\text{M}_x\text{O}_y} \approx xF^{\text{vib}}(T,\bar{\omega}^{\text{bulk}}_{\text{M}}) + yF^{\text{vib}}(T,\bar{\omega}^{\text{bulk}}_{\text{O}}) \tag{4.26}$$

and

$$F^{\text{vib,bulk}}_{\text{M}} \approx F^{\text{vib}}(T,\bar{\omega}^{\text{bulk}}_{\text{M}}) \quad . \tag{4.27}$$

Substituting Eq. (4.25) – (4.27) into Eq. (4.24) results in the following expression for the vibrational contribution to the surface free energy of a metal oxide

$$\begin{aligned} \gamma^{\text{vib}}_{\text{O-poor}}(T, V) = &\frac{3}{A}\Big(N^{\text{surf}}_{\text{M}}\big[F^{\text{vib}}(T,\bar{\omega}^{\text{surf}}_{\text{M}}) - F^{\text{vib}}(T,\bar{\omega}^{\text{bulk}}_{\text{M}})\big] \\ &+ N^{\text{surf}}_{\text{O}}\big[F^{\text{vib}}(T,\bar{\omega}^{\text{surf}}_{\text{O}}) - F^{\text{vib}}(T,\bar{\omega}^{\text{bulk}}_{\text{O}})\big]\Big) \quad . \end{aligned} \tag{4.28}$$

In Fig. 4.4 $\gamma^{\text{vib}}_{\text{O-poor}}$ is shown for temperatures up to 1000 K, using $\bar{\omega}^{\text{bulk}}_{\text{M}} = 20\,\text{meV}$ and $\bar{\omega}^{\text{bulk}}_{\text{O}} = 70\,\text{meV}$ as a coarse estimate for the characteristic frequencies of the metal and oxygen bulk atoms (considering as example for the characteristic frequencies PdO [81]). Since the change of the vibrational modes at the surface might be quite significant due to the change in coordination, the characteristic frequencies at the surface are allowed to vary ±50 % from the bulk values (two black, solid lines in Fig. 4.4). The surface area A is set to 20 Å^2 having one metal and one oxygen atom at the surface, i.e. $N^{\text{surf}}_{\text{M}} = N^{\text{surf}}_{\text{O}} = 1$. Changing the characteristic frequencies for the bulk atoms by ±50 % does not change the magnitude of the vibrational contribution

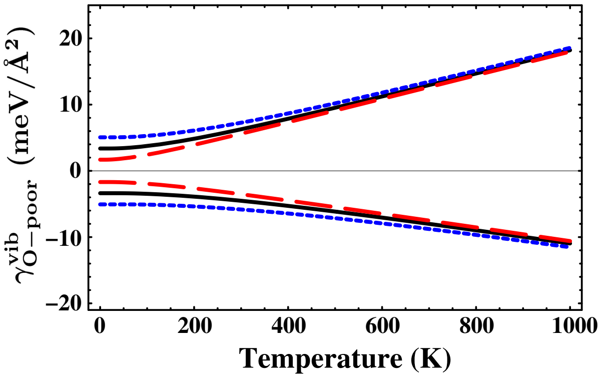

Figure 4.4: Estimate of the vibrational contribution to the surface free energy in the O-poor limit. The Einstein model has been used to approximate the phonon DOS. To account for the change of the vibrational modes of atoms at the surface compared to bulk atoms, the characteristic frequencies of the surface atoms are varied ±50 % compared to the bulk frequencies. The dashed-red and dotted-blue lines represent an additional ±50 % variation of the selected characteristic frequencies of the bulk atoms.

very much, as can be seen from the dashed-red (-50 %) and dotted-blue (+50 %) curves in Fig. 4.4. Here again the frequencies at the surface are varied by ±50 % with respect to the bulk value.

It becomes obvious, that even for temperatures up to 1000 K the vibrational contribution to the surface free energy is rather moderate. Nevertheless it has to be stressed, that this might not in general apply to other surfaces. But the scheme for obtaining a first coarse estimate of the order of magnitude of the vibrational contribution can just as well be adapted to other systems. Also the accuracy needed in the surface free energy is an important factor. If in any case the vibrational contribution turns out not to be negligible, the calculation of the phonon DOS would become necessary to include this contribution correctly.

The discussion shows that for the surface free energy of a metal oxide surface the total energy E^{tot} is indeed the leading term, whereas for the other contributions, F^{vib}, TS^{conf} and pV, a rough estimate showed, that they are only of minor importance for the present applications. Again it should be stressed, that this not necessarily valid in general, but has to carefully tested for every new system.

4.3 The Gibbs Free Energy Of Adsorption

4.3.1 One-Component Gas Phase

As a second example for combining DFT and thermodynamics the Gibbs free energy of adsorption ΔG^{ads} for a metal surface in equilibrium with a surrounding gas phase is evaluated in this Section. The Gibbs free energy of adsorption can be used to compare the stability of different adsorbate phases depending on the gas phase conditions. The stability of the different adsorbate phases is compared with respect to the clean metal surface. For an adsorbate phase in equilibrium with an oxygen gas phase, ΔG^{ads} is given by

$$\begin{aligned}\Delta G^{\mathrm{ads}}(T,p) &= \gamma_{\mathrm{M}}(T,p,N'_{\mathrm{M}}) - \gamma_{\mathrm{O@M}}(T,p,N_{\mathrm{M}},N_{\mathrm{O}}) \\ &= -\frac{1}{A}\left(G^{\mathrm{surf}}_{\mathrm{O@M}}(T,p) - G^{\mathrm{surf}}_{\mathrm{M}}(T,p) - \Delta N_{\mathrm{M}}\mu_{\mathrm{M}}(T,p) - N_{\mathrm{O}}\mu_{\mathrm{O}}(T,p)\right) \quad ,\end{aligned} \tag{4.29}$$

where $G^{\mathrm{surf}}_{\mathrm{O@M}}$ is the Gibbs free energy of the metal surface with N_{O} adsorbed oxygen atoms, $G^{\mathrm{surf}}_{\mathrm{M}}$ is the Gibbs free energy of the clean metal surface and μ_{O} is the chemical potential of the oxygen atoms. If the number of metal atoms in the adsorbate phase and the clean surface are not equal, i.e. $\Delta N_{\mathrm{M}} = N_{\mathrm{M}} - N'_{\mathrm{M}} \neq 0$, the excess/deficiency atoms are taken from/put into a bulk reservoir, represented by the gibbs free energy of the bulk phase, $g^{\mathrm{bulk}}_{\mathrm{M}}$. A is again the surface area. Substituting μ_{O} by $\Delta\mu_{\mathrm{O}}$, cf. Eq. (4.38), yields

$$\begin{aligned}\Delta G^{\mathrm{ads}}(\Delta\mu_{\mathrm{O}}) &= -\frac{1}{A}\left(G^{\mathrm{surf}}_{\mathrm{O@M}} - G^{\mathrm{surf}}_{\mathrm{M}} - \Delta N_{\mathrm{M}} g^{\mathrm{bulk}}_{\mathrm{M}} - N_{\mathrm{O}}(1/2E^{\mathrm{tot}}_{\mathrm{O_2}} + \Delta\mu_{\mathrm{O}})\right) \\ &= -\frac{N_{\mathrm{O}}}{A}\Delta G^{\mathrm{bind}}_{\mathrm{O@M}} + \frac{N_{\mathrm{O}}}{A}\Delta\mu_{\mathrm{O}} \quad ,\end{aligned} \tag{4.30}$$

with $\Delta G^{\mathrm{bind}}_{\mathrm{O@M}}$ being the binding energy per adsorbed oxygen atom. The Gibbs free energy of adsorption shows a linear dependence on the chemical potential of the gas phase. The slope depends only on the coverage, i.e. the number of oxygen atoms N_{O} per surface area A. A structure with a higher coverage will therefore depend more strongly on the oxygen chemical potential than a structure with low coverage. The Gibbs free energy of adsorption of the clean metal surface is independent of $\Delta\mu_{\mathrm{O}}$ and serves as a zero reference (cf. Fig. 4.5). The y-axis intercept is given by the binding energy per surface area, $-N_{\mathrm{O}}\Delta G^{\mathrm{bind}}_{\mathrm{O@M}}/A$, whereas the x-axis intercept is simply given by the binding energy per oxygen atom, $\Delta G^{\mathrm{bind}}_{\mathrm{O@M}}$. Since the most stable structure will be the one with the lowest surface free energy, an adsorbate structure will be stable with respect to the clean surface, if $\gamma_{\mathrm{O@M}} < \gamma_{\mathrm{M}}$, i.e. if $\Delta G^{\mathrm{ads}} > 0$. For plotting the Gibbs free energy of adsorption vs. the chemical potential of the gas phase the y-axis as been inverted in Fig. 4.5, so that the most stable structure always exhibits the *lowest* ΔG^{ads} . For $\Delta\mu_{\mathrm{O}} = 0$, i.e. for very oxygen rich conditions, the adsorbate phase with the most strongly bound adsorbates will be the most stable one.

Range Of Chemical Potential

A meaningful range of $\Delta\mu_{\mathrm{O}}$ for plotting ΔG^{ads} has to be found. As already mentioned above the stability of the different structures is compared with respect to the clean metal surface, i.e. any structure with a *higher* surface free energy (resulting in a

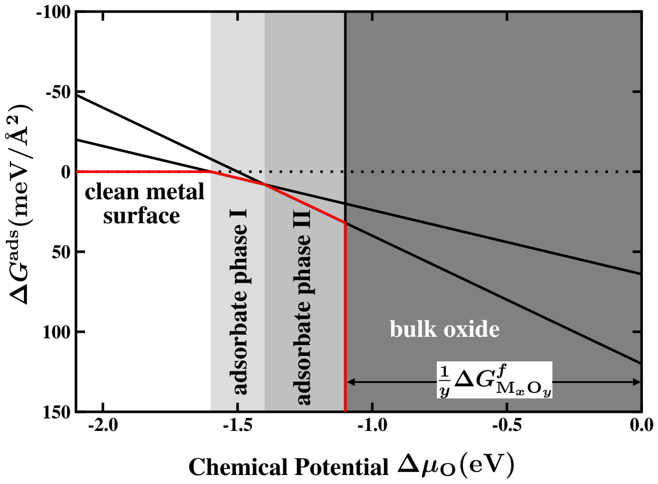

Figure 4.5: Gibbs free energy of adsorption for a surface in equilibrium with a surrounding gas phase. The clean metal surface serves as a zero reference, $\Delta G^{\text{ads}} = 0$. An adsorbate phase will become stable, if its Gibbs free energy of adsorption is *lower* than the one of the clean metal surface ($\Delta G^{\text{ads}} > 0$). If there is more than one adsorbate phase, always the one with the *lowest* ΔG^{ads} will be the most stable one. Here, this is indicated by the red line. With increasing gas phase chemical potential first the metal phase is stable, then the first and second adsorbate phases become stable. Finally, if $\Delta\mu_{\text{O}} > \frac{1}{y}\Delta G^{f}_{\text{M}_x\text{O}_y}$, the oxide will be more stable than any adsorbate phase on the metal surface.

negative Gibbs free energy of adsorption, $\Delta G^{\text{ads}} < 0$) will not be stable under the given gas phase conditions. Since all lines have a positive slope, every adsorbate phase will eventually become unstable with decreasing gas phase chemical potential. Therefore a meaningful lower bound for the gas phase chemical potential is given by the last intersection of an adsorbate phase with the clean surface, i.e. below this $\Delta\mu_{\text{O}}$ the clean metal surface is always the most stable phase.

The upper bound for the oxygen chemical potential is given by the heat of formation of the corresponding bulk oxide $\Delta G^{f}_{\text{M}_x\text{O}_y}$. Since the metal oxide contains basically an *infinite* number of oxygen atoms, its stability range is marked by a vertical line. For oxygen chemical potentials greater than the heat of formation ($\Delta\mu_{\text{O}} > \frac{1}{y}\Delta G^{f}_{\text{M}_x\text{O}_y}$) any oxide phase would always be thermodynamically more stable than any adsorbate phase on the metal surface.

Comparing this to the range obtained for the oxide surfaces (cf. Eq. (4.12)) it becomes obvious, that the thermodynamic stability range of the adsorbate phases ends at the point, where the stability range of the oxide surfaces begins (not considering any metastable states or kinetic effects). For the case of a metal in thermodynamic equilibrium with an oxygen gas phase one therefore usually finds the sequence *metal surface → adsorbate phase → oxide surface* with increasing oxygen chemical potential.

Evaluating The Gibbs Free Energy

The discussion of the different contributions to the Gibbs free energy is analogous to the one for the surface free energy (cf. Sec. 4.2). For the pV-term the same arguments hold, since also the Gibbs free energy of adsorption is normalized to the surface area, i.e. the pV-term will be negligible small up to rather high pressures. Also for the contribution from the configurational entropy the discussion is equivalent, since in this work the Gibbs free energy of adsorption will only be compared for several well-ordered adsorbate phases at low enough temperatures. Again for highly disordered phases the configurational entropy becomes much more important and statistical methods to sample the configurational space have to be utilized (cf. Chapter 5).

The vibrational contribution to the Gibbs free energy of adsorption can also be estimated in a similar way as for the surface free energy. As can be seen from Eq. (4.30), in contrast to the surface free energy, where the vibrational contribution was mainly determined by the difference between bulk and surface atoms, here the decisive contribution will arise from a change in the vibrational energy of molecules in the gas phase and adsorbed on the surface. This also depends on the mode of adsorption. In the case of a dissociative adsorption, as for the oxygen molecule, the O-O vibration would be *changed* into a O-M vibration, whereas for a unimolecular adsorption, as e.g. carbon monoxide, the C-O vibration would be changed and an additional C-M vibration would be introduced. In addition, if $\Delta N_{\mathrm{M}} \neq 0$, also the change in vibrational energy of metal atoms in the adsorbate structure, the clean metal surface and the bulk reservoir has to be considered.

Depending on the magnitude of the vibrational contribution and the aspired accuracy the vibrational modes of the molecules and the phonon DOS of the adsorbate phase and of the clean surface have to be evaluated to obtain the exact value. For the problems investigated in this work, an estimate of the vibrational contribution will be quantified explicitly in the second Part.

It should be stressed, that substituting the Gibbs free energy by only the total energy is in principle not necessary. In practice though evaluating all contributions to the Gibbs free energy is often too involved compared to the gain in accuracy.

4.3.2 Two-Component Gas Phases

Gibbs Free Energy Of Adsorption

The Gibbs free energy of adsorption can also be evaluated for surfaces in equilibrium with more than one gas phase component. Here this will be exemplified for a gas phase consisting of oxygen and carbon monoxide. Assuming in a first approach, that the two gas phase components do not interact with each other, the Gibbs free energy of adsorption is given by

$$\begin{aligned}
&\Delta G^{\mathrm{ads}}(\Delta\mu_{\mathrm{O}},\Delta\mu_{\mathrm{CO}}) = \\
&= -\frac{1}{A}\Big(G^{\mathrm{surf}}_{\mathrm{O,CO@M}} - G^{\mathrm{surf}}_{\mathrm{M}} - \Delta N_{\mathrm{M}} g^{\mathrm{bulk}}_{\mathrm{M}} - N_{\mathrm{O}}(1/2E^{\mathrm{tot}}_{\mathrm{O_2}} + \Delta\mu_{\mathrm{O}}) - N_{\mathrm{CO}}(E^{\mathrm{tot}}_{\mathrm{CO}} + \Delta\mu_{\mathrm{CO}})\Big) \\
&= -\frac{1}{A}\Delta G^{\mathrm{bind}}_{\mathrm{O,CO@M}} + \frac{N_{\mathrm{O}}}{A}\Delta\mu_{\mathrm{O}} + \frac{N_{\mathrm{CO}}}{A}\Delta\mu_{\mathrm{CO}} \quad .
\end{aligned} \tag{4.31}$$

Here, $\Delta G^{\mathrm{bind}}_{\mathrm{O,CO@M}}$ is the total binding energy of all adsorbed atoms/molecules on the surface. For a gas phase of non-interacting components the surface is then just independently in equilibrium with the two components. Since in Eq. (4.31) the Gibbs free energy of adsorption depends on two variables, one obtains a 3D-plot with a plane for each adsorbate structure instead of a line as in Fig. 4.5. The slope in x, resp. y direction only depends on the coverage of the different species. For any additional gas phase species Eq. (4.31) can simply be extended by adding the appropriate term.

To obtain the Gibbs free energy of adsorption for a surface in equilibrium with a non-interacting multi-component gas phase is thus straightforward. It is important to note that within this approach, as it is applied here, the gas phase components are assumed to be *non-interacting*, which is also called a *constrained equilibrium*, i.e. thermodynamic equilibrium is not considered between all the different subsystems. In this example thermodynamic equilibrium is only assumed between the surface and each of the two gas phases, but not between the two gas phases. If such a constraint is justified and how it influences the interpretation of the obtained results has to be discussed separately for every new system.

Bulk Oxide Stability

Considering again a metal in contact with an oxygen gas phase, the stability of the corresponding bulk oxide does usually also depend on the second gas phase component. In the case of CO as the second gas phase component, the metal oxide will eventually be decomposed into CO_2 and the metal with increasing CO content in the gas phase, which determines its stability region [82]. In a pure CO environment the stability condition of a metal oxide M_xO_y is given by

$$g^{\mathrm{bulk}}_{\mathrm{M}_x\mathrm{O}_y} + y\mu_{\mathrm{CO}} < x g^{\mathrm{bulk}}_{\mathrm{M}} + y\mu_{\mathrm{CO_2}} \quad , \tag{4.32}$$

where g are the Gibbs free energies per formula unit. Approximating the chemical potential of CO_2, $\mu_{\mathrm{CO_2}}$, by only its total energy, $E^{\mathrm{tot}}_{\mathrm{CO_2}}$, Eq. (4.32) can be rearranged similar to the stability condition of a bulk oxide in the pure oxygen gas phase (cf.

Page 30), yielding

$$\begin{aligned}\Delta\mu_{\mathrm{CO}} &\lesssim -\frac{1}{y}\Delta G^{f}_{\mathrm{M}_x\mathrm{O}_y}(0,0) + E^{\mathrm{tot}}_{\mathrm{CO}_2} - E^{\mathrm{tot}}_{\mathrm{CO}} - \frac{1}{2}E^{\mathrm{tot}}_{\mathrm{O}_2} \\ &= -\frac{1}{y}\Delta G^{f}_{\mathrm{M}_x\mathrm{O}_y}(0,0) + E^{\mathrm{bind}}_{\mathrm{CO}_2} - E^{\mathrm{bind}}_{\mathrm{CO}} - \frac{1}{2}E^{\mathrm{bind}}_{\mathrm{O}_2} \\ &= -\frac{1}{y}\Delta G^{f}_{\mathrm{M}_x\mathrm{O}_y}(0,0) + \Delta E^{\mathrm{mol}} \quad ,\end{aligned} \tag{4.33}$$

with $\Delta\mu_{\mathrm{CO}} = \mu_{\mathrm{CO}} - E^{\mathrm{tot}}_{\mathrm{CO}}$. Combining this equation with the stability condition for a bulk oxide in a pure oxygen gas phase

$$\Delta\mu_{\mathrm{O}} \gtrsim \frac{1}{y}\Delta G^{f}_{\mathrm{M}_x\mathrm{O}_y}(0,0) \quad , \tag{4.34}$$

gives the stability conditions in a constrained equilibrium with a gas phase containing both oxygen and CO

$$\Delta\mu_{\mathrm{CO}} - \Delta\mu_{\mathrm{O}} < -\frac{2}{y}\Delta G^{f}_{\mathrm{M}_x\mathrm{O}_y}(0,0) + \Delta E^{\mathrm{mol}} \quad . \tag{4.35}$$

4.4 Gas Phase Chemical Potential

The surrounding gas phases are described as ideal-gas-like reservoirs. For an ideal gas the chemical potential at a given temperature T and pressure p is given by

$$\mu(T,p) = \frac{G}{N} = \frac{F + pV}{N} = \frac{-kT\ln Z + pV}{N} \quad , \tag{4.36}$$

where Z is the partition function of N indistinguishable particles

$$Z = \frac{1}{N!}\left(z^{\mathrm{trans}} \cdot z^{\mathrm{vib}} \cdot z^{\mathrm{rot}} \cdot z^{\mathrm{e}} \cdot z^{\mathrm{n}}\right)^N \quad . \tag{4.37}$$

z is the partition function of one gas particle. The translational, vibrational, rotational, electronic and nuclear contribution to the chemical potential can be evaluated using statistical thermodynamics [79]. Thus for any simple gas phase molecule (like O_2, CO, CO_2 etc.) the chemical potential can be directly calculated within the ideal gas approximation for any temperature and pressure. For more complicated molecules the use of tabulated values [83] might be more favorable. Since the total energy contribution to the chemical potential does not depend on temperature and pressure, it can be useful to separate $\mu(T,p)$ into the total energy and the remaining part

$$\mu(T,p) = E^{\mathrm{tot}} + \Delta\mu(T,p) \quad . \tag{4.38}$$

$\Delta\mu(T,p)$ contains then all the temperature and pressure dependent terms of μ.

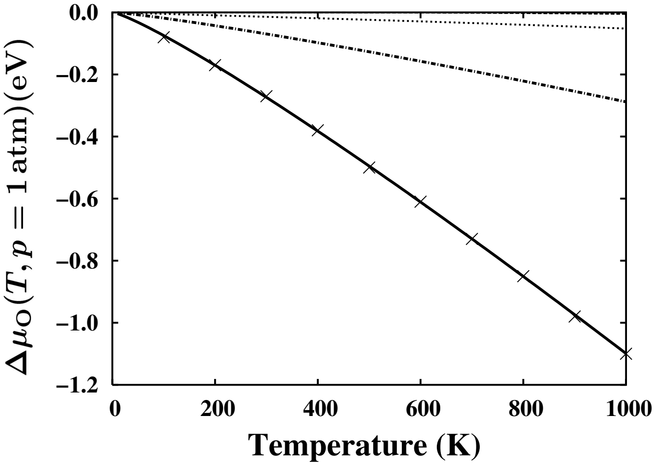

Figure 4.6: Temperature dependence of the relative oxygen chemical potential $\Delta\mu_{\mathrm{O}}(T,p)$ at $p = 1\,\mathrm{atm}$. Compared are the tabulated values from Ref. [83] (crosses) to the calculated ones within the ideal gas approximation. Additionally shown are the sums of the individual contributions: vibrational (dashed line, almost coinciding with the zero axis), vibrational+nuclear (dotted line), vibrational+nuclear+rotational (dash-dotted line). The remaining large difference to the full result (solid line) is due to the translational contribution (from Ref. [84])

The approximation of the real gas phase by an ideal gas will only introduce a negligible error in the temperature and pressure range considered in this work, which can be shown by comparing the calculated values within the ideal gas approximation to the experimentally derived, tabulated ones [83]. In Fig. 4.6 this is illustrated for the for the (T,p)-dependent part of the oxygen chemical potential $\Delta\mu_{\mathrm{O}}(T,p)$ at a pressure of $p_{\mathrm{O}_2} = 1\,\mathrm{atm}$ and temperatures up to $T = 1000\,\mathrm{K}$.

4.5 Summary

Combining DFT calculations with thermodynamic concepts provides a very useful tool to extend the knowledge gained in the microscopic regime to the meso- and macroscopic properties of a system. This approach can be used to describe systems that are in thermodynamic equilibrium, but it does not contain information about the kinetics involved to reach the final equilibrated state. Also open systems in a *steady state*, which is governed by a continuous supply and removal of particles, can not be described within this approach. Nevertheless identifying the thermodynamic equilibrium state can often already provide a first, valuable insight into a given system.

The general concept of *ab initio atomistic thermodynamics* is illustrated using the surface free energy and the Gibbs free energy of adsorption as example. In addition the different contributions to the Gibbs free energy have been discussed. Here, it is important to note, that the magnitude of the different contributions has to be carefully evaluated for every system. Usually a coarse estimate of an upper bound of the contributions besides the total energy can be obtained rather easy, whereas the exact calculation of all contributions to the Gibbs free energy can become fairly involved.

The atomistic thermodynamics approach, as it is outlined here, is an indirect approach, i.e. it can only be used to *compare* different structures, but it will not predict any new phases. Thus, having a given set of experimentally and/or theoretically proposed structures their thermodynamic stability can directly be compared over a wide range of temperature and pressure conditions. Also any new suggested structure can then be included at a rather low computational cost. But all obtained results are only valid within the restricted set of investigated structures, i.e. any configuration that is not considered within this set of structures can also not appear as a stable structure. Therefore, it is important to compare a rather large set possible configurations, at least including all experimentally identified ones, but still it can not be excluded, that an important structure might have been missed. Nevertheless the advantage of this approach is the relatively small computational demand, so that a first insight from the thermodynamic description can be obtained rather fast.

In the following Chapter an approach considering statistical mechanics is discussed, which can overcome some of the drawbacks of the atomistic thermodynamics approach, but is usually much more costly.

Chapter 5

DFT And Statistical Mechanics

In the previous Chapter the combination of density-functional theory with concepts from thermodynamics has been discussed. Despite the very useful insight that can be obtained about the stability of different phases in a wide range of temperatures and pressures, this approach has two main limitations. First, the explicit time evolution of the system can not be treated and second, in the first-principles atomistic thermodynamics approach as it has been discussed here the sampling of the configurational space is rather limited.

In this Chapter the combination of DFT and statistical mechanics is described, which provides a more general concept to bridge the time and length scales between the electronic, meso- and macroscopic regimes as aspired by the multiscale modeling approach (cf. Fig. 4.1). *Equilibrium Monte Carlo* simulations can e.g. be used to identify again the thermodynamically most stable structure under different environmental conditions, but allows a wider sampling of configurational space. Using *kinetic Monte Carlo* simulations it is possible to explicitly treat the involved kinetics and therefore to also describe non-equilibrium situations. DFT will provide the basis to obtain the parameters needed as input to the simulations.

5.1 Monte Carlo Simulations

Computer simulations are a widespread tool to explicitly follow the trajectory of a system involving up to 10^4 degrees of freedom. A statistical analysis of the trajectory might then be used to predict properties of the simulated assembly of particles. Two general classes of simulations are *molecular dynamics* (MD) and *Monte Carlo* (MC) simulations.

In a molecular dynamics simulation atoms and molecules are viewed in a classical dynamical picture. Using forces extracted from the corresponding potential energy surface the trajectory can be formed by integrating Newton's equation of motion [85, 86]. If the forces are obtained from first-principles without any empirical or fitted parameters, the simulations are referred to as *ab initio* molecular dynamics.

A typical time scale that can be reached with such an *ab initio* molecular dynamics simulations [87] is of the order of picoseconds.

In a Monte Carlo method [86, 88], on the other hand, the configurational space is sampled in a stochastic manner to evaluate the partition function of the system. With such an *equilibrium* MC simulation one can obtain thermal averages of many particle systems, but the sequence of generated configurations does not reflect the real time evolution of the system. Thus the time connected to the simulation (so-called *MC time*) is not directly related to the *real time*.

In *kinetic* MC (kMC) simulations a proper relationship between MC time and real time is formed and a description of the dynamical evolution of the system becomes possible again. In contrast to a MD simulation only state-to-state transitions are treated rather than following the full microscopic trajectory. The resulting macroscopic trajectory, though, should be indistinguishable from the results of a MD simulation. As a consequence much larger time scales are accessible in a kMC simulation compared to a MD simulation.

Since in this work the simulations are used to investigate a system in a steady state of heterogenous catalysis, kinetic Monte Carlo is the most suitable choice. The rest of this Chapter will therefore be focussed on kMC.

5.1.1 Kinetic Monte Carlo

As already mentioned above a kinetic Monte Carlo step describes the transition from one system state into the next, while appropriately averaging over the whole microscopic motion of the atoms around their equilibrium position. The process of moving from one state to the next is also called a *rare event*, since on the time scale of atomic vibrations such a transition occurs only very seldom. Considering such a rare event it is assumed, that because the system stays relatively long in one state (compared to a vibrational period), there is no memory of how it got into this state. The probability to move from the present state S_i into the next state S_j is thus independent of whatever state preceded state S_i. The sequence of states generated for such a system is called a Markov chain, which as a result is a basic concept in Monte Carlo simulations. The probability for the transition from state S_i to state S_j, W_{ij}, can be expressed by the conditional probability, that the system is in state S_j at a time step t_n, if it has been in state S_i at the previous time step t_{n-1}

$$W_{ij} = W(S_i \to S_j) = P(X_{t_n} = S_j | X_{t_{n-1}} = S_i) \quad , \tag{5.1}$$

where X_t is the state of the system at time t. The total probability of the system being in a state S_j at a time t_n is then given by

$$\begin{aligned} P(X_{t_n} = S_j) &= P(X_{t_n} = S_j | X_{t_{n-1}} = S_i) P(X_{t_{n-1}} = S_i) \\ &= W_{ij} P(X_{t_{n-1}} = S_i) \quad . \end{aligned} \tag{5.2}$$

The time dependence of this probability is described by a *master equation* (transforming time from a discrete to a continuous variable and setting $P(X_{t_n} = S_j) = P(S_j, t)$)

$$\frac{dP(S_j,t)}{dt} = -\sum_i W_{ji} P(S_j,t) + \sum_i W_{ij} P(S_i,t) \quad . \tag{5.3}$$

A numerical solution of this master equation is provided by kinetic Monte Carlo simulations [89, 90, 91, 92, 93], i.e. with a kMC simulation it is possible to describe the time evolution of a system, that is characterized by Eq. (5.3). To ensure, that the system will attain thermal equilibrium the detailed balance criterion has to be fulfilled

$$W(S_j \rightarrow S_i) P_{\text{eq}}(S_j) = W(S_i \rightarrow S_j) P_{\text{eq}}(S_i) \quad , \tag{5.4}$$

where P_{eq} denotes the equilibrium probability. If a system is in thermal equilibrium and the detailed balance criterion is satisfied, then the average number of processes from state $S_j \rightarrow S_i$ will be the same as for the reverse process $S_i \rightarrow S_j$, i.e. every process is balanced to its reverse one. Thus the probability of any given system state will be constant and the system remains in equilibrium.

A classical example for a rare event is the diffusion of a particle from a lattice site st to a neighboring site st'. Here, the particle adsorbed on site st vibrates around its equilibrium position typically once every picosecond, whereas the diffusion of this particle to any neighboring site st' would happen on a time scale of microseconds. In a MD simulation the particle would correspondingly vibrate for roughly 10^9 time steps before a diffusion event would happen. If the diffusion event is the actually interesting part, it would just be computational unfeasible to do this in a MD simulation. In contrast, a kinetic Monte Carlo simulation would concentrate only on the diffusion event, the rare event in this example. Thus, the time scale reached in a kMC simulation is much larger than in a MD simulation and can be even in the order of seconds.

To practically perform a kMC simulation in a first step the investigated system is mapped onto a lattice. This is done to keep the number of included processes in a manageable range. There are also lattice free kMC simulations (cf. Section 5.3), which are computational much more demanding and will not be discussed here. In a second step a list of *all relevant* processes p on the lattice has to be set up and a rate has to be assigned to each process. The rate r_p then characterizes the probability to escape from the present system state by the process p. The simulation starts in some initial configuration of the system. A total rate R is defined as the sum over rates of all *possible* processes in the current configuration, $R = \sum_p r_p$. A certain process k is then randomly chosen by

$$\sum_{p=0}^{k-1} r_p \leq \rho_1 R \leq \sum_{p=0}^{k} r_p \quad , \tag{5.5}$$

with $\rho_1 \in \,]0,1[$ being a random number. The probability of selecting a process k is weighted by its rate r_k, i.e. a process with a large rate has a higher probability to be

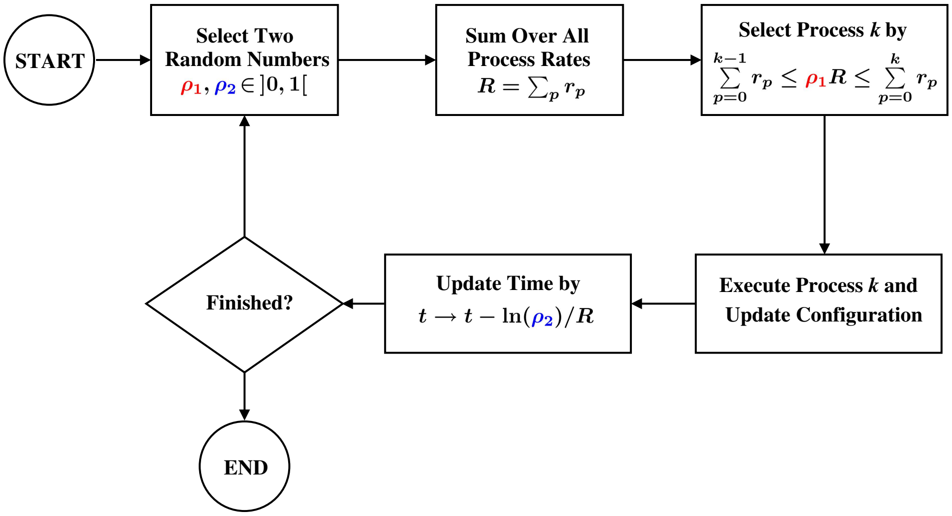
START
Select Two Random Numbers $\rho_1, \rho_2 \in]0,1[$
Sum Over All Process Rates $R = \sum_p r_p$
Select Process k by $\sum_{p=0}^{k-1} r_p \leq \rho_1 R \leq \sum_{p=0}^{k} r_p$
Execute Process k and Update Configuration
Update Time by $t \rightarrow t - \ln(\rho_2)/R$
Finished?
END

Figure 5.1: General flow chart for a kinetic Monte Carlo simulation. For each kinetic Monte Carlo step two random numbers are needed. Starting from some initial configuration the total rate is calculated as the sum over the rates of all possible processes. One process is selected by the first random number, it is then executed, the system configuration is updated and the time is advanced using the second random number.

chosen than a process with a very small rate. The selected process is executed and the configuration is updated. Since the kMC algorithm simulates a Poisson process, an explicit relationship between the MC time and the real time can be established [93]. After each kMC step the simulation time is updated according to

$$t \longrightarrow t - \frac{\ln(\rho_2)}{R} \quad , \tag{5.6}$$

where $\rho_2 \in]0,1[$ is a second random number. For the new configuration again a new total rate R is determined, a process is selected and executed and the time is updated (cf. Fig. 5.1). Thus, the kMC simulation generates a sequence of system configurations on a realistic time scale.

Although the kMC algorithm is rather simple, there are several aspects, that have to be carefully considered. The identification of all possibly relevant processes and the determination of the corresponding process rates are crucial for the simulation. But the mapping onto a lattice and the identification of the relevant processes might not be obvious, which is one of the main problems in kMC simulations. If it is not desired or even possible to map the system onto a suitable lattice, so that a lattice free kMC simulation has to be performed, the setting up of a list of relevant processes and their corresponding rates is much more involved, still requiring further conceptional developments in this field. Additionally, such lattice free kMC simulations are computational very costly.

In the past the process rates were often obtained by fitting the results of the simulation to experimental data. Although this might lead to quite good results for the specific system, the rates have been fitted to, the transferability to other systems or other system conditions is highly questionable. An alternative way to calculate the process rates is given by using DFT or other electronic structure methods. If the rates are obtained without relying on experimental data, the method is referred to as *ab initio* kMC (for one of the first *ab initio* kMC simulations cf. Ref. [94]). The biggest advantage of a kMC simulation is, that for a system, where the considered rare events are well described by a Markov chain and where all possible processes and their rates are known, the kMC trajectory will be statistically indistinguishable from a MD trajectory, but on a much longer time scale.

5.1.2 Lattice Gas Hamiltonian

To calculate the process rates based on DFT it is necessary to evaluate the potential energy surface (PES) of the system in any possible configuration. Regarding the size of the simulated system and the number of possible configurations a direct calculation of the PES for each configuration with DFT is often computationally unfeasible.

If the investigated system can be mapped onto a lattice reflecting the different sites for the different species in the system, a lattice gas Hamiltonian (LGH) can be developed (analogous to an *Ising type model* [95] or a *cluster expansion* [96, 97]; the first *ab initio* LGH for surfaces has been published by Stampfl *et al.* [98]). Any system configuration can then be defined by the occupation of sites on the lattice, and the total energy can be expanded into a sum over the on-site energies F_i^0 (i.e. the energy of an isolated species on a lattice site i) and the interactions V between the different lattice sites .

$$H = \sum_i n_i F_i^0 + \sum_{ij} V_{ij} n_i n_j + \sum_{ijk} V_{ijk} n_i n_j n_k + \dots \tag{5.7}$$

The sums run over all lattice sites. V_{ij} is the interaction between two particles on lattice sites i and j (also called pair-interaction) and resp. V_{ijk} is the interaction parameter involving three particles on sites i, j and k (trio-interaction). The interaction parameters must be symmetric, i.e. $V_{ij} = V_{ji}$. n_l are the occupation numbers, i.e. $n_l = 0$ denotes, that site l is empty, and $n_l = 1$, that site l is occupied. If one could sum over all possible interactions, one should in principle obtain the correct energy. In practise the sum has to be truncated somewhere, which is a decisive task in constructing a LGH. Eq. (5.7) describes the lattice gas Hamiltonian for a system with only one particle species. Multiple sites are already included, but it should be noted that for an increasing number of site types, the number of non-equivalent interaction parameters increases rapidly. Also the description of a multicomponent, multisite system is straightforward by suitably expanding Eq. (5.7), with a resulting huge number of interaction parameters.

The on-site energies F_i^0 as well as the interaction parameters V contain a total energy as well as vibrational energy part. If the vibrational contribution of an adsorbate turns out to be rather independent of the surrounding atoms, the vibrational part of the interaction parameter V can be neglected, which would be expected for the here discussed systems. To include the vibrational contribution in the on-site energies it is often sufficient to consider only the ZPE, since in the here discussed temperature range the vibrational contribution shows only a weak temperature dependence.

The evaluation of such a LGH is extremely fast, since just a simple sum has to be computed. The challenge in this approach is to determine the correct interaction parameters. Using DFT to calculate the parameters from first principles is the most reliable, but also the most demanding approach. A number of structures (at least as many as the number of interaction parameters) is calculated and the corresponding lattice gas Hamiltonian for every structure is set up, exploiting the periodic boundary conditions (i.e. also the interactions between the particle in the unit cell and its periodic images have to be considered). The obtained set of linear equations can be solved in several ways. If the number of equations is equal to the number of interactions, the interaction parameters can simply be calculated by direct inversion. If the number of calculated structures exceeds the number of interactions, the simplest approach would be a least square fit. Since the results obtained by direct inversion are usually not very accurate, the number of calculated structures should always be larger than the number of interaction parameters.

Another, more difficult task, is to decide, which interaction parameters have to be included in Eq. (5.7) and which can be set to zero. Since there is no automatized scheme for the truncation of the LGH, this is not obvious at all. Often the constructed LGH relies on intuition. One possibility to test the convergence of the LGH is its ability to predict the energy of computed configurations, that have not been included into the fitting procedure.

In this work the LGH approach has been used to determine the binding energies E^{bind} of different adsorbed species, that are needed to calculate the rates for the kinetic Monte Carlo simulation (cf. Section 5.2). Using Eq. (5.7) the binding energy of a particle on site i is given by

$$\begin{aligned} E_i^{\text{bind}} &= H(n_i = 1) - H(n_i = 0) \\ &= F_i^0 + 2\sum_j V_{ij} n_j + 3\sum_{jk} V_{ijk} n_j n_k + \dots \end{aligned} \tag{5.8}$$

By evaluating Eq. (5.8) any binding energy of a particle on any lattice site in any configuration can be obtained by a simple summation over the interaction parameters.

5.2 Determining The Process Rates

If the possible pathways for the transition from a state i to a state j are known, the rates for these processes needed in the kMC simulation can be calculated by transition state theory (TST). In this Section a derivation of the rates of the four main *types* of processes (adsorption, desorption, diffusion and reaction) included in the kMC simulation of heterogeneous catalysis is presented (following the derivation given in Ref. [99]).

5.2.1 Transition State Theory

In the following discussion, transition state theory (TST) is only considered in its harmonic approximation, also often referred to as Vineyard theory [100]. In the harmonic TST the pathway connecting the initial and final state is characterized by a saddle point, the transition state (TS). The vibrational modes in the initial state and the vibrational modes perpendicular to the reaction coordinate at the transition state are assumed to be harmonic. The transition rate r^{TST} can then be expressed as [101]

$$r^{\mathrm{TST}} = \frac{\prod_{i=0}^{N} \nu_i^{\mathrm{init}}}{\prod_{i=0}^{N-1} \nu_i^{\mathrm{TS}}} \exp\left(-\frac{\Delta E^{\mathrm{TS}}}{k_{\mathrm{B}}T}\right) \quad , \tag{5.9}$$

where ν_i^{init} and ν_i^{TS} are the vibrational modes in the initial and transition state, respectively. N is the number of vibrational degrees of freedom and ΔE^{TS} is the energy difference between the transition state and the initial state. Since the harmonic approximation for the vibrational modes is used, which is valid for $h\nu \ll k_{\mathrm{B}}T$, the vibrational partition function for the initial $Z_{\mathrm{vib}}^{\mathrm{init}}$ and transition state $Z_{\mathrm{vib}}^{\mathrm{TS}}$ can simply be expressed by

$$Z_{\mathrm{vib}}^{\mathrm{init}} = \prod_{i=0}^{N} \frac{k_{\mathrm{B}}T}{h\nu_i^{\mathrm{init}}} \quad , \quad Z_{\mathrm{vib}}^{\mathrm{TS}} = \prod_{i=0}^{N-1} \frac{k_{\mathrm{B}}T}{h\nu_i^{\mathrm{TS}}} \quad . \tag{5.10}$$

Eq. (5.9) can then be reformulated to give an expression often seen in TST

$$r^{\mathrm{TST}} = \frac{k_{\mathrm{B}}T}{h} \frac{Z_{\mathrm{vib}}^{\mathrm{TS}}}{Z_{\mathrm{vib}}^{\mathrm{init}}} \exp\left(-\frac{\Delta E^{\mathrm{TS}}}{k_{\mathrm{B}}T}\right) \quad . \tag{5.11}$$

In addition to the prerequisite of having a saddle point another basic assumption in TST is that there is no recrossing of the TS, i.e. once the saddle point is reached the process will in any case follow the trajectory into the final state. However, if in reality recrossing of the TS takes place, the TST rate constant overestimates the exact rate, because some reactive events use up more than a single outgoing crossing. Although there are quite some approximations involved in deriving the process rates from TST, the obtained results are usually quite good at solid surface, where the potential energy surface is rather smooth. For such a simple system the dynamical bottleneck for transitions most often coincides with the saddle points on the PES. Especially for determining the rates of diffusion of ad-atoms on a surface this approximation has been proven very useful.

5.2.2 Adsorption

The rate of the adsorption of a gas molecule on a surface depends on the impingement rate and the sticking coefficient. The impingement rate can be calculated using kinetic gas theory, so that the rate of the adsorption of a gas phase species i on a surface site of type st can be written as

$$r^{\text{ads}}_{i,st}(T,p_i) = \tilde{S}_{i,st}(T)\frac{p_i A}{\sqrt{2\pi m_i k_{\text{B}} T}} \quad . \tag{5.12}$$

Here, A is the size of the surface unit cell and $\tilde{S}_{i,st}$ is the local sticking coefficient, which gives the fraction of impinging particles, that actually stick to the surface. Since the impinging gas phase particles have randomly distributed lateral positions as well as a random distribution over their internal degrees of freedom and Maxwell-Boltzmann distributed velocities, $\tilde{S}_{i,st}$ provides a statistical average over these degrees of freedom. The local sticking coefficient will become equal to the more commonly investigated initial sticking coefficient $S_{i,0}$ [102, 87], if there is only one site within the surface unit cell. For a kMC simulation, though, a specific rate of the adsorption for each site has to be considered, therefore $S_{i,0}$ can not be used for systems with more than one site type, since it does not contain site specific information.

To consider the influence of the lateral position of the impinging particles over the unit cell the concept of an *active area* inspired by the so-called hole model for adsorption [103] is applied. Here, it is assumed, that only particles of species i with an initial lateral position within a certain area $A_{i,st}$ around the adsorption site st of the total area A can actually stick to this site. The index i indicates that the active area can vary for different gas phase species. The local sticking coefficient will then be reduced by a factor

$$\frac{A_{i,st}}{A} \leq 1 \quad . \tag{5.13}$$

Inserting this expression into Eq. (5.12) it becomes obvious, that this factor effectively reduces the impingement rate. Only particles impinging within the active area $A_{i,st}$ can contribute to the site specific adsorption rate $r^{\text{ads}}_{i,st}$. The adsorption rate is thus independent of the choice of a specific surface unit cell, but only depends on the active area for the respective site type and particle species. The sum over all active areas in a surface unit cell can not be larger than the unit cell area itself, i.e.

$$\sum_{st} A_{i,st} \leq A \quad , \tag{5.14}$$

because otherwise the number of considered sticking particles would exceed the original overall impingement rate.

In a classical picture an average over the internal degrees of freedom and the velocities would be described by the ability to overcome an energy barrier $\Delta E^{\text{ads}}_{i,st}$ along the pathway to the surface. If all particles within the same active area would see the same adsorption barrier, the local sticking coefficient would be given by

$$\tilde{S}_{i,st}(T) = \left(\frac{A_{i,st}}{A}\right) \exp\left(-\frac{\Delta E^{\text{ads}}_{i,st}}{k_{\text{B}}T}\right) \quad . \tag{5.15}$$

In the more general case of a high dimensional potential energy surface (PES) $\Delta E^{\text{ads}}_{i,st}$ would correspond to the highest barrier along the minimum energy pathway (MEP), cf. Fig. 5.2. It can be expected, that on a more complicated PES not all the particles having a sufficiently high kinetic energy to overcome $\Delta E^{\text{ads}}_{i,st}$ actually follow the MEP. Some of the particles will travel along pathways exhibiting higher energy barriers, at which they can be reflected. This will further decrease the sticking probability by a factor $f^{\text{ads}}_{i,st} \leq 1$, so that Eq. (5.15) can be written in a more general form as

$$\tilde{S}_{i,st}(T) = f^{\text{ads}}_{i,st}(T) \left(\frac{A_{i,st}}{A}\right) \exp\left(-\frac{\Delta E^{\text{ads}}_{i,st}}{k_{\text{B}}T}\right) \quad . \tag{5.16}$$

Whether a particle is steered along the MEP or not, depends on its initial state, i.e. the initial lateral position inside the surface unit cell A and the internal degrees of freedom. The calculation of $f^{\text{ads}}_{i,st}$ would require dynamical simulations of trajectories of particles impinging on the surface. Since quite a number of such trajectories are needed to obtain a statistically meaningful average and each trajectory requires information about a large part of the PES [87], the computation of $f^{\text{ads}}_{i,st}$ is rather demanding.

An alternative way to determine $f^{\text{ads}}_{i,st}$ is TST. As explained in Section 5.2.1 the application of TST requires a saddle point, i.e. the adsorption process needs to be activated. Since $f^{\text{ads}}_{i,st}$ quantifies the dependance of the sticking probability on the lateral position and internal degrees of freedom of the initial state, it can then be approximated by the ratio of all accessible states at the TS and in the initial gas phase state

$$f^{\text{ads}}_{i,st} \approx f^{\text{ads,TST}}_{i,st} = \frac{z^{\text{vib}}_{i,st,\text{TS}}}{z_{i,\text{gas}}} \quad . \tag{5.17}$$

In the harmonic approximation all degrees of freedom in the TS are vibrational, so that only the vibrational partition function $z^{\text{vib}}_{\text{TS},i,st}$ is needed. To calculate the partition function at the TS and in the gas phase comparably less information about the PES are needed than for the dynamical simulations mentioned above. Nevertheless the identification of the TS is essential to this approach. Several methods have been developed to find the minimum energy pathway and in particular the corresponding saddle point. Depending on the complexity of the investigated PES identifying the TS can easily become the computational bottleneck in determining the rates. For an overview about transition state search algorithms see e.g. Ref. [104].

5.2.3 Desorption

Since the desorption process is the reverse process to the adsorption, the detailed balance criterion (Eq. (5.4)) has to be fulfilled. The probabilities for going from the

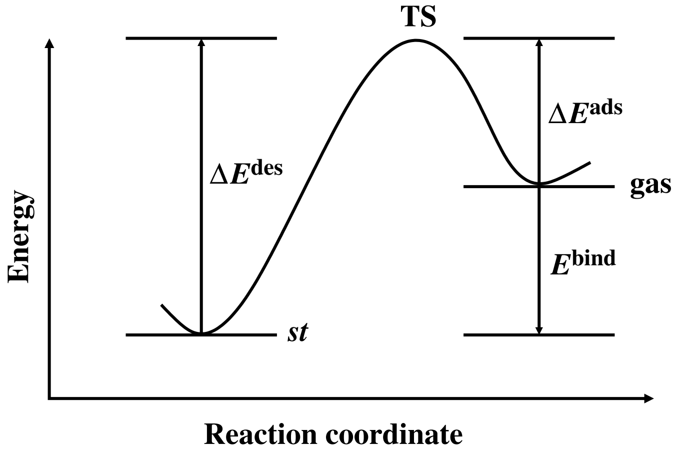

Figure 5.2: Schematic figure of a 1D reaction coordinate of a adsorption/desorption process. “*st*” refers to the adsorbed state of the particle on site *st*, “gas” to the gas phase state and “TS” to the transition state. If the transition state is clearly defined, the adsorption (ΔE^{ads}) and desorption barrier (ΔE^{des}) are determined as shown in the figure.

adsorbed into the desorbed state and vice versa ($W(S_{\mathrm{ads}} \rightarrow S_{\mathrm{des}})$ and $W(S_{\mathrm{des}} \rightarrow S_{\mathrm{ads}})$) are characterized by the desorption resp. adsorption rate. The ratio of the equilibrium occupation of the adsorbed and the desorbed state is given by the Boltzmann factor. The desorption and adsorption rates are then related by

$$\frac{r_{i,st}^{\mathrm{ads}}}{r_{i,st}^{\mathrm{des}}} = \exp\left(\frac{\Delta G_{i,st}(T,p_i)}{k_{\mathrm{B}}T}\right) \quad . \tag{5.18}$$

$\Delta G_{i,st}$ is the change in the Gibbs free energy between the particle in the gas phase and in the adsorbed state. If the pV term in the adsorbed state is neglected (i.e. $G \approx F$) the change in the Gibbs free energy can be expressed as

$$\Delta G_{i,st}(T,p_i) \approx \mu_{i,\mathrm{gas}}(T,p_i) - F_{i,st}(T) \quad , \tag{5.19}$$

where $\mu_{i,\mathrm{gas}}$ is the chemical potential of the gas phase and $F_{i,st}$ the free energy of the particle in the adsorbed state. The gas phase chemical potential can be further separated into a total energy part $E_{i,\mathrm{gas}}^{\mathrm{tot}}$ and a part $\Delta\mu_{i,\mathrm{gas}}$ (cf. Eq. (4.38)) containing the translational and internal (i.e. rotational and vibrational) degrees of freedom

$$\mu_{i,\mathrm{gas}}(T,p_i) = E_{i,\mathrm{gas}}^{\mathrm{tot}} + \Delta\mu_{i,\mathrm{gas}}(T,p_i) \quad . \tag{5.20}$$

The free energy of the particle in the adsorbed state can also be divided into a total energy part and a vibrational contribution

$$F_{i,st}(T) = E_{i,st}^{\mathrm{tot}} + F_{i,st}^{\mathrm{vib}}(T) = E_{i,st}^{\mathrm{tot}} - k_{\mathrm{B}}T\ln(z_{i,st}^{\mathrm{vib}}) \quad . \tag{5.21}$$

Combining Eq. (5.18) to (5.21) the ratio between adsorption and desorption rate can be rewritten as

$$\begin{aligned}\frac{r_{i,st}^{\mathrm{ads}}}{r_{i,st}^{\mathrm{des}}} =& \exp\left(\frac{(E_{i,\mathrm{gas}}^{\mathrm{tot}} + \Delta\mu_{i,\mathrm{gas}}(T,p_i)) - (E_{i,st}^{\mathrm{tot}} - k_{\mathrm{B}}T\ln(z_{i,st}^{\mathrm{vib}}))}{k_{\mathrm{B}}T}\right) \\ =& z_{i,st}^{\mathrm{vib}} \exp\left(\frac{\Delta\mu_{i,\mathrm{gas}}(T,p_i) - E_{i,st}^{\mathrm{bind}}}{k_{\mathrm{B}}T}\right) \quad ,\end{aligned} \tag{5.22}$$

where $E_{i,st}^{\mathrm{bind}}$ is the binding energy of a particle i at site st with respect to the gas phase as shown in Fig. 5.2, i.e. $E_{i,st}^{\mathrm{bind}} = E_{i,st}^{\mathrm{tot}} - E_{i,gas}^{\mathrm{tot}}$. Thus in addition to the adsorption rate only the binding energy $E_{i,st}^{\mathrm{bind}}$ as well as the vibrational partition function $z_{i,st}^{\mathrm{vib}}$ in the adsorbed state have to be known to calculate the desorption rate.

Also for the desorption rate an expression based on TST can be derived. Starting from Eq. (5.22) the explicit expression for the adsorption rate obtained from TST is inserted

$$\begin{aligned}r_{i,st}^{\mathrm{des}} =& r_{i,st}^{\mathrm{ads}} \frac{1}{z_{i,st}^{\mathrm{vib}}} \exp\left(-\frac{\Delta\mu_{i,\mathrm{gas}}(T,p_i) - E_{i,st}^{\mathrm{bind}}}{k_{\mathrm{B}}T}\right) \\ =& \frac{z_{i,st,\mathrm{TS}}^{\mathrm{vib}}}{z_{i,\mathrm{gas}}} \left(\frac{A_{i,st}}{A}\right) \exp\left(-\frac{\Delta E_{i,st}^{\mathrm{ads}}}{k_{\mathrm{B}}T}\right) \frac{p_i A}{\sqrt{2\pi m_i k_{\mathrm{B}}T}} \\ & \cdot \frac{1}{z_{i,st}^{\mathrm{vib}}} \exp\left(-\frac{\Delta\mu_{i,\mathrm{gas}}(T,p_i) - E_{i,st}^{\mathrm{bind}}}{k_{\mathrm{B}}T}\right)\end{aligned} \tag{5.23}$$

This expression can be much simplified by the following considerations. The partition function $z_{\mathrm{gas},i}$ for a particle in the initial state of an adsorption process (cf. Eq. (5.17)) can be divided into a translational part and the internal degrees of freedom, i.e.

$$z_{i,\mathrm{gas}} = z_{i,\mathrm{gas}}^{\mathrm{trans,2D}}\, z_{i,\mathrm{gas}}^{\mathrm{int}} = A\,\frac{2\pi m_i k_{\mathrm{B}}T}{h^2}\, z_{i,\mathrm{gas}}^{\mathrm{int}} \quad . \tag{5.24}$$

Also the translational and internal contribution to the chemical potential of the gas phase can be separated, giving

$$\Delta\mu_{i,\mathrm{gas}}(T,p_i) = -k_{\mathrm{B}}T\ln\left[\left(\frac{2\pi m_i k_{\mathrm{B}}T}{h^2}\right)^{3/2}\frac{k_{\mathrm{B}}T}{p_i}\right] - k_{\mathrm{B}}T\ln(z_{i,\mathrm{gas}}^{\mathrm{int}}) \tag{5.25}$$

Substituting $z_{i,\mathrm{gas}}$ and $\Delta\mu_{i,\mathrm{gas}}(T,p_i)$ in Eq. (5.23) by the expressions given in Eq. (5.24) and (5.25) will then yield the again rather simple expression for a desorption rate

$$r_{i,st}^{\mathrm{des}} = \left(\frac{A_{i,st}}{A}\right)\left(\frac{z_{i,st,\mathrm{TS}}^{\mathrm{vib}}}{z_{i,st}^{\mathrm{vib}}}\right)\left(\frac{k_{\mathrm{B}}T}{h}\right)\exp\left(-\frac{\Delta E_{i,st}^{\mathrm{des}}}{k_{\mathrm{B}}T}\right) \quad , \tag{5.26}$$

with

$$\Delta E^{\mathrm{des}}_{i,st} = \Delta E^{\mathrm{ads}}_{i,st} - E^{\mathrm{bind}}_{i,st} = E^{\mathrm{tot}}_{i,st\to\mathrm{gas,TS}} - E^{\mathrm{tot}}_{i,st} \tag{5.27}$$

being the desorption energy as shown in Fig 5.2. Thus for the calculation of the desorption rate based on TST again only knowledge of the transition state and the initial state, in this case the adsorbed state, is needed. By applying TST in the harmonic approximation the prefactor for the rate can be estimated without involving computationally demanding dynamical simulations. If the accuracy of this approximation is sufficient, depends on the investigated problem. Also, if there is no defined TS for a specific process, the application of harmonic TST is in any case invalid.

5.2.4 Diffusion

In a diffusion process the particle i moves from a site st to a site st'. If an appropriate saddle point along the diffusion pathway can be identified, analogous to the previous considerations harmonic TST can be applied to obtain the corresponding rate of diffusion. Similarly to Eq. (5.26) the diffusion rate is given by

$$r^{\mathrm{diff}}_{i,st\to st'}(T) = f^{\mathrm{diff,TST}}_{i,st\to st'}(T)\left(\frac{k_{\mathrm{B}}T}{h}\right)\exp\left(-\frac{\Delta E^{\mathrm{diff}}_{i,st\to st'}}{k_{\mathrm{B}}T}\right) \tag{5.28}$$

with

$$f^{\mathrm{diff,TST}}_{i,st\to st'}(T) = \frac{z^{\mathrm{vib}}_{i,st\to st',\mathrm{TS}}}{z^{\mathrm{vib}}_{i,st}} \tag{5.29}$$

and

$$\Delta E^{\mathrm{diff}}_{i,st\to st'} = E^{\mathrm{tot}}_{i,st\to st',\mathrm{TS}} - E^{\mathrm{tot}}_{i,st} \quad . \tag{5.30}$$

Just as the adsorption and desorption barriers (cf. Eq. (5.16) and (5.26)) the diffusion barrier denotes the maximum barrier along the minimum energy pathway of the diffusion process. The reverse process for the diffusion $st \to st'$ is simply the backward diffusion $st' \to st$. Thus, in determining the process rates for these two events the detailed balance criterion (Eq. (5.4)) must be considered to assure the attainment of thermal equilibrium.

5.2.5 Reaction

Following the above outlined derivation for the different rates, also a reaction process can be treated equivalently. If a reaction coordinate containing a saddle point can be established, the reaction rate can be determined using TST. The general form of the reaction rate is then given by

$$r^{\mathrm{reac}}_{i\to f}(T) = f^{\mathrm{reac,TST}}_{i\to f}(T)\left(\frac{k_{\mathrm{B}}T}{h}\right)\exp\left(-\frac{\Delta E^{\mathrm{reac}}_{i\to f}}{k_{\mathrm{B}}T}\right) \quad , \tag{5.31}$$

with now i denoting simply the initial state and f the final state of the reaction process. $\Delta E^{\mathrm{reac}}_{i\to f}$ is the reaction barrier determined by the difference in energy between the initial and the transition state

$$\Delta E^{\mathrm{reac}}_{i\to f} = E^{\mathrm{tot}}_{i\to f,\mathrm{TS}} - E^{\mathrm{tot}}_{i} \tag{5.32}$$

The prefactor $f^{\mathrm{reac,TST}}_{i\to f}$ can again be obtained from the ratio of the partition functions in the transition and initial state. With this, a rate of every possible reaction process can in principle be calculated. The most difficult task here is finding an appropriate reaction coordinate and transition state. If the rates are used in a kMC simulation it is also important to consider detailed balance (cf. Section 5.1.1). Thus the reverse reaction process has to be defined and an appropriate rate has to be taken into account.

In the kMC simulations presented in this work the considered reaction processes can in general be described by two particles A and B adsorbed on lattice sites st and st' reacting to form the product C, which then readily desorbs into the gas phase, i.e.

$$A_{st} + B_{st'} \rightarrow C_{\mathrm{gas}} \quad . \tag{5.33}$$

Such a reaction can equivalently be described as an associative desorption process, where the desorption barrier is given by the corresponding reaction barrier. The reverse process is then the dissociative adsorption of C onto the lattice sites st and st'. The adsorption barrier for this process is given by the sum of the reaction barrier and the binding energy of the reacting particles A and B on the surface (cf. Eq. (5.27)).

5.3 Summary

The combination of density functional theory and statistical mechanics provides a possibility to transfer information gained in the microscopic regime into the meso- and macroscopic one. Using kinetic Monte Carlo simulations the actual time evolution of the system can be followed over an extended time up to even seconds. This is achieved by only considering so called rare events, while appropriately coarse graining over the original microscopic motions of the system. The decisive parameters of a kMC simulation are then the lattice representing the system, the processes describing the evolution of the system and the corresponding process rates. A connection between kMC and DFT is established in the determination of the process rates. The rates can be derived using transition state theory and the for this needed information about the potential energy surface is provided by DFT.

The clear advantage of this approach is the independence of the simulation parameters from experimental results. Thus the results of the simulations can be analyzed on the basis of the included processes. By comparison with experimental data the quality of the kMC model (lattice and processes) can be checked and possibly improved. If the rates are not obtained from electronic structure calculations but by fitting to experimental results, the quality of the model is much more difficult to verify. Processes, which have been overlooked in the modeling, might be summarized in some effective (unphysical) parameter with an effective rate obtained within the fitting procedure. Usually such fitted parameters exhibit a very small or no transferability to other systems or environmental conditions.

The most difficult and unsystematic part in a kMC simulation to date is the identification of relevant processes. Although some processes might be rather obvious, others might be overlooked or be completely unexpected. If a relevant process is missing from the beginning, of course also the results of a kMC simulation will miss the true physical behavior of the real system.

To overcome this limitation, some alternative approaches have been developed within recent years. One possibility is *on-the-fly kMC* [105], where the relevant processes are identified during the simulation by finding (all) possible pathways for the escape from the current state and the corresponding saddle points using the dimer-method [106]. Another possibility is *accelerated molecular dynamics* [107, 108]. Here, the classical trajectory is retained, but stimulated to find an appropriate escape pathway faster then a classical MD simulation. It should be noted though, that on the one hand such methods do not depend on the setup of a complete rate catalog, but on the other hand also here there is no guarantee for finding all possibly relevant processes. In addition these methods are usually computationally much more demanding. If a system is well described within a kMC approach as discussed in this Chapter, the kMC simulation provides a much more efficient way to follow the trajectory of a system over a mesoscopic time scale.

Part II

CO Oxidation At Pd(100)

Chapter 6

Palladium In A Pure Oxygen Gas Phase

6.1 Oxidation Stages Of Pd(100)

The structure and composition of a surface can be altered significantly depending on the surrounding gas phase conditions. In the particular case of a metal surface in contact with a pure oxygen gas phase it is usually expected, that with increasing oxygen content in the gas phase the surface will eventually be oxidized, which can be preceded by several stages of oxygen adlayers or so-called surface oxides. In this context the term *surface oxide* is mostly used for structures, that are more complex than a simple, ordered, on-surface adlayer, but still only represent a sub-nanometer thin film of an oxide-like structure on the metal surface.

The oxidation of the Pd(100) surface is a complex process, passing through several stages. Experimentally, four different phases have been observed, when exposing the Pd(100) surface to oxygen [109, 110, 111, 112, 113]. These include a $p(2\times2)$, a $c(2\times2)$, a (5×5) and a $(\sqrt{5}\times\sqrt{5})R27°$ structure. In a last stage the surface roughens and bulk palladium oxide (PdO) is formed. In this Section the geometric structures of the different phases are briefly discussed. Here, the (5×5) phase has not been considered, since the structure and state of the oxygen atoms has not been well established so far, i.e. there exists no well defined structural model. In addition, the (5×5) phase appears to be only of metastable character. The formation of a (5×5) structure is very sensitive to the surface preparation and oxygen exposure range, so that in the oxidation as well as in the reduction process the (5×5) structure can be bypassed going directly from a (2×2) to a $(\sqrt{5}\times\sqrt{5})R27°$ structure and vice versa [113].

Clean Metal Surface

Palladium is a late $4d$ transition metal, that crystallizes in the face-centered cubic (fcc) structure. The experimentally determined lattice constant at $T = 298\,\mathrm{K}$ is $a_0 = 3.880\,\text{Å}$ [11]. For the setup of the different Pd(100) surface structures, though, the

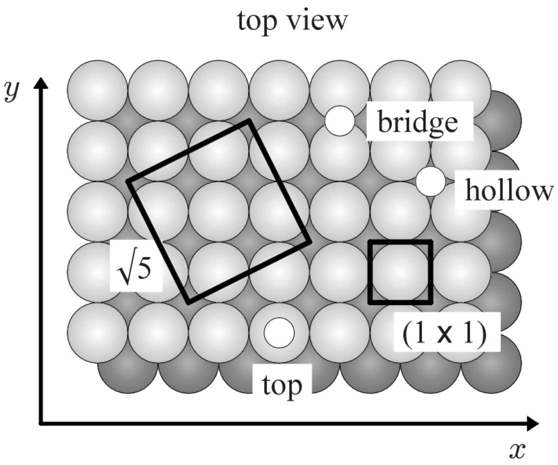

Figure 6.1: Schematic illustration of the Pd(100) surface. In addition to the different adsorption sites (white circles) the $(\sqrt{5}\times\sqrt{5})R27°$ and (1×1) surface unit cells are indicated.

	PBE	RPBE	LDA	Exp. [11]
Pd-fcc, bulk, a_0	3.95	3.99	3.84	3.880
(1×1)-Pd(100), $a_0/\sqrt{2}$	2.79	2.82	2.71	2.744
$(\sqrt{5}\times\sqrt{5})R27°$-Pd(100), $a_0\sqrt{5}/\sqrt{2}$	6.24	6.31	6.07	6.135

Table 6.1: Optimized cubic lattice constant of Pd obtained within the PBE, RPBE and LDA approximation for the exchange-correlation functional. For comparison also the experimental value is given. The experimental value is measured at $T = 298\,\mathrm{K}$, whereas the theoretical results are given at $T = 0\,\mathrm{K}$ without ZPV. In addition the resulting surface unit cell length of of the (1×1) and $(\sqrt{5}\times\sqrt{5})R27°$ structures are shown. All values are in Å.

theoretically optimized lattice constants are used. Since the theoretically determined lattice constant usually deviates slightly from the experimental one, the use of the experimental lattice constant could induce lateral strain effects. The results for the equilibrium lattice constant are listed in Tab. 6.1 for the PBE, the RPBE and the LDA as approximation to the exchange-correlation functional (cf. Section 2.5). The values have been obtained within the FP-(L)APW+lo approach (cf. Chapter 3) using the WIEN2k-code [67]. The muffin-tin radius for palladium is set to $R_{\mathrm{MT}}^{\mathrm{Pd}} = 2.0\,\mathrm{bohr}$, the wave function expansion inside the muffin-tins is considered up to $l_{\mathrm{max}}^{\mathrm{wf}} = 12$, and the potential expansion up to $l_{\mathrm{max}}^{\mathrm{pot}} = 6$. The Brillouin zone (BZ) integration is performed using a $[10\times10\times10]$ Monkhorst-Pack (MP) grid [61]. The energy cutoff for the plane wave representation in the interstitial region is $E_{\mathrm{max}}^{\mathrm{wf}} = 20\,\mathrm{Ry}$ for the wave function and $E_{\mathrm{max}}^{\mathrm{pot}} = 196\,\mathrm{Ry}$ for the potential (a detailed discussion of the convergence with respect to the chosen parameters in given in Appendix A).

In addition to the optimized bulk lattice constant the length of the resulting surface unit cell vectors of a simple (1×1) and the $(\sqrt{5}\times\sqrt{5})R27°$ structure are shown. As

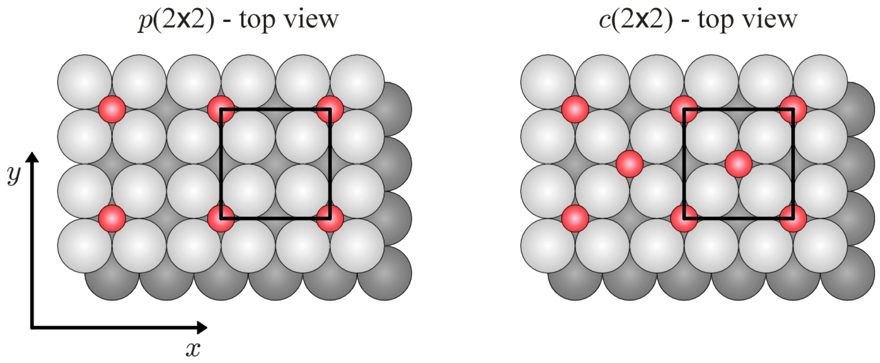

Figure 6.2: Schematic illustration of the $p(2 \times 2)$ (left) and $c(2 \times 2)$ (right) adlayer structures on Pd(100). The small, red spheres indicate oxygen atoms, large, light-grey ones are Pd atoms, and Pd atoms in the second layer are darkened.

expected, the LDA values reflect an overbinding tendency resulting in a $\sim 1\,\%$ smaller lattice constant compared to the experimental value, whereas the gradient corrected functionals overcorrect the LDA leading to $\sim$2–3 % too large lattice constants. For the results presented in this work the surface unit cells are constructed using the respective optimized lattice constant for each functional.

In Fig. 6.1 a schematic representation of the Pd(100) surface is shown. The surface exhibits three different, high-symmetry adsorption sites, a bridge, a top and a hollow site. Also the surface unit cells of the (1×1) and the $(\sqrt{5} \times \sqrt{5})R27^\circ$ structure are indicated.

Adlayers

Exposing the Pd(100) surface to an oxygen gas phase leads in the first stage to the formation of adlayer structures. Depending on the temperature and pressure conditions of the oxygen gas phase a variety of ordered and disordered structures might occur. This study, however, will focus in a first approach only on the two experimentally characterized ordered adlayers, the $p(2 \times 2)$ and the $c(2 \times 2)$. In both structures the oxygen atoms are adsorbed in the fourfold hollow site with a coverage of 0.25 monolayers (ML) and 0.5 ML, respectively. A top view of the two structures is shown in Fig. 6.2. The $c(2 \times 2)$ structure is also referred to as checkerboard pattern.

Surface Oxide

A further oxidation of the Pd(100) surface results in the formation of a $(\sqrt{5} \times \sqrt{5})R27^\circ$ structure accompanied by a reconstruction of the topmost palladium layer. A detailed experimental and theoretical investigation by Todorova *et al.* [18] revealed, that the structure of the $(\sqrt{5} \times \sqrt{5})R27^\circ$ surface oxide can essentially be described by a PdO(101) overlayer on Pd(100). The surface unit cell contains four palladium and four oxygen atoms on-top of five Pd(100) substrate atoms, cf. Fig 6.3. The four

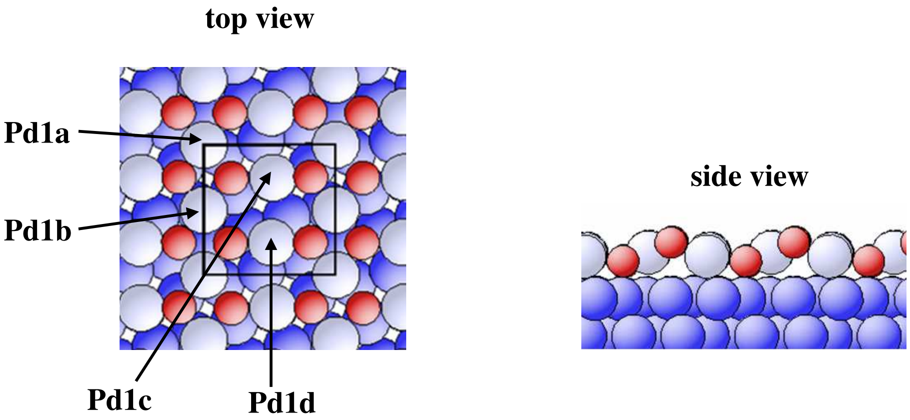

Figure 6.3: Schematic illustration of the $(\sqrt{5} \times \sqrt{5})R27°$ surface oxide structure on Pd(100). The small, red circles indicate oxygen atoms, the large, light-blue ones Pd atoms in the reconstructed oxide layer and the dark blue ones Pd atoms of the Pd(100) substrate.

palladium atoms can be divided into two groups, two of them are fourfold (Pd1a and Pd1b) and two are twofold (Pd1c and Pd1d) coordinated by oxygen atoms. Also the four oxygen atoms split into two groups, two of them sit at the interface between the surface oxide layer and the substrate and two on-top of the topmost palladium layer. Because of this oxide-like trilayer structure the $(\sqrt{5} \times \sqrt{5})R27°$ is considered as a surface oxide rather than a simple adlayer.

Bulk Oxide

Exposing the Pd(100) surface to an even higher oxygen pressure it has been observed experimentally, that in a last stage of the oxidation process the surface will finally be fully oxidized and bulk-like PdO forms on the surface. The oxide formation induces a substantial restructuring of the surface, which is indicated by an increasing roughness during the oxidation process [113, 23].

Palladium oxide crystallizes in the tetragonal PtS-structure with space group D_{4h}^{9} [114]. Each Pd atom is planar coordinated by four oxygen atoms and each O atom is tetrahedrally surrounded by four Pd atoms. The tetragonal unit cell contains two PdO units with Pd atoms at all corners and in the center, and oxygen atoms at (0, 1/2, 1/4), (0, 1/2, 3/4) resp. (1, 1/2, 1/4), (1, 1/2, 3/4), cf. Fig. 6.4. Also for the palladium oxide the lattice constants are optimized individually for every exchange-correlation functional. The experimental lattice constants at room temperature are $a_0 = 3.043\,\text{Å}$ and $c_0 = 5.336\,\text{Å}$ $(c/a = 1.753)$ [114]. The calculated values are compiled in Tab. 6.2. Again, the LDA overestimates the binding energy giving slightly too small lattice constants (∼0.8–1.7 %), whereas the gradient corrected functionals yield slightly too large lattice constants (∼0.3–3.5 %).

The values have been obtained using the following parameters: muffin-tin radii for

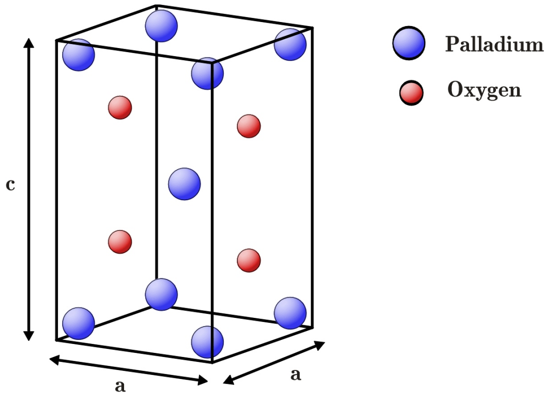

Figure 6.4: Tetragonal unit cell of PdO.

	PBE	RPBE	LDA	Exp. [114]
PdO a_0 (Å)	3.05	3.09	2.99	3.043
PdO c_0 (Å)	5.50	5.53	5.29	5.336
PdO c/a	1.80	1.79	1.77	1.753

Table 6.2: Optimized lattice constants for the tetragonal unit cell of PdO obtained within the PBE, RPBE and LDA approximation for the exchange-correlation functional. For comparison also the experimental values are given. The experimental values are measured at room temperature, whereas the theoretical results are are given $T = 0\,\mathrm{K}$ without ZPV.

palladium $R_{\mathrm{MT}}^{\mathrm{Pd}} = 1.8\,\mathrm{bohr}$ and oxygen $R_{\mathrm{MT}}^{\mathrm{O}} = 1.3\,\mathrm{bohr}$, wave function expansion inside the muffin tins up to $l_{\mathrm{max}}^{\mathrm{wf}} = 12$ and potential expansion up to $l_{\mathrm{max}}^{\mathrm{pot}} = 6$. A $[12 \times 12 \times 7]$ MP-grid is used for the BZ integration and the energy cutoff for the planewave representation in the interstitial is $E_{\mathrm{max}}^{\mathrm{wf}} = 20\,\mathrm{Ry}$ for the wave function and $E_{\mathrm{max}}^{\mathrm{pot}} = 196\,\mathrm{Ry}$ for the potential (a detailed discussion of the convergence with respect to the chosen parameters in given in Ref. [115]).

6.2 Atomistic Thermodynamics - Stability In Thermodynamic Equilibrium With An O_2 Gas Phase

In the previous Section the geometric structures of the different oxidation stages of the Pd(100), that will be considered in this work, have been introduced shortly. In this Section the atomistic thermodynamics approach (cf. Chapter 4) is applied to evaluate the stability of these different phases in thermodynamic equilibrium with an oxygen gas phase. The atomistic thermodynamics approach appears to be most suitable at this point, since this Section only focuses on the comparison of the stability of already known structures. Also, kinetic effects in the oxidation process are not considered here, but only the final, thermodynamic stable phases are investigated.

As a quantity to compare the stability of the different phases the Gibbs free energy of adsorption ΔG^{ads} is used as defined in Eq. (4.29). In a first approach the Gibbs free energies of the different subsystems are approximated by the total energies, which are the leading terms and directly accessible by DFT calculations. The contributions of the remaining terms to the Gibbs free energy will be discussed below. Using only the total energies, the Gibbs free energy of adsorption for the different oxidation stages of the Pd(100) surface is then determined by

$$\begin{aligned}\Delta G^{\mathrm{ads}}(\Delta\mu_{\mathrm{O}}) &= -\frac{1}{A}\left(E^{\mathrm{tot}}_{\mathrm{O@Pd(100)}} - E^{\mathrm{tot}}_{\mathrm{Pd(100)}} - \Delta N_{\mathrm{Pd}} E^{\mathrm{tot}}_{\mathrm{Pd,bulk}} - N_{\mathrm{O}}(1/2 E^{\mathrm{tot}}_{\mathrm{O_2}} + \Delta\mu_{\mathrm{O}})\right) \\ &= -\frac{N_{\mathrm{O}}}{A}\widetilde{E}^{\mathrm{bind}}_{\mathrm{O@Pd(100)}} + \frac{N_{\mathrm{O}}}{A}\Delta\mu_{\mathrm{O}} \quad .\end{aligned} \tag{6.1}$$

For the two adlayer structures $\Delta N_{\mathrm{Pd}} = 0$, whereas due to the reconstruction of the topmost Pd layer $\Delta N_{\mathrm{Pd}} = -1$ for the surface oxide. $\widetilde{E}^{\mathrm{bind}}_{\mathrm{O@Pd(100)}}$ is the average binding energy per oxygen atom, also including possible contributions arising from a difference in the number of surface atoms ($\Delta N_{\mathrm{Pd}} \neq 0$).

Computational Details

The different surfaces are simulated within the supercell approach using inversion symmetric slabs with 5–7 layers and 14–20 Å vacuum between subsequent slabs. The outermost 3–5 layers are fully relaxed. The muffin-tin radii are set to $R^{\mathrm{Pd}}_{\mathrm{MT}} = 2.0\,\mathrm{bohr}$ for palladium and $R^{\mathrm{O}}_{\mathrm{MT}} = 1.0\,\mathrm{bohr}$ for oxygen. Inside the muffin-tins the wave functions are expanded up to $l^{\mathrm{wf}}_{\mathrm{max}} = 12$ and the potential up to $l^{\mathrm{pot}}_{\mathrm{max}} = 6$. For the $p(2\times 2)$ and $c(2\times 2)$ structure a $[5\times 5\times 1]$ and for the $(\sqrt{5}\times\sqrt{5})R27^\circ$ a $[4\times 4\times 1]$ MP-grid is used to integrate the BZ. Since calculations with different MP-grids are not fully comparable, the energies of the clean metal surface, $E^{\mathrm{tot}}_{\mathrm{Pd(100)}}$, and the bulk palladium, $E^{\mathrm{tot}}_{\mathrm{Pd,bulk}}$, needed to evaluate the Gibbs free energy of adsorption as defined in Eq. (6.1) are calculated in the same supercell as the corresponding adlayers or surface oxide structure. The different MP-grids of the different supercells are then chosen to provide a similar convergence of the average binding energies per oxygen atom. The energy cutoff for the expansion of the wave function in the interstitial is $E^{\mathrm{wf}}_{\mathrm{max}} = 20\,\mathrm{Ry}$ and for the potential $E^{\mathrm{pot}}_{\mathrm{max}} = 196\,\mathrm{Ry}$. Using these basis set parameters the average binding energies per oxygen atom are converged within 50 meV, so that the Gibbs free energies of adsorption are converged within 1–5 meV/Å^2 (for a detailed discussion of the computational setup cf. Appendix A.2). Since the results are converged with respect to the binding energy per oxygen atom, a higher coverage induces a larger error in ΔG^{ads}. But then again, a higher coverage structure corresponds to a line with a steeper slope within the respective phase diagram, so that the x-positions of the crossing points with other lines, which determine the stability range of a certain structure, are less sensitive to small changes in ΔG^{ads} than for low coverage structures. The total energy of the O_2 molecule is calculated by $E^{\text{tot}}_{O_2} = 2E^{\text{tot}}_{O} + E^{\text{bind}}_{O_2}$. The oxygen atom is calculated within a $(13 \times 14 \times 15)$ bohr supercell using only the Γ-point. The calculations are performed spin-polarized and with the same muffin-tin radius, $l^{\text{wf}}_{\text{max}}$, $l^{\text{pot}}_{\text{max}}$, $E^{\text{pot}}_{\text{max}}$, and $E^{\text{wf}}_{\text{max}}$ as above.

To determine the binding energy of the oxygen molecule, $E^{\text{bind}}_{O_2}$, the muffin tin radius for the oxygen in the O_2 molecule and O atom is set to $R^{\text{O}}_{\text{MT}} = 1.1$ bohr. The calculations are performed in a $(13 \times 14 \times 18)$ bohr supercell for the molecule, resp. a $(13 \times 14 \times 15)$ bohr supercell for the atom, using again only the Γ-point. Both, the atom and the molecule are treated spin-polarized. $l^{\text{wf}}_{\text{max}}$, $l^{\text{pot}}_{\text{max}}$, and $E^{\text{pot}}_{\text{max}}$ are chosen as above, the energy cutoff for the expansion of the wave function in the interstitial is increased up to $E^{\text{wf}}_{\text{max}} = 37$ Ry. The bond length in the O_2 molecule is fully optimized for each exchange-correlation functional. Within this highly converged basis set the binding energy of the O_2 molecule is calculated as $E^{\text{bind}}_{O_2} = -6.20$ eV (PBE), -5.75 eV (RPBE) and -7.56 eV (LDA) (for a detailed discussion cf. Appendix A.3).

Surface Phase Diagrams

The binding energies and the corresponding Gibbs free energies of adsorption of the different structures are listed in Tab. 6.3 for the PBE, the RPBE and the LDA as approximation to the exchange-correlation functional. The dependence of the Gibbs free energy of adsorption on the chemical potential of the oxygen gas phase is visualized in Fig. 6.5, using the PBE results. Focussing first on the left graph in Fig. 6.5, there are five different lines for the clean Pd(100) surface, the $p(2 \times 2)$, the $c(2 \times 2)$, the $(\sqrt{5} \times \sqrt{5})R27^\circ$ structure and for the PdO bulk with increasing slope corresponding to the increasing oxygen coverage from 0.0 ML (clean) to 0.8 ML ($(\sqrt{5} \times \sqrt{5})R27^\circ$) and finally a vertical line indicating the stability region of the bulk oxide (*infinite* number of oxygen atoms). As explained in detail in Section 4.3 the thermodynamically most stable structure is always the one that maximizes ΔG^{ads}. Since the y-axis in the left plot of Fig. 6.5 is inverted this thermodynamically most stable structure will be the one with the *lowest* line. It should be noted that at finite temperatures the transition between the different phases will not be sharp, but due to contributions from the configurational entropy coexistence regions will develop, containing a mixture of energetically neighboring structures.

Starting at a very low oxygen chemical potential the clean Pd(100) surface has to be the most stable phase. At $\Delta\mu_{\text{O}} = -1.35$ eV the line of the $p(2 \times 2)$ structure crosses the zero line and the $p(2 \times 2)$ is the most stable phase. With further increasing $\Delta\mu_{\text{O}}$ the $(\sqrt{5} \times \sqrt{5})R27^\circ$ surface oxide becomes stable ($\Delta\mu_{\text{O}} = -1.15$ eV) and finally the stability region of the bulk oxide is reached ($\Delta\mu_{\text{O}} = -0.87$ eV), which is determined by the heat of formation of PdO. The PBE value for the heat of formation of PdO in the low temperature limit, $\Delta G^{f}(T = 0\,\text{K}, p = 0) = -0.87$ eV, compares rather well with the experimental value of $\Delta G^{f}_{\text{exp}}(T \rightarrow 0\,\text{K}, p = 1\,\text{atm}) = -0.97$ eV [11]. For the top two x-axes of the left graph in Fig.6.5 the chemical potential has been converted

		$p(2 \times 2)$	$c(2 \times 2)$	$(\sqrt{5} \times \sqrt{5})R27^\circ$
PBE	$\widetilde{E}^{\mathrm{bind}}$	-1.35	-1.10	-1.20
	$\Delta G^{\mathrm{ads}}(\Delta\mu_{\mathrm{O}} = 0)$	-43.20	-70.33	-123.35
RPBE	$\widetilde{E}^{\mathrm{bind}}$	-0.98	-0.77	-0.92
	$\Delta G^{\mathrm{ads}}(\Delta\mu_{\mathrm{O}} = 0)$	-30.84	-48.66	-92.96
LDA	$\widetilde{E}^{\mathrm{bind}}$	-2.15	-1.79	-1.77
	$\Delta G^{\mathrm{ads}}(\Delta\mu_{\mathrm{O}} = 0)$	-73.06	-121.76	-192.46

Table 6.3: Average binding energy per oxygen atom in eV and Gibbs free energy of adsorption in meV/Å^2 for $\Delta\mu_{\mathrm{O}} = 0$ for the two adlayers and the surface oxide on Pd(100). The different values obtained using the PBE, the RPBE and the LDA as approximation to the exchange correlation functional are listed.

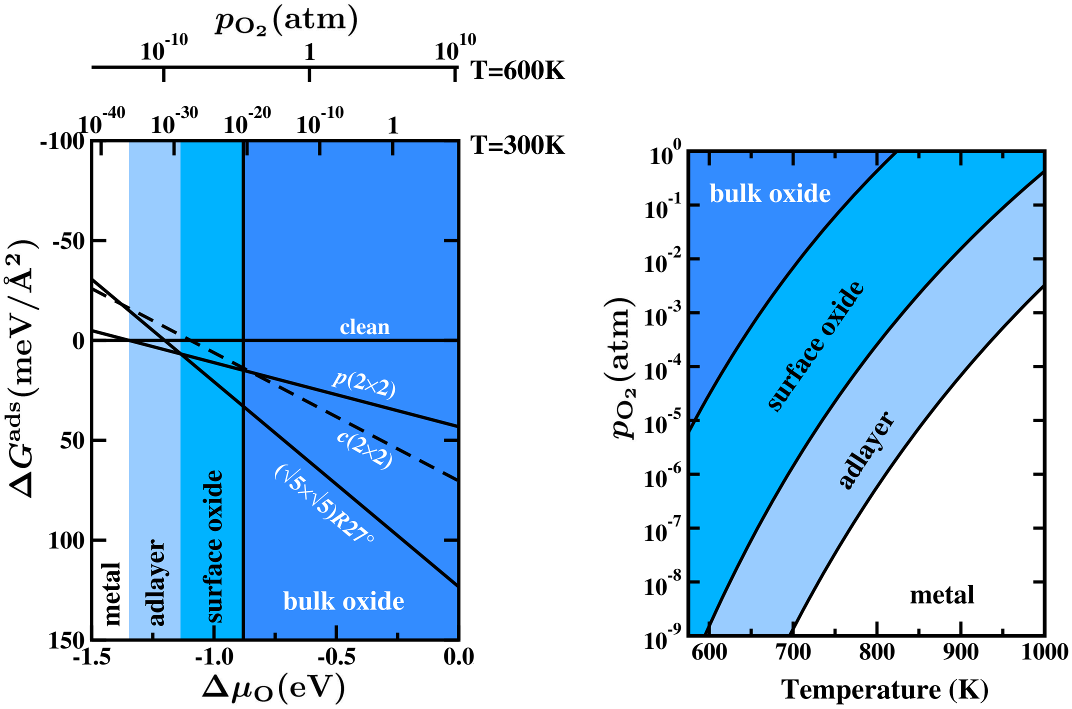

Figure 6.5: Surface phase diagram of Pd(100) in thermodynamic equilibrium with an oxygen gas phase using the DFT-PBE results. In the left graph the Gibbs free energy of adsorption is plotted vs. the oxygen chemical potential. In the right graph the $\Delta\mu_{\mathrm{O}}$ values marking the stability regions for every phase are converted into the respective (T, p)-conditions, showing the thermodynamically most stable phase at any given T and p.

E_{xc}	metal → $p(2 \times 2)$	$p(2 \times 2) \to (\sqrt{5} \times \sqrt{5})R27°$	$(\sqrt{5} \times \sqrt{5})R27° \to$ PdO bulk
PBE	-1.35	-1.15	-0.87
RPBE	-0.98	-0.90	-0.62
LDA	-2.15	-1.64	-1.42

Table 6.4: Values of the oxygen chemical potential $\Delta\mu_{\mathrm{O}}$ in eV for the phase boundaries between the different oxidation phases of the Pd(100) surface obtained using the PBE, RPBE and LDA exchange-correlation functional.

into pressures scales at two fixed temperatures (cf. Section 4.4), which can provide a more intuitive understanding of this figure. An even more intuitive representation of the stability of the different phases is shown in the right plot of Fig. 6.5. Here, the one-dimensional dependence on the chemical potential is transferred into a two-dimensional dependence on temperature and pressure. The plot then only shows the most stable structures in the corresponding (T, p)-range. At high temperatures and low pressures the clean metal surface is stable, lowering the temperature or increasing the pressure corresponds to an increase in the oxygen chemical potential and thus results again in a stabilization of the oxygen containing structures.

In Fig. 6.5 it can be seen, that the $c(2 \times 2)$ structure observed in ultra high vacuum (UHV) experiments does not appear to be thermodynamically stable under any oxygen gas phase conditions. Thus, the $c(2 \times 2)$ phase is most likely a meta-stable state produced by the exposure kinetics. On the other hand, the $p(2 \times 2)$ and the $(\sqrt{5} \times \sqrt{5})R27°$ structure are both stable over an extended (T, p)-range. The stability of the surface oxide structure notably exceeds the one of the bulk oxide, so that the surface oxide can actually be considered as a separate phase, which might exhibit properties different from a simple adlayer structure as well as from the bulk oxide phase.

To investigate the influence of the chosen exchange-correlation functional on the obtained results, the surface phase diagram is also calculated using the RPBE and LDA (cf. Tab. 6.3). The results for all three exchange-correlation functionals are shown in Fig. 6.6 together with experimental results obtained by surface x-ray diffraction (SXRD) measurements [23]. Focussing first on the three theoretical plots it becomes obvious, that there is a significant shift in the phase boundaries for the different functionals (cf. Tab. 6.4). Nevertheless, all three functionals show the same phases and the same ordering of phases with respect to the (T, p)-conditions. The $c(2 \times 2)$ phase does not appear in any of the phase diagrams and the surface oxide is stable over a wide (T, p)-range independent of the functional used.

Comparing the theoretical phase diagrams to the experimental one (lower right plot in Fig 6.6), it can be seen, that also in the SXRD measurements the $c(2 \times 2)$ structure is not observed. Concentrating on the experimental and PBE results, the two phase diagrams actually show a quite good agreement over a wide range of environmental conditions. Especially the transition from the metal to the $p(2 \times 2)$ to the $(\sqrt{5} \times \sqrt{5})R27°$ in going form high temperatures and low pressures to lower T and

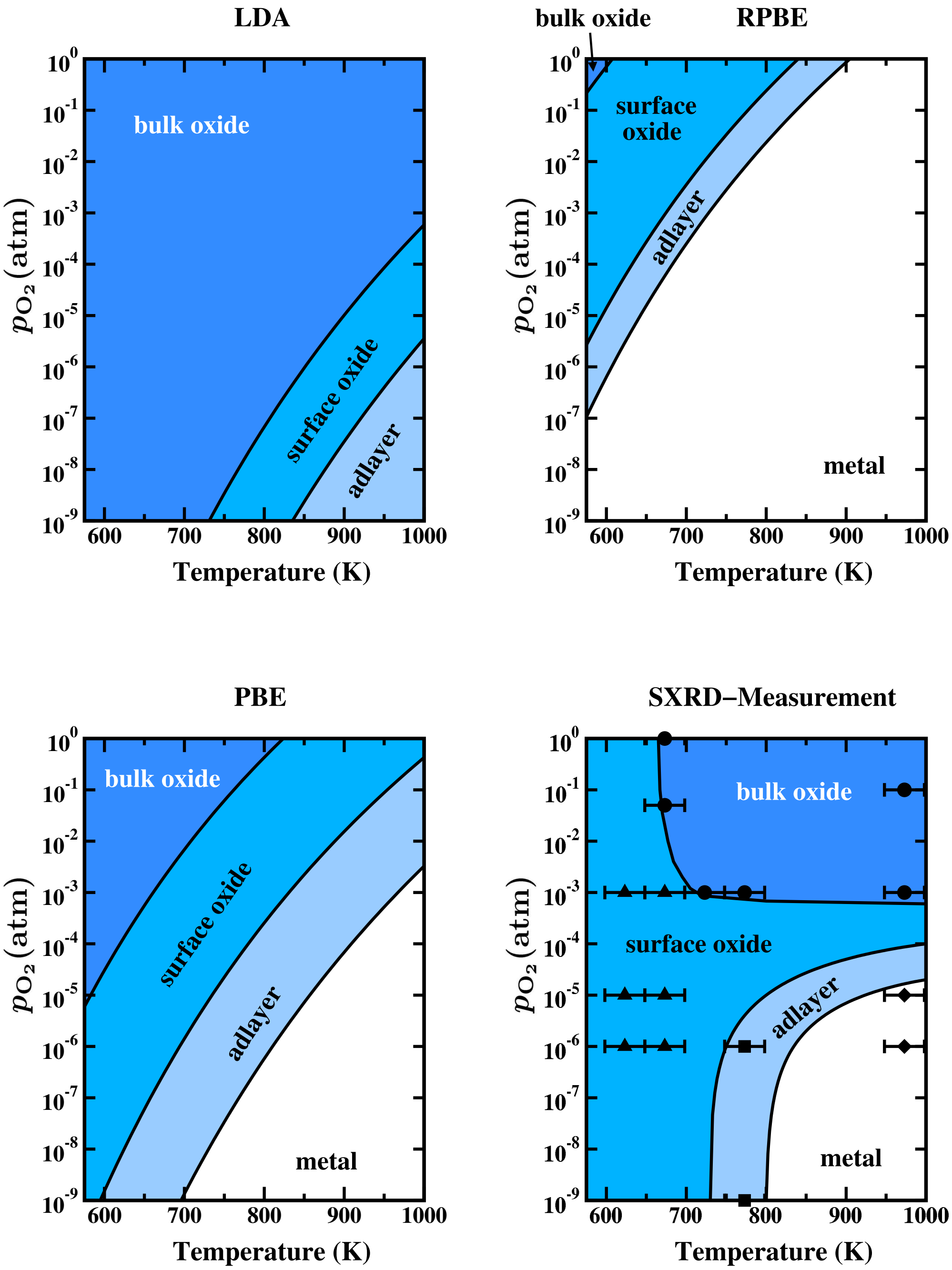

Figure 6.6: Surface phase diagrams for the Pd(100) surface in equilibrium with an oxygen gas phase for the LDA, RPBE and PBE exchange-correlation functional. The lower right figure shows experimental results obtained by surface x-ray diffraction (SXRD) measurements [23].

higher p is rather well reproduced. There is, however, one noticeable difference, which can not be explained by the uncertainties underlying the atomistic thermodynamics approach as well as the experimental setup. In the upper left corner of the experimental phase diagram (low temperatures, high pressure) the $(\sqrt{5} \times \sqrt{5})R27^\circ$ surface oxide is observed. Since the atomistic thermodynamics approach, which assumes full thermodynamic equilibrium of all phases, predicts the bulk oxide to be stable under such (T, p)-conditions, this can be interpreted as a kinetic limitation to the growth of the bulk oxide. Even without the theoretical phase diagrams, this interpretation is still consistent. In thermodynamic equilibrium the different phases are separated by lines of constant chemical potential, which have to be always parallel to the ones shown in the theoretical phase diagrams. The phase boundary between the surface oxide and the bulk oxide in the experimental phase diagram is certainly not parallel to such a line of constant $\Delta\mu_{\mathrm{O}}$, which confirms the assumption that the formation of the bulk oxide is hindered by kinetic effects on the time scale accessible to the SXRD experiments.

Evaluating The Gibbs Free Energy

The discussed theoretical phase diagrams are based on DFT total energies only, neglecting all other contributions to the Gibbs free energy. The uncertainty in the presented results introduced by such a simplification can be examined by an order of magnitude estimate of the different contributions to ΔG^{ads} besides the total energy, as discussed in Section 4.3.1. If this first approximation reveals, that the drawn physical conclusions are significantly changed by considering all contributions to ΔG^{ads}, the respective terms have to be calculated explicitly. However, the order of magnitude estimate can already be obtained with much less computational effort and is thus very helpful to decide, whether or not it is necessary to evaluate the entire Gibbs free energy.

For the here investigated structures the contributions arising from the pV-term as well as from the configurational entropy will be in the same range as for the general case discussed in Section 4.3.1, i.e. the two terms will only contribute less than $3\,\mathrm{meV/Å}^2$ to the Gibbs free energy, which will not significantly influence the results shown here (cf. Fig. 6.5).

The vibrational contribution, though, can be somewhat larger and will vary for every considered structure. Following the approach outlined in Section 4.2 the vibrational contribution to the Gibbs free energy of adsorption of the $p(2 \times 2)$ phase is approximately given by

$$\Delta G^{\mathrm{ads,vib}}(T) \approx -\frac{1}{A}\left(F^{\mathrm{vib}}(T, \bar{\omega}^{\mathrm{surf}}_{\mathrm{O-Pd}}) - \frac{1}{2}F^{\mathrm{vib,ZPVE}}(\bar{\omega}^{\mathrm{gas}}_{\mathrm{O}_2})\right) \quad , \tag{6.2}$$

where $\bar{\omega}^{\mathrm{surf}}_{\mathrm{O-Pd}}$ is the averaged Einstein frequency of an oxygen atom adsorbed in a fourfold hollow site on the Pd(100) surface. Here, the change in the vibrational contribution of the Pd atoms in the clean and the adlayer structure is neglected, so that

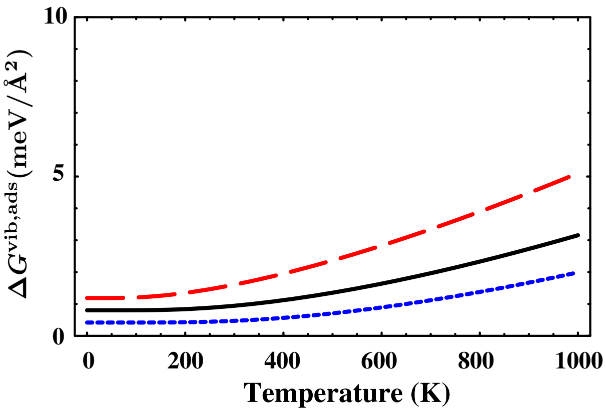

Figure 6.7: Vibrational contribution to the Gibbs free energy of adsorption for the $p(2 \times 2)$ adlayer on Pd(100) within a simple Einstein-approximation (see text).

the vibrational contribution to ΔG^{ads} is approximated by the change in the vibrational energy of the oxygen molecule in the gas phase and the oxygen atom adsorbed on the surface. For the oxygen molecule only the zero-point vibration energy (ZPVE, not included in the presented DFT total energies) has to be considered, since the (T, p)-dependent contributions are already summarized in $\Delta\mu_{\mathrm{O}}$. Assuming a characteristic frequency of $\bar{\omega}^{\mathrm{surf}}_{\mathrm{O-Pd}} = 48\,\mathrm{meV}$ for the Pd-O stretch frequency [116] of the adsorbed oxygen and $\bar{\omega}^{\mathrm{gas}}_{\mathrm{O_2}} = 196\,\mathrm{meV}$ for the O-O vibration in the gas phase [117] the vibrational contribution to ΔG^{ads} for the $p(2 \times 2)$ stays below $\sim 3\,\mathrm{meV/Å^2}$ for temperatures up to 1000 K (cf. black line in Fig. 6.7). Even if the characteristic frequency of the Pd-O stretching frequency is changed by ±50 % (red-dashed, −50 %, blue-dotted, +50 %, lines in Fig. 6.7) the contribution does not increase considerably.

For the $c(2 \times 2)$ phase this contribution simply doubles, since there are two oxygen atoms in the (2×2) surface unit cell. But still for the temperature range considered here, which is up to 600 K, this only leads to a maximum estimated contribution of $\sim 6\,\mathrm{meV/Å^2}$, which would not lead to an appearance of the $c(2 \times 2)$ structure as a thermodynamically stable phase.

Considering the surface oxide structure an additional contribution arising from the change in the vibrational energy between bulk and surface Pd atoms has to be taken into account, since the $(\sqrt{5} \times \sqrt{5})R27°$ structure contains one surface atom less then the corresponding Pd(100) surface, which has to be balanced by the bulk reservoir $(\Delta N_{\mathrm{Pd}} = -1)$. The vibrational contribution to ΔG^{ads} for the surface oxide structure can then be estimated by

$$\begin{aligned}\Delta G^{\mathrm{ads,vib}}(T) \approx & -\frac{1}{A}\left(4F^{\mathrm{vib}}(T, \bar{\omega}^{\mathrm{surf}}_{\mathrm{O-Pd}}) - \frac{4}{2}F^{\mathrm{vib,ZPVE}}(\bar{\omega}^{\mathrm{gas}}_{\mathrm{O_2}})\right) \\ & - \frac{3}{A}\left(F^{\mathrm{vib}}(T, \bar{\omega}^{\mathrm{bulk}}_{\mathrm{Pd}}) - F^{\mathrm{vib}}(T, \bar{\omega}^{\mathrm{surf}}_{\mathrm{Pd}})\right) \quad .\end{aligned} \tag{6.3}$$

Using a characteristic frequency of $\bar{\omega}_{\mathrm{Pd}}^{\mathrm{bulk}} = 20\,\mathrm{meV}$ for bulk Pd [118] and allowing a $\pm 50\,\%$ change for the surface atoms this contribution will again be below $\sim 6\,\mathrm{meV/Å^2}$ for temperatures up to 600 K. Allowing also for an uncertainty of $\pm 50\,\%$ in the characteristic frequencies of the bulk Pd and the adsorbed oxygen will slightly change this contribution, but it will still be below $\sim 10\,\mathrm{meV/Å^2}$ for all temperatures up to 600 K. However, even if the Gibbs free energy of the adsorption of the surface oxide is changed by $\pm 10\,\mathrm{meV/Å^2}$, the surface oxide will still be a thermodynamically stable phase over an extended (T, p)-range, which is one of the important conclusions of this study.

The previous discussion shows, that the uncertainty arising from approximating the Gibbs free energy by the leading total energy term only does not significantly affect any of the above drawn conclusions. Regarding the absolute values of ΔG^{ads} and the resulting phase boundaries, the uncertainty introduced by the choice of the exchange-correlation functional is in any case much larger than any error introduced by not considering all contributions to ΔG^{ads}. Thus, an explicit evaluation of all terms included in ΔG^{ads} does not appear to be necessary in this case.

6.3 PdO Low-Index Surfaces

Despite the different stages involved in the oxidation of the Pd(100) surface, in an oxygen rich atmosphere the formation bulk oxide is usually observed as the final stage. Experimentally, a roughening of the surface is found along with the formation of PdO [113, 23]. This suggests that the bulk oxide growth does not proceed via a thickening of the PdO(101) template provided by the $(\sqrt{5} \times \sqrt{5})R27°$ surface oxide, but instead 3-dimensional PdO nanoparticles are formed through faceting. The facets of such a nanoparticle will be built up by different PdO surface structures.

To obtain a first insight into the morphology of PdO crystals, the structure and stability of different PdO surfaces in equilibrium with an oxygen gas phase are discussed in this Section. Since there is as good as no experimental information about the atomic structure and composition of crystalline PdO surfaces, the discussion is limited to all possible (1×1) terminations of the low-index surfaces of PdO. An investigation of possible surface reconstructions is hardly feasible without any information about the surface composition and periodicity. Nevertheless, with the knowledge of the surface energetics it is then possible to determine a first approximation to the equilibrium shape of a single crystal by setting up a so-called Wulff construction within the compiled data set.

6.3.1 Structure And Stability

Due to the tetragonal structure of the PdO unit cell (cf. Fig. 6.4) there are five inequivalent low-index surface orientations as illustrated in Fig. 6.8. Each of these surface orientations exhibits 2–3 different (1×1) surface terminations depending on at

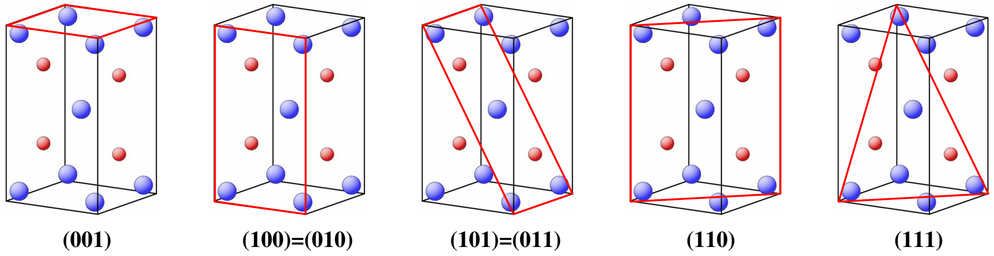

Figure 6.8: Schematic illustration of the low-index PdO surfaces. The respective planes are indicated by the red lines. Small red spheres represent oxygen atoms, large blue ones palladium atoms.

which layer the bulk-stacking sequence is truncated at the surface. For the PdO(001) surface, parallel to the xy-plane, there are two different surface terminations, one with only Pd atoms [PdO(001)-Pd] and one with only O atoms [PdO(001)-O] in the topmost layer. A schematic illustration of all discussed surface terminations is shown as inset in Fig. 6.9 – Fig. 6.11. The PdO(100) surface (parallel to the yz-plane), which is equivalent to the PdO(010) surface (parallel to the xz-plane), shows also two different terminations, one again containing only Pd atoms in the topmost layer [PdO(100)-Pd] and the other Pd as well as O atoms [PdO(100)-PdO]. The PdO(101) orientation, which is equivalent to the PdO(011) orientation, exhibits an O-Pd_2-O trilayer stacking structure. For this orientation there exist three different terminations. For the stoichiometric termination the layer stacking is truncated just between two consecutive O-Pd_2-O trilayers [PdO(101)]. The other two terminate either after the Pd layer [PdO(101)-Pd] or after the second O layer [PdO(101)-O], yielding two O layers at the top. The remaining two orientations, PdO(110) and PdO(111), are both characterized by alternating layers of Pd and O atoms along the surface normal. Thus, there are two possible terminations for each orientation, one having just Pd atoms [PdO(110)-Pd and PdO(111)-Pd] and the other having only O atoms in the topmost layer [PdO(110)-O and PdO(111)-O].

Out of these 11 different (1×1) terminations only one is stoichiometric, the PdO(101) termination, whereas the other 10 exhibit either an excess of oxygen or palladium atoms. These 10 surface terminations would therefore be considered as so-called *polar* surfaces, which from an electrostatic point of view were traditionally thought to be rather unstable [119, 120]. Theoretically, the stability of polar oxide surfaces has been predicted for several cases, e.g. for different iron oxide surfaces as well as for RuO_2 surfaces terminations [74, 76, 121]. A possible connection between the stability and the polarity of the different PdO surface terminations is discussed in Section 6.3.3.

To compare the stability of the different surface structures in thermodynamic equilibrium with the surrounding oxygen gas phase the atomistic thermodynamics approach is used as discussed in Section 4.2. For palladium oxide the surface free energy in the oxygen poor limit ($\Delta\mu_{\mathrm{O}} = \Delta G^{f}_{\mathrm{PdO}}$, i.e. now a range of $\Delta\mu_{\mathrm{O}}$ beyond the one shown in Fig. 6.5 and Fig. 6.6 is discussed) is given by

$$\gamma_{\mathrm{O-poor}} \approx \frac{1}{A}\Big[E^{\mathrm{surf}}_{\mathrm{PdO}}(N_{\mathrm{Pd}}, N_{\mathrm{O}}) - N_{\mathrm{O}} E^{\mathrm{bulk}}_{\mathrm{PdO}} - \Big(N_{\mathrm{Pd}} - N_{\mathrm{O}}\Big) E^{\mathrm{bulk}}_{\mathrm{Pd}}\Big] \quad . \tag{6.4}$$

Correspondingly, the surface free energy in the oxygen rich limit ($\Delta\mu_{\mathrm{O}} = 0$) is

$$\gamma_{\mathrm{O-rich}} = \gamma_{\mathrm{O-poor}} + \frac{1}{A}\left(N_{\mathrm{O}} - N_{\mathrm{Pd}}\right)\Delta G^{f}_{\mathrm{PdO}}(T = 0\,\mathrm{K}, p = 0) \quad . \tag{6.5}$$

Again, the Gibbs free energies have been approximated by the total energies in a first step. Following the discussion in Section 4.2 the contribution from the pV-term as well as from the configurational entropy to the Gibbs free energy can be estimated as below $3\,\mathrm{meV/Å^2}$. To obtain an order of magnitude estimate of the vibrational contribution to the surface free energy the Einstein approximation to the phonon DOS can be employed as explained in Section 4.2. Experimental results are used to estimate the characteristic frequencies of palladium and oxygen in PdO bulk with $\bar{\omega}^{\mathrm{bulk}}_{\mathrm{Pd}} = 20\,\mathrm{meV}$ and $\bar{\omega}^{\mathrm{bulk}}_{\mathrm{O}} = 70\,\mathrm{meV}$ [81]. To now evaluate Eq. (4.28) the number of Pd and O atoms at the surface has to be identified for every surface termination. An atom is considered to be *at* the surface, if its nearest neighbor coordination is changed compared to the coordination in the bulk structure, i.e. in the case of the PdO(101) termination one Pd and one O atom would be counted as surface atoms, whereas e.g. for the PdO(001)-Pd termination only the topmost Pd layer is considered as surface atoms. Within this approximation the vibrational contribution to the surface free energy stays within a range of about 10–$20\,\mathrm{meV/Å^2}$ for all temperatures up to $T = 600\,\mathrm{K}$ and for all considered PdO terminations. This is certainly not a very small contribution, but in the discussion of the results it will become apparent below that even a 10–$20\,\mathrm{meV/Å^2}$ change in the surface free energies will not affect the conclusions drawn.

Computational Details

To simulate the different PdO surfaces the supercell approach is applied using symmetric slabs with 7–11 layers and a 12–15 Å vacuum between subsequent slabs. The outermost 2–4 layers are fully relaxed for all surfaces. Within this setup of the supercells the absolute surface energies are converged within $3\,\mathrm{meV/Å^2}$. The muffin tin radii for palladium and oxygen are set to $R^{\mathrm{Pd}}_{\mathrm{MT}} = 1.8\,\mathrm{bohr}$ and $R^{\mathrm{O}}_{\mathrm{MT}} = 1.3\,\mathrm{bohr}$. The wave function expansion inside the muffin tins is considered up to $l^{\mathrm{wf}}_{\mathrm{max}} = 12$ and the potential expansion up to $l^{\mathrm{pot}}_{\mathrm{max}} = 6$. The BZ-integration is performed using MP grids. The MP grids and number of **k**-points in the irreducible part of the BZ are listed in Tab. 6.5. The energy cutoff for the planewave representation in the interstitial region is $E^{\mathrm{wf}}_{\mathrm{max}} = 17\,\mathrm{Ry}$ for the wave function and $E^{\mathrm{pot}}_{\mathrm{max}} = 196\,\mathrm{Ry}$ for the potential. With these basis sets the absolute surface energies of the different PdO surfaces are converged within 1–$2\,\mathrm{meV/Å^2}$ regarding the **k**-points and 3–$4\,\mathrm{meV/Å^2}$ regarding the planewave cutoff in the interstitial $E^{\mathrm{wf}}_{\mathrm{max}}$. Errors in the relative energies

PdO surface	MP grid	no. of irred. **k**-points
(100) ≡ (010)	[3×7×1]	8
(001)	[7×7×1]	16
(101) ≡ (011)	[1×3×7]	8
(110)	[4×3×1]	6
(111)	[2×4×1]	6

Table 6.5: Employed Monkhorst-Pack grids and corresponding number of **k**-points in the irreducible part of the Brillouin zone for the different (1×1) surface unit cells of the low-index PdO surfaces.

comparing different surfaces terminations are even smaller (for a detailed discussion of the computational setup cf. Appendix A.1).

Surface Free Energy

In Fig. 6.9 – Fig. 6.11 the surface free energy plots of all eleven (1×1) terminations are shown. As expected from the general discussion in Section 4.2 terminations with an oxygen excess show a negative slope, i.e. they become more stable in a more oxygen-rich gas phase, whereas terminations with an oxygen deficiency and a positive slope become less stable with increasing oxygen chemical potential. The vertical dotted lines mark the stability range of the oxide surfaces (cf. Section 4.2), determined by the heat of formation of PdO, $\Delta G^f_{\mathrm{PdO}}(T = 0\,\mathrm{K}, p = 0) = -0.87\,\mathrm{eV}$ (PBE). To take into account the uncertainty in these theoretically well defined but computational only approximate limits, the x-axes of the surface free energy plots are somewhat extended outside these boundaries.

Comparing the five plots for the different surface orientations in Fig. 6.9 – Fig. 6.11 the very low surface energy, i.e. high stability, of the PdO(100)-PdO termination is clearly observable. Only the PdO(101) and towards the O-rich limit the PdO(110)-O and the PdO(111)-O surfaces exhibit a comparably low surface free energy. All other terminations show a rather high surface free energy over the whole range of $\Delta\mu_{\mathrm{O}}$, especially all those terminations with Pd atoms in the outermost layer. Considering the energy scale of the surface free energy plots it can be noted, that the uncertainty of 10–20 $\mathrm{meV/Å^2}$ in γ introduced by neglecting the vibrational contributions to the Gibbs free energies does not affect the ordering of the different surface terminations with respect to their thermodynamic stability.

To obtain an estimate for the uncertainty introduced by the choice of the PBE as approximation to the exchange-correlation functional all surface free energies are also calculated within the LDA. To set up the supercells for these LDA calculations the respective optimized lattice constants for PdO bulk are used (cf. Tab. 6.2). The surface free energies of all 11 surface terminations in the oxygen-poor limit obtained within the PBE and LDA are listed in Tab. 6.6. Comparing the values for $\gamma_{\text{O-poor}}$

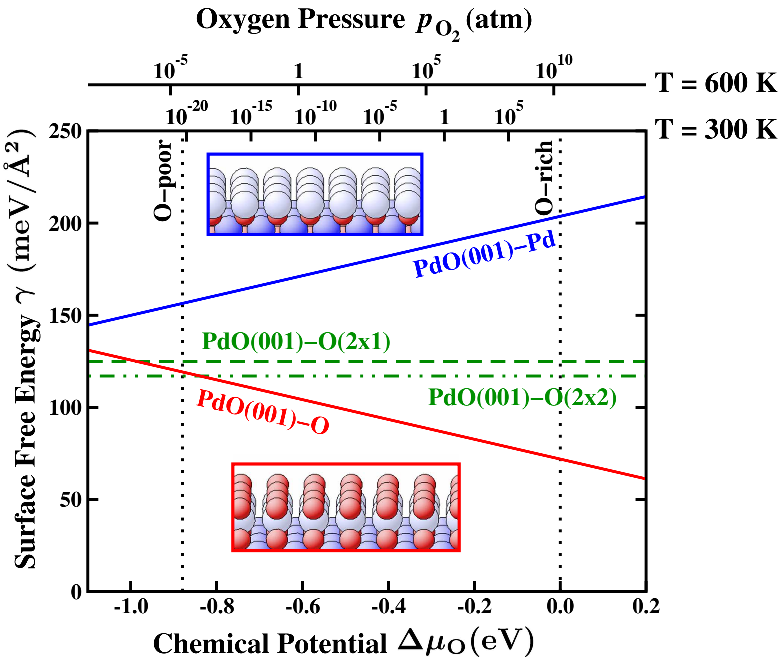

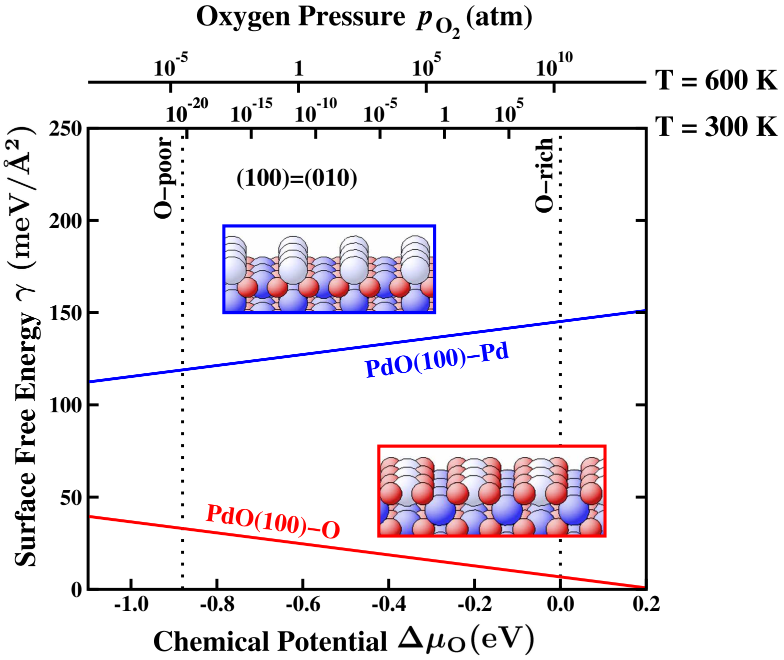

Figure 6.9: Surface free energies for the PdO(001) and PdO(100) surfaces. Solid lines indicate (1×1) terminations and dashed lines larger unit cell reconstructions. The vertical dotted lines specify the range of $\Delta\mu_O$. In the top two x-axes the dependence on the oxygen chemical potential has been converted into pressure scales at $T = 300$ K and 600 K. The insets show the surface geometries of the corresponding (1×1) terminations, where the small red spheres illustrated O atoms and large blue spheres Pd atoms. In the upper graph, additionally shown are the lines of two reconstructions discussed in Section 6.3.3.

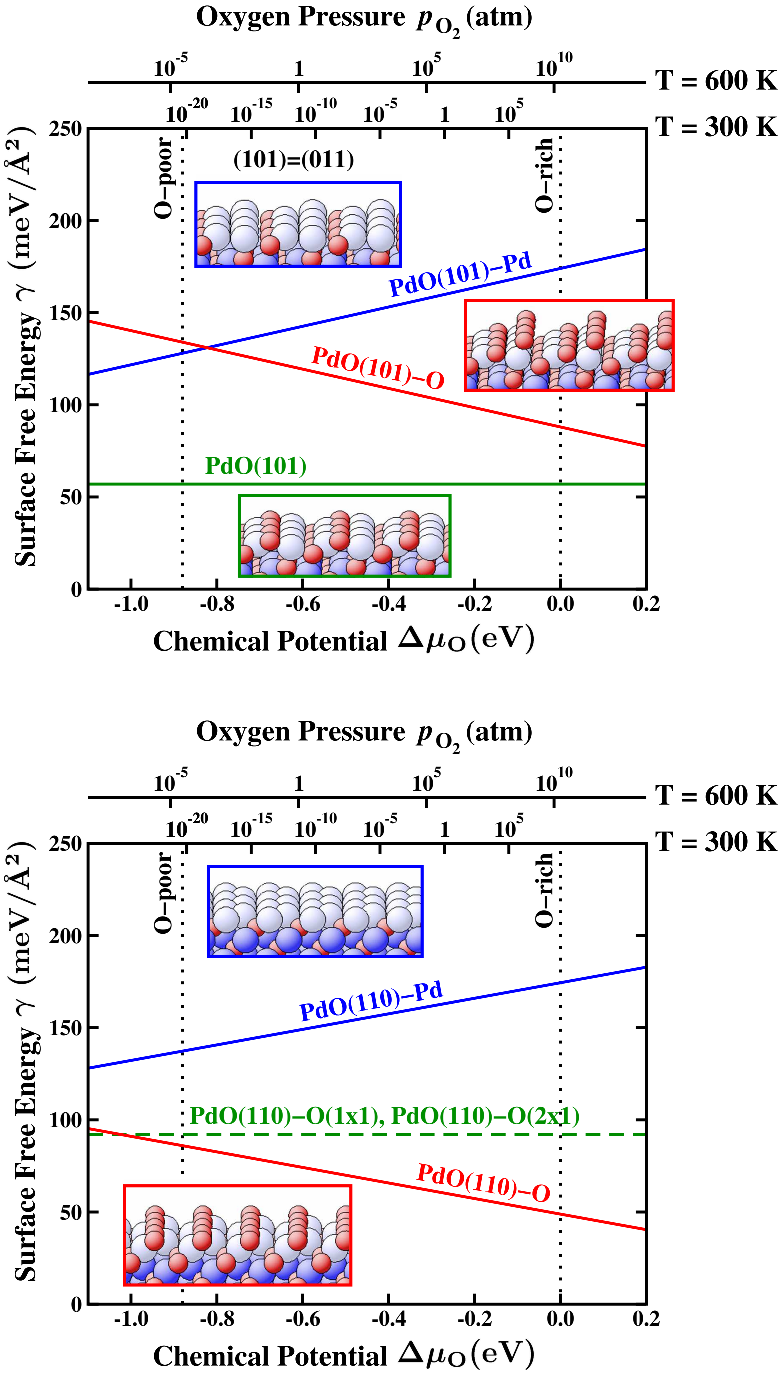

Figure 6.10: Surface free energies for the PdO(101) and PdO(110) surfaces. Solid lines indicate (1×1) terminations and dashed lines larger unit cell reconstructions. The vertical dotted lines specify the range of $\Delta\mu_O$. In the top two x-axes the dependence on the oxygen chemical potential has been converted into pressure scales at $T = 300\,\text{K}$ and $600\,\text{K}$. The insets show the surface geometries of the corresponding (1×1) terminations, where the small red spheres illustrated O atoms and large blue spheres Pd atoms. In the lower graph, additionally shown are the lines of two reconstructions discussed in Section 6.3.3.

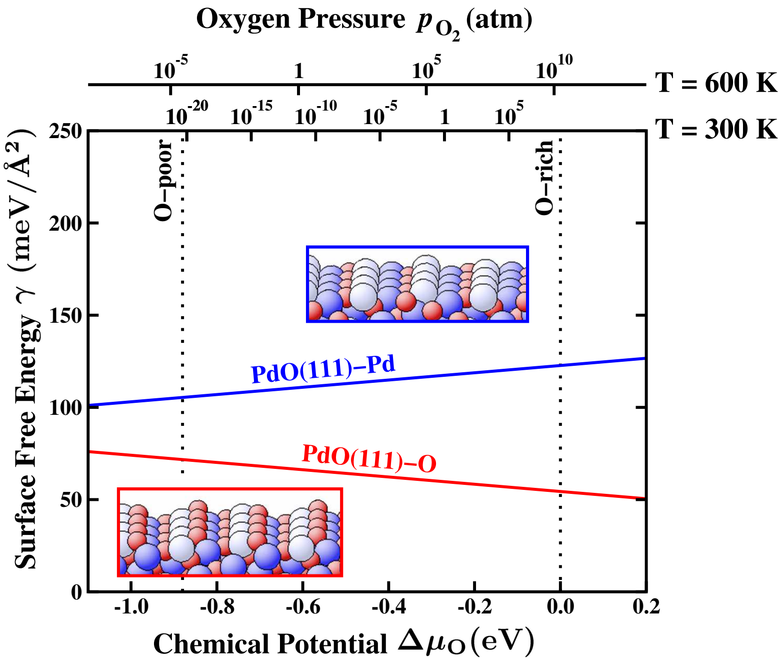

Figure 6.11: Surface free energies for the PdO(111) surface. Solid lines indicate (1×1) terminations. The vertical dotted lines specify the range of $\Delta\mu_O$. In the top two x-axes the dependence on the oxygen chemical potential has been converted into pressure scales at $T = 300$ K and 600 K. The insets show the surface geometries of the corresponding (1×1) terminations, where the small red spheres illustrated O atoms and large blue spheres Pd atoms.

calculated using these two different exchange-correlation functionals it can be observed that the absolute values of the LDA surface energies are 30–50 meV/Å^2 higher than the PBE surface energies. Focussing however on the relative differences between the different surface terminations the two approaches agree within 10–30 meV/Å^2. These relative energetic differences with respect to the PdO(100)-PdO termination, which is the lowest energy surface in both the LDA and PBE approach, are also indicated in Tab. 6.6. The energetic ordering does not seem to depend very much on the choice of the exchange-correlation functional, and since only these relative energy differences are decisive in determining the equilibrium shape of a single crystal, the DFT accuracy is expected to be rather high for this specific quantity.

Surface termination	$\gamma_{\text{O-poor}}$ PBE		$\gamma_{\text{O-poor}}$ LDA	
PdO(100)-PdO	33	(0)	59	(0)
PdO(100)-Pd	119	(+86)	170	(+111)
PdO(001)-O	119	(+86)	162	(+103)
PdO(001)-Pd	156	(+123)	212	(+153)
PdO(101)	57	(+24)	86	(+27)
PdO(101)-O	134	(+101)	180	(+121)
PdO(101)-Pd	128	(+95)	173	(+114)
PdO(110)-O	86	(+53)	119	(+60)
PdO(110)-Pd	137	(+104)	173	(+114)
PdO(111)-O	72	(+39)	109	(+50)
PdO(111)-Pd	105	(+72)	143	(+84)

Table 6.6: Surface free energies of all low-index PdO (1×1) terminations at the oxygen-poor limit, as calculated within the GGA-PBE and the LDA. All energies are in meV/Å^2, and the numbers in brackets denote the energetic difference with respect to the lowest-energy PdO(100)-PdO termination.

6.3.2 Wulff Construction

With the results obtained for the surface free energies of the different (1×1) PdO terminations a Wulff construction [122] for a PdO single crystal is set up. The Wulff construction gives the shape of a single crystal in its thermodynamic equilibrium, providing a (simple) graphical method to find the shape with the lowest free energy. For this construction vectors normal to all crystallographic faces are drawn originating from one arbitrary point. On each vector a mark is placed at a distance from the center point, that is proportional to the corresponding surface energy. Through this mark a plane normal to the vector is constructed, i.e. planes belonging to a termination with a low surface energy are closer to the center than planes of high surface energy terminations. The intersecting planes result in a closed polyhedron, which then yields the equilibrium crystal shape.

Since here only the afore discussed eleven (1×1) terminations are considered, the resulting *constrained* Wulff construction is more intended to compare and evaluate the relative energies of the different surface orientations rather than to actually quantitatively predict the equilibrium PdO crystallite shape. To generate a complete Wulff construction possible surface reconstructions would have to be taken into account, which might significantly influence the theoretical equilibrium shape of a crystal.

Since the surface free energy of each termination exhibits a different dependence on the chemical potential of the surrounding oxygen gas phase, also the resulting Wulff constructions will vary with $\Delta\mu_{\mathrm{O}}$. Thus, in Fig. 6.12 the obtained Wulff polyhedra are presented for the two extreme environmental conditions, i.e. for very low oxygen chemical potential (the O-poor limit) and for high oxygen chemical potential (the O-rich limit). Due to the tetragonal symmetry of the PdO unit cell (cf. Fig. 6.4) the polyhedra must be symmetric with respect to the xy-plane. Therefore in Fig. 6.12 only the upper half of each polyhedron is shown, and the beginning of the lower half is only indicated by the light-red part.

As already expected from comparing the values of the surface free energies, the PdO(100)-PdO termination forms largely dominating facets (red, rectangular facets in Fig. 6.12) in both the O-rich and O-poor limit. The other triangular, blue facets correspond to the stoichiometric PdO(101) termination. All other investigated surface terminations do not contribute to the Wulff construction, since their surface free energies are so high, that the resulting planes lie completely outside of the shown polyhedra and do not cross them at any point. The two polyhedra in Fig. 6.12 are scaled in such a way, that the area of the PdO(101) facets is equal in the O-poor and O-rich limit, since also the surface energy of this termination is constant with respect to the oxygen chemical potential. Correspondingly, the area of the PdO(100)-PdO facets in the Wulff construction increases strongly in going from the oxygen-poor to the oxygen-rich limit as the surface energy of this termination decreases. Already in the O-poor limit the PdO(100)-PdO termination forms 72 % of the whole area of the polyhedron. In the O-rich limit the fraction covered by PdO(100)-PdO facets rises up to 94 %. If the Wulff construction is set up using the surface free energies

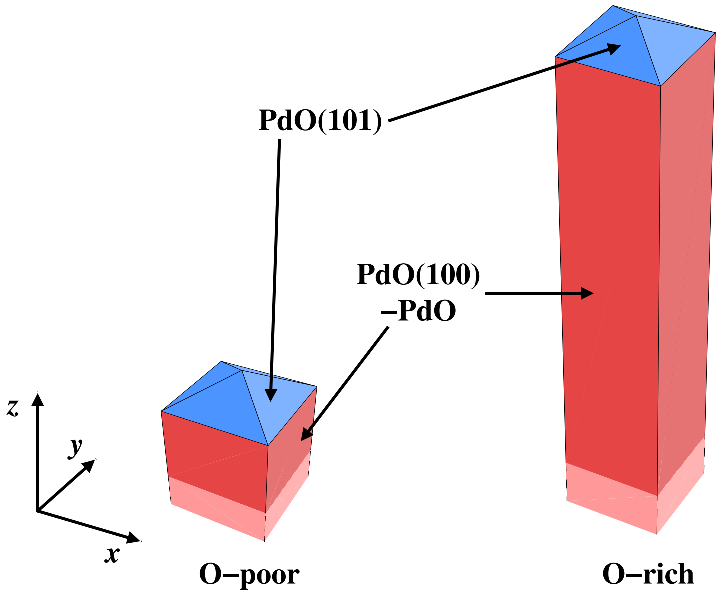

Figure 6.12: Constrained Wulff construction at the oxygen-poor (left) and oxygen-rich (right) limits. The construction is constrained to the investigated (1 × 1) terminations. The two polyhedra are symmetric with respect to the xy-plane and only the upper half is shown correspondingly. The red planes correspond to the PdO(100)-PdO, the blue ones to the PdO(101) termination.

obtained within the LDA-DFT approach, the resulting polyhedra exhibit the same facets as the ones obtained with the PBE exchange-correlation functional, i.e. only the PdO(100)-PdO and PdO(101) terminations contribute to the shape. Again the PdO(100)-PdO facets are the prevailing ones covering 66 % of the surface area in the O-poor limit and 82 % in the O-rich limit. The good agreement of the PBE and LDA results supports the previous assumption, that although the absolute surface free energies depend strongly on the choice of the exchange-correlation functional, the relative energetic ordering of the different terminations does not very much. Thus, the shape of the constrained Wulff construction seems to be described rather well within the chosen DFT setup.

Nevertheless, the main limitation of this approach is the constrained configurational space of considered surface terminations. As already mentioned briefly, surface reconstructions could lead to an extreme decrease in the surface free energy, which could then correspondingly show a strong influence on the overall shape of the Wulff polyhedra. Unfortunately, up to now there is no experimental information available about single crystal PdO surface reconstructions. Without any information about the periodicity or approximate composition the phase space of possible reconstructions is by far too huge to be investigated at present by *ab initio* methods alone. Here, some methodological work should be mentioned employing simulated annealing [17]

	PBE		LDA	
Orientation	Touching	10% area	Touching	10% area
Oxygen-poor:				
(001)	-54 (-45%)	-67 (-56%)	-63 (-39%)	-83 (-51%)
(110)	-40 (-47%)	-44 (-51%)	-36 (-30%)	-44 (-37%)
(111)	-7 (-10%)	-16 (-22%)	-6 (-5%)	-19 (-18%)
Oxygen-rich:				
(001)	-7 (-10%)	-42 (-58%)	-14 (-12%)	-29 (-26%)
(110)	-39 (-80%)	-41 (-84%)	-36 (-45%)	-39 (-49%)
(111)	-1 (-2%)	-20 (-37%)	-1 (-1%)	-10 (-11%)

Table 6.7: Minimum energy by which surface reconstructions at the various facets would have to lower the surface free energy, in order for the facets to touch the presently obtained constrained Wulff polyhedron (touching). Additionally, the corresponding lowering required for the facet to cover approximately 10% of the total surface area of the polyhedron is listed (10% area). All energies in meV/Å^2 (and percent changes) are given with respect to the lowest-energy (1×1) termination of the corresponding orientation.

or genetic [123, 124, 125] algorithms to reach an improved sampling in the future.

With the compiled results, though, it is still possible to get an estimate of how much the surface energy of a specific termination would have to decrease to play a significant role in the Wulff construction. Here, this is done for the three orientations (001), (110) and (111), that do not contribute to the present shape of the Wulff polyhedra in the O-poor and O-rich limit. Tab. 6.7 lists the corresponding values for each orientation, of how much the surface free energy would have to be lowered by a reconstruction (with respect to the lowest (1×1) termination in this orientation considered so far), so that the facet would just touch the current polyhedron. In addition the decrease in surface energy required for a specific orientation to significantly contribute to the Wulff polyhedra is listed. Here, a contribution is considered as being significant, if the facets of a certain termination cover approximately 10 % of the total area of the polyhedron. From the values compiled in Tab 6.7 it becomes obvious that for the (001) and (110) orientation rather massive changes in the surface free energy would have to be introduced by a possible reconstruction to show any recognizable influence on the Wulff construction, regardless of the environmental conditions (O-poor or O-rich limit) or the exchange-correlation functional (PBE or LDA). For the (111) orientation, though, only a much smaller reduction is needed, so that changes in the shape of the polyhedra are more likely with respect to this termination.

6.3.3 Stability vs. Polarity

Out of the eleven considered (1×1) terminations only the PdO(101) termination is stoichiometric, whereas all other terminations exhibit either an excess of oxygen or palladium atoms. Since oxide surfaces are often described within an ionic model, an

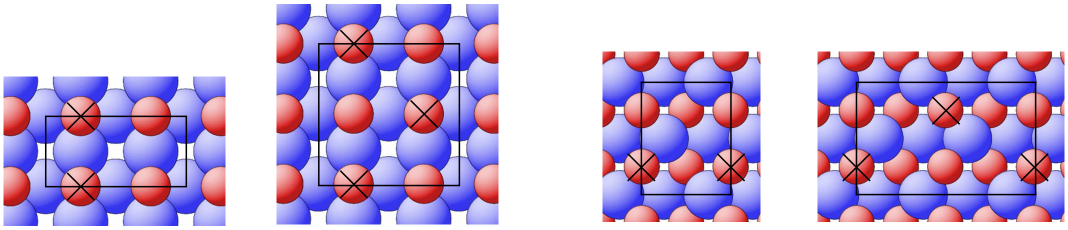

PdO(001)–O(2x1) **PdO(001)–O(2x2)** **PdO(110)–O(1x1)** **PdO(110)–O(2x1)**

Figure 6.13: Unit cells for stoichiometric reconstructions of the PdO(001)-O and PdO(110)-O terminations, achieved by simply removing the oxygen atoms marked with crosses.

unequal number of O and Pd atoms would lead to a so-called polar surface, which is traditionally not considered to be stable on electrostatic grounds [119, 120]. Theoretically, though, it has been shown that also polar oxide surfaces can indeed be stable [74, 76, 121]. Despite the known limitations of the ionic model, regarding the stability of the three different terminations in the (101) orientation (cf. Fig. 6.10) it seems to reflect very well the found stability ordering. Here, the stoichiometric PdO(101) termination has a much lower surface free energy than the polar PdO(101)-O and PdO(101)-Pd terminations. For all other low-index orientations the layer stacking is such, that it is not possible to truncate the tetragonal PdO structure in a (1 × 1) cell and achieve charge neutrality within the assignment of formal charges (Pd^{2+} and O^{2-}). The resulting polarity at the surface could e.g. be a reason, why the (1 × 1) terminations in the (001) and (110) orientation exhibit comparably high surface free energies. To investigate in a first approach the effect of the polarity on the stability of these two surface orientations, larger unit cells of the O-terminated structures are set up, where half of the oxygen atoms in the topmost layer is removed to obtain formal charge neutrality. Considering the periodicity of the surface unit cell, the remaining oxygen atoms can be arranged in two different ways for both orientations (cf. Fig. 6.13), one showing a striped pattern of full and empty rows of oxygen atoms and the other a checkerboard pattern. The surface free energies of the fully relaxed, stoichiometric surfaces are also indicated in the stability plots of the (001) and (110) orientation (Fig. 6.9 and Fig. 6.10) by the green, dashed lines. As can be seen, these stoichiometric overlayers are not at all more stable than the corresponding (1 × 1) O-terminated structures. These results therefore disagree with the suggestion formulated by Ciuparu *et al.* [126], that a simple removal of O atoms in the topmost layer should lead to charge compensated and thus stable PdO(001) and PdO(110) surfaces.

Obviously, formal charge neutrality does not appear to be the decisive factor in the stability of the PdO surface terminations, which is already reflected in the very low surface free energy of the polar PdO(100)-PdO termination. These findings stress the most obvious shortcoming of the electrostatic model, which is the assumption that all atoms of a certain element are identical and in the same charge state, regardless of

O-terminated	Φ (eV)	Pd-terminated	Φ (eV)	stoichiometric	Φ (eV)
PdO(001)-O	7.9	PdO(100)-Pd	4.0	PdO(101)	5.4
PdO(101)-O	7.7	PdO(001)-Pd	4.8	PdO(001)-O(2×1)	6.6
PdO(110)-O	7.2	PdO(101)-Pd	4.5	PdO(001)-O(2×2)	6.6
PdO(111)-O	5.9	PdO(110)-Pd	4.4	PdO(110)-O(1×1)	5.9
		PdO(111)-Pd	4.7	PdO(110)-O(2×1)	5.8

PdO-terminated	Φ (eV)
PdO(100)-PdO	6.4

Table 6.8: Work function of the 11 different (1×1) PdO surface terminations and the 4 stoichiometric terminations of the (001) and (110) termination with larger surface unit cells considered in this work. All values are in eV. PBE is used as exchange-correlation functional.

whether they are e.g. in the bulk or at the surface. It has been shown, though, that structural and electronic relaxation at the surface can significantly change this simple picture [76, 74]. Other factors like an appropriate excess stoichiometry at oxygen-rich conditions might then become more important than the polarity issue.

Nevertheless, regarding the work functions of the different PdO surface terminations (cf. Tab. 6.8) it can be seen, that there is actually a notably different surface dipole moment associated with the different terminations. Focussing first on the (1×1) terminations the calculated work functions fit actually quite well to the ionic model. The work function of the stoichiometric PdO(101) termination exhibits a medium value of 5.4 eV, whereas the work functions of all Pd-terminated surface are 0.6–1.4 eV lower and the work functions of the O-terminated surfaces are 0.5–2.5 eV higher. Remarkable is the comparably low work function of the PdO(111)-O termination. This can be explained by the rather dense stacking in the (111) direction and the resulting small interlayer distance between the topmost oxygen layer and the second layer Pd atoms of only 0.51 Å, which can then lead to a smaller dipole moment and respectively smaller work function. Also the work functions of the stoichiometric (001) and (110) superstructure terminations fit nicely into this scheme. Compared to their corresponding O-terminated surfaces a clear decrease in the work function of 1.1–1.4 eV can be observed, i.e. the stoichiometric surfaces have a smaller surface dipole moment. As discussed before though, the stability is not enhanced in these stoichiometric surface terminations.

Apparently, the polarity is not the main factor in determining the stability of the PdO surfaces. As a next step a possible correlation between the stability and the binding energy of the surface oxygen atoms is investigated, since the most stable (1×1) termination of a specific orientation has always O atoms in the topmost layer. The binding energies with respect to gas phase O_2 are given in Tab. 6.9. Indeed the binding energies of the topmost oxygen atoms show a clear correlation to the found stability ordering. The PdO(100)-PdO and PdO(101) terminations, which solely build up the

Surface termination	Binding energy (eV)	Coordination
PdO(100)-PdO	-2.4	3
PdO(101)	-2.3	3
PdO(111)-O	-1.8	2
PdO(110)-O	-1.6	2
PdO(001)-O	-1.3	2
PdO(101)-O	0.5	1

Table 6.9: Binding energy of the topmost oxygen atom of the low-index PdO surfaces with respect to the O_2 molecule. In addition the number of Pd atoms, to which the corresponding O atom is coordinated, are listed.

Wulff construction, also exhibit the most strongly bound surface oxygen atoms. Also the binding energies of the other terminations clearly reflect their surface stability. The PdO(111)-O termination, which is already very close to contribute to the equilibrium Wulff construction, has actually also the third most strongly bound surface oxygen atoms.

In addition the binding energies can be connected to the coordination of the surface atoms. In PdO bulk the oxygen atoms are tetrahedrally surrounded by four palladium atoms. In the two most stable terminations, PdO(100)-PdO and PdO(101), the oxygen atoms are still coordinated to three palladium atoms, whereas in the intermediate stable structures, PdO(111)-O, PdO(110)-O and PdO(001)-O, the O atoms are only coordinated to two Pd atoms and in the rather unstable PdO(101)-O termination to one Pd atom. Thus, the stability of the studied (1×1) terminations seems to be primarily determined by the openness of the surface orientation, i.e. if the surface structure exhibits highly coordinated oxygen binding sites.

6.4 Conclusions

The *ab initio* atomistic thermodynamics approach is used to obtain a first insight into the structure and composition of the Pd(100) surface in contact with an oxygen gas phase. Within this approach the stability of different surface phases can be compared over a wide temperature and pressure range of the surrounding gas phase.

There are, however, several uncertainties in the obtained results introduced by the accuracy in the total energies, determined by the employed basis set and exchange-correlation functional, by the approximations in evaluating the thermodynamic functions, mainly due to the vibrational contribution to the Gibbs free energy, as well as by the restricted sampling of the configurational space. A detailed discussion of the different factors shows, that for comparing the stability range of the different oxidation stages of the Pd(100) surface (clean, adlayers, surface oxide, bulk oxide) the exchange-correlation functional induces the largest uncertainty, whereas for determining the equilibrium shape of a PdO single crystal the sampling of the configurational space is the limiting factor.

Considering the stability of different adlayer structures and the $(\sqrt{5} \times \sqrt{5})R27^\circ$ surface oxide there are, nevertheless, some conclusions, that are not affected by the choice of the exchange-correlation functional. It is found, that the $c(2 \times 2)$ oxygen adlayer on Pd(100) does not appear as stable phase over the investigated temperature and pressure range, although this structure has been frequently observed in UHV experiments. This suggests that the $c(2 \times 2)$ phase is a meta-stable state, which only forms due to the adsorption kinetics. Furthermore it can be seen that the $(\sqrt{5} \times \sqrt{5})R27^\circ$ surface oxide is a stable phase over an extended (T, p)-range regardless of the chosen exchange-correlation functional. Thus, the surface oxide can be regarded as separate phase, clearly distinguished from the bulk oxide and adlayer structures. The actual position of the boundaries between the different phases in the (T, p)-space, though, does strongly depend on the exchange-correlation functional (cf. Fig. 6.6). Comparing the PBE and RPBE results there is an uncertainty in the phase boundaries of as much as $\sim$ 4 orders of magnitude in pressure and $\sim$ 200 K in temperature. Comparing the two extremes in the employed exchange-correlation functionals, the LDA and the RPBE, the uncertainty is even larger with $\sim$ 10 orders of magnitude in pressure and $\sim$ 450 K in temperature.

The determined equilibrium shape of a PdO single crystal appears not to be affected that much by the uncertainty arising from the exchange-correlation functional. In both, the PBE and LDA, the same low-index surfaces contribute to the equilibrium shape and the same surface termination forms the dominant facet. In contrast to the traditional assumption, that so-called polar surface are rather unstable (which is based on an ionic description of oxide surfaces), for the low-index PdO surface terminations the polarity does not have any significant influence on the stability. It is rather the coordination of the first-layer oxygen atoms that appears to be decisive for the stability. A much large uncertainty in the equilibrium shape of the PdO single crystal is introduced by the restricted configurational sampling. Possible surface reconstructions leading to a lowering of the surface energy of a certain surface orientation could notably change the equilibrium shape. However, an estimate of how much a reconstruction would have to influence the corresponding surface energy is given.

Chapter 7

Palladium In An Oxygen And CO Gas Phase

As a next step towards a better understanding of the CO oxidation reaction on the Pd(100) surface, also the second reactant, the CO, has to be taken into account. Again the atomistic thermodynamics approach is used to obtain a first idea about the stability of the different structures under realistic gas phase conditions, i.e. temperatures and pressures as applied in heterogeneous catalysis ($p \approx 1\,\text{atm}$, $T \approx 300 - 600\,\text{K}$). Since in this work the atomistic thermodynamics approach is used to compare the stability of all considered structures, it is important to include as many potentially relevant structures as possible. Thus, at the beginning of this Chapter the considered surface structures are introduced and in the last Section their thermodynamic stability in a constrained equilibrium with an oxygen and CO gas phase is evaluated.

7.1 CO Adsorption On Pd(100)

As already discussed in Section 6.1 the Pd(100) surface exhibits three high symmetry adsorption sites, a bridge, a top and a fourfold hollow site. Experimentally, the adsorption of CO on Pd(100) has been studied intensively [127, 128, 129, 130, 131, 132, 133, 134]. One of the first and most detailed studies is the work by Bradshaw and Hoffmann [127] combining infrared adsorption spectroscopy (IRAS) and low-energy electron diffraction (LEED). They find that at all coverages CO adsorbs upright in bridge position. At a coverage of $\Theta = 0.5\,\text{ML}$ an ordered $(2\sqrt{2} \times \sqrt{2})R45^\circ$ overlayer is formed, which is compressed to a $(3\sqrt{2} \times \sqrt{2})R45^\circ$ structure at $\Theta = 0.67\,\text{ML}$ and a $(4\sqrt{2} \times \sqrt{2})R45^\circ$ at $\Theta = 0.75\,\text{ML}$. These results have been confirmed by further LEED [129, 130, 131, 134] and IRAS [132] studies as well as high resolution electron energy loss spectroscopy (HREELS) [129, 131] and surface core-level shift (SCLS) measurements [133].

The formation of the $(2\sqrt{2} \times \sqrt{2})R45^\circ$ rather than a simple $c(2 \times 2)$ structure has been attributed to the minimization of the strongly repulsive interactions between

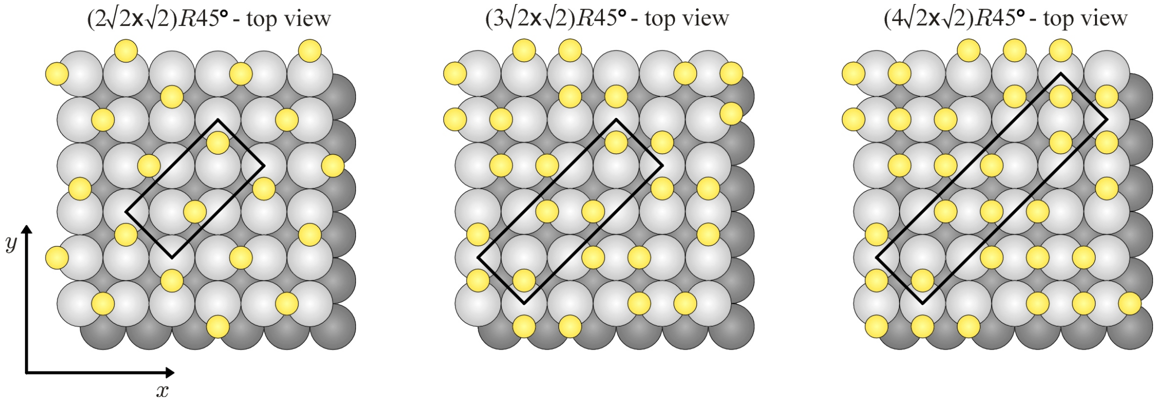

Figure 7.1: Schematic illustration of the three experimentally characterized adlayer structures of CO on Pd(100). From left to right the coverage increases from $\Theta = 0.5$ to $\Theta = 0.67$ and $\Theta = 0.75$ ML. The yellow small spheres represent the CO molecules, the grey large spheres the Pd(100) surface (second layer atoms are darkened).

the adsorbed CO molecules. In the $c(2 \times 2)$ structure each molecule has four nearest neighbors at a distance of $\sqrt{2}\,a$, where a is the length of the (1×1) surface unit cell. In the $(2\sqrt{2} \times \sqrt{2})R45^\circ$ structure, however, the CO molecules form a distorted hexagonal overlayer with only two neighbors at a distance of $\sqrt{2}\,a$ and four neighbors slightly further away at $\sqrt{5/2}\,a$.

A schematic illustration of the three experimentally characterized adlayer structures is shown in Fig. (7.1). In addition to these structures also simple (1×1) and (2×2) overlayers with CO in bridge, top and hollow sites will be considered in this study. The binding energies of all considered structures are listed in Tab. 7.1 for the PBE, RPBE and LDA exchange-correlation functional. The muffin tin radius for the carbon is set to $R_{\mathrm{MT}}^{\mathrm{C}} = 1.0$ bohr and a $[10 \times 10 \times 1]$ MP grid is used for the (1×1) structures. For the three $(n\sqrt{2} \times \sqrt{2})R45^\circ$ structures $[4 \times 8 \times 1]$ (for $n = 2$) and $[2 \times 8 \times 1]$ (for $n = 3, 4$) MP-grids are used. All other computational parameters are equivalent to the ones given on Page 66. For a detailed discussion of the computational setup cf. Appendix A.2.

Looking at the binding energies it can be seen that the average binding energy per CO molecule is almost constant up to a coverage of $\Theta = 0.5$ ML. For higher coverages the binding energy decreases rapidly. It should be noted that in agreement with the experimental findings the bridge site is also the energetically most stable one at all coverages for the two GGA functionals. For the LDA functional, though, the hollow site seems to be preferred at low coverages. The failure in the prediction of the right adsorption site for CO in the low coverage limit on transition metal surfaces due to the approximate exchange-correlation functional is a known problem within DFT. The most prominent example for this is the adsorption of CO on the platinum (111) surface. Here, it is experimentally observed, that the CO occupies the low-coordination top site, whereas in DFT calculations for both the LDA and the PBE the high-coordinated

	Coverage	PBE	RPBE	LDA
$(2\sqrt{2}\times\sqrt{2})R45°$	0.50	-1.92	-1.55	-2.74
$(3\sqrt{2}\times\sqrt{2})R45°$	0.67	-1.73	-1.36	-2.55
$(4\sqrt{2}\times\sqrt{2})R45°$	0.75	-1.63	-1.25	-2.45
$p(2\times 2)$-CO$^{\mathrm{br}}$	0.25	-1.92	-1.55	-2.73
$p(2\times 2)$-CO$^{\mathrm{hol}}$	0.25	-1.84	-1.40	-2.86
$p(2\times 2)$-CO$^{\mathrm{top}}$	0.25	-1.52	-1.21	-2.20
$c(2\times 2)$-CO$^{\mathrm{br}}$	0.50	-1.92	-1.54	-2.74
$c(2\times 2)$-CO$^{\mathrm{hol}}$	0.50	-1.71	-1.26	-2.72
$c(2\times 2)$-CO$^{\mathrm{top}}$	0.50	-1.50	-1.19	-2.17
(1×1)-CO$^{\mathrm{br}}$	1.00	-1.31	-0.90	-2.21
(1×1)-CO$^{\mathrm{hol}}$	1.00	-0.83	-0.39	-1.83
(1×1)-CO$^{\mathrm{top}}$	1.00	-0.96	-0.60	-1.75

Table 7.1: Average binding energies per CO molecule on Pd(100). All values are in eV.

hollow site is preferred [135]. Nevertheless, for the here discussed system, the GGA functionals do predict the correct adsorption site and for a coverage of $\Theta = 0.5$ ML also within the LDA the bridge site is again the most stable one. At $\Theta = 0.5$ ML, the experimentally proposed $(2\sqrt{2}\times\sqrt{2})R45°$ structure shows only a negligible lower binding energy than the $c(2\times 2)$ structure (few meV). Overall, DFT seems to work rather well for the prediction of the right adsorption site as well as of the lowest energy adlayer for this system, independent of the chosen exchange-correlation functional. The absolute values of the binding energies, though, show strong deviations for the different functionals, which is another known problem in DFT, the consequences of which will be discussed at the end of this Chapter. Comparing to previous DFT studies the obtained results are fully consistent [51, 136].

7.2 Co-Adsorption Of Oxygen And CO

Simple Adlayers

With the present understanding two different kinds of co-adsorption structures of O and CO can be identified in this particular system. They can either form some adlayer structure on the Pd(100) surface or they can involve the reconstructed $(\sqrt{5}\times\sqrt{5})R27°$ surface oxide structure. Focusing first on the mixed adlayers of oxygen and CO on Pd(100) it should be noted that experimentally no ordered overlayer structures of O and CO have hitherto been observed. If the Pd(100) surface is exposed to both gas phase species, it has instead been found that the two adsorbates form separate domains [110]. In these low energy electron diffraction (LEED) experiments they observed that for a fully developed $p(2\times 2)$-O/Pd(100) surface the $p(2\times 2)$ LEED pattern disappeared upon exposure to CO at $T = 80$ K. Assuming an approximate

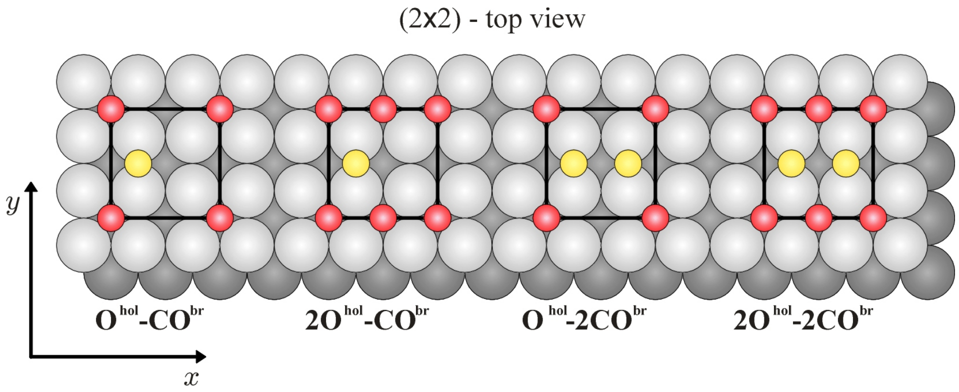

Figure 7.2: Schematic illustration of the co-adsorbed overlayer structures of oxygen and CO on Pd(100). The small red spheres correspond to oxygen atoms, the small yellow spheres represent the CO molecules and the large grey spheres the Pd(100) surface.

	Coverage	PBE	RPBE	LDA
(2×2)-O^{hol}-CO^{br}	0.50	-2.95	-2.26	-4.53
(2×2)-2O^{hol}-CO^{br}	0.75	-2.93	-1.91	-5.12
(2×2)-O^{hol}-2CO^{br}	0.75	-3.96	-2.85	-6.40
(2×2)-2O^{hol}-2CO^{br}	1.00	-3.64	-2.22	-6.69

Table 7.2: Total binding energies of O and CO on Pd(100) with respect to gas phase O_2 and CO. All values are in eV.

barrier of 1.0 eV for the reaction of O and CO on the Pd(100) surface to form CO_2 [137, 138] it is rather unlikely that the adsorbed oxygen was reacted with the CO at this low temperature. The vanishing of the LEED pattern was thus interpreted as a CO induced disordering of the oxygen islands. This behavior was explained by strongly repulsive, lateral interactions between the adsorbates. To nevertheless obtain an idea about the binding energies of O and CO in such mixed overlayer structures, different models that seem to be most obvious from a combinatorial point of view are set up. For this a (2×2) surface unit cell is used containing 1–2 O and CO adsorbates. Here, the adsorbates are only considered in their most favorite adsorption sites, i.e. the oxygen atoms sit in hollow sites and the CO atoms in bridge sites. Discarding structures, in which the adsorbates sit at distances smaller than the length of the (1×1) surface unit cell, this leads to the four different structures shown in Fig. 7.2. The corresponding total binding energies of all adsorbates, given by

$$E^{\text{bind}}_{\text{O,CO@Pd(100)}} = E^{\text{tot}}_{\text{O,CO@Pd(100)}} - E^{\text{tot}}_{\text{Pd(100)}} - N_{\text{O}} 1/2 E^{\text{tot}}_{\text{O}_2} - N_{\text{CO}} E^{\text{tot}}_{\text{CO}} \quad , \tag{7.1}$$

are listed in Tab. 7.2. The computational setup for obtaining these values is equivalent to the one described in the previous Section.

Similar to the pure adlayer structures of O and CO on Pd(100) also the mixed overlayers show a decrease in the binding energy per adsorbate with increasing coverage, which reflects the afore mentioned repulsive interactions between the two species. A comparison of the thermodynamic stability of the co-adsorption structures in a constrained equilibrium with an O_2 and CO gas phase, will be discussed in the next Section. Comparing the values of the binding energies for the different exchange-correlation functionals they do not seem to agree very well. It is a known problem, though, that the LDA and GGA exchange-correlation functionals do not describe the O-O binding energy in the O_2 and the C-O binding energy in the CO molecule very well. The average deviation in the binding energies per O atom resp. per CO molecule on the surface between the different functionals appears to be rather constant. Considering, e.g., an average deviation of 1.0 eV per O and 1.3 eV per CO between the RPBE and LDA binding energies the obtained results are consistent. Similarly, for the difference between the RPBE and PBE binding energies an average deviation of 0.3 eV per O and 0.4 eV per CO can be observed. For a coverage of $\Theta = 0.5$ ML the binding energy of the co-adsorbed phase is ∼30–70 meV smaller than the sum of the binding energies of the respective $c(2 \times 2)$ phases for each species. Thus, the repulsive interactions between O and CO are even stronger than the interactions between O and O, resp. CO and CO in the pure phases. The adsorption of both O and CO in hollow sites in a $c(2 \times 2)$ structure gives an even smaller binding energy.

Also on Pd(111) it has been observed that adsorbed O and CO aggregate into separate domains rather than building a mixed phase [139, 140]. It should be noted that the findings for the two Pd surfaces are in contrast to the findings for the Ru(0001), Rh(111), Ni(111) and Pt(111) surfaces. Here, several O and CO co-adsorbed structures have been identified (cf. Ref. [141] and references therein).

O And CO On The $(\sqrt{5} \times \sqrt{5})R27^\circ$ Surface Oxide

A second possibility to obtain co-adsorbed structures of oxygen and CO is the additional adsorption of CO on and/or partial substitution of oxygen by CO in the $(\sqrt{5} \times \sqrt{5})R27^\circ$ surface oxide structure. As can been seen in Fig. 7.3 the surface oxide structure exhibits top, bridge and hollow sites. Due to the symmetry of the underlying Pd(100) substrate multiple sites of one type are very similar, but not completely equivalent. Only the top sites differ substantially, depending if the corresponding palladium atom is twofold or fourfold coordinated by oxygen atoms. For the adsorption of CO on the $(\sqrt{5} \times \sqrt{5})R27^\circ$ structure there has been no experimental information available. Consequently, a systematic search starting with the adsorption sites depicted in Fig. 7.3 is performed. A schematic illustration of all considered structures in given in Appendix B.1. Adsorbing only one additional CO molecule on the surface oxide in any of the ten shown sites already shows that the four hollow sites are not stable at all. Upon relaxation, the CO molecule always moves to the corresponding bridge site. The binding energies of the 2 bridge sites are almost degenerated, as expected from the symmetry of the surface unit cell. The same is observed for the 2 twofold and the 2 fourfold by oxygen coordinated top sites, respectively. Thus, in the

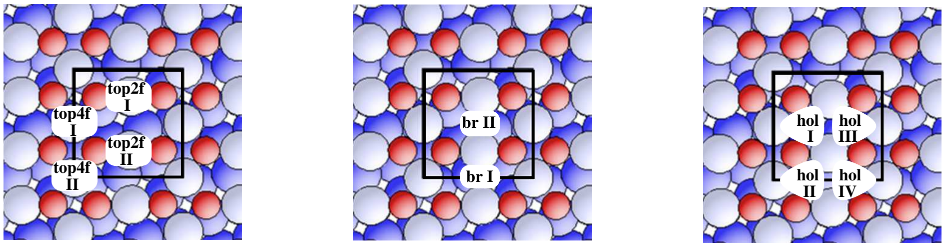

top sites **bridge sites** **hollow sites**

Figure 7.3: High-symmetry adsorption sites on the $(\sqrt{5} \times \sqrt{5})R27°$ surface oxide structure. Red small spheres represent the lattice oxygen atoms, large light-blue ones the reconstructed Pd atoms and large dark-blue spheres Pd atoms belong to the underlying Pd(100) substrate.

Adsorption Structure	E^{bind}	Adsorption Structure	E^{bind}
$\mathrm{CO}^{\mathrm{br}}$	-0.93	$2\mathrm{CO}^{\mathrm{br}}$	-0.75
$\mathrm{CO}^{\mathrm{top2f}}$	-0.62	$2\mathrm{CO}^{\mathrm{top2f}}$	-0.51
$\mathrm{CO}^{\mathrm{top4f}}$	-0.13	—	—

Table 7.3: Average binding energies of CO on $(\sqrt{5} \times \sqrt{5})R27°$ surface oxide structure calculated within PBE. All values are per CO molecule and in eV.

following such pairs of sites will be treated as equivalent from an energetic point of view. Similar to the CO adsorption on the clean Pd(100) surface, also here the bridge site is the most stable one. The binding energies with respect to the surface oxide structure, i.e.

$$E^{\mathrm{bind}}_{\mathrm{CO@}(\sqrt{5}\times\sqrt{5})R27°} = E^{\mathrm{tot}}_{\mathrm{CO@}(\sqrt{5}\times\sqrt{5})R27°} - E^{\mathrm{tot}}_{(\sqrt{5}\times\sqrt{5})R27°} - N_{\mathrm{CO}} E^{\mathrm{tot}}_{\mathrm{CO}} \quad , \tag{7.2}$$

where N_{CO} is the number of adsorbed CO molecules , are given in Tab. 7.3 for one and two CO molecules per surface unit cell (structures 1–3, 15–17 in Appendix B.1). A structure with two CO molecules adsorbed on both of the fourfold coordinated top sites ($2\mathrm{CO}^{\mathrm{top4f}}$, structure 17) is not stable upon relaxation. Mixing the adsorption sites (structures 18–20), i.e. placing e.g. one CO in a bridge site and a second one in a twofold top site does always yield less stable structures than the adsorption in like sites due to strongly repulsive interactions between the adsorbed molecules. Also for the same reason, any structure containing more than two additional CO molecules per surface unit cell results as unstable.

Instead of adsorbing two CO molecules it is also possible to simultaneously adsorb one CO and one O in the different sites (structures 81–89). This leads to stable structures, only if both O and CO are sitting in a bridge or a twofold coordinated top site or O in bridge and CO in a fourfold coordinated top site (structures 81,82,87). Again the adsorption in bridge sites gives the most stable structure.

Since there are noticeable nearest neighbor interactions between the adsorbates within the $(\sqrt{5} \times \sqrt{5})R27^{\circ}$ surface unit cell, calculations in larger $(\sqrt{5} \times \sqrt{5})R27^{\circ}$ surface unit cells are performed to check, if there are also interactions between adsorbates in neighboring surface unit cells. For this oxygen and CO are adsorbed in bridge sites in (2×1) and (1×2) surface unit cells (a detailed description can be found in Appendix B.2). It could be shown, that the nearest neighbor interactions do not extend beyond the "(1×1)" surface unit cell.

To increase the configurational space of considered co-adsorption structures, configurations, in which the original surface oxide is modified, are also considered. In a first step, one of the upper, hollow site oxygen atoms (cf. Fig 6.3) is removed from the $(\sqrt{5} \times \sqrt{5})R27^{\circ}$ structure and CO and O are again adsorbed in the afore described sites (structures 8–11, 29–32 and 47–49). Here, Eq. (7.2) is not applicable anymore to directly compare the binding energies of the adsorbates with those on the unmodified surface oxide structure. Instead, the stability of all these structures will be compared within the atomistic thermodynamics approach in Section 7.3.

If both of the upper oxygen atoms are removed, the surface oxide structure is already somewhat destabilized. Since this leads to a rather open structure (only four reconstructed Pd atoms on five Pd(100) substrate atoms), the structural relaxation showed, that the palladium atoms can then move quite easily in lateral directions on the surface. Here, the additional adsorption of one or two CO molecules or one O and one CO leads only to stable structures, if just CO sits in bridge or twofold top sites (structures 37–39, 61–63 and 69–71).

A further considered modification of the $(\sqrt{5}\times\sqrt{5})R27^{\circ}$ structure is the substitution of one or both of the upper oxygen atoms by CO. Again it is then possible to adsorb additional CO on the other 4 top sites and 2 bridge sites (structures 4–7, 21–28, 40–46, 54–59, 64, 72–74, 78–80 and 90–92). If the CO substitutes the upper oxygen atoms, also the additional adsorption of a sole O atom in any of the sites does still give a mixed structure. This is only possible in bridge sites, though, whereas almost all structures with O adsorbed on top sites are not stable upon relaxation. Substituting only one of the upper O atoms in the surface oxide structure by CO and removing the second one leads to the same findings (structures 12–14, 33–36, 50–53, 60, 65–68 and 75–77).

Leaving out the four unstable hollow sites, from a pure combinatorial point of view there are 168 possible co-adsorption structures involving the reconstructed $(\sqrt{5} \times \sqrt{5})R27^{\circ}$ surface unit cell. Since there is only little known about the co-adsorption of O and CO on the $(\sqrt{5} \times \sqrt{5})R27^{\circ}$ surface oxide, none of the possible structures can easily be excluded. Nevertheless, considering e.g. the interactions between the adsorbates already quite a number of structures can be discarded without performing extensive DFT calculations. Since all structures with two adsorbates on mixed site types (i.e. br-top2f etc.) appear to be rather unstable, the number of reasonable structures is already reduced to 92 (cf. Appendix B.1). Out of these structures only 55 are stable upon relaxation. All other structures exhibit either too strongly repulsive interactions between the different adsorbates leading effectively to a desorption of the adsorbates, or the reconstructed palladium layer is so much distorted, that the adsorbates can not be considered as being in their original adsorption sites anymore.

Confirming The Adsorption Site — SCLS Measurements

Only very recently surface core level shift (SCLS) measurements have been performed for the surface oxide structure having additional CO adsorbed [142]. Since the core-level position is sensitive to the local coordination of an atom, a comparison between the SCLS spectrum of the *clean* $(\sqrt{5} \times \sqrt{5})R27^\circ$ structure and the surface oxide structure + CO could provide information about the adsorption site.

As discussed in Section 3.7.3 the experimentally measured SCLS comprises both initial and final state effects, whereas theoretically initial as well as total SCLSs can be calculated. For a comparison between experiment and theory the total shifts (containing initial and final state contributions) are more suitable. In a previous study on the $(\sqrt{5} \times \sqrt{5})R27^\circ$ phase, where the SCLSs were used to identify the structure of the surface oxide [18], some deviations between the absolute experimental and theoretical values were observed. A reason for this could be the assumption, that there is a *complete screening* (cf. Section 3.7.3), i.e. that the energy of the photoelectron contains the whole screening energy. This complete screening picture, which works very well for transition metals [66], might not work as well for oxidic structures. If highly resolved experimental data would be available, an analysis of the line shape using a time dependent formulation [143] could provide further insight into this problem.

The calculated total SCLSs of the Pd-3d level are listed in Tab. 7.4 for the surface oxide, the surface oxide with one/two CO adsorbed in bridge sites and with one CO on a twofold by oxygen coordinated top site (top2f). The labeling of the palladium atoms follows the one shown in Fig. 6.3. Pd2a–Pd2e are the atoms in the second layer, i.e. the first Pd(100) substrate layer. For the clean $(\sqrt{5} \times \sqrt{5})R27^\circ$ structure the SCLS measurements show 3 peaks at 1.32 eV, 0.34 eV and -0.31 eV, which can directly be assigned to the fourfold, twofold and second layer Pd atoms, respectively (cf. Ref. [18]). The adsorption of CO leads to quite some changes in the SCLSs in the theoretical as well as in the experimental values. As can be seen in Tab. 7.4 the CO sitting in a bridge site induces a strong shift of $\sim$ 0.6 eV in the SCLS of the two involved palladium atoms (Pd1c and Pd1d), whereas the other two palladium atoms in the topmost layer are only weakly affected ($\sim$ 0.15 eV). Adsorbing two CO molecules in bridge site even leads to a shift of $\sim$ 1.2 eV for the Pd1c and Pd1d atoms compared to the clean surface oxide structure. For the CO molecule in top site it can be seen, that the SCLS of the corresponding Pd atom is strongly shifted by $\sim$ 1.0 eV, whereas the SCLSs of the remaining Pd atoms are almost unchanged. As exemplified for the $(\sqrt{5} \times \sqrt{5})R27^\circ$+CO$^{\mathrm{br}}$ structure, the SCLSs of the second layer Pd atoms are nearly not affected by the adsorption of CO. This could already be concluded by comparing the SCLSs in the initial state approximation, so that only for the $(\sqrt{5} \times \sqrt{5})R27^\circ$+CO$^{\mathrm{br}}$ structure the more involved final states calculations

Pd-atom	$\sqrt{5}$	$\sqrt{5}$+CO$^{\mathrm{br}}$	$\sqrt{5}$+2CO$^{\mathrm{br}}$	$\sqrt{5}$+CO$^{\mathrm{top2f}}$
Pd1a(4f)	1.05	1.21	1.22	1.10
Pd1b(4f)	1.09	1.22	1.31	1.18
Pd1c(2f)	0.35	0.92	1.56	1.29
Pd1d(2f)	0.32	0.92	1.58	0.28
Pd2a	-0.24	-0.26	–	–
Pd2b	-0.25	-0.21	–	–
Pd2c	0.18	0.16	–	–
Pd2d	-0.02	0.02	–	–
Pd2e	-0.28	-0.25	–	–

Table 7.4: Calculated total SCLSs of the Pd-3d level of the $(\sqrt{5} \times \sqrt{5})R27^\circ$ surface oxide (here abbreviated with $\sqrt{5}$) and the surface oxide with one and two CO adsorbed in bridge site and one CO in a twofold by oxygen coordinated top site (top2f). The labeling of the Pd atoms follows the one in Fig. 6.3, Pd2a–Pd2e are the atoms in the first Pd(100) substrate layer. All values are in eV.

have been performed.

Experimentally, five peaks are found for the surface oxide structure with adsorbed CO, at 1.50 eV, 1.32 eV, 0.97 eV, 0.37 eV and -0.26 eV [142]. Again the negative shift can be assigned to the second layer Pd atoms. Comparing the remaining values to the calculated ones shows, that the Pd-3d SCLSs are not very conclusive, especially since in the experiments the coverage of CO and the ordering of the CO adlayer could not be determined. Thus, there could even be a mixture of signals coming from parts of the surface covered by the *clean* surface oxide and from parts covered by the surface oxide with one or two CO molecules in bridge sites. But also the adsorption of CO in the twofold top site can neither be confirmed, nor excluded based on these data.

Much more information about the adsorption site can be obtained by comparing the C-1s level of the adsorbed CO molecules. Since the theoretically determined absolute values of the core-level position is not very accurate, a proper reference state has to be found. Here, the C-1s level of the CO adsorbed in the $(2\sqrt{2} \times \sqrt{2})R45^\circ$ structure on Pd(100) is taken as zero reference. The calculated shifts are given in Tab. 7.5. The SCLS measurements of the C-1s level for the $(2\sqrt{2}\times\sqrt{2})R45^\circ$ and the $(\sqrt{5}\times\sqrt{5})R27^\circ$ structures with adsorbed CO are shown in Fig. 7.4. It can be seen, that the C-1s level shifts about 0.2 eV between CO adsorbed in the $(2\sqrt{2} \times \sqrt{2})R45^\circ$ and the one on the $(\sqrt{5} \times \sqrt{5})R27^\circ$. Comparing this to the theoretical results a clear distinction between the top and the bridge site can be made. For the two structures with CO in bridge sites likewise a shift of $\sim$ 0.2 eV compared to the $(2\sqrt{2} \times \sqrt{2})R45^\circ$ is found, whereas for the CO in top site a shift of $\sim$ 0.9 eV is calculated. The calculated C-1s SCLSs of the surface oxide structure with one and two CO in bridge sites, leading to an effective coverage of $\Theta_{\mathrm{CO,br}} = 0.2$ ML and $\Theta_{\mathrm{CO,br}} = 0.4$ ML with respect to the underlying Pd(100) substrate, differ only slightly. Thus, the C-1s SCLSs appear to be rather independent of the CO coverage within this range, so that it is not possible

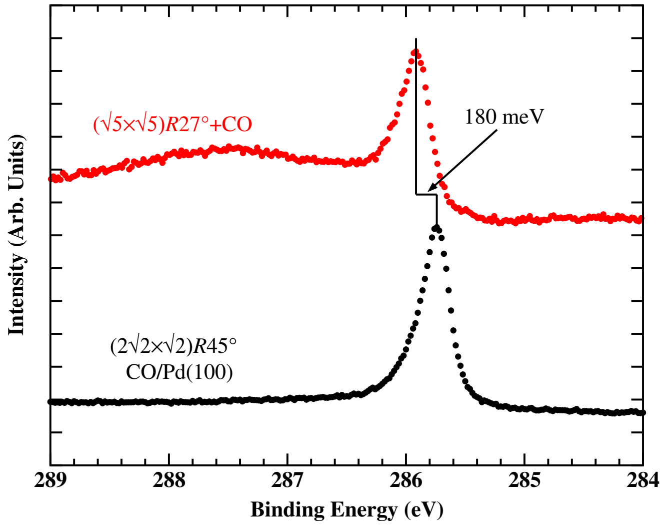

Figure 7.4: Measured C-1s surface core-level shifts of the $(2\sqrt{2} \times \sqrt{2})R45°$-CO/Pd(100) structure (black spectrum) and the $(\sqrt{5} \times \sqrt{5})R27°$+CO structure (red spectrum). In the two structures the C-1s core-level is shifted by 180 meV [142].

C-atom	$\sqrt{5}$+CO$^{\mathrm{br}}$	$\sqrt{5}$+2CO$^{\mathrm{br}}$	$\sqrt{5}$+CO$^{\mathrm{top2f}}$
C-brI	—	0.19	—
C-brII	0.18	0.21	—
C-top2f	—	—	0.89

Table 7.5: Calculated total SCLSs of the C-1s level of the $(\sqrt{5} \times \sqrt{5})R27°$ surface oxide (here abbreviated with $\sqrt{5}$) with one and two CO adsorbed in bridge site and one CO in a twofold top site. The labeling of the adsorption sites follows the one in Fig. 7.3. The shifts are given with respect to the C-1s level of CO adsorbed in the $(2\sqrt{2} \times \sqrt{2})R45°$ structure on Pd(100). All values are in eV.

to extract information from the calculated shifts about the CO coverage during the experiments. Hence, it remains unclear, how much CO was adsorbed on the surface during the SCLS measurements.

Even though the calculated SCLSs include some uncertainties regarding the computational setup and the artificial interaction between the charged, periodic images due to the supercell approach (cf. Section 3.7.3), these results are rather definite with respect to the adsorption site. Thus, experimentally as well a theoretically the bridge site appears to be the most favorable for the adsorption of CO on the $(\sqrt{5} \times \sqrt{5})R27°$ surface oxide structure.

7.3 Phase Diagram For Pd(100) In An O_2 And CO Gas Phase

Within the atomistic thermodynamics approach it is now possible to directly compare the stability of all proposed structures in equilibrium with an oxygen and CO gas phase. In the here discussed case of a two-component gas phase a *constrained* equilibrium is considered, i.e. the surface is in equilibrium with both the oxygen and the CO gas phase, but the two gas phases are not in thermodynamic equilibrium with each other (cf. Page 39). Thus, the formation of CO_2 is neglected in the gas phase, as well as on the surface. In the gas phase this assumption seems to be reasonable, since in reality the reaction of O_2 and CO is kinetically hindered due to a huge reaction barrier. At the surface, though, where the reaction is actually supposed to take place, this is only appropriate as long as the on-going catalytic formation of CO_2 is less frequent than all O_2 and CO adsorption and desorption processes, so that the surface can still maintain its equilibrium with the two gas phase components. Thus, the constrained atomistic thermodynamics approach can be used here only to obtain a first idea of relevant surface phases in the whole (T, p)-range of gas phase conditions. These results can then provide the basis for the next refining step, the consideration of the reaction kinetics on the average surface composition by kinetic Monte Carlo simulations, which will be discussed in the next Chapter.

To calculate the Gibbs free energy of adsorption depending on both the O_2 and CO gas phase conditions Eq. (4.31) is used

$$
\begin{aligned}
&\Delta G^{\mathrm{ads}}(\Delta\mu_{\mathrm{O}}, \Delta\mu_{\mathrm{CO}}) = \\
&= -\frac{1}{A}\left(E^{\mathrm{surf}}_{\mathrm{O,CO@Pd}} - E^{\mathrm{surf}}_{\mathrm{Pd}} - \Delta N_{\mathrm{Pd}} E^{\mathrm{bulk}}_{\mathrm{Pd}} - N_{\mathrm{O}}(1/2 E^{\mathrm{tot}}_{\mathrm{O}_2} + \Delta\mu_{\mathrm{O}}) - N_{\mathrm{CO}}(E^{\mathrm{tot}}_{\mathrm{CO}} + \Delta\mu_{\mathrm{CO}})\right) \\
&= -\frac{1}{A}\Delta\widetilde{E}^{\mathrm{bind}}_{\mathrm{O,CO@Pd}} + \frac{N_{\mathrm{O}}}{A}\Delta\mu_{\mathrm{O}} + \frac{N_{\mathrm{CO}}}{A}\Delta\mu_{\mathrm{CO}} \quad .
\end{aligned}
\tag{7.3}
$$

Just as in the previous Section the Gibbs free energies of the different subsystem are approximated by the DFT total energies (for a detailed discussion of the computational setup cf. Appendix A). As discussed in Section 6.2, for the here investigated systems the pV-term as well as the configurational entropy term stay below 3 meV/Å^2, which does not decisively influence the results. The magnitude of the vibrational contribution, on the other hand, has to be estimated for every considered structure. For oxygen containing structures this has already been done in Section 6.2. New vibrational contributions arise from CO containing structures. Here, the vibrational contribution comprises two different components, the change in the C-O vibration due to the adsorption and an additional Pd-C vibration. For the $(2\sqrt{2} \times \sqrt{2})R45°$-CO/Pd(100) structure this is given by (cf. Section 6.2)

$$
\Delta G^{\mathrm{ads,vib}}(T) = -\frac{2}{A}\left(F^{\mathrm{vib}}(T, \bar{\omega}^{\mathrm{surf}}_{\mathrm{C-Pd}}) + F^{\mathrm{vib}}(T, \bar{\omega}^{\mathrm{surf}}_{\mathrm{O-C@Pd}}) - F^{\mathrm{vib,ZPVE}}(\bar{\omega}^{\mathrm{gas}}_{\mathrm{CO}})\right) \quad . \tag{7.4}
$$

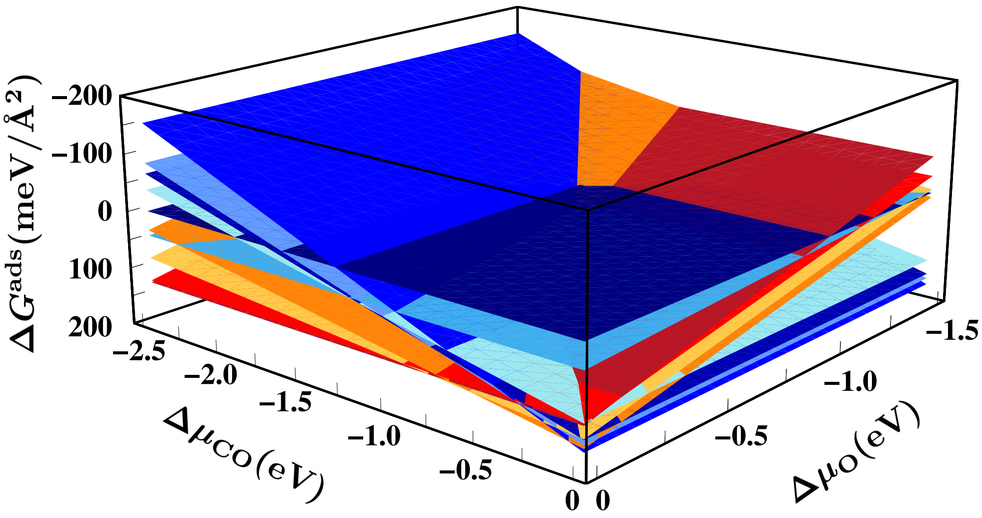

Figure 7.5: Gibbs free energy of adsorption for the Pd(100) surface in a constrained equilibrium with an O_2 and CO gas phase. The different planes represent the 9 most stable structures. Depending on their O and CO coverage the different planes have a slope with respect to $\Delta\mu_{\mathrm{O}}$ and/or $\Delta\mu_{\mathrm{CO}}$

Assuming average frequencies of $\bar{\omega}^{\mathrm{surf}}_{\mathrm{C-Pd}} = 41\,\mathrm{meV}$ [129], $\bar{\omega}^{\mathrm{surf}}_{\mathrm{O-C@Pd}} = 242\,\mathrm{meV}$ [127] and $\bar{\omega}^{\mathrm{gas}}_{\mathrm{CO}} = 269\,\mathrm{meV}$ [11], the vibrational contribution to the Gibbs free energy of adsorption for this structure stays below $2\,\mathrm{meV/Å^2}$ for temperatures up to $T = 600\,\mathrm{K}$. Since this contribution is proportional to the coverage, even for a (1×1) structure it will only increase up to $4\,\mathrm{meV/Å^2}$, which is still rather small. Regarding mixed structures containing oxygen and CO the different contributions will simple add up, e.g. for a (2×2) unit cell with one O in hollow and one CO in bridge site the vibrational contribution is less than $1.6 + 0.8 = 2.4\,\mathrm{meV/Å^2}$ in the investigated temperature range (cf. Page 71). Similarly this is done for the co-adsorbed structures on the surface oxide. The additional adsorption of one CO molecule in the $(\sqrt{5} \times \sqrt{5})R27°$ surface unit cell results in an increase of less than $1\,\mathrm{meV/Å^2}$ in the vibrational contribution, so that for these structures the estimate given in Section 6.2 is almost unchanged. The phase diagram discussed in the following is not significantly changed, if these estimated, maximum values for the vibrational contribution are included, i.e. there are some small shifts in the boundaries between stable phases, but none of the stable structures disappears from and none of the unstable ones appears in the phase diagram.

In Fig. 7.5 the Gibbs free energy of adsorption is shown as a function of the chemical potentials of oxygen and CO. Every plane in this graph belongs to a specific structure and its slope in x- and y-direction depends on the oxygen and CO coverage, respectively. In this study the thermodynamic stability of a total number of 189 structures is compared, comprising of all the afore described possibilities to adsorb O and/or CO on Pd(100) including the (modified) $(\sqrt{5} \times \sqrt{5})R27°$ surface oxide structures. Only the planes belonging to the 11 most stable phases are shown in Fig. 7.5. The most stable phase is again the one that maximizes ΔG^{ads} for any given chemical potential $\Delta\mu_{\text{O}}$ and $\Delta\mu_{\text{CO}}$, i.e., since the z-axis is inverted in Fig. 7.5, this is the structure with the *lowest* plane (cf. Section 4.3). Two structures having the same number of oxygen and CO atoms/molecules per surface area will result in parallel planes, so that the one with the smaller binding energy $\Delta\widetilde{E}^{\text{bind}}_{\text{O,CO@Pd}}$ can directly be excluded as a stable structure (cf. Appendix B.1).

In this 3-dimensional plot, the dependence of ΔG^{ads} on the chemical potentials is nicely visualized, but the most stable phase at a specific value of $\Delta\mu_{\text{O}}$ and $\Delta\mu_{\text{CO}}$ is rather difficult to identify. For this the 3D-plot can be converted into a 2D-plot by looking from below at the graph in Fig. 7.5. The resulting 2D-surface phase diagram is shown in Fig. 7.6. Here, only the most stable phases at any given chemical potential of oxygen and CO are displayed. For a more intuitive understanding the chemical potentials have been converted into the respective pressure scales at $T = 300\,\text{K}$ and $600\,\text{K}$ in the top two x-axes for oxygen and in the right two y-axes for CO. Starting at the lower left corner of Fig. 7.6, which corresponds to both very O-poor and CO-poor gas phase conditions, the clean metal surface must obviously result as the most stable system state. Moving from this situation to the right, i.e. keeping the CO chemical potential at this very low value and increasing the oxygen chemical potential leads to the same result as discussed for the pure O_2 gas phase in Section 6.2. First, the $p(2 \times 2)$ adlayer becomes stable, then the $(\sqrt{5} \times \sqrt{5})R27^\circ$ surface oxide and finally the bulk oxide.

If instead the oxygen content is kept low and the CO content is gradually increased in the gas phase, i.e. moving from the lower left corner upwards, a series of ordered CO adlayer phases on Pd(100) with increasing coverage is stabilized. At first the also experimentally observed $(2\sqrt{2} \times \sqrt{2})R45^\circ$ (0.5 ML), $(3\sqrt{2} \times \sqrt{2})R45^\circ$ (0.67 ML) and $(4\sqrt{2} \times \sqrt{2})R45^\circ$ (0.75 ML) structures are found and finally for a very high CO content in the gas phase a (1×1) structure with CO in bridge site (1.0 ML) is stable.

Starting again in the lower left corner and moving along the diagonal, i.e. increasing now both the oxygen as well as the CO content in the gas phase, one would intuitively expect a mixture of the so far discussed phases, i.e. co-adsorbed structures of oxygen and CO, to become favorable. As can be seen in Fig. 7.6 none of the above presented structural models for ordered overlayers of O and CO on Pd(100) (cf. Fig. 7.2) is a thermodynamically most stable phase under any gas phase conditions. This is in agreement with the already above mentioned experimental findings, that on Pd(100) O and CO prefer to form separate domains rather than any ordered co-adsorbed overlayers [110]. The low stability of these ordered co-adsorbed phases can thus be explained by the strongly repulsive interactions between the two adsorbates leading to a significant decrease in the binding energies. Nevertheless, it can not be excluded that ordered arrangements with another periodicity would not lead to a lowering in the repulsive interactions. To take a reasonable part in the phase diagram, though, the binding energies would have to increase by as much as 0.3–0.5 eV per O atom/CO

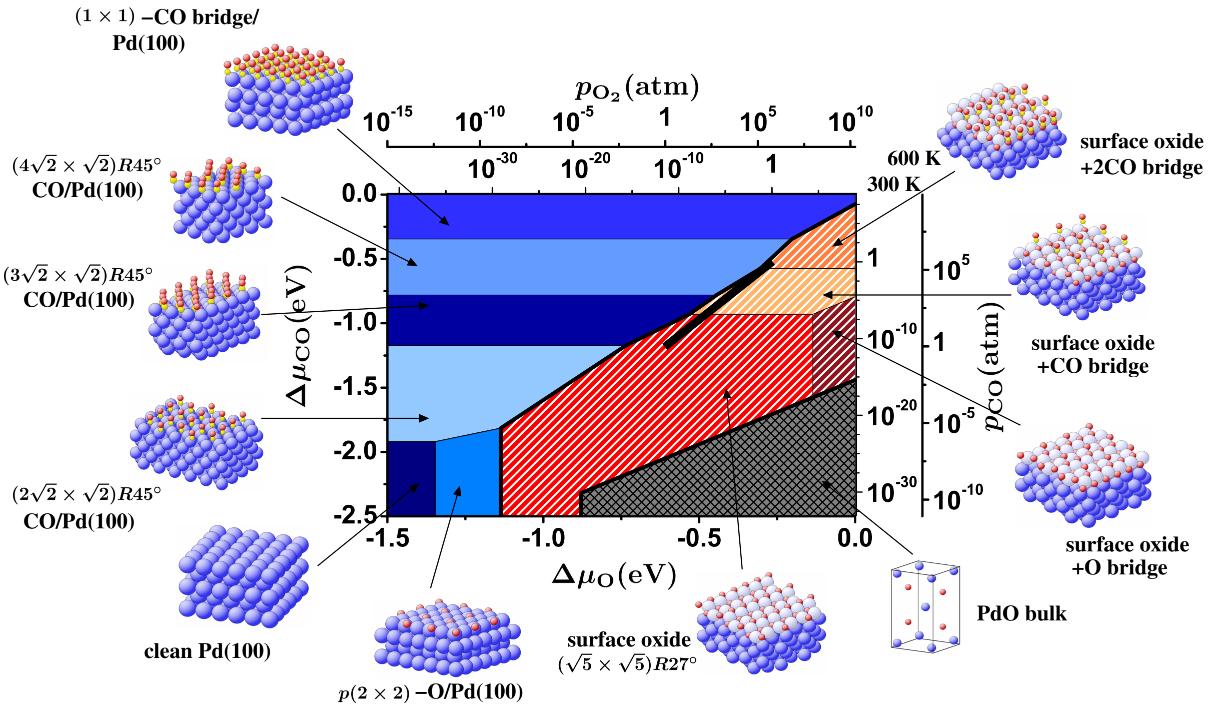

Figure 7.6: Surface phase diagram for the Pd(100) surface in a constrained equilibrium with an O_2 and CO gas phase. The atomic structures underlying the various stable (co-)adsorption phases on the metal and the surface oxide as well as a thick bulk-like oxide film (indicated by the bulk unit cell) are also shown (Pd = large blue spheres, O = small red spheres and C = small yellow spheres). The black bar marks gas phase conditions representative of technological CO oxidation catalysis, i.e. partial pressures of 1 atm and temperatures between 300–600 K.

molecule compared to the now proposed structures. Compared to the pure overlayer structures this would even imply attractive interactions between the two species.

Instead of co-adsorbed structures on Pd(100), for high oxygen and high CO content in the gas phase (upper right part in Fig. 7.6) co-adsorbed structures involving the $(\sqrt{5} \times \sqrt{5})R27°$ surface oxide become stable (two orange-white hatched regions). These two structures correspond to the surface oxide with one and two additional CO adsorbed in bridge sites, respectively (cf. Fig. 7.3 and structures 1 and 15 in Appendix B.1). Additional oxygen adsorption in the bridge site of the surface oxide leads also to a stable phase in a small range of very oxygen-rich and intermediate CO conditions (dark red-white hatched region, structure 99). It is remarkable, that the bulk oxide is already decomposed to CO_2 and the pure Pd metal under these conditions, whereas the surface oxide is still stable. The stability region of the bulk oxide has been determined via Eq. (4.35), yielding for the specific case of PdO

$$\Delta\mu_{CO} - \Delta\mu_{O} < -2\Delta G^{f}_{PdO}(0,0) + \Delta E^{mol} \quad . \tag{7.5}$$

The calculated as well as the experimental values of the binding energies of the three

	PBE	RPBE	LDA	Exp. [11]
O_2	-6.20	-5.75	-7.56	-5.17
CO	-11.65	-11.20	-12.93	-11.16
CO_2	-17.99	-17.09	-20.43	-16.68
ΔE^{mol}	-3.24	-3.02	-3.72	-2.93

Table 7.6: Theoretical and experimental binding energies of O_2, CO and CO_2. All values are in eV.

involved gas phase species needed to evaluate ΔE^{mol} are listed in Tab. 7.6. A detailed discussion of the accuracy of the molecular binding energies is given in Appendix A.3. The heat of formation $\Delta G^{f}_{\mathrm{PdO}}(0,0)$ is given in Tab. 6.4.

All other investigated adlayer structures on Pd(100) or structures involving the $(\sqrt{5} \times \sqrt{5})R27°$ surface oxide (listed in Appendix B.1) do not appear as stable phase in the shown range of O and CO chemical potentials.

Looking again at the whole phase diagram 11 different phases can therefore be identified, divided into three groups. All phases involving adlayer structures on the Pd(100) surface are colored in blue, all phases involving the $(\sqrt{5} \times \sqrt{5})R27°$ surface oxide are red/orange-white hatched and the bulk oxide is grey cross-hatched. In addition, gas phase conditions representative of technological CO oxidation catalysis, i.e. partial pressures of 1 atm and temperatures between 300–600 K, are marked by a black bar. Focusing only on these three different groups of phases two important conclusions with respect to the relevance of the surface oxide under reaction conditions can be drawn. First, the formation of bulk oxide (grey cross-hatched) at the surface under ambient gas phase conditions of O_2 and CO (black bar) can be ruled out. And second, the stability region of the surface oxide does, however, extend to such conditions. In fact, it is either this monolayer thin surface oxide or the CO adlayers on Pd(100) as neighboring phases around the catalytically active region in (T, p)-space.

As already done for the phase diagram in a pure oxygen gas phase in Section 6.2 the dependence of the obtained results on the employed exchange-correlation functional is checked by reevaluating the phase diagram using the RPBE and LDA. For this only the 11 different phases identified using the PBE functional above are recalculated. The Gibbs free energies of adsorption are listed in Tab 7.7 and the two respective phase diagrams are shown in Fig. 7.7. The phase diagram obtained within the RPBE approximation (left graph in Fig. 7.7) looks in fact very similar to the previously discussed one. There are some shifts in the phase boundaries and the high coverage phases of oxygen and CO, $(\sqrt{5} \times \sqrt{5})R27°$+$O^{\mathrm{br}}$ and (1×1)-CO^{br}/Pd(100), are not stable anymore in the shown range of chemical potentials, but again the catalytically active region (black bar) is directly at the phase boundary between surface oxide structures and CO adlayers on Pd(100). Due to the smaller heat of formation (cf. Tab. 6.4) the stability region of the bulk oxide is even further away from ambient conditions of oxygen and CO. Even if the LDA is used as exchange-correlation func-

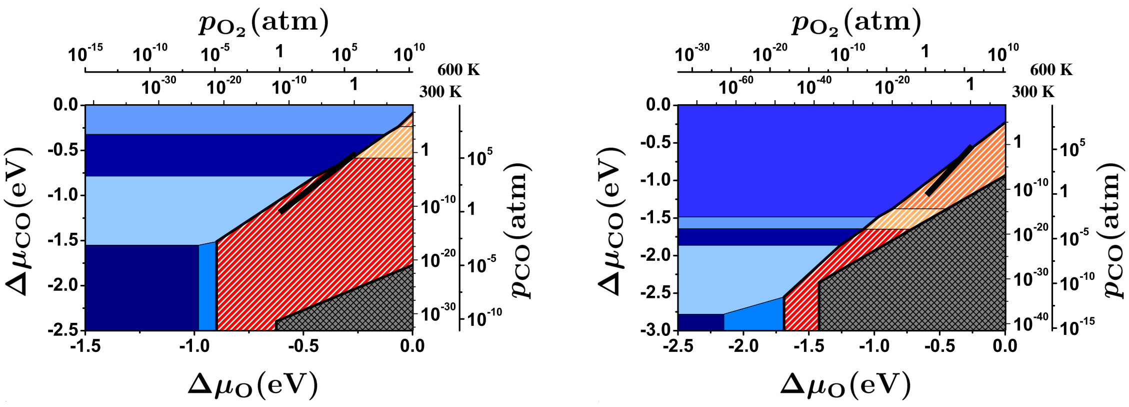

Figure 7.7: Surface phase diagram for the Pd(100) surface in a constrained equilibrium with an O_2 and CO gas phase. The left plot shows the RPBE results and the right one the LDA results. The color coding of the different phases is equivalent to the one used in Fig. 7.6. The black bar marks again gas phase conditions representative of technological CO oxidation catalysis, i.e. partial pressures of 1 atm and temperatures between 300–600 K.

			$\Delta G^{\mathrm{ads}}(0,0)$		
	Θ_O	Θ_{CO}	PBE	RPBE	LDA
clean Pd(100)	0.00	0.00	0	0	0
$p(2 \times 2)$-O/Pd(100)	0.25	0.00	-43	-31	-73
$(\sqrt{5} \times \sqrt{5})R27°$	0.80	0.00	-123	-93	-199
$(\sqrt{5} \times \sqrt{5})R27°$+$O^{br}$	1.00	0.00	-127	-90	-219
$(2\sqrt{2} \times \sqrt{2})R45°$-CO/Pd(100)	0.00	0.50	-123	-98	-186
$(3\sqrt{2} \times \sqrt{2})R45°$-CO/Pd(100)	0.00	0.67	-148	-114	-231
$(4\sqrt{2} \times \sqrt{2})R45°$-CO/Pd(100)	0.00	0.75	-157	-117	-250
(1×1)-CO^{br}/Pd(100)	0.00	1.00	-168	-113	-300
$(\sqrt{5} \times \sqrt{5})R27°$+$CO^{br}$	0.80	0.20	-147	-108	-244
$(\sqrt{5} \times \sqrt{5})R27°$+$2CO^{br}$	0.80	0.40	-162	-114	-282

Table 7.7: Gibbs free energy of adsorption for of all relevant structures of the Pd(100) surface in a constrained thermodynamic equilibrium with an O_2 and CO gas phase. The coverage is given with respect to a Pd(100)-(1×1) surface unit cell. All values are in meV/Å^2.

tional (right plot in Fig. 7.7), which shows a strong over-binding in the here discussed systems, the stability region of the bulk oxide does not extend to the catalytically relevant gas phase conditions, although it covers a much larger range compared to the phase diagrams obtained within the two GGA functionals. It should also be noted, that in the LDA phase diagram the range of O and CO chemical potentials is enlarged to somewhat lower values to include the stability region of the clean metal surface.

7.4 Conclusions

The stability of the Pd(100) surface has been investigated in a constrained equilibrium with an O_2 and CO gas phase. To setup the surface phase diagram a large number of different structures having O and CO adsorbed in high symmetry sites on the Pd(100) surface and on the $(\sqrt{5} \times \sqrt{5})R27^\circ$ surface oxide structure have been included. It is found that under gas phase conditions of ambient temperatures and pressures, as applied in heterogenous oxidation catalysis, it is either the nanometer thin surface oxide structure or a CO covered Pd(100) surface that is stable, whereas the stability region of the bulk oxide does not extend to these conditions.

To obtain an estimate of the uncertainty introduced by the choice of a specific exchange-correlation functional the calculations are performed using the PBE, RPBE and LDA. Comparing the phase diagrams for these three different exchange-correlation functionals shifts in the positions of the boundaries between the different stable phases can be observed. But it can also be seen that the position of the boundary between the CO covered Pd(100) phases and the $(\sqrt{5} \times \sqrt{5})R27^\circ$ surface oxide structures does in fact agree very well. In all three cases, the catalytically active region is very close to this boundary, but still within the stability range of the surface oxide, whereas the formation bulk oxide appears to be unfavorable. Thus, these conclusions seem to be independent of the chosen exchange-correlation functional.

Since in this approach a constrained equilibrium is assumed, the stability of the surface oxide could still be reduced by the reaction kinetics, if the catalytic CO_2 formation consumes the surface oxygen species faster than they can be replenished from the gas phase. The onset of the surface oxide decomposition including the ongoing catalytic reaction will be discussed in the next Chapter.

Chapter 8

The Onset Of Surface Oxide Decomposition

Using the atomistic thermodynamics approach it was possible to obtain a first, large scale picture of the possible stability of different (co-)adsorption structures on Pd(100) over a wide range of O and CO gas phase conditions. Nevertheless, for the here discussed system describing the catalytic CO oxidation at the Pd(100) surface, especially the assumption of a constrained thermodynamic equilibrium has to be qualified. The neglected CO_2 formation at the surface might have a significant influence on the stability of the different phases, since during the catalytic reaction the different subsystems, i.e. surface and gas phase, are most likely not in a full thermodynamic equilibrium as implied in the atomistic thermodynamics approach.

To explicitly include the on-going catalytic reaction at the surface, kinetic Monte Carlo (kMC) simulations (cf. Chapter 5) are performed. For the simulations the system is mapped onto a lattice to keep the number of possible processes manageable. At this point lattice-free kMC simulations based on *ab initio* input parameters would be computationally unfeasible. To include all phases identified in the afore discussed phase diagram (cf. Fig. 7.6), three different lattices would be needed to represent the three different parts indicated in Fig. 7.6, namely phases including the Pd(100) surface, the reconstructed $(\sqrt{5} \times \sqrt{5})R27^\circ$ surface oxide and the bulk oxide. Since the bulk oxide appears to be too unstable to play a role already in the atomistic thermodynamics approach and kinetic effects would be expected to reduce its stability region even further, it would be sufficient to consider only two lattices to model the catalytically active region representing the Pd(100) surface and the $(\sqrt{5} \times \sqrt{5})R27^\circ$ surface oxide structure. As discussed in Section 7.3 the area of catalytically relevant gas phase conditions ($p \approx 1\,\text{atm}$, $T \approx 300 - 600\,\text{K}$) is right at the boundary between phases involving the surface oxide structure and a CO covered Pd(100) surface. Thus, it would be necessary to also include the transition between the two phase, and respectively two kMC lattices, going from the Pd(100) surface to the $(\sqrt{5} \times \sqrt{5})R27^\circ$ surface oxide and vice versa. The reconstructed palladium layer in the surface oxide structure does, however, not only exhibit a different symmetry compared to the

Pd(100) surface, but it has also a different density, since there are only four Pd atoms in the $(\sqrt{5} \times \sqrt{5})R27°$ surface unit cell on five Pd(100) substrate atoms. Thus, the transition from the reconstructed surface oxide to the Pd(100) surface and vice versa appears to involve rather complex processes. An explicit modeling of both phases including a reversible transition between them is therefore extremely involved. In a first approach the present study will instead be restricted to only one phase. Starting at the catalytically relevant gas phase conditions in the stability region of the surface oxide, the focus will be on the stability of the $(\sqrt{5} \times \sqrt{5})R27°$ surface oxide structure under increasingly CO-rich gas phase conditions. Hence, in a first approach the kMC simulations are used to investigate the onset of surface oxide decomposition under reaction conditions and to compare these findings to the results obtained within the constrained atomistic thermodynamics approach. Focusing the kMC simulations on the $(\sqrt{5} \times \sqrt{5})R27°$ surface oxide structure only, a single lattice is sufficient to represent the different structures.

8.1 The Model

As shown in Fig. 7.3 the surface unit cell of the $(\sqrt{5} \times \sqrt{5})R27°$ structure contains 10 additional adsorption sites and 2 oxygen atoms in the upper hollow sites, which can also be removed or substituted by CO. These 12 sites can be reduced to 8, since the four additional hollow sites depicted in Fig. 7.3 are not stable adsorption sites, i.e. any adsorbate (O or CO) initial placed in such a hollow site moves to the corresponding bridge site upon relaxation. For the kMC lattice representing the $(\sqrt{5} \times \sqrt{5})R27°$ surface oxide the number of included sites can be further decreased, if the two sites of a corresponding site type (bridge, twofold by oxygen coordinated top, fourfold by oxygen coordinated top and hollow) within the surface unit cell are considered as being equivalent. Neglecting the small deviations in the energetics of such two like sites resulting from the symmetry of the underlying Pd(100) substrate (cf. Section 7.2), the $(\sqrt{5} \times \sqrt{5})R27°$ surface unit cell can be reduced to half its size, so that for the kMC lattice only four different sites need to be taken into account. In Fig. 8.1 a schematic illustration of the $(\sqrt{5} \times \sqrt{5})R27°$ surface is shown and the surface unit cell with the four adsorption sites as well as the respective kMC lattice are indicated.

The oxygen atoms in the surface oxide structure located below the reconstructed Pd layer at the interface to the Pd(100) substrate are treated as part of the kMC lattice (small red spheres in Fig. 8.1). This is done, since the reconstructed Pd layer shows already quite some distortion, if only the upper oxygen atoms are removed from their hollow sites. If in addition also the lower oxygen atoms are removed from the $(\sqrt{5} \times \sqrt{5})R27°$ surface oxide structure, the palladium atoms in the top layer are so much displaced, that they would not be properly described by the lattice depicted in Fig. 8.1 anymore.

As already mentioned above, the kMC simulations are performed to obtain a first insight into the stability of the surface oxide structure under reaction conditions. The

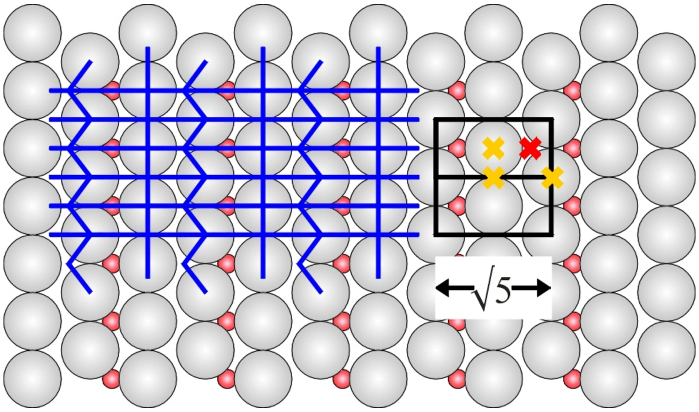

Figure 8.1: Schematic illustration of the $(\sqrt{5} \times \sqrt{5})R27^\circ$ surface oxide structure. The surface unit cell as well as the adsorption sites and the respective kMC lattice are indicated. The large, grey spheres represent Pd atoms, the small, red ones O atoms. The two lower oxygen atoms of the surface oxide are included in the fixed kMC lattice, and not explicitly considered as flexible adsorbates.

simulations are thus started under gas phase conditions, where the surface oxide is a stable phase in the thermodynamic phase diagram (cf. Fig. 8.2). Keeping the oxygen pressure fixed at $p_{O_2} = 1\,\text{atm}$ the CO pressure is gradually increased from $p_{CO} = 10^{-5}\,\text{atm}$ to $p_{CO} = 10^{5}\,\text{atm}$ as indicated by the green arrows in Fig. 8.2 for three different temperatures of $T = 300\,\text{K}$, $T = 400\,\text{K}$ and $T = 600\,\text{K}$. Since the kMC simulations are restricted to a lattice representing the surface oxide, the onset of the surface oxide decomposition will be monitored by the occupation of the hollow sites (red cross in Fig. 8.1) by oxygen. If all hollow sites are occupied by oxygen the structure of the surface oxide is certainly maintained, a depletion of the oxygen atoms in the upper hollow sites will then be taken as indication of the onset of surface oxide decomposition. As discussed above, the entire transition from the surface oxide structure to the Pd(100) surface with increasing CO pressure (as expected from the thermodynamic phase diagram, cf. Fig. 8.2) can not be described within the chosen model.

The four different sites in the kMC lattice are arranged in a square, forming rows of alternating twofold top and hollow sites and rows of alternating bridge and fourfold top sites (the notation twofold and fourfold refers to the coordination of the top site palladium atoms by oxygen in the original surface oxide structure as shown in Fig. 7.3). Moving within one row from one site to the left or right neighboring site is not equivalent due to the lower oxygen atoms included in the lattice, whereas moving to the upper or lower neighboring site along a column is identical. This asymmetry in the lattice sites has to be explicitly considered in the determination of possible processes in the kMC simulation that involve more than one lattice site (dissociative adsorption, associative desorption, diffusion and reaction), as well as in the calculation of process rates that depend on the interactions between neighboring sites.

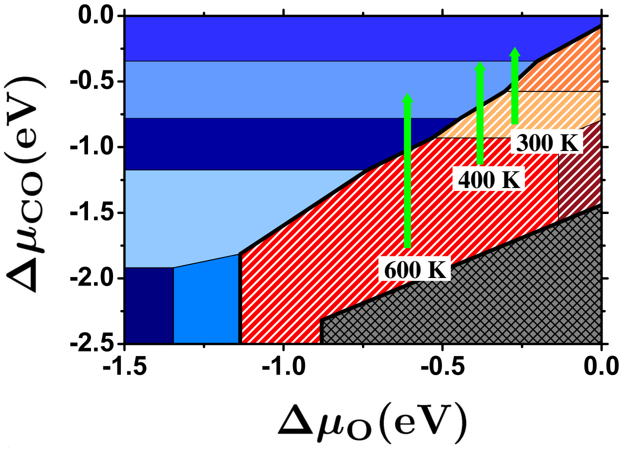

Figure 8.2: Thermodynamic phase diagram as obtained within the PBE exchange-correlation functional. The green bars indicate the pressure conditions of the kMC simulations for a temperature of $T = 300\,\mathrm{K}$, $T = 400\,\mathrm{K}$ and $T = 600\,\mathrm{K}$. The oxygen pressure is always fixed at $p_{O_2} = 1\,\mathrm{atm}$, while the CO pressure is varied between $10^{-5} \leq p_{CO} \leq 10^5\,\mathrm{atm}$.

Initial Considerations Of Sites

To investigate the relevance of the different sites in the kMC lattice representing the surface oxide, some initial tests are performed. Within these test simulations not all imaginable processes are included right from the beginning, but they are used to find out, which processes are important and which might be further coarse-grained in the setup of the final kMC simulation.

In a first test the hollow sites (marked by the red cross in Fig. 8.1) are not considered in the simulation, but simply taken as always completely filled by oxygen atoms, representing the original surface oxide structure. This structure is stable under a sufficiently high oxygen chemical potential and a low CO chemical potential, gas phase conditions which will be taken as starting point for studying the onset of the decomposition of the surface oxide structure (cf Fig. 8.2). Thus, in this first model the interactions of CO with the remaining adsorption sites will be evaluated under these initial conditions. Only 6 process types are considered in this model, which are the unimolecular adsorption and desorption of CO in the three remaining sites, namely the bridge, the twofold top and the fourfold top site. The corresponding rates are obtained by applying Eq. (5.12) and Eq. (5.23). A detailed discussion of all parameters entering the calculation of the different rates is given in Section 8.2 for the final kMC model. For the here described initial considerations a qualitative discussion appears to be sufficient. If no lateral interactions are included, the only difference between the three sites is the binding energy of the CO in each site, which influences the respective desorption rate. Consequently, the simulations yield that with increasing CO chemical potential, which is determined by the temperature and pressure of the CO gas phase, first the bridge site, where the CO is bound most strongly (cf. Tab. 7.3), is occupied, then the twofold top site and finally the fourfold top site. Looking again at the DFT results it is found, that a structure with one CO in bridge and a second one in a twofold top site is not stable (cf. Page 93, and structure 18 in Appendix B.1), due to the strongly repulsive interactions between the two adsorbed molecules. In the kMC simulation this can be realized, if the adsorption of CO on the two twofold top sites neighboring a bridge site, that is already occupied by CO, is excluded, and vice versa. This restriction in the availability of adsorption sites leads to a preference in the occupation of bridge sites.

This preference becomes even more pronounced, if diffusion processes are included in a second test model. In addition to the 6 adsorption and desorption processes, 4 diffusion processes between the twofold top site and the bridge site (top2f ↔ bridge) as well as between the fourfold top site and the bridge site (top4f ↔ bridge) are considered. For the diffusion from either top site to the bridge site only a very small diffusion barrier is calculated ($\Delta E^{\mathrm{diff}}_{\mathrm{CO,top}\rightarrow\mathrm{bridge}} < 0.1\,\mathrm{eV}$), whereas for the diffusion from the bridge to either top site this barrier is increased by the difference in binding energy between the two sites, so that $\Delta E^{\mathrm{diff}}_{\mathrm{CO,bridge}\rightarrow\mathrm{top2f}} = 0.4\,\mathrm{eV}$ and $\Delta E^{\mathrm{diff}}_{\mathrm{CO,bridge}\rightarrow\mathrm{top4f}} = 0.9\,\mathrm{eV}$. With these very small diffusion barriers effectively every CO molecule that is initially adsorbed on a top site will immediately diffuse to an empty neighboring bridge site at the temperatures of interest. Simulations within this model show, that the twofold top sites are then no longer significantly populated by CO anymore, but every CO initially adsorbed in a twofold top site now contributes to the occupation of the bridge sites. This can be explained, since the adsorption on the twofold top sites is only possible, if the neighboring bridge sites are empty, and thus also the diffusion is always possible. The fourfold top sites can still be populated, but only at a very high CO chemical potential, after all bridge sites are already occupied.

In the next step also the adsorption and desorption of oxygen on the three sites is considered, while still keeping all hollow sites occupied with oxygen atoms. Since the oxygen molecules adsorb dissociatively, always two empty sites are needed. This can in principle be realized in 6 different ways, 3 on two like sites (bridge–bridge, top2f–top2f, top4f–top4f) and 3 on mixed sites (bridge–top2f, bridge–top4f, top2f–top4f). Comparing to the DFT calculations, only the adsorption in two neighboring bridge sites appears reasonable, whereas all other combinations of adsorption sites result in energetically unstable geometries, i.e. the oxygen atoms do simply not bind to any of the top sites. Thus, also the diffusion of oxygen atoms from one bridge site to the next is not considered as possible process, since on a simple reaction coordinate the most likely transition state for this diffusion process is the unstable twofold top site. From these initial test simulations it can be seen, that the twofold top site has no relevance in the kMC model representing the surface oxide. For the oxygen it does not serve as a stable adsorption site at all, and for the CO it is basically only a transition state between two bridge sites. In the following simulations, the twofold top site is correspondingly not further considered.

With increasing CO chemical potential (following the green arrows in Fig. 8.2) the surface oxide structure will become less stable. Thus, a 100 % occupation of the hollow sites by oxygen will not be justified anymore and processes including also the hollow sites have to be considered in a further test model. As additional processes, the CO adsorption and desorption at hollow sites, as well as the dissociative adsorption and associative desorption of oxygen involving hollow sites have to be considered. For the O_2 molecule there are now 3 different possibilities to adsorb, respectively desorb, namely the already included adsorption/desorption on/from bridge–bridge sites and in addition the adsorption/desorption in/from hollow–hollow and bridge–hollow sites. Running the simulations it turns out, that depending on the oxygen and CO gas phase conditions the hollow and bridge sites are either empty or occupied by O and/or CO, whereas the fourfold top sites can again only be occupied at very high CO chemical potential. In addition, the CO molecules adsorbed on a fourfold top site can now also diffuse to an empty hollow site, again with a computed very small barrier of $\Delta E^{\mathrm{diff}}_{\mathrm{CO,top4f}\rightarrow\mathrm{hollow}} < 0.1\,\mathrm{eV}$, whereas the barrier for the diffusion from the hollow to the fourfold top site is rather large with $\Delta E^{\mathrm{diff}}_{\mathrm{CO,hollow}\rightarrow\mathrm{top4f}} = 0.8\,\mathrm{eV}$. Thus, the fourfold top sites are only populated, if all bridge and all hollow sites are already filled. Moreover, the DFT calculations show, that the additional adsorption of CO on a fourfold top site, if all hollow and all bridge sites are occupied, leads to an unstable structure. This can be included in the kMC simulation by considering strongly repulsive interactions between the adsorbates. The fourfold top site is then never occupied, since as long as there are still empty, neighboring bridge or hollow sites, an adsorbed CO molecule will always diffuse there, and if all neighboring bridge and hollow sites are already occupied, the adsorption on the fourfold hollow sites is not possible anymore. Therefore, also the fourfold top site will not be explicitly considered in the following simulations, but always be treated as empty site.

The Final kMC Model

In the final kMC model only the bridge and the hollow sites are included, whereas the two top sites remain always unoccupied and are not available for any of the kMC processes. On this lattice containing only the bridge and the hollow site the following processes are considered:

1. Adsorption
    - CO bridge
    - CO hollow
    - O_2 bridge–bridge
    - O_2 hollow–hollow
    - O_2 bridge–hollow

2. Desorption
    - CO bridge
    - CO hollow
    - O_2 bridge–bridge
    - O_2 hollow–hollow
    - O_2 bridge–hollow
3. Diffusion
    - CO bridge ↔ bridge
    - CO hollow ↔ hollow
    - CO bridge ↔ hollow
    - O hollow ↔ hollow
    - O bridge ↔ hollow
4. Reaction (modeled as associative desorption)
    - O hollow + CO bridge ↔ CO_2
    - O bridge + CO hollow ↔ CO_2

This list contains the most obvious kinds of processes with respect to the chosen lattice. It can not be excluded, that other, more complicated processes might have some influence on the here discussed system. Nevertheless, the suggested setup does at least provide a reasonable starting point.

8.2 The Rates

For every process listed in the previous Section a process rate has to be determined. The general derivation of the rates for the four different process types (adsorption, desorption, diffusion and reaction) is given in Section 5.2. Here, the different parameters entering the rates for the simulation of the surface oxide are discussed.

8.2.1 Adsorption

To determine the impingement rate entering Eq. (5.12) the only parameters, that are system specific, are the mass of the impinging gas phase molecules ($m_{O_2} = 5.31 \cdot 10^{-26}\,\mathrm{kg}$ and $m_{CO} = 4.65 \cdot 10^{-26}\,\mathrm{kg}$) and the surface area, whereas temperature and pressure are varied for the different simulations. According to the model described in the previous Section the surface area corresponds to half the surface unit cell of the $(\sqrt{5} \times \sqrt{5})R27^\circ$ surface oxide, i.e. $A = 1/2\, A_{(\sqrt{5}\times\sqrt{5})R27^\circ} = 19.47\,\mathrm{Å}^2$. The determination of the local sticking coefficient $\tilde{S}_{i,st}$, on the other hand, is much more complicated. As discussed in Section 5.2.2 for a proper determination of $\tilde{S}_{i,st}$ the full, high-dimensional potential energy surface (PES) for the adsorption process is needed. On this PES molecular dynamics (MD) simulations have to be performed for a statistically relevant number of trajectories [87]. For the present study, though, only a first, rough order of magnitude estimate of the local sticking coefficient is needed. Thus, it is first determined, if there are any significant adsorption barriers along the minimum energy pathway (MEP) for any of the five different adsorption processes (cf. Eq. (5.16)). For the CO molecule this is done by vertically lifting the CO in an upright geometry from a bridge or a hollow site. The energy of the whole system is then minimized with respect to all other degrees of freedom for different heights of the CO molecule above its adsorption site. For neither of the two sites a barrier is found along this desorption, respectively adsorption, pathway. For the dissociative adsorption of the oxygen molecule a PES is mapped out, in which the energy is given as a function of the bond length between the two O atoms and the height of their center of mass above the surface. The lateral position of the center of mass above the surface, as well as the orientation of the O_2 molecule are kept fixed (i.e. there is no rotation of the molecule around its center of mass). Due to its shape such a plot is also called an *elbow plot*. Since there are only two hollow sites within the $(\sqrt{5} \times \sqrt{5})R27°$ surface unit cell, a lifting of two oxygen atoms would correspond to a complete removal of all upper oxygen atoms in the surface oxide structure due to the periodic supercell setup of the DFT calculations. Thus, these calculations are performed in a (1×2)-$(\sqrt{5} \times \sqrt{5})R27°$ surface unit cell. For the O_2 adsorption on neighboring hollow sites the energy decreases smoothly along the elbow plot apart from a small molecular physisorption well $\sim 0.3\,\text{Å}$ above the optimal adsorption site of the dissociated oxygen atoms. The dissociation of an O_2 molecule in this particular orientation along the respective elbow plot can therefore be considered as non-activated. A similar plot is also found for the O_2 adsorption in neighboring bridge–hollow sites and equivalent results are also expected for the adsorption in two neighboring bridge sites. Since in these calculations only one molecular orientation at a fixed lateral position within the surface unit cell is evaluated for each adsorption process, this is by far not enough to describe the full, high-dimensional PES underlying any of the adsorption processes. Nevertheless, if there exists one barrier free entrance channel connecting the gas phase and the adsorbed state, then also the maximum barrier along the MEP must be zero. As a result, the adsorption barrier in Eq. (5.16) is set to zero, $\Delta E^{\text{ads}} = 0$, for all five adsorption processes.

As a next parameter the factor $f^{\text{ads}}_{i,st}$ is considered. As already explained in Section 5.2.2 this factor reduces the number of impinging gas phase particles by the fraction, that is not traveling along the MEP and might therefore be reflected at some higher energy barrier along a different pathway. Since the here performed simulations are in a temperature range of $T = 300 - 600\,\text{K}$, where the impinging gas phase molecules can still be considered as rather slow, it is assumed, that the molecules are rather efficiently steered along the barrier free pathways [87] and thus the value of

f^{ads} is approximated by $f^{\text{ads}} \approx 1$ for all five adsorption processes. Trying out a few trajectories on the barrier free PESs does indeed lead to the conclusion that the local sticking coefficient can roughly be approximated by $\tilde{S}_{i,st} \approx 1$.

The last parameter is the size of the active area $A_{i,st}$. Following the previous discussion, there is no argument, why either of the two adsorption sites should be favored. The most obvious choice is then to equally divide the surface area A among the different adsorption sites, yielding $A_{\text{CO,br}} = A_{\text{CO,hol}} = 1/2A$ for the adsorption of CO and $A_{\text{O}_2\text{,br}-\text{br}} = A_{\text{O}_2\text{,hol}-\text{hol}} = A_{\text{O}_2\text{,br}-\text{hol}} = 1/3A$ for the adsorption of O_2. Thus, also the adsorption of molecules impinging on top sites and immediately diffusing to neighboring bridge or hollow sites is included in an effective way.

Using these approximations for the different parameters the calculation of the rates for the five different adsorption processes is straightforward. From the above discussion, though, it becomes clear, that there are still some uncertainties in the rates due to the well reasoned, but still approximate determination of parameters. This uncertainty will be considered in the discussion of the simulation results at the end of this Chapter.

8.2.2 Desorption

The desorption rates are connected to the adsorption rates by the detailed balance criterion (cf. Eq. 5.18). Thus, having determined the adsorption rates the corresponding desorption rates can be obtained by applying Eq. (5.23). In a first approach the vibrational partition function in the adsorbed state is set to unity, $z_{i,st}^{\text{vib}} = 1$, for all desorption processes. In the gas phase the vibrational partition function of oxygen and CO can very well be approximated by unity over the here investigated temperature range ($T = 300 - 600\,\text{K}$), i.e. only the first vibrational state is excited. In the adsorbed state this might be changed, though, due to the lower frequency modes resulting from the adsorbate–substrate bond, which could then lead to a somewhat larger partition function, $z_{i,st}^{\text{vib}} > 1$.

The second parameter, that is needed to determine the desorption rate, is the binding energy. The binding energies of oxygen and CO in the bridge and hollow sites do in general depend on the interaction between neighboring sites. Thus, a lattice gas Hamiltonian (LGH) is set up (cf. Section 5.1.2) to determine the binding (resp. desorption) energies during the simulation using Eq. (5.8). From the DFT calculations it becomes obvious that the interactions between the adsorbates do not extend beyond the $(\sqrt{5} \times \sqrt{5})R27^\circ$ surface unit cell for the here assumed level of accuracy of the binding energies, i.e. the change in the binding energies is $< 0.1\,\text{eV}$ (cf. Appendix B.2). Consequently, in the LGH only nearest neighbor pair interactions

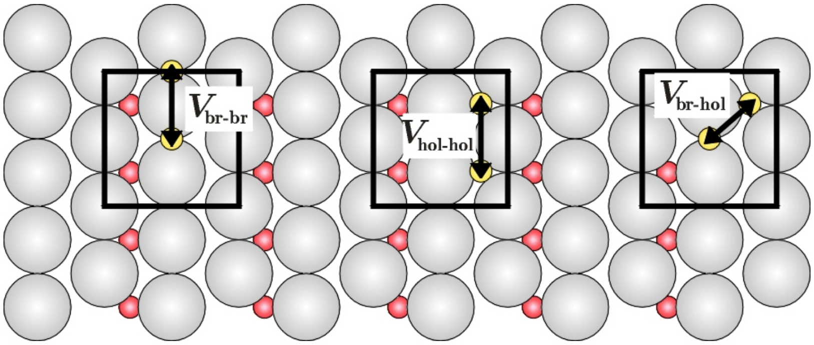

Figure 8.3: First nearest neighbor pair interactions between adsorbates on the $(\sqrt{5}\times\sqrt{5})R27°$ surface oxide. An adsorbate sitting in a bridge site does only interact with adsorbates in right neighboring hollow sites, whereas the left neighboring hollow sites are too far away. Large, grey spheres represent Pd atoms, small, red spheres oxygen atoms included in the kMC lattice and small yellow spheres adsorbed O and/or CO.

are included

$$\begin{aligned} H = &\sum_i \left[n_{\mathrm{O},i}E^0_{\mathrm{O},i} + n_{\mathrm{CO},i}E^0_{\mathrm{CO},i}\right] \\ &+ \sum_{ij}\left[V_{\mathrm{O-O},ij}\, n_{\mathrm{O},i}\, n_{\mathrm{O},j} + V_{\mathrm{CO-CO},ij}\, n_{\mathrm{CO},i}\, n_{\mathrm{CO},j} + V_{\mathrm{O-CO},ij}\, n_{\mathrm{O},i}\, n_{\mathrm{CO},j}\right] \quad , \end{aligned} \tag{8.1}$$

where j only runs over the corresponding neighboring sites. The binding energy of a CO molecule in a site i is then e.g. given by

$$\begin{aligned} E^{\text{bind}}_{\mathrm{CO},i} &= H(n_{\mathrm{CO},i}=1) - H(n_{\mathrm{CO},i}=0) \\ &= E^0_{\mathrm{CO},i} + 2\sum_j \left[V_{\mathrm{CO-CO},ij}\, n_{\mathrm{CO},j} + V_{\mathrm{O-CO},ij}\, n_{\mathrm{O},j}\right] \quad . \end{aligned} \tag{8.2}$$

Equivalently, the binding energy of an oxygen atom is calculated. For the associative desorption of an O_2 molecule, respectively, two neighboring sites are depleted, which can be expressed similarly using the LGH. As shown in Fig. 8.3 the first nearest neighbor pair interactions correspond to interactions between two neighboring bridge sites, two neighboring hollow sites and between neighboring bridge and hollow sites. Thus, there are six different interaction parameters between like species ($V_{\mathrm{O-O,br-br}}$, $V_{\mathrm{O-O,hol-hol}}$, $V_{\mathrm{O-O,br-hol}}$, $V_{\mathrm{CO-CO,br-br}}$, $V_{\mathrm{CO-CO,hol-hol}}$, $V_{\mathrm{CO-CO,br-hol}}$) and four different between unlike species ($V_{\mathrm{O-CO,br-br}}$, $V_{\mathrm{O-CO,hol-hol}}$, $V_{\mathrm{O-CO,br-hol}}$, $V_{\mathrm{O-CO,hol-br}}$). Together with the four on-site energies there is thus a total of 14 parameters, which have to be determined for the LGH. The parameters can be obtained by fitting to DFT results (cf. Section 5.1.2). The on-site terms can either be determined in the fitting procedure, or they are taken from a low coverage limit. Calculating the on-site energies in a low-coverage limit is often preferred, if long-range interactions are not expected to have an important contribution. A direct evaluation of the on-site terms

$E^0_{\mathrm{O,br}}$	$E^0_{\mathrm{O,hol}}$	$E^0_{\mathrm{CO,br}}$	$E^0_{\mathrm{CO,hol}}$
-0.51	-1.95	-1.40	-1.92
$V_{\mathrm{O-O,br-br}}$	$V_{\mathrm{O-O,hol-hol}}$	$V_{\mathrm{O-O,br-hol}}$	
0.08	0.07	0.08	
$V_{\mathrm{CO-CO,br-br}}$	$V_{\mathrm{CO-CO,hol-hol}}$	$V_{\mathrm{CO-CO,br-hol}}$	
0.08	0.13	0.14	
$V_{\mathrm{O-CO,br-br}}$	$V_{\mathrm{O-CO,hol-hol}}$	$V_{\mathrm{O-CO,br-hol}}$	$V_{\mathrm{O-CO,hol-br}}$
0.06	0.11	0.13	0.12

Table 8.1: Four on-site energies E and ten first nearest neighbor interaction parameters V for the lattice gas hamiltonian describing the adsorption of O and CO in hollow and bridge sites of the surface oxide. All values are in eV.

can then become favorable, since the on-site terms are usually at least one order of magnitude larger than the interaction parameters, but within the fitting procedure all parameters will have the same relative error, which correspondingly leads to a much larger absolute error in the on-site terms. For the surface oxide structure, though, only the on-site energies for the hollow sites could be determined from a low coverage limit. Occupying only one bridge site leaving both hollow sites empty within the $(\sqrt{5} \times \sqrt{5})R27°$ surface unit cell leads again to a strong displacement of the atoms in the reconstructed palladium layer. It was therefore not possible to obtain reliable on-site energies for O or CO in bridge position in a low coverage limit. Consequently, in the present work the interaction parameters as well as the on-site energies are included in the fitting procedure. To fit the 14 parameters 29 different configurations of O and/or CO in bridge and hollow sites are calculated within the $(\sqrt{5} \times \sqrt{5})R27°$ surface unit cell and the respective energy of each configuration is expressed in term of a lattice gas expansion (for a detailed discussion cf. Appendix C) . Since in the kMC model the lower oxygen atoms are part of the lattice, the energies of the different configurations are calculated with respect to the *empty* lattice, i.e.

$$\Delta E = E_{\mathrm{O,CO@}(\sqrt{5}\times\sqrt{5})R27°} - E_{(\sqrt{5}\times\sqrt{5})R27°-2\mathrm{O}} - N_{\mathrm{O}} 1/2 E^{\mathrm{tot}}_{\mathrm{O}_2} - N_{\mathrm{CO}} E^{\mathrm{tot}}_{\mathrm{CO}} \quad , \tag{8.3}$$

where $E_{(\sqrt{5}\times\sqrt{5})R27°-2\mathrm{O}}$ corresponds to the surface oxide structure without the two upper oxygen atoms (structure 117 in Appendix B.1). All energies are calculated using the PBE as approximation to the exchange-correlation functional. Using the 29 different configurations the 14 parameters are obtained by a least-square fit. In Tab. 8.1 the four on-site energies and the 10 interaction parameters are listed. The fitted on-site energies of O or CO in hollow sites compare rather well to the binding energies in the low coverage limit, $E^{\mathrm{bind}}_{\mathrm{O,hol}} = -1.83\,\mathrm{eV}$ and $E^{\mathrm{bind}}_{\mathrm{CO,hol}} = -1.92\,\mathrm{eV}$, within the here aspired level of accuracy. All interaction parameters are positive reflecting the purely repulsive interaction between neighboring adsorbates. Comparing the on-site energies it can be seen, that both O and CO prefer the hollow site. If competing for the same site, though, the oxygen binds more strongly on the hollow site, whereas the CO is more strongly bound on the bridge site. Including the repulsive interactions this trend is maintained for all possible configurations.

Using these parameters the binding energy of every adsorbate can be evaluated for any random configuration by utilizing Eq. (8.2), and the respective desorption rate can be calculated via Eq. (5.23).

8.2.3 Diffusion

To calculate the diffusion rates by applying Eq. (5.28) the transition states along the diffusion pathways are needed. For the diffusion from one bridge site to a neighboring one, the transition state is simply given by the twofold top site. The transition state for the diffusion from a hollow to a neighboring bridge or hollow site is more difficult to define, which is mainly due to the mobility of the topmost Pd layer, if an adsorbate is moved away from a hollow site. If, e.g., an oxygen atom sitting in a hollow site is displaced in y-direction, the topmost Pd layer will follow this displacement, so that, if all but the oxygen y-coordinate are relaxed, the whole reconstructed surface oxide layer is simply shifted with respect to the underlying substrate, whereas the displaced O atom remains perfectly in the hollow site. It has been shown previously that the reconstructed surface oxide layer can be shifted over the Pd(100) substrate rather easily, exhibiting an energetic corrugation of $< 0.65\,\mathrm{eV/unit\ cell}$ [144]. Compared to the binding energy of an oxygen atom in hollow site ($E^{\mathrm{bind}}_{\mathrm{O,hol}} = -1.83\,\mathrm{eV}$) this is rather small. Thus, it becomes energetically more favorable to shift the surface oxide layer instead of displacing an oxygen atom from a hollow site when using smaller (periodic boundary conditions) surface unit-cells. In a larger surface unit cell, though, the difference in energy that is needed to shift the surface oxide layer compared to displacing one oxygen atom from a hollow site becomes smaller and eventually in a huge supercell the effect would vanish. Unfortunately, doubling the surface unit cell in x- or y-direction appears not to be sufficient to prevent the shifting of the reconstructed palladium layer and calculations in even larger surface unit cells were computational too demanding at this time.

To obtain at least approximate values for the diffusion barriers the xy-coordinates of the palladium atoms in the surface oxide layer are additionally fixed during the transition state search. The resulting values of the diffusion barriers are listed in Tab. 8.2. They are calculated within the $(1 \times 1) - (\sqrt{5} \times \sqrt{5})R27°$ surface unit cell, with both hollow sites occupied by O (CO diffusion bridge → bridge, structure 1 in Appendix B.1), only one hollow site occupied by O (CO/O diffusion bridge → hollow, structures 29 → 28 and 106 → 105) and one hollow site occupied by CO/O (CO/O diffusion hollow → hollow, structures 60 and 113). In this structural setup, the initial and final state for the diffusion between like sites have the same energy, as shown in the left part of Fig. 8.4. For the diffusion between unlike sites or like sites with different nearest neighbor interactions, though, the energy of the initial and final state well differ. Here, the values listed in Tab. 8.2 are taken as minimum values for the

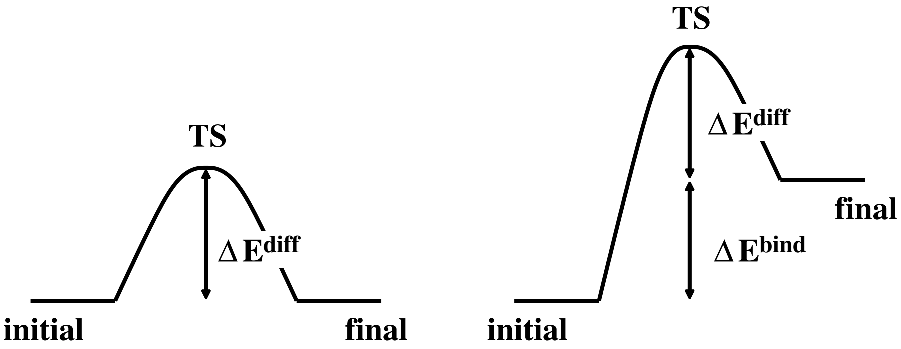

Figure 8.4: Schematic illustration of the diffusion barrieres between energetically like and unlike sites.

	$\Delta E^{\mathrm{diff}}_{\mathrm{br}\to\mathrm{br}}$	$\Delta E^{\mathrm{diff}}_{\mathrm{hol}\to\mathrm{hol}}$	$\Delta E^{\mathrm{diff}}_{\mathrm{br}\to\mathrm{hol}}$
O	–	1.4	0.1
CO	0.4	0.6	0.3

Table 8.2: Barriers for the diffusion between the different sites within the $(\sqrt{5} \times \sqrt{5})R27°$ surface unit cell. All values are in eV.

diffusion barriers, i.e. if the final state has the same or a lower energy than the initial state the diffusion barrier is fixed to this value. Only if the final state is higher in energy the difference in binding energies between the initial and final state is added to the diffusion barrier (right part in Fig. 8.4) to ensure that the detailed balance criterion is fulfilled for the two time reversed diffusion processes.

To determine the remaining factor $f^{\mathrm{diff,TST}}_{i,st\to st'}$ in Eq. (5.29) it is assumed, that the vibrational partition functions of the adsorbate in the initial and at the transition state are approximately the same, i.e. $z^{\mathrm{vib}}_{i,st} \approx z^{\mathrm{vib}}_{i,st\to st',\mathrm{TS}}$, yielding $f^{\mathrm{diff,TST}}_{i,st\to st'} \approx 1$.

In this way, the rates of the different diffusion events were calculated for all possible system configurations. Since it turns out that the diffusion processes do not have any significant influence on the results of the kMC simulations and can actually be neglected, also the uncertainties in the rates introduced by the described approximations are irrelevant for the discussion of the results.

8.2.4 Reaction

The rates for the reaction of adsorbed O and CO to form CO_2 is calculated using Eq. (5.31). To determine the reaction barrier $\Delta E^{\mathrm{reac}}_{\mathrm{O+CO}\to\mathrm{CO_2}}$ the respective transition states have to be determined for the two included reactions O hollow + CO bridge and O bridge + CO hollow. Here, the transition state is searched by mapping out a 2-dimensional potential energy surface (PES), where the energy is plotted as a function

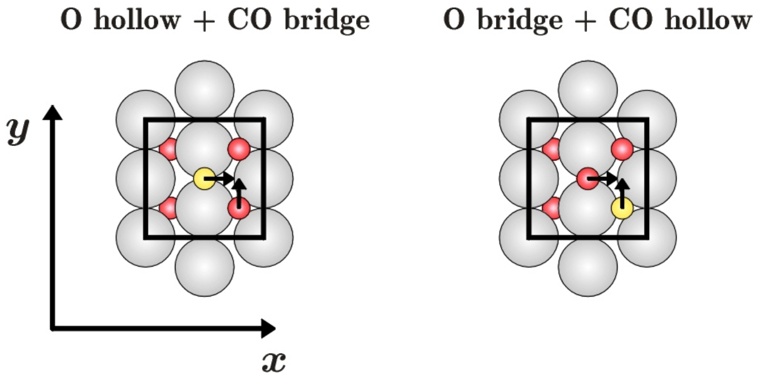

Figure 8.5: Geometries for the transition state search for the reaction of O hollow + CO bridge (left) and O bridge + CO hollow (right). The x- respectively y-coordinate of the O (red spheres) resp. C (yellow spheres) atom are fixed along the black arrows. To avoid a lateral shifting of the complete surface oxide structure with respect to the underlying Pd(100) substrate the xy-coordinates of the palladium atoms in the reconstructed layer (grey spheres) are additionally fixed.

of the x-coordinate of the CO/O in bridge site and the y-coordinate of the O/CO in hollow site with respect to their initial position within the $(\sqrt{5} \times \sqrt{5})R27°$ surface unit cell as shown in Fig 8.5. All other degrees of freedom are completely relaxed. As already mentioned in the previous Section, the topmost Pd layer shows a rather high mobility with respect to a lateral shift along the substrate, when using small surface unit cells. When mapping out the PES in a (1×1) surface unit cell the effect appears to be again so large, that it is not possible to find a proper transition state. Also in $(1 \times 2)-$ and $(2 \times 1) - (\sqrt{5} \times \sqrt{5})R27°$ surface unit cells a shifting of the surface oxide layer was still present, while calculations in even larger cells are at this time unfortunately prohibitive.

To circumvent this problem a two-step approach is chosen to obtain at least approximate values for the reaction barriers. In a first step the xy-coordinates of the Pd atoms in the reconstructed surface oxide layer are additionally fixed (cf. Fig. 8.5) and the energy is only minimized with respect to the remaining coordinates. The resulting PESs are shown in Fig. 8.6. The respective transition states are marked by a yellow circled cross. The barrier for the reaction O hollow + CO bridge is rather high with $\Delta E^{\text{reac}}_{\text{Ohol+CObr}} = 1.3\,\text{eV}$, whereas for the reaction of O bridge + CO hollow only a barrier of $\Delta E^{\text{reac}}_{\text{Obr+COhol}} = 0.6\,\text{eV}$ is found. In a second step the transition state geometries are now also relaxed with respect to the xy-coordinates of the topmost palladium atoms, while fixing all three coordinates of the reactants O and CO, to release some of the lateral stress that was induced by fixing the lateral positions of the palladium atoms in the first step. In this second relaxation step the barrier of the first reaction (O hollow + CO bridge) is lowered by $\sim 0.4\,\text{eV}$ giving $\Delta E^{\text{reac}\prime}_{\text{Ohol+CObr}} = 0.9\,\text{eV}$, whereas for the second reaction the effect is much smaller, yielding $\Delta E^{\text{reac}\prime}_{\text{Obr+COhol}} = 0.5\,\text{eV}$. Also the remaining, maximum forces on the fixed O and C atoms are rather moderate, $\sim 46\,\text{mRy/bohr}$ for the first reaction and $\sim 20\,\text{mRy/bohr}$ for the second reaction.

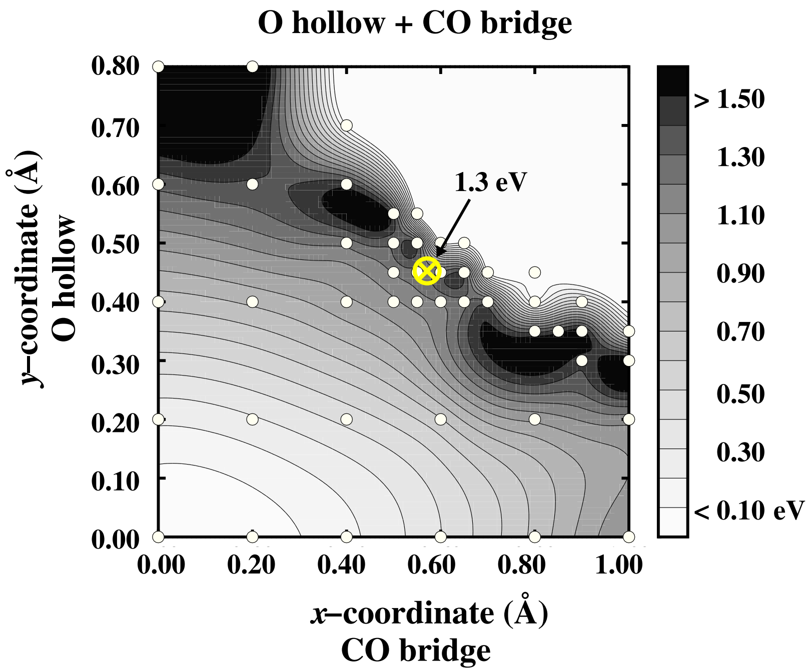

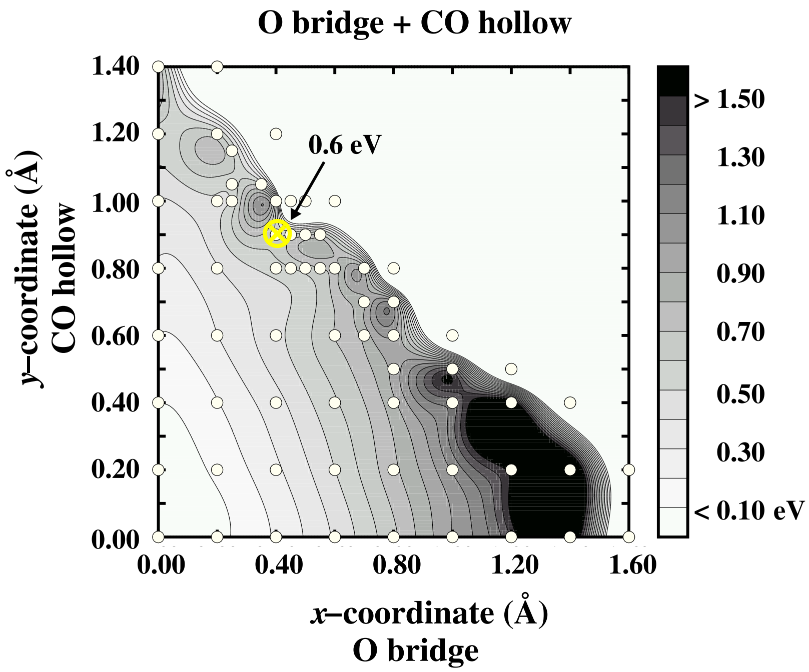

Figure 8.6: Potential energy surfaces for the reaction of O hollow + CO bridge (top) and O bridge + CO hollow (bottom). The x- and y-coordinates are given with respect to the initial adsorption site in the surface unit cell. The actually calculated points are indicated by white circles. The energy zero corresponds to the initial configuration. The transition state is marked by a yellow circled cross. All energies are in eV.

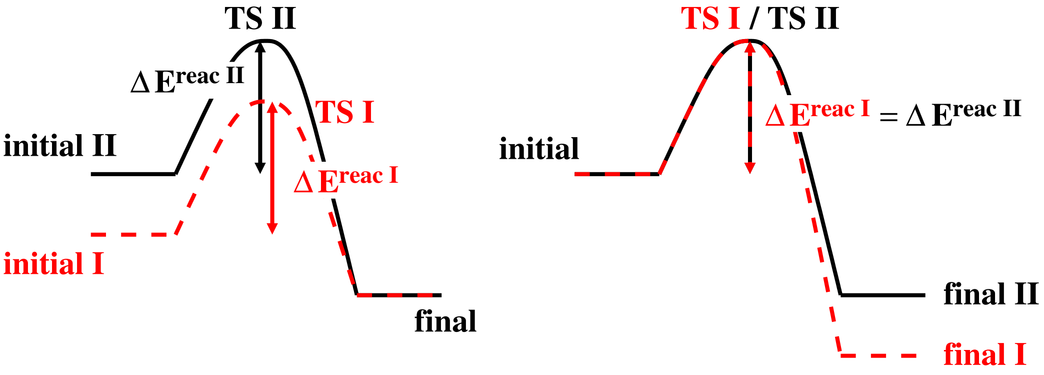
TS II
$\Delta E^{\mathrm{reac\ II}}$
TS I
initial II
$\Delta E^{\mathrm{reac\ I}}$
initial I
final
TS I / TS II
initial
$\Delta E^{\mathrm{reac\ I}} = \Delta E^{\mathrm{reac\ II}}$
final II
final I

Figure 8.7: Schematic illustration of the reaction barrieres for different initial and final states. Here, the transition state is dominated by the initial state, thus the reaction barriers maintain constant.

Thus, the transition states obtained within this two step approach can be considered as good approximations to the real transition states. Due to the constraints in the degrees of freedom the energies of the real transition states can be expected to be slightly lower than the here presented values, but in any case they will not lead to higher barriers.

For the reaction processes the energies of the initial, transition and final states will be influenced by the nearest neighbor interactions. Since the geometries of the transition states are still quite similar to the initial states, it is assumed that the energies of the transition states will be equally influenced by these interactions. Thus, the energy differences between the initial and transition states will not be affected by the nearest neighbor interactions, i.e. the reaction barriers will be constant with respect to different configurations (cf. Fig. 8.7). The energies of the final states, though, containing the desorbed CO_2 are not considered to have any influence on the transition states.

The remaining prefactor $f^{\mathrm{reac,TST}}$ is again given as the ratio of the partition functions in the transition and initial state. As already mentioned above, for the reaction processes the initial and transition states are considered as similar leading also to comparable partition functions, so that the prefactor is approximated by $f^{\mathrm{reac,TST}} \approx 1$ for both reaction processes.

Since the reaction processes are modeled as associative desorption (cf. Section 5.2.5), the corresponding time reversed process is the dissociative adsorption of CO_2 into the respective adsorption sites. The activation barrier for such a process can be obtained from the reaction barrier and the corresponding binding energies using Eq. (5.27). Since the energy of CO_2 in the gas phase is much lower than the energy of adsorbed O and CO, the activation barriers for the CO_2 adsorption are rather high. Taking even the lowest resulting barrier of $\Delta E^{\mathrm{ads}}_{\mathrm{CO_2,br-hol}} = 1.4\,\mathrm{eV}$ and a temperature of $T = 600\,\mathrm{K}$, the local sticking coefficient (cf. Eq. 5.16) would still only be of the order of 10^{-12}. Even if the CO_2 generated at the surface is not readily transported away, and a noticeable CO_2 pressure would build up, the readsorption of CO_2 will be negligible due to this very low sticking coefficient compared to the non-activated adsorption of O_2 and CO.

8.3 The Simulations

After having setup the kMC lattice and determining the different processes and their respective process rates, the simulations can be performed. This is done in two steps, starting with simulations, where only the adsorption, desorption and diffusion processes are considered, whereas the reaction processes are excluded. This reflects then the same situation as in the constrained atomistic thermodynamics approach, where likewise the formation of CO_2 was not considered. In the second step then, also the reaction events are included, hereby focusing on a change in the stability of the surface oxide structure.

8.3.1 Reproducing The Constrained Equilibrium

Within the kMC simulation it is possible to follow the evolution of the modeled system starting from some random initial state. If the simulation runs long enough, the system should eventually always reach the same so-called steady-state. For the here discussed problem the steady-state of the system is reached, if the average surface population becomes constant. If no reaction events are included in the simulation, the occupation at the surface under steady-state conditions corresponds then to a surface in a constrained thermodynamic equilibrium with an oxygen and CO gas phase, just as described by the atomistic thermodynamics approach, but including the effect of configurational entropy in the considered adsorption sites. The results obtained in the kMC simulations can therefore directly be compared to the atomistic thermodynamics results discussed in Section 7.3, which also provides a possibility to validate the chosen kMC setup. As it was discussed above, the kMC model does only represent the structure of the $(\sqrt{5} \times \sqrt{5})R27°$ surface oxide, i.e. the kMC results can only be compared to the part of the phase diagram, where the surface oxide structure is stable (red/orange-white striped phases in Fig. 7.6).

The average occupation of a site-type st by a species i is calculated as

$$\overline{\Theta}_{i,st} = \frac{\sum_k \Theta_{i,st,k} \cdot \Delta t_k}{\sum_k \Delta t_k} \quad , \tag{8.4}$$

where Δt_k is the time step of the k's Monte Carlo move (cf. Eq. (5.6)), i.e. the longer the system is in a specific state, the more this state will contribute to the average occupation. Depending on the initial configuration and the chosen temperature and pressure conditions the steady-state is reached at quite different times. Thus, to begin with the simulations are run for a fixed number of kMC steps to obtain an order of magnitude estimate of the real time interval. But also the number of kMC steps

300K						
p_{O_2}	p_{CO}	$\overline{\Theta}_{O,hol}$	$\overline{\Theta}_{CO,hol}$	$\overline{\Theta}_{O,br}$	$\overline{\Theta}_{CO,br}$	phase diagram
10^{-10}	10^{-10}	1.00	0.00	0.00	0.00	surface oxide
10^{-5}	10^{-10}	1.00	0.00	0.00	0.00	surface oxide
10^{-5}	10^{-5}	1.00	0.00	0.00	0.50	surface oxide + CO bridge
1	10^{-10}	1.00	0.00	0.00	0.00	surface oxide
1	10^{-5}	1.00	0.00	0.00	0.50	surface oxide + CO bridge
1	1	1.00	0.00	0.00	1.00	surface oxide + 2 CO bridge
10^{10}	10^{-10}	steady-state not reached				surface oxide + O bridge
10^{10}	1	steady-state not reached				surface oxide + 2 CO bridge
600K						
p_{O_2}	p_{CO}	$\overline{\Theta}_{O,hol}$	$\overline{\Theta}_{CO,hol}$	$\overline{\Theta}_{O,br}$	$\overline{\Theta}_{CO,br}$	phase diagram
1	1	1.00	0.00	0.00	0.00	surface oxide
10^3	1	1.00	0.00	0.00	0.00	surface oxide
10^3	10^3	1.00	0.00	0.00	0.50	surface oxide + CO bridge
10^6	1	1.00	0.00	0.10	0.01	surface oxide
10^6	10^3	1.00	0.00	0.00	0.50	surface oxide + CO bridge
10^6	10^6	1.00	0.00	0.00	0.99	surface oxide + 2 CO bridge
10^{10}	1	1.00	0.00	0.49	0.00	surface oxide + O bridge
10^{10}	10^6	1.00	0.00	0.00	0.99	surface oxide + 2 CO bridge

Table 8.3: Average occupation of hollow and bridge sites by oxygen and CO for various pressures at $T = 300\,\text{K}$ and $600\,\text{K}$ representing the stability range of the surface oxide structure as determined within the atomistic thermodynamics approach. In the last column the corresponding thermodynamically most stable structure is listed. All pressures are in atm.

necessary to reach the steady-state can vary significantly. Therefore, the convergence of the average surface population was checked carefully for every initial surface configuration and (T, p)-conditions, by running the simulation for different numbers of kMC steps and averaging over different time intervals.

For the simulations a (20×20) lattice containing 100 bridge and 100 hollow sites is used. Test calculations are performed also for larger lattice sizes up to a (50×100) lattice, but no noticeable differences regarding the steady-state populations were observed. The simulations are performed at two different temperature $T = 300\,\text{K}$ and $T = 600\,\text{K}$ and pressure ranges of oxygen and CO of $p_{O_2} = 10^{-10} - 10^{10}\,\text{atm}$ and $p_{CO} = 10^{-10} - 1\,\text{atm}$, respectively $p_{O_2} = 1 - 10^{10}\,\text{atm}$ and $p_{CO} = 1 - 10^{6}\,\text{atm}$ for the higher temperature, to cover the whole stability region of the surface oxide considered in the atomistic thermodynamics approach discussed before. As initial configurations a completely empty lattice, and a lattice, where all hollow sites are occupied by oxygen, are chosen. The steady-state is reached in almost all simulations, nicely reproducing the surface oxide configurations shown in the thermodynamic phase diagram (Fig. 7.6), except for very high oxygen and CO pressures at $T = 300\,\text{K}$. Under these conditions, the adsorption/desorption process of O_2 in two neighboring bridge sites is so fast, that it actually takes place on a different time scale compared to all other processes. In this part of the thermodynamic phase diagram the surface oxide having two CO adsorbed in bridge site is the most stable one, i.e. in the kMC simulation all hollow sites should be occupied by oxygen and all bridge sites by CO. Running the simulation at $T = 300\,\mathrm{K}$ the hollow sites are found to be 100 % occupied by oxygen, whereas the occupation of the bridge sites varies depending on the initial configuration due to the predominance of the O_2 adsorption/desorption processes. Even with longest simulation times it was not possible to reach the steady-state situation. At $T = 600\,\mathrm{K}$, though, and gas phase conditions representing the same oxygen and CO chemical potentials as before for $T = 300\,\mathrm{K}$, the system reaches its steady-state rather quickly, so that also this part of the phase diagram can be reproduced.

Repeating the simulations without considering any of the diffusion processes does not change any of the discussed results. Since the hollow sites are almost always completely filled by oxygen, the only relevant diffusion process is the diffusion of CO from one bridge site to a neighboring one. This does, however, not have a noticeable influence on the average surface population. Since the diffusion processes do not appear to be important and can actually be excluded from the kMC simulation, also the uncertainties in the diffusion rates due to the only approximate transition states do not have any influence on the discussed results.

It can be concluded that using the above introduced kMC model without any reaction processes the 4 different surface oxide phases appearing in the thermodynamic phase diagram are well reproduced. Depending on the temperature and pressure conditions the bridge site is either empty, 50 % occupied by O, 50 % occupied by CO or completely filled by CO, whereas the hollow site is always occupied by oxygen (cf. Tab. 8.3).

8.3.2 Onset Of Surface Oxide Decomposition Under Reaction Conditions

To evaluate the stability of the surface oxide structure under reaction conditions the two reaction processes are now also included into the kMC simulations. As already mentioned above the simulations can not be performed over the whole range of oxygen and CO gas phase conditions evaluated in the thermodynamic phase diagram, since the kMC lattice can only represent the structure of the surface oxide. Thus, a restructuring of the surface palladium atoms upon decomposition of the surface oxide to form a Pd(100) surface can not be investigated within the here described model. As a measure to determine the *onset* of the decomposition of the surface oxide structure the average occupation of the hollow sites by oxygen atoms, $\overline{\Theta}_{\mathrm{O,hol}}$, is evaluated. If the average occupation drops below 90 %, the surface oxide structure is considered as starting to destabilize. This is a rather conservative limit, but it ensures the validity of the kMC model, since up to this coverage a reconstruction of the surface is not expected. Since the average occupation is a global measure over the whole simulation cell, the situation would be different, though, if a local decomposition of the surface oxide takes place. A decrease in the average occupation of hollow sites by oxygen of 10 % could then correspond to a locally complete decomposition of 10 % of the surface oxide area requiring also a local restructuring of the palladium atoms, instead of indicating the global onset of the decomposition of the complete surface oxide layer. In the present simulations such a local decomposition has not been observed and thus the average occupation, $\overline{\Theta}_{\mathrm{O,hol}}$, appears to be suitable to determine the onset of the surface oxide decomposition.

The simulations are performed for three different temperatures, $T = 300\,\mathrm{K}$, $400\,\mathrm{K}$ and $600\,\mathrm{K}$, and a fixed oxygen pressure of $p_{\mathrm{O}_2} = 1\,\mathrm{atm}$, whereas the CO pressure is increased from 10^{-5} up to $10^{5}\,\mathrm{atm}$. Comparing to the phase diagram in Fig. 8.2 this corresponds to evaluating the stability of the surface oxide along the vertical green arrows marking gas phase conditions of constant oxygen pressure. Starting in the stability region of the surface oxide the CO pressure is increased moving upward towards the stability region of the CO covered Pd(100) surface. Similar to the results discussed in the previous Section, the average surface occupations are evaluated for the system under steady-state conditions. To ensure that the system has reached its steady-state, the simulations are again performed with different initial configurations and the average occupations are calculated over different time intervals.

In Fig. 8.8 the average occupation of hollow sites by oxygen depending on the CO pressure is shown for $T = 300\,\mathrm{K}$. The green line represents the results obtained by using the determined reaction barrier of $\Delta E^{\mathrm{reac}}_{\mathrm{Ohol+CObr}} = 0.9\,\mathrm{eV}$ and $\Delta E^{\mathrm{reac}}_{\mathrm{Obr+COhol}} = 0.5\,\mathrm{eV}$. For CO pressures of $p_{\mathrm{CO}} < 10^{-1}\,\mathrm{atm}$ the surface oxide is clearly stable. If the CO pressure is further increased, the occupation of the hollow sites by oxygen starts to slowly decrease for $p_{\mathrm{CO}} > 10^{-1}\,\mathrm{atm}$. Finally, for CO pressures of $p_{\mathrm{CO}} > 1\,\mathrm{atm}$ the surface oxide is completely destabilized and all hollow sites are then occupied by CO. At $p_{\mathrm{CO}} = 1\,\mathrm{atm}$ the average occupation could not be clearly determined, since under these temperature and pressure conditions the steady-state of the system is rather difficult to define. Due to the rather low temperature of $T = 300\,\mathrm{K}$ the reaction dynamics are much slower than the fast adsorption/desorption dynamics of the CO in bridge sites. Even for the longest simulation times different initial configurations did not converge to the same steady-state. Starting with a configuration, where all hollow sites are filled by oxygen, a reaction process occurs only rather seldom compared to the adsorption/desorption of CO in a bridge site. Nevertheless, the average occupation of the hollow sites by oxygen shows a slow but constant decay with the number of kMC steps. In the longest simulations the average occupation is already less than 90 %, reflecting that under such gas phase conditions the surface oxide clearly starts to decompose. Starting the simulations with a completely empty or randomly filled lattice the average occupation stays below 50 %. Although the exact occupation under steady-state conditions could not be evaluated under these temperature and pressure conditions, the tendency to decompose the surface oxide can already be observed.

To compare the results to the ones obtained within the atomistic thermodynamics approach, the stability region of the surface oxide as determined in the phase dia-

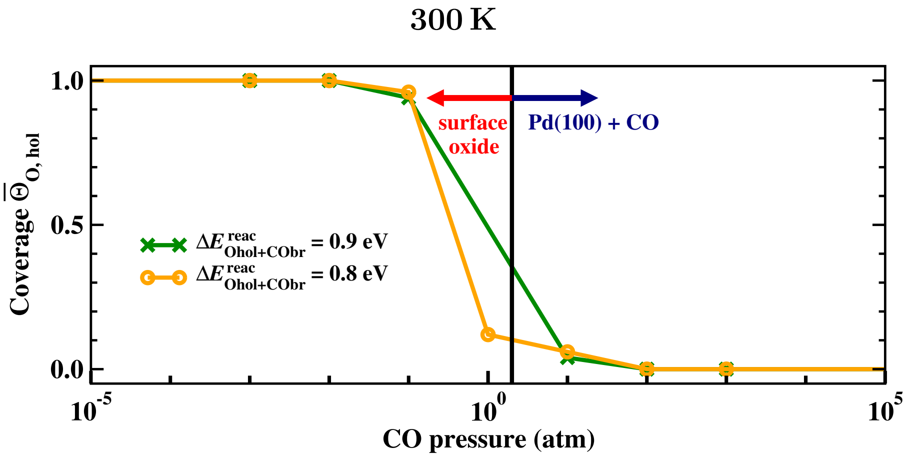

Figure 8.8: Average occupation of hollow sites by oxygen vs. CO pressure for $T = 300\,\mathrm{K}$. The vertical black line marks the boundary between the surface oxide and a CO covered Pd(100) surface as determined within the atomistic thermodynamics approach.

gram is indicated by the vertical black line in Fig. 8.8. Following the green arrow in Fig. 8.2 for $T = 300\,\mathrm{K}$ and $p_{O_2} = 1\,\mathrm{atm}$ starting at a CO pressure of $p_{CO} = 10^{-5}\,\mathrm{atm}$ up to $p_{CO} = 10^{5}\,\mathrm{atm}$ the phase boundary between the surface oxide structure and a CO covered Pd(100) surface is reached for a CO pressure of $p_{CO} \approx 30\,\mathrm{atm}$, i.e. within the atomistic thermodynamics approach the surface oxide will be stable for $p_{CO} \lesssim 30\,\mathrm{atm}$, whereas for $p_{CO} \gtrsim 30\,\mathrm{atm}$ the CO covered Pd(100) surface will be the thermodynamically most stable phase. Running the kMC simulations under these conditions including the ongoing CO_2 formation all of the hollow sites would already be occupied by CO instead of oxygen, clearly indicating that the surface oxide structure would not be stable. Looking again at Fig. 8.8 a depletion of oxygen atoms in hollow sites, and thus the destabilization of the surface oxide structure, starts at already lower CO pressures of $p_{CO} > 10^{-1}\,\mathrm{atm}$, compared to the transition from the stability region of the surface oxide to the one of a CO covered Pd(100) surface in the thermodynamic phase diagram at $p_{CO} \approx 30\,\mathrm{atm}$. This indicates that the stability region of the surface oxide structure is slightly decreased by the ongoing catalytic CO_2 formation.

Since the determined reaction barriers are somewhat approximate, the simulations are also repeated with slightly lower barriers to evaluate the influence on the average surface occupation. Lowering the barrier of the reaction process O bridge + CO hollow by 0.1 eV does not have any effect on the occupation of the different sites. If the barrier of the other reaction process O hollow + CO bridge is reduced to $\Delta E^{\mathrm{reac}}_{\mathrm{Ohol+CObr}} = 0.8\,\mathrm{eV}$, some slight changes occur, shown by the orange line in Fig. 8.8. Due to the lower reaction barrier the reaction dynamics is somewhat enhanced, i.e. the steady-state of the system can be reached faster. For a CO pressure of $p_{CO} = 1\,\mathrm{atm}$ there are now already 90 % of the hollow sites occupied by CO and only 10 % by

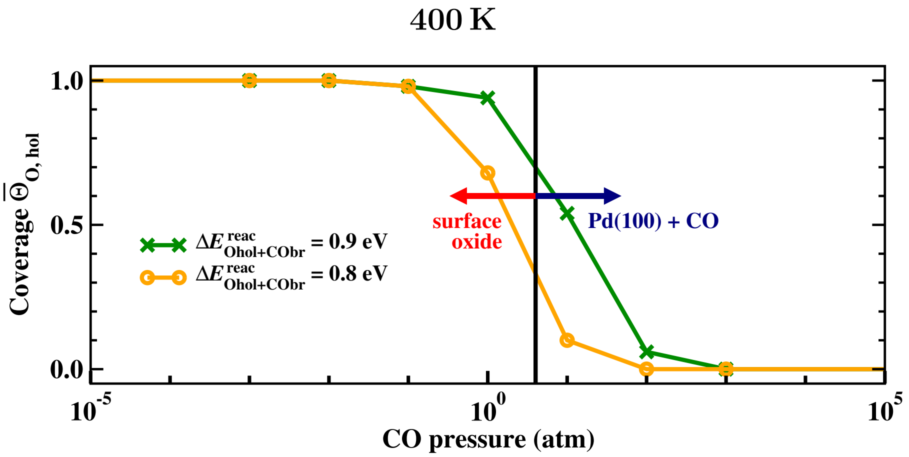

Figure 8.9: Average occupation of hollow sites by oxygen vs. CO pressure for $T = 400\,\mathrm{K}$. The vertical black line marks the boundary between the surface oxide and a CO covered Pd(100) surface as determined within the atomistic thermodynamics approach.

oxygen, but also for this lower barrier the surface oxide structure is clearly stabilized for $p_{\mathrm{CO}} < 10^{-1}\,\mathrm{atm}$.

Although the simulations are mainly dominated by the adsorption/desorption processes the consideration of the CO_2 formation at the surface leads thus to a decrease in the stability of the surface oxide compared to the constrained thermodynamic equilibrium results. Diffusion processes are again of minor importance. Simulations performed without considering any diffusion processes show equivalent results. It can be concluded, that under reaction conditions slightly oxygen rich conditions ($p_{\mathrm{O}_2}/p_{\mathrm{CO}} \approx 10$) are needed to stabilize the surface oxide structure at this temperature.

In Fig. 8.9 equivalent results to Fig. 8.8 are shown for $T = 400\,\mathrm{K}$. The green line represents the results for $\Delta E^{\mathrm{reac}}_{\mathrm{Ohol+CObr}} = 0.9\,\mathrm{eV}$, the orange one for $\Delta E^{\mathrm{reac}}_{\mathrm{Ohol+CObr}} = 0.8\,\mathrm{eV}$, the vertical black line the corresponding boundary between the surface oxide and a CO covered Pd(100) surface in the thermodynamic phase diagram (cf. Fig. 8.2). Compared to the simulations at $T = 300\,\mathrm{K}$ much more reaction processes are detected due to the higher temperature. For CO pressures of $p_{\mathrm{CO}} > 10\,\mathrm{atm}$, though, there are almost no reaction processes counted in the steady-state, since here the surface is completely, i.e. both hollow and bridge sites, covered by CO. Yet, this corresponds already to gas phase conditions, where also in a constrained thermodynamic equilibrium the CO covered Pd(100) surface appears as most stable phase (cf. Fig. 8.2). Similar to the results for $T = 300\,\mathrm{K}$ the surface oxide is completely stabilized for CO pressures of $p_{\mathrm{CO}} < 10^{-1}\,\mathrm{atm}$. For equal pressures of oxygen and CO (1 atm) and a reaction barrier of $\Delta E^{\mathrm{reac}}_{\mathrm{Ohol+CObr}} = 0.9\,\mathrm{eV}$ there are still 94 % of all hollow sites occupied by oxygen, whereas for the slightly lower barrier of 0.8 eV the occupation is decreased to 68 %. Thus, for this temperature, the stability of the surface oxide under equal pressures of O_2 and CO appears to be rather sensitive to the barrier height.

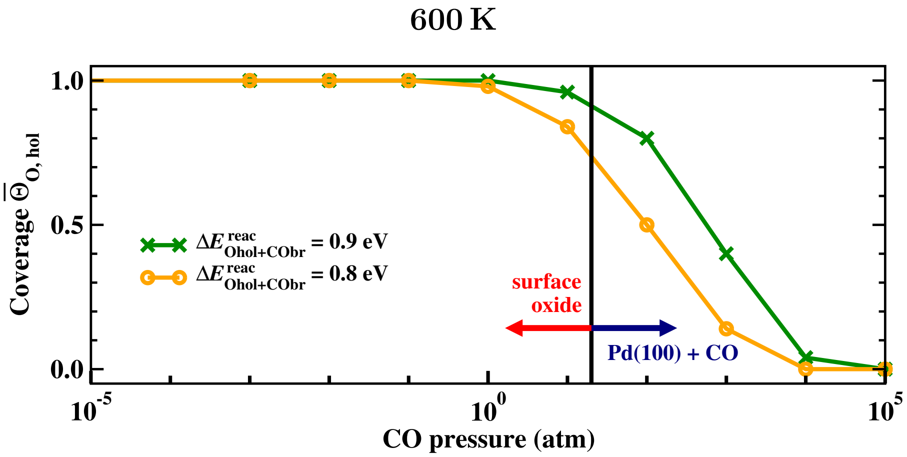

Figure 8.10: Average occupation of hollow sites by oxygen vs. CO pressure for $T = 600\,\mathrm{K}$. The vertical black line marks the boundary between the surface oxide and a CO covered Pd(100) surface as determined within the atomistic thermodynamics approach.

Simulations with an even lower barrier of $\Delta E^{\mathrm{reac}}_{\mathrm{Ohol+CObr}} = 0.7\,\mathrm{eV}$ revealed that the oxygen occupation of hollow sites decreases even further to $\sim 30\,\%$. The uncertainty in the reaction barrier due to the difficulties in finding the transition state, but also due to the choice of the exchange-correlation functional, therefore also introduces an uncertainty in the CO pressure needed to decompose the surface oxide. However, for lower CO pressures of $p_{\mathrm{CO}} < 10^{-1}\,\mathrm{atm}$, the surface oxide is equally stabilized for all three barriers and for CO pressures of $p_{\mathrm{CO}} > 10^{1}\,\mathrm{atm}$ the surface oxide structure is equally destabilized, so that the onset of the surface oxide decomposition can be expected in between CO pressures of $0.1 < p_{\mathrm{CO}} < 10\,\mathrm{atm}$. Considering the uncertainties in the reaction rates and the constraint to a single kMC lattice representing only the surface oxide structure, these results agree rather nicely with the reactor STM experiments by Hendriksen and Frenken [29], where they applied similar temperature and pressure conditions ($T = 408\,\mathrm{K}$, $p_{\mathrm{tot}} = p_{\mathrm{CO}} + p_{\mathrm{O_2}} = 1.23\,\mathrm{atm}$). Depending on the gas phase conditions Hendriksen and Frenken observed a change in the morphology of the surface together with a change in the reaction rate for the CO_2 formation, which was assigned to a change from a metallic to an oxidic phase. It was found that the oxidic phase could only be stabilized under slightly oxygen rich conditions, whereas for an excess of CO the oxidic phase is decomposed by the ongoing CO_2 formation.

The results obtained for an even higher temperature of $T = 600\,\mathrm{K}$ are shown in Fig. 8.10. For this high temperature it is observed, that the surface oxide is actually stable up to rather high CO pressures. Only for CO pressures has high as $p_{\mathrm{CO}} = 10\,\mathrm{atm}$ the decomposition of the surface oxide begins, which is already at the border of its thermodynamic stability. Looking again at the thermodynamic phase diagram in Fig. 8.2 it can be seen that for a temperature of $T = 600\,\mathrm{K}$ and an oxygen pressure of $p_{\mathrm{O_2}} = 1\,\mathrm{atm}$, CO is not stabilized as adsorbate on the surface oxide. Therefore it is also not readily available as reaction partner and the stability of the surface oxide is hardly influenced by the ongoing reaction. With increasing CO pressure eventually the CO would again be stabilized in the bridge sites, but following the thermodynamic phase diagram this is already in a (T, p)-range, where a CO covered Pd(100) surface would be stable.

8.4 Conclusions

It could be shown that the ongoing catalytic reaction of O and CO to form CO_2 does in fact have some influence on the onset of the surface oxide decomposition. At temperature of $T = 300\,\mathrm{K}$ and $400\,\mathrm{K}$ slightly oxygen-rich conditions are needed to stabilize the surface oxide, whereas in the constrained thermodynamic equilibrium the surface oxide is stable up to and CO excess of 10–30 atm. At a higher temperature of $T = 600\,\mathrm{K}$ the stability of the surface oxide is only very weakly influenced by the ongoing reaction, since under these gas phase conditions CO is not stabilized in an adsorbed state on the surface. These results suggest that under catalytically relevant gas phase conditions of elevated temperatures and ambient pressures the surface oxide structures can actually be stabilized despite the ongoing CO_2 formation and thus might also be a candidate for the catalytically active state of the Pd(100) surface.

If the surface oxide forms under catalytic reaction conditions, then also the reaction rate for the CO_2 formation can be changed compared to the clean surface. Such an effect was also observed in the reactor STM experiments by Hendriksen and Frenken [29]. In going from the smooth metallic Pd(100) surface to a rough oxidic phase a step up in the CO_2 production rate by a factor of 1.5 was observed. Returning to the metal surface led again to a decrease in the reaction rate.

Since in the thermodynamic phase diagram (cf. Fig 7.6) as well as in the kMC simulations the catalytically relevant gas phase conditions appear to be right at the boundary between a CO covered Pd(100) surface and the surface oxide the ongoing catalytic reaction could also lead to a continuous formation and decomposition of the surface oxide structure depending on the local pressure conditions. The oxidation reaction might then not only involve the metal surface or the surface oxide, but might actually induce a change back and forth between the two phases. Thus, in a next step also the transition from the surface oxide to the Pd(100) surface and vice versa would have to be considered in the modeling allowing for a complete decomposition/formation of the surface oxide structure.

Chapter 9

Summary And Outlook

New developments within material science will eventually rely on a microscopic understanding of the desired functionalities. An important field, where such a predictive modeling or rational design would be priceless, is heterogeneous catalysis. The results presented in this work aim to provide a step towards a better understanding of the processes taking place in heterogeneous oxidation catalysis from a microscopic point of view. As a model system the CO oxidation reaction on the Pd(100) surface has been investigated. Recent experimental results for this system suggest that under conditions of ambient oxygen pressures, as applied in industrial oxidation catalysis, the Pd(100) surface might actually be oxidized. The nature of the oxidic phase (a thick bulk oxide or a monolayer thin surface oxide), though, as well as the active state of the Pd(100) surface under reaction conditions (metal or oxidic phase) is still being discussed.

In the present work a multiscale modeling approach has been employed to address this topic. Density-functional theory (DFT) has been used to quantitatively describe the elementary processes occurring on electronic and atomic length and time scales (fs–ps, Å). To assure the required high accuracy in the underlying energetics the full-potential-(L)APW+lo method has been used, and all surface calculations were performed within the supercell approach. The DFT results are then combined with concepts from thermodynamics and statistical mechanics to achieve an appropriate linking to the meso-/macroscopic regime covering length scales large enough to capture the statistical interplay among the manifold of elementary processes, as well as covering times up to seconds or longer. Since the here applied methods do not rely on any empirical or fitted parameters, they are referred to as *first-principles* (or *ab initio*) methods.

In a first step within the here employed multiscale modeling hierarchy, the Pd(100) surface has been investigated in contact with a pure oxygen gas phase. The *ab initio* atomistic thermodynamics approach has been used to compare the stability of the clean metal surface, different oxygen adlayers, the $(\sqrt{5} \times \sqrt{5})R27^\circ$ surface oxide and the bulk oxide in thermodynamic equilibrium with the oxygen gas phase. Within this approach it was possible to cover the entire range of possible gas phase conditions, ranging from UHV to ambient pressures. It was found that a $c(2 \times 2)$ adlayer experimentally observed under UHV conditions does not appear as a stable phase under any temperature and pressure conditions of the oxygen gas phase. This suggests that the $c(2 \times 2)$ structure is only a meta-stable phase, which forms due to the adsorption kinetics in the UHV experiments. The $(\sqrt{5} \times \sqrt{5})R27^\circ$ surface oxide structure, on the other hand, turns out to be stable over an extended temperature and pressure range, forming a new phase aside from simple oxygen adlayers and thick bulk-like oxide films. These findings are in excellent agreement with recent surface x-ray diffraction (SXRD) measurements. It could be shown that these conclusions are not influenced by the remaining uncertainties underlying the DFT calculations (computational setup, approximate exchange-correlation functional), as well as the atomistic thermodynamics approach (approximations to the Gibbs free energy). However, the exact temperature and pressure conditions for the transition between the different phases does strongly depend on the choice of the employed exchange-correlation functional. Comparing to the SXRD measurements the accuracy of the PBE exchange-correlation functional appears to be superior to the RPBE and LDA in this respect.

Under very oxygen-rich conditions the PdO bulk oxide is eventually the most stable phase. Also experimentally the formation of PdO on Pd(100) is observed with increasing oxygen content in the gas phase, which is accompanied by a roughening of the surface, suggesting that the growth of PdO proceeds via the formation of small, three-dimensional crystallites. To obtain a first insight into the shape of these crystallites, the stability of all low-index PdO surfaces has been investigated to set up a Wulff construction representing the equilibrium shape of a single crystal. It was found that the determined shape is rather independent of the chosen exchange-correlation functional. The main limitation of this approach is the restricted configurational space sampled in this study. Surface reconstructions, which could lower the surface energy and thus influence the equilibrium shape, could not explicitly be considered at this point. However, estimates on their effects allow the conclusion that reconstructions on the (111) facet are most likely most efficient in affecting the deduced equilibrium shape. It could further be shown that the stability of the oxide surfaces is not determined by their polarity as expected from a traditional electrostatic point of view. It is rather the coordination of the surface oxygen atoms that appears to be decisive for the stability of the different surface terminations.

Increasing the complexity in the here employed hierarchical approach, the Pd(100) system has been studied in a second step in contact with a two component gas phase containing both reactants, the O_2 and the CO. The atomistic thermodynamics approach has been used to investigate the Pd(100) surface in a *constrained* thermodynamic equilibrium with an oxygen and CO gas phase. In this approach the formation of CO_2 in the gas phase and at the surface is not considered, and the effect of the surrounding gas phase on the surface structure and composition is modeled to a first approximation through the contact with independent reservoirs representing the reactants. The resulting surface phase diagram, presenting the possibly most stable structures for the entire range of possible temperature and pressure conditions of the

O_2 and CO gas phase, can be divided into three parts. In one part of the surface phase diagram simple adlayer structures of O or CO on the Pd(100) surface are stable, in a second part structures involving the reconstructed $(\sqrt{5} \times \sqrt{5})R27°$ surface oxide structure are stable, and the third part marks the stability region of thick bulk-like oxide films. It could be shown that ordered co-adsorbed layers of O and CO on the Pd(100) surface are not stable under any of the investigated temperature and pressure conditions, due to strongly repulsive interactions between the two adsorbed species. This is in good agreement with experimental results, where it was found that O and CO prefer to form separate domains on Pd(100). The additional adsorption of CO on the $(\sqrt{5} \times \sqrt{5})R27°$ surface oxide does, however, lead to stable structures. Focusing on gas phase conditions representative for technological oxidation catalysis ($T = 300 - 600\,\mathrm{K}$, $p \approx 1\,\mathrm{atm}$) it was found that within the constrained atomistic thermodynamics approach it is either the surface oxide structure or a CO covered Pd(100) surface that is stable under such conditions. The stability region of the bulk oxide, on the other hand, does not extend to these gas phase conditions. Again these conclusions are not affected by the choice of the exchange-correlation functional. Using different exchange-correlation functionals shifts the boundaries between the different phases in the phase diagram to some extent. For all three employed functionals (PBE, RPBE and LDA), though, the catalytically relevant gas phase conditions are always right at the boundary between the surface oxide structure and the CO covered Pd(100) surface, whereas the bulk oxide is not important. This suggests the monolayer thin surface oxide structure as a most relevant structure for the CO oxidation reaction on Pd(100). It has to be considered, though, that within the constrained atomistic thermodynamics approach, as it has been applied in this work, configurational entropy is not included. At finite temperatures a first effect of configurational entropy would be to smear out the phase boundaries in the phase diagram and create coexistence regions, where e.g. parts of the Pd(100) surface are covered by CO whereas other parts exhibit the reconstructed surface oxide structure. Additionally, the kinetics of the on-going catalytic CO_2 formation might significantly change the stability of the different phases as obtained in the constrained equilibrium approach.

Building on the knowledge obtained in the previous modeling steps, in a last refining step this study has therefore been focussed on the relevant (T, p)-range to investigate the stability of the surface oxide with first-principles kinetic Monte Carlo (kMC) simulations, i.e. by now explicitly including the on-going CO_2 formation. Since at present a lattice-free first-principles kMC simulation to describe the transition between structurally different phases would require some more conceptional developments and in addition would still be computationally prohibitive to perform, a suitable lattice model had to be developed. To avoid the explicit and involved modeling of the actual decomposition of the surface oxide structure, the modeling is concentrated on the onset of the decomposition process. Starting under temperature and pressure conditions, where the surface oxide is certainly the most stable phase in the thermodynamic surface phase diagram, this onset of the surface oxide decomposition under reaction conditions (i.e. including the CO_2 formation) was followed with increasing

CO content in the gas phase by evaluating the presence of surface oxygen species in the oxide lattice. Compared to the results obtained in the constrained atomistic thermodynamics approach the on-going catalytic reaction at the surface is found to slightly decrease the stability region of the surface oxide for $T = 400\,\mathrm{K}$. It could be shown, though, that for a pressure ratio of $p_{O_2}/p_{CO} \approx 10$, i.e. slightly oxygen-rich conditions, the surface oxide structure is stabilized even despite the CO_2 formation. This is in excellent agreement with recent reactor-STM experiments performed under very similar (T,p)-conditions. For a temperature of $T = 600\,\mathrm{K}$ the stability of the surface oxide is even more enhanced. Here, the simulation results predict that the surface oxide is stable even for a pressure ratio of $p_{O_2}/p_{CO} = 1$, i.e. for gas phase conditions representative of technological CO oxidation catalysis.

Employing a multiscale modeling approach it was thus possible to obtain a first insight into the structure and composition of the Pd(100) surface under reaction conditions based on a microscopic understanding. It could be shown that under temperature and pressure conditions as typically applied in industrial catalytic CO oxidation it is well possible that the $(\sqrt{5} \times \sqrt{5})R27^\circ$ surface oxide contributes to the active state of the Pd(100) surface. The results suggest furthermore that there might actually be a coexistence between patches of metallic Pd(100) covered by CO, and patches of the surface oxide (possibly also with adsorbed CO). Under steady-state conditions this could then lead to a continuous formation and decomposition of the oxidic phase. Such oscillations in the morphology of the catalyst's surface could again significantly influence the catalytic behavior of this surface. A full understanding of the catalytic function of this surface can therefore not be obtained by either concentrating on the metallic or on the oxidic phase alone.

Experimentally, this would require further developments in the field of so-called *in-situ* techniques allowing to investigate the surface under reaction conditions, and thus providing information about the catalyst in its active state. From a theoretical point of view following the results obtained in this work, the description of the transition between the metallic and oxidic phase would become necessary in a next step in order to achieve first a quantitative modeling of the possibly heterogeneous surface structure and composition in the reactive environment, and then also of the corresponding catalytic activity.

Part III

Appendix

Appendix A

Convergence Tests

All DFT results presented in this work have been obtained within the FP-(L)APW+lo method (cf. Chapter 3) as implemented in the WIEN2k code. Besides the error introduced by the only approximate exchange-correlation functional the accuracy of the results does also depend on several other computational parameters, which have to be carefully tested for every new investigated problem. Within the (L)APW+lo method the most important parameters that have to be considered are the muffin-tin radii, R_{MT}, the planewave cutoff for the expansion of the wave function in the interstitial, $E_{\mathrm{max}}^{\mathrm{wf}}$, and the **k**-point mesh for the sampling of the Brillouin zone. The remaining parameters have usually a much smaller influence on the computational time as well as on the accuracy and are therefore always set to rather conservative values.

The muffin-tin radii have to be carefully chosen at the beginning of each new project. Since the muffin-tin spheres are not allowed to overlap, the smallest possible nearest neighbor distance has to be estimated to obtain an upper limit for R_{MT}. With respect to this upper limit the muffin-tin radii should always be chosen as large as possible to minimize the interstitial region, which reduces the number of required planewaves and thus the computational cost. Since in the (L)APW+lo method the core states are only treated within the muffin-tin spheres, the muffin-tin radius has to be large enough to include the spatial extension of the core states. Thus, heavier atoms usually require a larger R_{MT} than lighter atoms. Absolute energies of the same system obtained with different muffin-tin radii are not comparable.

The planewave cutoff for the expansion of the wave function in the interstitial, $E_{\mathrm{max}}^{\mathrm{wf}}$, determines the number of basis functions. With increasing $E_{\mathrm{max}}^{\mathrm{wf}}$ the basis set can be systematically improved by an increasing number of planewaves. Since it is not possible to include an infinite number of basis functions, the expansion has to be truncated by a suitable choice of $E_{\mathrm{max}}^{\mathrm{wf}}$. The size of the required basis set depends on the aspired accuracy, as well as on the muffin-tin radii and the investigated system. Usually it is much more efficient to test the basis set with respect to the investigated physical quantity instead of the total energy of the system.

In the present work careful tests have been performed to check the convergence of the results with respect to the applied basis set and **k**-point mesh. In all test calculations only the PBE exchange-correlation functional has been used, since the convergence behavior is not expected to depend much on the choice of the exchange-correlation functional. In the following, tests regarding the PdO surfaces, the adsorption on the Pd(100) surface and the $(\sqrt{5} \times \sqrt{5})R27^\circ$ surface oxide structure, as well as the molecular binding energies of O_2, CO and CO_2 are presented. For the palladium and palladium oxide bulk systems convergence tests with respect to the different parameters have already been performed previously [115].

A.1 PdO Surfaces

To determine the required basis set and number of **k**-points the convergence of the surface energy γ as defined in Eq. (6.4) is tested, since the surface energy is needed to compare the stability of the different PdO surface terminations (cf. Chapter 6). As discussed in Ref. [115] the muffin-tin radii are set to $R_{\mathrm{MT}}^{\mathrm{O}} = 1.3\,\mathrm{bohr}$ for oxygen and $R_{\mathrm{MT}}^{\mathrm{Pd}} = 1.8\,\mathrm{bohr}$ for palladium. The same muffin-tin radii have to be used in all calculations entering the surface energy, i.e. the PdO surface slabs, the PdO bulk and the Pd bulk calculations. Also referring to Ref. [115] the wave function expansion inside the muffin-tin spheres is considered up to $l_{\mathrm{max}}^{\mathrm{wf}} = 12$ and the potential expansion up to $l_{\mathrm{max}}^{\mathrm{pot}} = 6$ and the energy cutoff for the planewave representation of the potential in the interstitial region is set to $E_{\mathrm{max}}^{\mathrm{pot}} = 196\,\mathrm{Ry}$.

Thus, the remaining parameters that need to be tested are the planewave cutoff for the expansion of the wave function in the interstitial, $E_{\mathrm{max}}^{\mathrm{wf}}$, and the number of **k**-points. Since the surface calculations are performed within the supercell approach additionally the number of layers and the vacuum thickness have to tested. The convergence behavior of the different parameters is usually independent, i.e. one parameter can be tested while setting the others to reasonable but not necessarily converged values. In all test calculations only one terminations for each low-index surface is used in the bulk truncated geometry without any relaxation.

In Fig. A.1 the dependence of the surface energy γ on the planewave cutoff $E_{\mathrm{max}}^{\mathrm{wf}}$ is illustrated for the five different low index surfaces. For the PdO(100)-PdO, PdO(101) and the PdO(110)-Pd terminations supercells containing 3 layer-thick slabs are used, for the PdO(001)-Pd and PdO(111)-Pd terminations the slabs consist of 5 layers. For all terminations the vacuum region is larger than 20 Å. The Monkhorst-Pack grids and corresponding numbers of **k**-points in the irreducible part of the Brillouin zone applied in the planewave cutoff tests for the different terminations are listed in Tab. A.1. Regarding the rather small scale of the y-axes of the different plots in Fig. A.1 it can be seen that the surface energy shows a rather fast convergence with respect to the planewave cutoff. Already at a value of $E_{\mathrm{max}}^{\mathrm{wf}} = 17\,\mathrm{Ry}$ the surface energies are converged within 3–4 $\mathrm{meV/Å^2}$ compared to the best obtained value.

The convergence of the surface energy with respect to the number of **k**-points in the irreducible part of the Brillouin zone is shown in Fig. A.2. The setup of the supercells

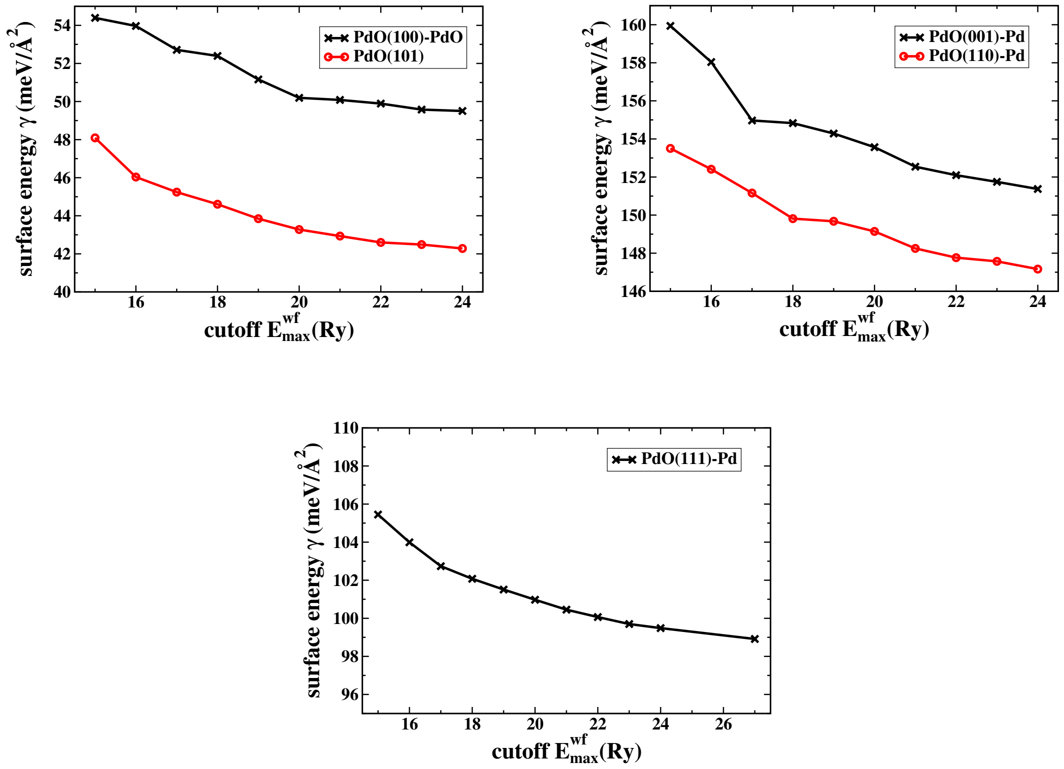

Figure A.1: Convergence of the surface energy γ with respect to the cutoff of the planewave representation of the wave function in the interstitial region, $E_{\rm max}^{\rm wf}$ for the five low-index PdO surface orientations.

PdO surface	MP grid	no. of irred. **k**-points
(100) ≡ (010)	[4×7×1]	12
(001)	[7×7×1]	16
(101) ≡ (011)	[1×3×7]	8
(110)	[4×3×1]	6
(111)	[3×5×1]	8

Table A.1: Employed Monkhorst-Pack grids during the planewave cutoff tests and corresponding number of **k**-points in the irreducible part of the Brillouin zone for the different (1 × 1) surface unit cells of the low-index PdO surfaces

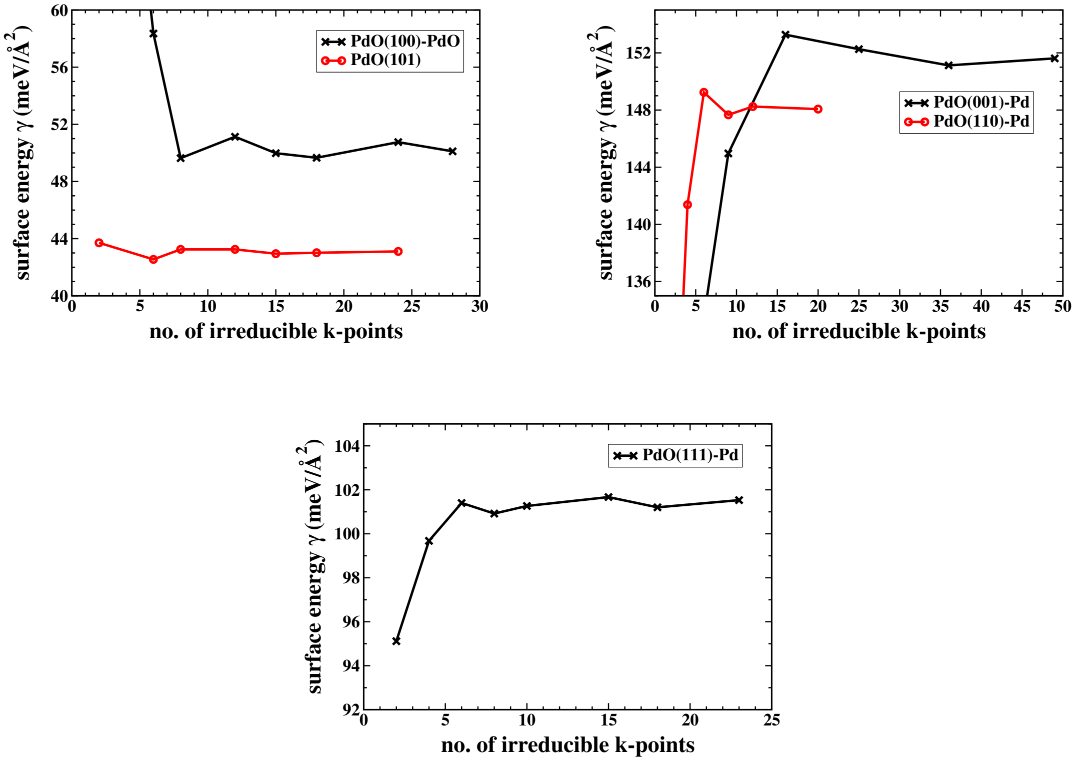

Figure A.2: Convergence of the surface energy γ with respect to the number of **k**-points in the irreducible part of the Brillouin zone for the five low-index PdO surface orientations.

is equivalent to the one used in the previous test, the planewave cutoff is set to $E^{\rm wf}_{\rm max} = 20\,{\rm Ry}$ (since the different test calculations were performed simultaneously, this rather high value for $E^{\rm wf}_{\rm max}$ was chosen; considering the results of the planewave cutoff test a value of $E^{\rm wf}_{\rm max} = 17\,{\rm Ry}$ would have been sufficient). In contrast to the very similar convergence behavior of all five terminations with respect to the planewave cutoff the convergence with respect to the number of **k**-points is not comparable for the different terminations. These differences originate from the different symmetry of the supercells representing the five terminations and the resulting different sampling of the Brillouin zone. Nevertheless it can be seen that with increasing density of the **k**-point grids the surface energy converges nicely for each of the five terminations. For the MP-grids listed in Tab. A.2 all surface energies are converged within 1–2 meV/Å^2 compared to the best obtained value.

Using the optimum number of **k**-points listed Tab. A.2 and a planewave cutoff of $E^{\rm wf}_{\rm max} = 20\,{\rm Ry}$ the number of layers within a slab that is needed to decouple the bottom and top surfaces of the slab is tested. The results are illustrated in Fig. A.3. For all surface terminations a clear convergence of the surface energy with an increasing number of layers in the slab can be observed. For the PdO(100)-PdO termination a minimum number of 7 layers per slab is chosen, for the PdO(001)-Pd, PdO(101)

PdO surface	MP grid	no. of irred. **k**-points
(100) ≡ (010)	[3×7×1]	8
(001)	[7×7×1]	16
(101) ≡ (011)	[1×3×7]	8
(110)	[4×3×1]	6
(111)	[2×4×1]	6

Table A.2: Optimal Monkhorst-Pack grids and corresponding number of **k**-points in the irreducible part of the Brillouin zone for the different (1×1) surface unit cells of the low-index PdO surfaces. Applying these MP-grids the respective surface energies are converged within 1–2 meV/Å^2.

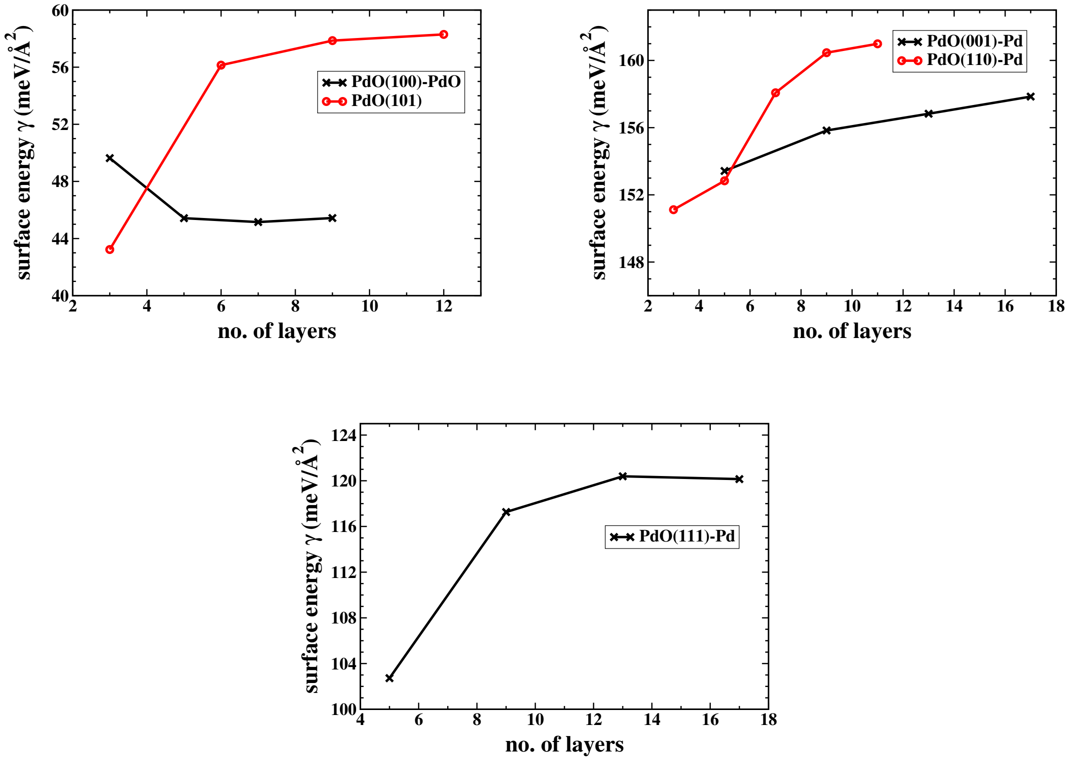

Figure A.3: Convergence of the surface energy γ with respect to the number of layers within the slab representing the five low-index PdO surface terminations.

and PdO(111)-Pd terminations at least 9 layers are used and for the PdO(110)-Pd termination the slab-thickness is set to 11 layers to achieve a convergence in the surface energy of $\approx 3\,\mathrm{meV/Å^2}$.

Since the z-length of the supercell is kept constant the vacuum will decrease with an increasing number of layers. For the largest number of layers the vacuum is still $\geq$ 12Å. Doubling the vacuum to ~ 25 Å leads to a change in the surface energy of $\leq 1\,\mathrm{meV/Å^2}$ for any of the investigated terminations. Thus, a minimum value for the vacuum of 12 Å appears to be sufficient.

The presented results of the surface energies for the different PdO low-index surface terminations can therefore be considered as well converged with respect to the here discussed computational setup.

A.2 Adsorption On Pd(100) And $(\sqrt{5} \times \sqrt{5})R27°$

Similar to the tests described in the previous Section again the size of the basis set, the number of **k**-points, as well as the setup of the supercell have to be considered. Yet, instead of comparing the surface energy, here the binding energy, $\Delta\widetilde{E}^{\mathrm{bind}}_{\mathrm{O,CO@Pd}}$, as defined in Eq. (7.3) is converged with respect to these parameters, since the binding energy $\Delta\widetilde{E}^{\mathrm{bind}}_{\mathrm{O,CO@Pd}}$ is the decisive quantity in comparing the stability of the different phase within the surface phase diagram.

Since the bond length in the CO molecule is only ~ 2.15 bohr the muffin-tin radius of the oxygen has to be slightly decreased compared to the PdO surface calculations and thus the muffin-tin radius of the palladium is slightly increased, yielding $R^{\mathrm{O}}_{\mathrm{MT}} = 1.0$ bohr, $R^{\mathrm{Pd}}_{\mathrm{MT}} = 2.0$ bohr and $R^{\mathrm{C}}_{\mathrm{MT}} = 1.0$ bohr.

Previous work by M. Todorova [144] already provided careful tests regarding the convergence of the binding energies on the Pd(100) surface as well as on the $(\sqrt{5} \times \sqrt{5})R27°$ surface oxide with respect to the employed Monkhorst-Pack **k**-point grids. In the present work these results have been used and led to a choice of $[10\times10\times1]$ MP-grid (6 **k**-points in the irreducible part of the BZ) for the (1×1)-Pd(100) surface unit cell and respectively smaller MP-grids for the (2×2), $(2\sqrt{2}\times\sqrt{2})R45°$, $(3\sqrt{2}\times\sqrt{2})R45°$ and $(4\sqrt{2}\times\sqrt{2})R45°$ surface unit cells. For the $(\sqrt{5}\times\sqrt{5})R27°$ surface oxide structure a $[4 \times 4 \times 1]$ MP-grid is used.

Similarly the number of layers per slab in the setup of the supercell representing the Pd(100) surface is adopted from Ref. [144]. Thus all calculations concerning the Pd(100) surface are performed using 5 layer slabs and a vacuum of at least 13 Å. For the $(\sqrt{5} \times \sqrt{5})R27°$ surface oxide structure the average binding energy per oxygen atom is shown in Tab. A.3 for slabs containing 3, 5 and 7 Pd(100) layers in between the upper and lower surface oxide trilayer. It can be clearly seen that the average binding energy hardly changes in going from 3 to 5 to 7 Pd(100) layers separating the surface oxide trilayers. All initial calculations involving the $(\sqrt{5} \times \sqrt{5})R27°$ surface oxide are thus performed using 3 Pd(100) layers, only the final structures entering the surface phase diagram (cf. Chapter 7) and the lattice gas Hamiltonian (cf. Appendix C) have

	$\widetilde{E}^{\text{bind}}_{\text{O@Pd(100)}}$
$(\sqrt{5} \times \sqrt{5})R27°$–3 Pd layer	-1.195
$(\sqrt{5} \times \sqrt{5})R27°$–5 Pd layer	-1.201
$(\sqrt{5} \times \sqrt{5})R27°$–7 Pd layer	-1.203

Table A.3: Average binding energy per oxygen atom in the $(\sqrt{5} \times \sqrt{5})R27°$ surface oxide structure for slabs containing 3, 5 and 7 Pd(100) layers in between the upper and lower surface oxide trilayer. All values are in eV.

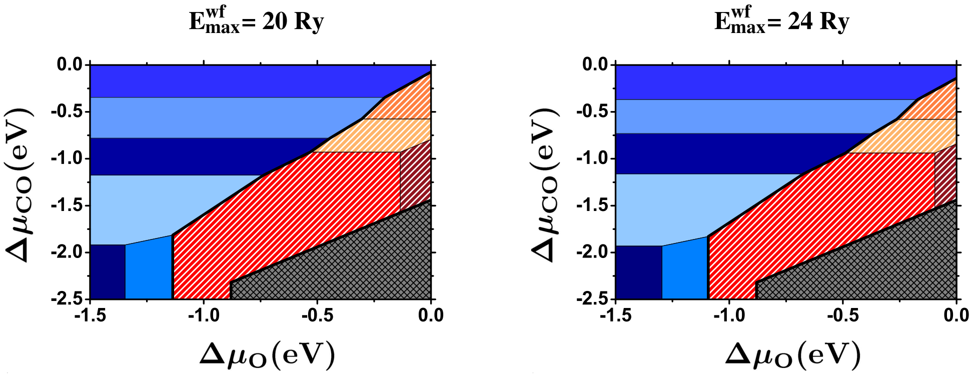
$E^{\text{wf}}_{\text{max}}$= 20 Ry

$E^{\text{wf}}_{\text{max}}$= 24 Ry

Figure A.4: Surface phase diagram for the Pd(100) surface in a constrained equilibrium with an O_2 and CO gas phase calculated using PBE exchange correlation functional. The left figure shows the results for a planewave cutoff of $E^{\text{wf}}_{\text{max}} = 20\,\text{Ry}$, the right figure for $E^{\text{wf}}_{\text{max}} = 24\,\text{Ry}$.

also been calculated using 5 Pd(100) layers in between the surface oxide trilayers.

Since in the previous work by Todorova [144] different muffin-tin radii have been used and instead of the here applied (L)APW+lo method the LAPW method has been used the results for the convergence of the binding energies with respect to the cutoff for the planewave representation of the wave function in the interstitial, $E^{\text{wf}}_{\text{max}}$, are not directly transferable. On the one hand, in the present work the smallest muffin-tin radius, which is the one for the oxygen, is smaller, so that an increase in the planewave cutoff would be expected. On the other hand, it could be shown that the (L)APW+lo method converges faster than the LAPW method [58] and thus a smaller planewave cutoff would be sufficient. Based on these considerations an initial planewave cutoff of $E^{\text{wf}}_{\text{max}} = 20\,\text{Ry}$ is chosen. Increasing the planewave cutoff up to $E^{\text{wf}}_{\text{max}} = 24\,\text{Ry}$ leads to a change in the binding energies of $\lesssim 50\,\text{meV}$ per oxygen atom resp. CO molecule. If comparing the binding energies of different structures, as it is done in the surface phase diagram, the change in the relative binding energies is even smaller. This can also directly be seen in Fig. A.4, where the surface phase diagram as discussed in Chapter 7 is shown for a planewave cutoff of $E^{\text{wf}}_{\text{max}} = 20\,\text{Ry}$ and 24 Ry. Only very small shifts in the phase boundaries can be observed. It is thus concluded that a planewave cutoff of $E^{\mathrm{wf}}_{\mathrm{max}} = 20\,\mathrm{Ry}$ is sufficient for the problems discussed in the present work.

A.3 Molecular Binding Energies

In the present work the binding energies of three different molecules, O_2, CO and CO_2 are needed. Within periodic boundary conditions the molecules as well as the respective atoms have to be calculated in a 3-dimensional box surrounded by enough vacuum to avoid interactions between the periodic images. Since the atomic and molecular states do not have any dispersion a sampling of the Γ-point only is sufficient. This leaves as the most important parameters the muffin-tin radii R_{MT} and the planewave cutoff for the representation of the wave function in the interstitial, $E^{\mathrm{wf}}_{\mathrm{max}}$. The remaining parameters are equivalent to the ones discussed in Section A.1. In the following the convergence of the binding energies of the three molecules with respect to $E^{\mathrm{wf}}_{\mathrm{max}}$ will be discussed.

Oxygen

In addition to determining ΔE^{mol} (cf. Eq. (7.5)) the binding energy of the O_2 molecule is needed to calculate the total energy of O_2 for any arbitrary muffin-tin radius. Since total energies converge differently for different muffin-tin radii with respect to the chosen basis set, the total energies of a system calculated using different muffin-tin radii are only comparable, if all basis set parameters are fully converged. To calculate a binding energy as the difference of total energies it is thus much more convenient to use the same muffin-tin radii for each subsystem to obtain a much faster convergence. Also the binding energy of an oxygen atom on a surface with respect to an O_2 molecule in the gas phase can therefore be determined with a much smaller basis set, if the same muffin-tin radius is used for the oxygen in both system. Due to the bond length in the O_2 molecule the best muffin-tin radius is $R^{\mathrm{O}}_{\mathrm{MT}} = 1.1\,\mathrm{bohr}$. Smaller muffin-tin radii would require a higher $E^{\mathrm{wf}}_{\mathrm{max}}$, whereas large muffin-tin radii are simply not possible due to overlapping spheres. This restriction might impose rather unfavorable choices for the oxygen muffin-tin radius in other systems. To circumvent this problem the total energy of the oxygen molecule is expressed as

$$E^{\mathrm{tot}}_{\mathrm{O}_2} = 2E^{\mathrm{tot}}_{\mathrm{O}} + E^{\mathrm{bind}}_{\mathrm{O}_2} \quad . \tag{A.1}$$

The oxygen atom can then be calculated for any given value of $R^{\mathrm{O}}_{\mathrm{MT}}$ and together with the O_2 binding energy the total energy of the O_2 molecule can be determined.

To obtain the binding energy of the O_2 molecule the calculations are performed spin-polarized in a $(13 \times 14 \times 18)$ bohr supercell for the molecule, resp. a $(13 \times 14 \times 15)$ bohr supercell for the atom. The supercells are setup asymmetric to provide a proper occupation of the orbitals, i.e. in the case of an oxygen atom there are 4 valence electrons distributed in 3 p-orbitals, 3 electron spin up and one electron spin down.

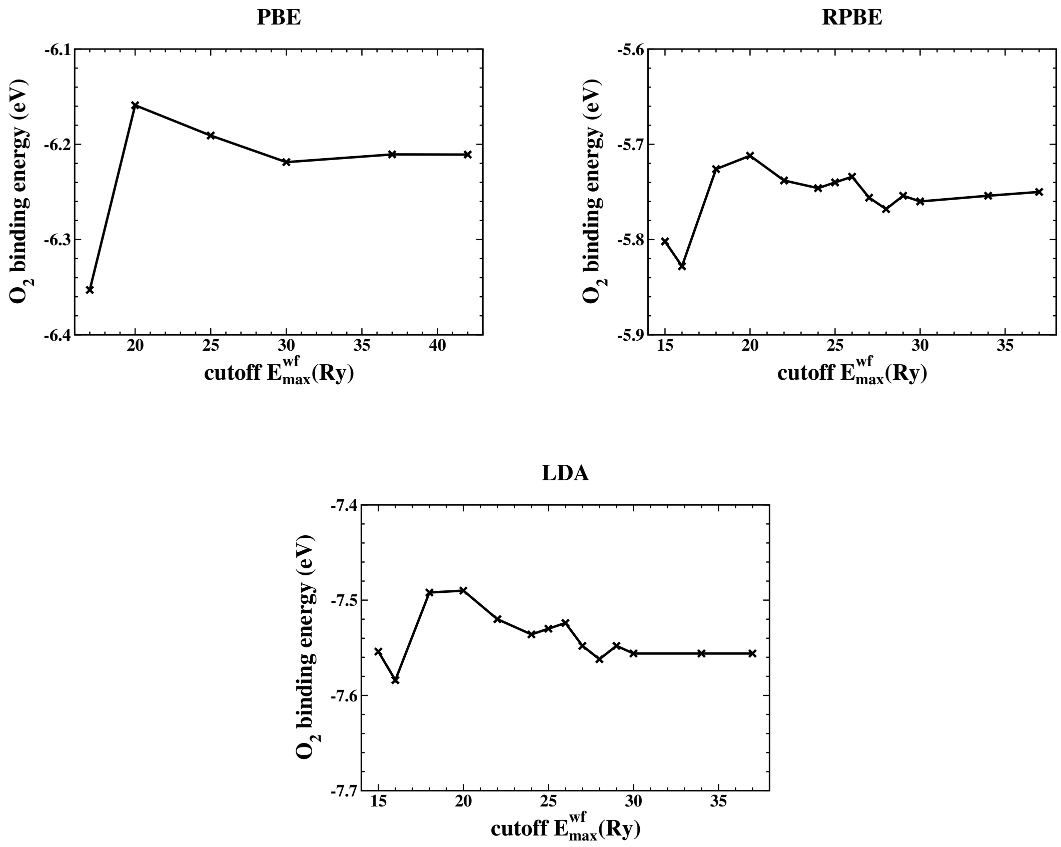

Figure A.5: Convergence of oxygen binding energy with respect to the cutoff of the planewave representation of the wave function in the interstitial for the PBE, RPBE and LDA exchange-correlation functional.

	$E^{\mathrm{bind}}_{\mathrm{O}_2}$	$d_{\mathrm{O-O}}$
PBE	-6.20	2.301
RPBE	-5.75	2.303
LDA	-7.56	2.281
Exp. [11]	-5.17	2.282

Table A.4: Binding energies and bond lengths of the O_2 molecule calculated using the PBE, RPBE and LDA as exchange-correlation functional and a planewave cutoff of $E^{\mathrm{wf}}_{\mathrm{max}} = 37\,\mathrm{Ry}$. The binding energies are given in eV, the bond lengths in bohr.

In a symmetric supercell the 3 p-orbitals would be degenerate and thus every p-orbital would be occupied with one electron spin up and 1/3 electron spin down.

In Fig. A.5 the convergence of the O_2 binding energy with respect to the planewave cutoff $E^{\mathrm{wf}}_{\mathrm{max}}$ is shown for all three exchange-correlation functionals, PBE, RPBE and LDA. By comparing the RPBE and LDA results it can be nicely observed that the

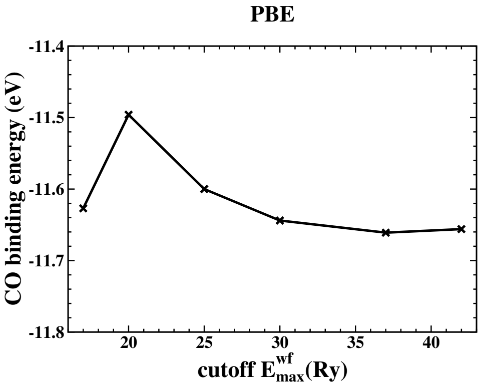

Figure A.6: Convergence of CO binding energy with respect to the cutoff of the planewave representation of the wave function in the interstitial for the PBE exchange-correlation functional

	E_{CO}^{bind}	d_{C-O}
PBE	-11.65	2.151
RPBE	-11.20	2.158
LDA	-12.93	2.133
Exp. [11]	-11.16	2.132

Table A.5: Binding energies and bond lengths for the CO molecule calculated using the PBE, RPBE and LDA as exchange-correlation functional and a planewave cutoff of $E_{max}^{wf} = 37\,\text{Ry}$. The binding energies are given in eV, the bond lengths in bohr.

convergence behavior is almost equivalent for the different exchange-correlation functionals. The same is also true for the PBE, which is not as obvious in Fig. A.5, since a different number of points has been calculated. For a planewave cutoff of $E_{max}^{wf} > 30\,\text{Ry}$ the binding energies are almost constant for all three functionals.

For the best planewave cutoff of $E_{max}^{wf} = 37\,\text{Ry}$ additionally the bond length of the O_2 molecule has been fully relaxed for each exchange-correlation functional. The binding energies and corresponding bond lengths are listed in Tab. A.4.

Carbon Monoxide

The CO molecule as well as the C and O atoms have been calculated in a $(13 \times 14 \times 15)$ bohr supercell using muffin-tin radii of $R_{MT}^{O} = R_{MT}^{C} = 1.0\,\text{bohr}$. The remaining parameters are equivalent to the ones previously described for the O_2 molecule, except that the CO molecule does not have to be treated spin-polarized. The convergence behavior of the binding energy with respect to the planewave cutoff, E_{max}^{wf}, is shown in Fig. A.6 for the PBE exchange-correlation functional. Again the convergence behavior for the different exchange-correlation functionals is expected to be similar. To obtain highly converged results a planewave cutoff of $E_{max}^{wf} = 37\,\text{Ry}$ is chosen for all

	$E_{\mathrm{CO_2}}^{\mathrm{bind}}$	$d_{\mathrm{C-O}}$
PBE	-17.99	2.218
RPBE	-17.09	2.226
LDA	-20.43	2.202
Exp. [11]	-16.68	2.192

Table A.6: Binding energies and bond lengths for the CO_2 molecule calculated using the PBE, RPBE and LDA as exchange-correlation functional and a planewave cutoff of $E_{\mathrm{max}}^{\mathrm{wf}} = 37\,\mathrm{Ry}$. The binding energies are given in eV, the bond lengths in bohr.

three functionals to calculate the binding energies and relaxed bond lengths listed in Tab. A.5.

Carbon Dioxide

To determine the binding energy of the CO_2 molecule muffin-tin radii of $R_{\mathrm{MT}}^{\mathrm{O}} = R_{\mathrm{MT}}^{\mathrm{C}} = 1.1\,\mathrm{bohr}$ are used. The CO_2 molecule is treated non-spin-polarized in a $(13 \times 14 \times 20)$ bohr supercell, the O and C atom spin-polarized in $(13 \times 14 \times 15)$ bohr supercells. The remaining parameters are equivalent to the ones previously described for the O_2 molecule. Since the convergence behavior of the binding energy with respect to the planewave cutoff is expected to be similar to the previously discussed O_2 and CO molecules the calculations have only been performed for a planewave cutoff of $E_{\mathrm{max}}^{\mathrm{wf}} = 20\,\mathrm{Ry}$ and $37\,\mathrm{Ry}$. Increasing the planewave cutoff from $20\,\mathrm{Ry}$ to $37\,\mathrm{Ry}$ the change in the binding energies is already $\lesssim 0.1\,\mathrm{eV}$ for all three functionals. The binding energies and respective bond lengths for $E_{\mathrm{max}}^{\mathrm{wf}} = 37\,\mathrm{Ry}$ are listed in Tab. A.6.

Appendix B

Adsorption Structures Involving The $(\sqrt{5} \times \sqrt{5})R27^\circ$

B.1 O And CO In A $(\sqrt{5} \times \sqrt{5})R27^\circ$ Surface Unit Cell

To setup the phase diagram of the Pd(100) surface in a constrained equilibrium with an oxygen and CO gas phase (cf. Chapter 7) a large number of possible configurations of O and/or CO adsorbed in the different high symmetry sites on the Pd(100) surface and on the $(\sqrt{5} \times \sqrt{5})R27^\circ$ surface oxide structure have been calculated. In the following all considered configurations involving the surface oxide structure are listed. As explained in Chapter 7 only the most stable structures, which minimize the Gibbs free energy of adsorption, ΔG^{ads}, for a given chemical potential of oxygen and CO, appear in the 2D-surface phase diagram as shown in Fig. 7.6 and Fig. 7.7. Since configurations having the same number of oxygen atoms (N_{O}) and CO molecules (N_{CO}) will have the same dependence on the oxygen and CO chemical potentials, only the one having the lowest binding energy, $\Delta \widetilde{E}^{\text{bind}}_{\text{O,CO@Pd}}$, as defined in Eq. 7.3 will appear as stable structure in the surface phase diagram. The presented configurations are thus grouped into structures having an equivalent oxygen and CO coverage and all energies, $\Delta E'_{N_{\text{O}},N_{\text{CO}}}$, are given with respect to the binding energy of the most favorable structure for each specific coverage, which is marked by a frame. All energies have been calculated using the PBE exchange-correlation functional and a computational setup as described on Page 66. The '$\gtrsim$' sign indicates that the structure has been calculated using a slab with only 3 palladium layers to separate the upper and lower surface oxide trilayer instead of the otherwise used 5 palladium layers. Unstable structures are marked by a '$-$' sign.

The different configurations are represented by schematic illustrations, where large grey spheres indicate palladium atoms in the reconstructed surface oxide layer, small red ones oxygen atoms and small yellow ones CO molecules. Additionally, in all figures the $(\sqrt{5} \times \sqrt{5})R27^\circ$ surface unit cell is shown.

4 O and 1 CO

Structure 001

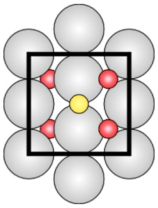

$\Delta E'_{4,1} = 0.00\,\mathrm{eV}$

Structure 002

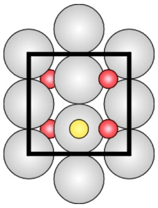

$\Delta E'_{4,1} = 0.31\,\mathrm{eV}$

Structure 003

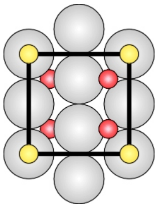

$\Delta E'_{4,1} = 0.81\,\mathrm{eV}$

Structure 004

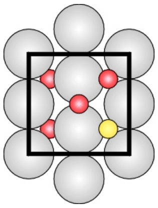

$\Delta E'_{4,1} = 1.13\,\mathrm{eV}$

Structure 005

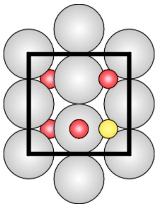

$\Delta E'_{4,1} = -$

Structure 006

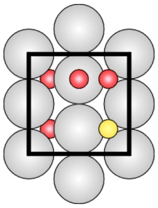

$\Delta E'_{4,1} = -$

Structure 007

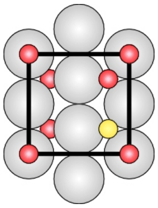

$\Delta E'_{4,1} = -$

Structure 008

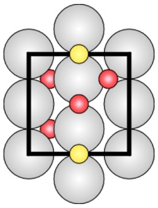

$\Delta E'_{4,1} = 1.36\,\mathrm{eV}$

Structure 009

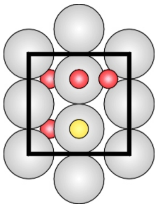

$\Delta E'_{4,1} \gtrsim 2.81\,\mathrm{eV}$

Structure 010

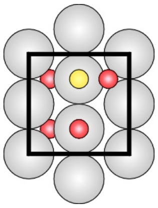

$\Delta E'_{4,1} = -$

Structure 011

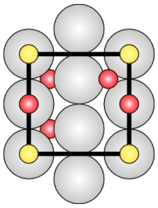

$\Delta E'_{4,1} = -$

Structure 012

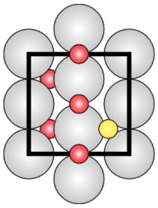

$\Delta E'_{4,1} = 2.65\,\mathrm{eV}$

Structure 013

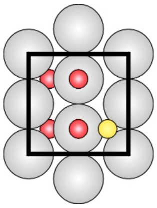

$\Delta E'_{4,1} = -$

Structure 014

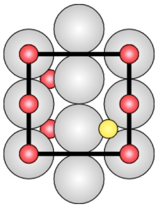

$\Delta E'_{4,1} = -$

4 O and 2 CO

Structure 015

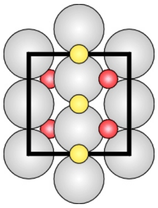

$\Delta E'_{4,2} = 0.00\,\mathrm{eV}$

Structure 016

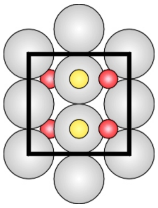

$\Delta E'_{4,2} = 0.48\,\mathrm{eV}$

Structure 017

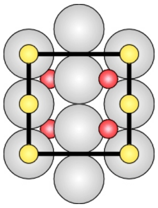

$\Delta E'_{4,2} = -$

Structure 018

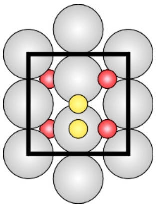

$\Delta E'_{4,2} = -$

Structure 019

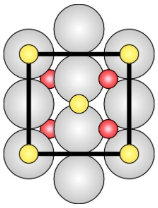

$\Delta E'_{4,2} \gtrsim 0.60\,\mathrm{eV}$

Structure 020

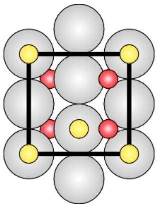

$\Delta E'_{4,2} \gtrsim 0.91\,\mathrm{eV}$

Structure 021

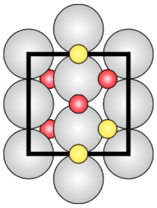

$\Delta E'_{4,2} = 0.93\,\mathrm{eV}$

Structure 022

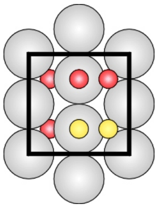

$\Delta E'_{4,2} \gtrsim 2.68\,\mathrm{eV}$

Structure 023

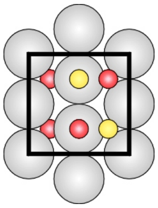

$\Delta E'_{4,2} = -$

Structure 024

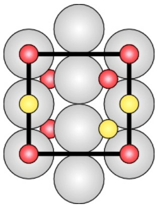

$\Delta E'_{4,2} = -$

Structure 025

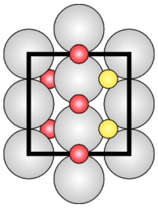

$\Delta E'_{4,2} = 2.27\,\mathrm{eV}$

Structure 026

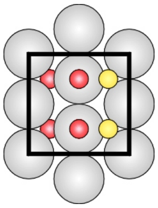

$\Delta E'_{4,2} = -$

Structure 027

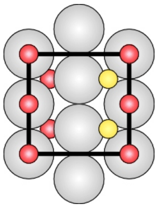

$\Delta E'_{4,2} = -$

3 O and 1 CO

Structure 028

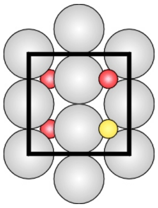

$\Delta E'_{3,1} = 0.00\,\mathrm{eV}$

Structure 029

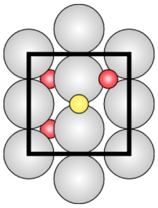

$\Delta E'_{3,1} = 0.20\,\mathrm{eV}$

Structure 030

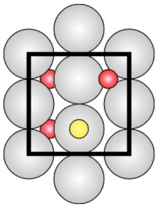

$\Delta E'_{3,1} \gtrsim 0.07\,\mathrm{eV}$

Structure 031

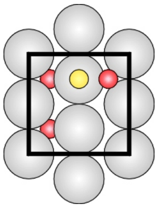

$\Delta E'_{3,1} \gtrsim 0.83\,\mathrm{eV}$

Structure 032

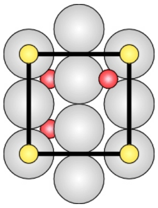

$\Delta E'_{3,1} \gtrsim 0.86\,\mathrm{eV}$

Structure 033

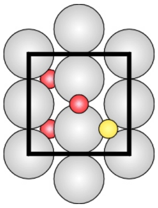

$\Delta E'_{3,1} = -$

Structure 034

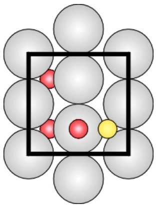

$\Delta E'_{3,1} \gtrsim 2.64\,\mathrm{eV}$

Structure 035

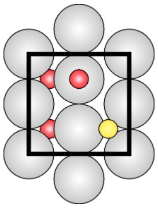

$\Delta E'_{3,1} = -$

Structure 036

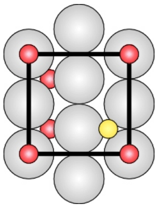

$\Delta E'_{3,1} = -$

Structure 037

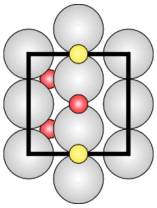

$\Delta E'_{3,1} = -$

Structure 038

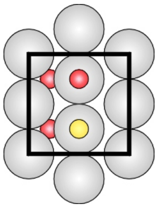

$\Delta E'_{3,1} = -$

Structure 039

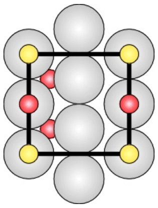

$\Delta E'_{3,1} = -$

3 O and 2 CO

Structure 040

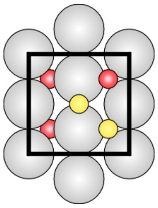

$\Delta E'_{3,2} = 0.00\,\mathrm{eV}$

Structure 041

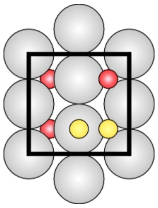

$\Delta E'_{3,2} \gtrsim 0.35\,\mathrm{eV}$

Structure 042

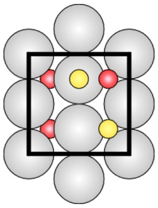

$\Delta E'_{3,2} \gtrsim 0.21\,\mathrm{eV}$

Structure 043

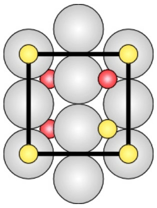

$\Delta E'_{3,2} \gtrsim 0.98\,\mathrm{eV}$

Structure 044

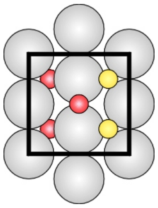

$\Delta E'_{3,2} = 0.95\,\mathrm{eV}$

Structure 045

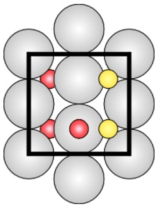

$\Delta E'_{3,2} \gtrsim 2.24\,\mathrm{eV}$

Structure 046

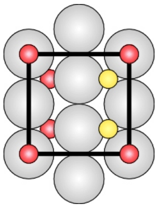

$\Delta E'_{3,2} = -$

Structure 047

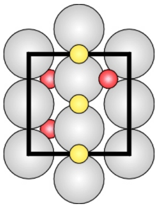

$\Delta E'_{3,2} = 0.32\,\mathrm{eV}$

Structure 048

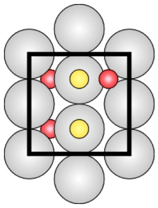

$\Delta E'_{3,2} \gtrsim 0.43\,\mathrm{eV}$

Structure 049

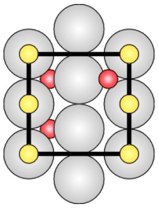

$\Delta E'_{3,2} \gtrsim 1.73\,\mathrm{eV}$

Structure 050

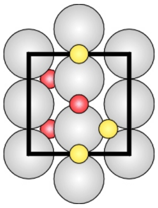

$\Delta E'_{3,2} = 1.27\,\mathrm{eV}$

Structure 051

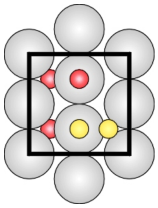

$\Delta E'_{3,2} = -$

Structure 052

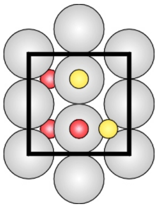

$\Delta E'_{3,2} \gtrsim 2.41\,\mathrm{eV}$

Structure 053

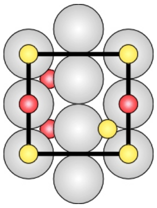

$\Delta E'_{3,2} = -$

3 O and 3 CO

Structure 054

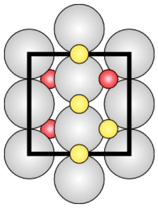

$\Delta E'_{3,3} = 0.00\,\mathrm{eV}$

Structure 055

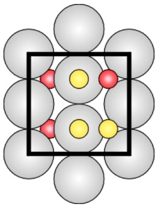

$\Delta E'_{3,3} \gtrsim 0.46\,\mathrm{eV}$

Structure 056

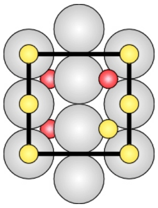

$\Delta E'_{3,3} = -$

Structure 057

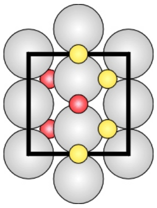

$\Delta E'_{3,3} \gtrsim 0.93\,\mathrm{eV}$

Structure 058

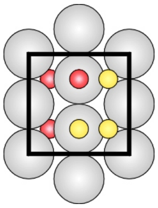

$\Delta E'_{3,3} = -$

Structure 059

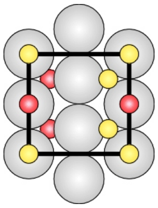

$\Delta E'_{3,3} = -$

2 O and 1 CO

Structure 060

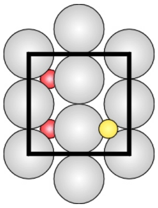

$\Delta E'_{2,1} = 0.00\,\mathrm{eV}$

Structure 061

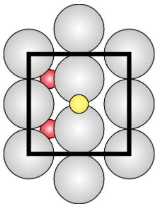

$\Delta E'_{2,1} = 0.03\,\mathrm{eV}$

Structure 062

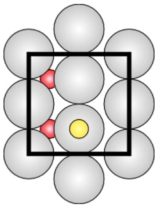

$\Delta E'_{2,1} \gtrsim 0.52\,\mathrm{eV}$

Structure 063

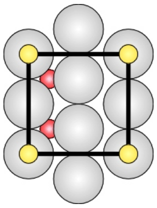

$\Delta E'_{2,1} = -$

2 O and 2 CO

Structure 064

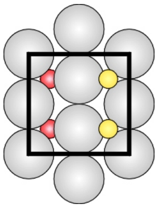

$\Delta E'_{2,2} = 0.00\,\mathrm{eV}$

Structure 065

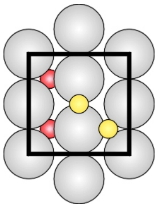

$\Delta E'_{2,2} = 0.21\,\mathrm{eV}$

Structure 066

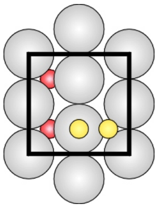

$\Delta E'_{2,2} \gtrsim 0.77\,\mathrm{eV}$

Structure 067

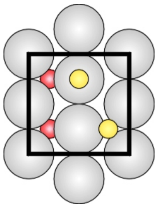

$\Delta E'_{2,2} \gtrsim 0.31\,\mathrm{eV}$

Structure 068

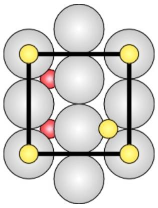

$\Delta E'_{2,2} = -$

Structure 069

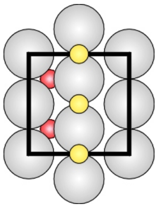

$\Delta E'_{2,2} = 0.05\,\mathrm{eV}$

Structure 070

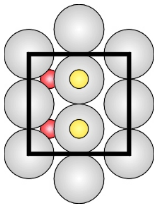

$\Delta E'_{2,2} \gtrsim 0.74\,\mathrm{eV}$

Structure 071

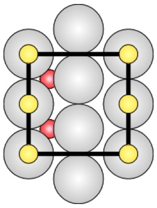

$\Delta E'_{2,2} \gtrsim 1.28$

2 O and 3 CO

Structure 072

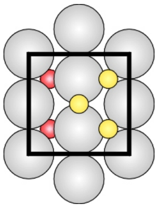

$\Delta E'_{2,3} = 0.00\,\mathrm{eV}$

Structure 073

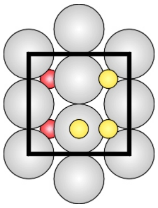

$\Delta E'_{2,3} \gtrsim 0.03\,\mathrm{eV}$

Structure 074

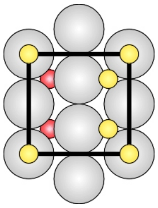

$\Delta E'_{2,3} = -$

Structure 075

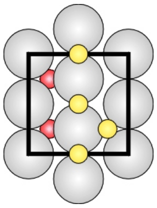

$\Delta E'_{2,3} = 0.18\,\mathrm{eV}$

Structure 076

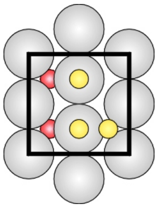

$\Delta E'_{2,3} \gtrsim 0.45\,\mathrm{eV}$

Structure 077

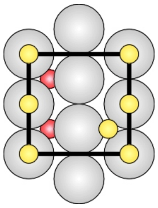

$\Delta E'_{2,3} \gtrsim 1.57\,\mathrm{eV}$

2 O and 4 CO

Structure 078

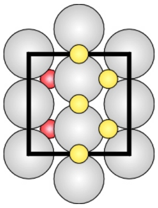

$\Delta E'_{2,4} = 0.00\,\mathrm{eV}$

Structure 079

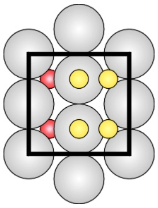

$\Delta E'_{2,4} \gtrsim 0.29\,\mathrm{eV}$

Structure 080

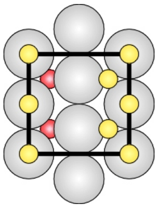

$\Delta E'_{2,4} \gtrsim 0.31\,\mathrm{eV}$

5 O and 1 CO

Structure 081

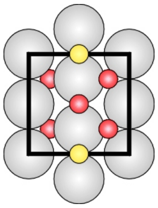

$\Delta E'_{5,1} = 0.00\,\mathrm{eV}$

Structure 082

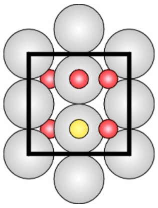

$\Delta E'_{5,1} \gtrsim 1.37\,\mathrm{eV}$

Structure 083

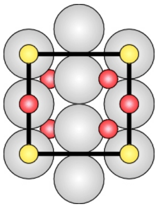

$\Delta E'_{5,1} = -$

Structure 084

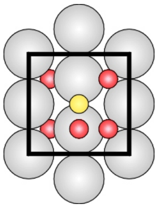

$\Delta E'_{5,1} = -$

Structure 085

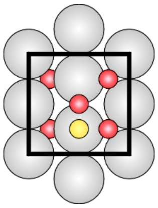

$\Delta E'_{5,1} = -$

Structure 086

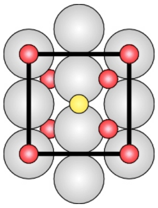

$\Delta E'_{5,1} = -$

Structure 087

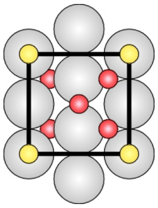

$\Delta E'_{5,1} \gtrsim 0.65\,\mathrm{eV}$

Structure 088

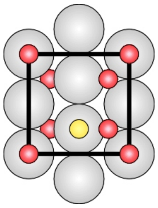

$\Delta E'_{5,1} = -$

Structure 089

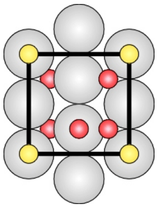

$\Delta E'_{5,1} = -$

Structure 090

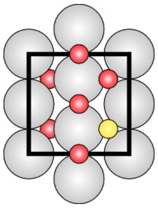

$\Delta E'_{5,1} = 1.12\,\mathrm{eV}$

Structure 091

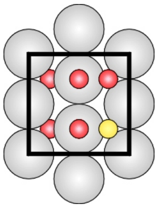

$\Delta E'_{5,1} = -$

Structure 092

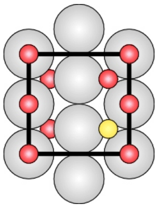

$\Delta E'_{5,1} = -$

6 O and 0 CO

Structure 093

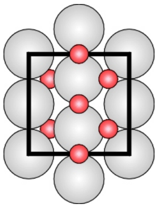

$\Delta E'_{6,0} = 0.00\,\mathrm{eV}$

Structure 094

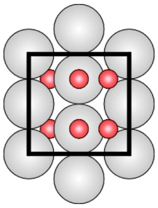

$\Delta E'_{6,0} = -$

Structure 095

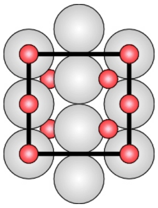

$\Delta E'_{6,0} = -$

Structure 096

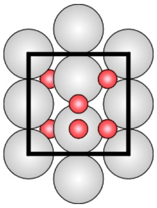

$\Delta E'_{6,0} = -$

Structure 097

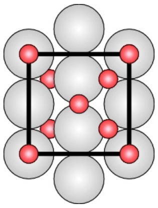

$\Delta E'_{6,0} = -$

Structure 098

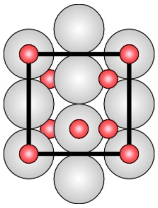

$\Delta E'_{6,0} = -$

5 O and 0 CO

Structure 099

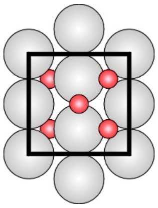

$\Delta E'_{5,0} = 0.00\,\mathrm{eV}$

Structure 100

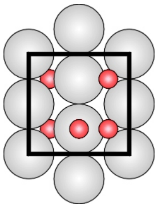

$\Delta E'_{5,0} = -$

Structure 101

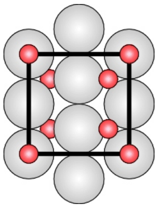

$\Delta E'_{5,0} = -$

Structure 102

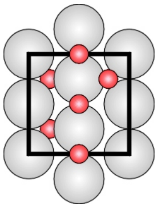

$\Delta E'_{5,0} \gtrsim 1.42\,\mathrm{eV}$

Structure 103

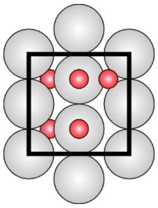

$\Delta E'_{5,0} = -$

Structure 104

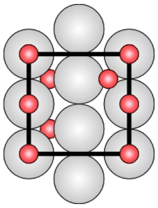

$\Delta E'_{5,0} = -$

4 O and 0 CO

Structure 105

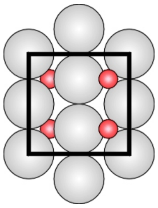

$\Delta E'_{4,0} = 0.00\,\mathrm{eV}$

Structure 106

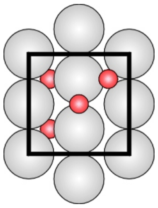

$\Delta E'_{4,0} = 1.27\,\mathrm{eV}$

Structure 107

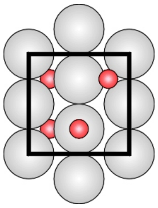

$\Delta E'_{4,0} = -$

Structure 108

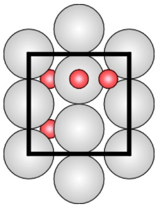

$\Delta E'_{4,0} \gtrsim 3.30\,\mathrm{eV}$

Structure 109

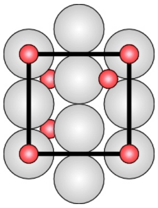

$\Delta E'_{4,0} = -$

Structure 110

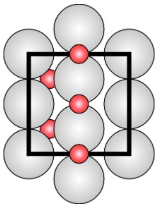

$\Delta E'_{4,0} = -$

Structure 111

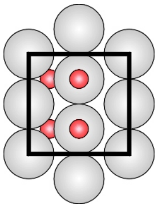

$\Delta E'_{4,0} = -$

Structure 112

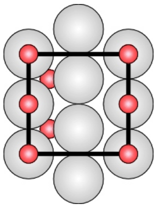

$\Delta E'_{4,0} = -$

3 O and 0 CO

Structure 113

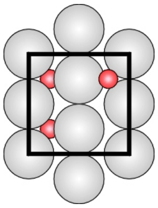

$\Delta E'_{3,0} = 0.00\,\mathrm{eV}$

Structure 114

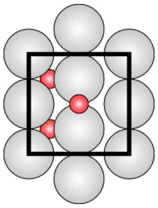

$\Delta E'_{3,0} \gtrsim 0.69\,\mathrm{eV}$

Structure 115

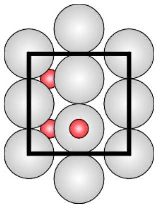

$\Delta E'_{3,0} \gtrsim 2.38\,\mathrm{eV}$

Structure 116

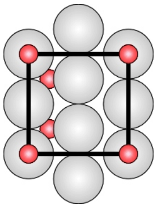

$\Delta E'_{3,0} = -$

2 O and 0 CO

Structure 117

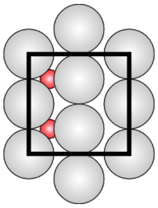

$\Delta E'_{2,0} = 0.00\,\mathrm{eV}$

B.2 O And CO In Larger $(\sqrt{5} \times \sqrt{5})R27^\circ$ Surface Unit Cells

The interactions between adsorbates in neighboring $(\sqrt{5} \times \sqrt{5})R27^\circ$ surface unit cells is investigated by calculations performed in larger surface unit cells. This is done for the adsorption of O and/or CO in bridge site in $(2 \times 1)-$ and $(1 \times 2) - (\sqrt{5} \times \sqrt{5})R27^\circ$ surface unit cells. The interactions between adsorbates in hollow sites beyond the "(1×1)" surface unit cell has not been considered at this point. Also the interactions between adsorbates on the different top sites has not been investigated in more detail, since the resulting structures appear to be rather unstable and will thus not contribute to the resulting surface phase diagram (cf. Chapter 7).

In structures 118–122 one or two CO molecules are adsorbed in bridge sites on the surface oxide structure. The binding energies are calculated with respect to the complete surface oxide, as given in Eq. (7.2), using the PBE exchange-correlation functional. Here, only the relative binding energies per CO molecule with respect to the lowest value are given. The structures exhibiting the lowest average binding energy per CO molecule is marked by a frame. Since structures 118, 120 and 121 are almost degenerate in the average binding energy, the interactions between CO molecules adsorbed in bridge sites at a distance ≥ 6.2Å, corresponding to the $(\sqrt{5} \times \sqrt{5})R27^\circ$ surface unit cell vector, seem to be negligible. CO molecules adsorbed in directly neighboring bridge sites, though, show repulsive, lateral interactions (structure 119, 122).

Structure 118

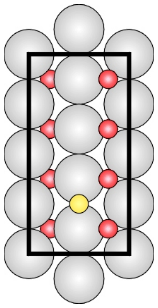

$\Delta E^{\text{bind}} = 0.00\,\text{eV}$

Structure 119

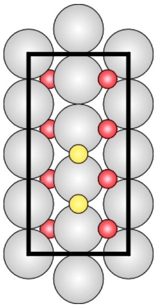

$\Delta E^{\text{bind}} \approx 0.10\,\text{eV}$

Structure 120

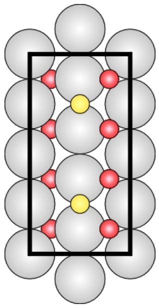

$\Delta E^{\text{bind}} \lesssim 0.05\,\text{eV}$

Structure 121

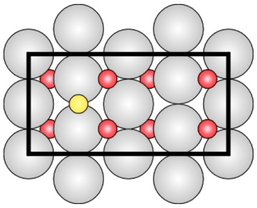

$\Delta E^{\mathrm{bind}} \approx 0.00\,\mathrm{eV}$

Structure 122

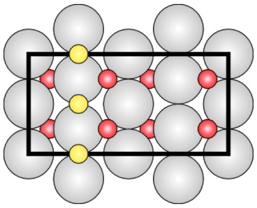

$\Delta E^{\mathrm{bind}} \approx 0.20\,\mathrm{eV}$

For the adsorption of oxygen in bridge sites a similar result is obtained (structures 123–126). Again the average binding energies per oxygen atom are given with respect to the lowest value. Also for the adsorption of oxygen in bridge sites a noticeable interaction is only observed for oxygen atoms adsorbed in directly neighboring bridge sites (structures 124, 126), whereas the interactions beyond the $(\sqrt{5}\times\sqrt{5})R27^{\circ}$ surface unit cell appear to be negligible (structures 123, 125) .

Structure 123

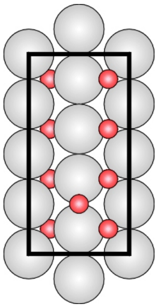

$\Delta E^{\mathrm{bind}} = 0.00\,\mathrm{eV}$

Structure 124

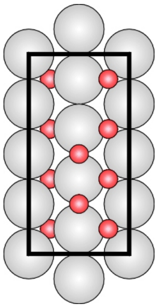

$\Delta E^{\mathrm{bind}} \approx 0.17\,\mathrm{eV}$

Structure 125

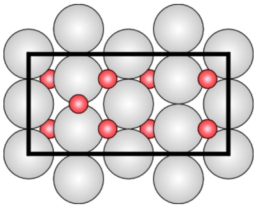

$\Delta E^{\mathrm{bind}} \lesssim 0.03\,\mathrm{eV}$

Structure 126

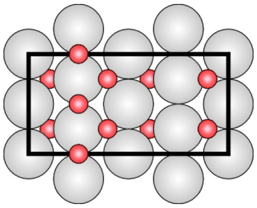

$\Delta E^{\mathrm{bind}} \approx 0.30\,\mathrm{eV}$

In structures 127–130 four different configurations are shown for the simultaneous adsorption of one oxygen atom and one CO molecule in bridge sites. The average binding energy of O and CO is calculated with respect to the complete surface oxide structure. Here, only relative values with respect to the lowest energy configuration (marked by a frame) are given. Also here, repulsive, lateral interactions are observed for the adsorption in neighboring bridge sites (structures 127,129), whereas almost no interactions between adsorbates in neighboring cells are observed.

Structure 127

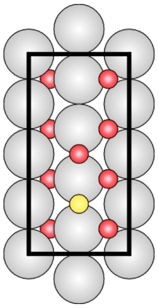

$\Delta E^{\text{bind}} \approx 0.10\,\text{eV}$

Structure 128

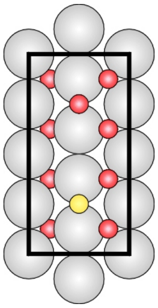

$\Delta E^{\text{bind}} \lesssim 0.01\,\text{eV}$

Structure 129

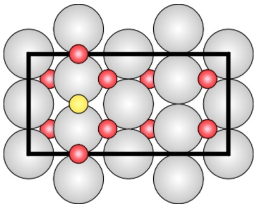

$\Delta E^{\text{bind}} \approx 0.32\,\text{eV}$

Structure 130

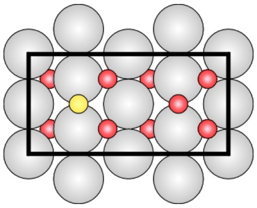

$\Delta E^{\text{bind}} = 0.00\,\text{eV}$

For the adsorption of oxygen and/or CO in bridge sites it is thus concluded, that within the $(\sqrt{5} \times \sqrt{5})R27°$ surface unit cell the lateral interactions lead to a reduction of the average binding energy, i.e. the adsorbate species show repulsive interactions. But these interactions do not appear to extend significantly beyond the $(\sqrt{5} \times \sqrt{5})R27°$ surface unit cell for the here aspired level of accuracy.

The setup of the lattice gas Hamiltonian (cf. Appendix C) can thus be restricted to first nearest neighbor interactions and the corresponding calculations can be performed within the $(\sqrt{5} \times \sqrt{5})R27°$ surface unit cell only.

Appendix C

Lattice Gas Hamiltonian

To evaluate the binding energies of the oxygen atoms and CO molecules during the kinetic Monte Carlo simulations (cf. Chapter 8) a lattice gas Hamiltonian (LGH) is used. Including only nearest neighbor pair interactions the LGH is given by

$$\begin{aligned} H = &\sum_i \left[n_{\mathrm{O},i} E^0_{\mathrm{O},i} + n_{\mathrm{CO},i} E^0_{\mathrm{CO},i} \right] \\ &+ \sum_{ij} \left[V_{\mathrm{O-O},ij}\, n_{\mathrm{O},i}\, n_{\mathrm{O},j} + V_{\mathrm{CO-CO},ij}\, n_{\mathrm{CO},i}\, n_{\mathrm{CO},j} + V_{\mathrm{O-CO},ij}\, n_{\mathrm{O},i}\, n_{\mathrm{CO},j} \right] \quad , \end{aligned} \tag{C.1}$$

where j only runs over the corresponding neighboring sites. Thus, the LGH contains 14 different parameters, including 4 on-site energies for O and CO in bridge or hollow sites on the $(\sqrt{5} \times \sqrt{5})R27°$ surface oxide structure ($E^0_{\mathrm{O,br}}$, $E^0_{\mathrm{O,hol}}$, $E^0_{\mathrm{CO,br}}$ and $E^0_{\mathrm{CO,hol}}$), and 10 nearest neighbor pair interactions including 6 different interactions between like species ($V_{\mathrm{O-O,br-br}}$, $V_{\mathrm{O-O,hol-hol}}$, $V_{\mathrm{O-O,br-hol}}$, $V_{\mathrm{CO-CO,br-br}}$, $V_{\mathrm{CO-CO,hol-hol}}$, $V_{\mathrm{CO-CO,br-hol}}$) and 4 between unlike species ($V_{\mathrm{O-CO,br-br}}$, $V_{\mathrm{O-CO,hol-hol}}$, $V_{\mathrm{O-CO,br-hol}}$, $V_{\mathrm{O-CO,hol-br}}$). In this Appendix the 29 different configurations of O and/or CO on the surface oxide, which have been used for the fitting of the 14 LGH parameters, are presented with the corresponding lattice gas expansion and DFT binding energies. The DFT binding energies of each configuration have been calculated employing Eq. (8.3). The PBE exchange-correlation functional has been used and the computational setup is equivalent to the one discussed on Page 66. The numbering of the listed structures follows the one used in Appendix B. The 14 LGH parameters have then been obtained by solving the resulting set of 29 linear equations using a least square fit.

The different configurations are represented by schematic illustrations, where large grey spheres indicate palladium atoms in the reconstructed surface oxide layer, small red ones oxygen atoms and small yellow ones CO molecules. Additionally, in all figures the $(\sqrt{5} \times \sqrt{5})R27°$ surface unit cell is shown.

1. Structure 001

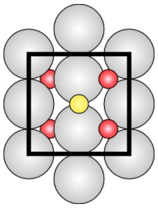

$$-4.643\,\mathrm{eV} = 2E^0_{\mathrm{O,hol}} + E^0_{\mathrm{CO,br}} + 4V_{\mathrm{O-O,hol-hol}} + 4V_{\mathrm{O-CO,hol-br}}$$

2. Structure 004

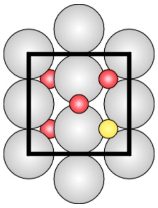

$$\begin{aligned}-3.519\,\mathrm{eV} = {} & E^0_{\mathrm{O,hol}} + E^0_{\mathrm{O,br}} + E^0_{\mathrm{CO,hol}} \\ & +2V_{\mathrm{O-O,br-hol}} + 4V_{\mathrm{O-CO,hol-hol}} + 2V_{\mathrm{O-CO,br-hol}}\end{aligned}$$

3. Structure 008

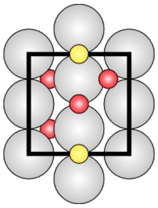

$$\begin{aligned}-3.293\,\mathrm{eV} = {} & E^0_{\mathrm{O,hol}} + E^0_{\mathrm{O,br}} + E^0_{\mathrm{CO,br}} \\ & +2V_{\mathrm{O-O,br-hol}} + 2V_{\mathrm{O-CO,hol-br}} + 4V_{\mathrm{O-CO,br-br}}\end{aligned}$$

4. Structure 012

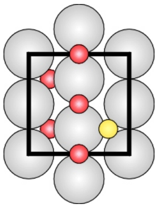

$$-2.016\,\mathrm{eV} = 2E^0_{\mathrm{O,br}} + E^0_{\mathrm{CO,hol}} + 4V_{\mathrm{O-O,br-br}} + 4V_{\mathrm{O-CO,br-hol}}$$

5. Structure 015

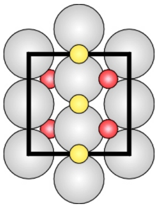

$$\begin{aligned}-5.214\,\mathrm{eV} = {} & 2E^0_{\mathrm{O,hol}} + 2E^0_{\mathrm{CO,br}} \\ & +4V_{\mathrm{O-O,hol-hol}} + 4V_{\mathrm{CO-CO,br-br}} + 8V_{\mathrm{O-CO,hol-br}}\end{aligned}$$

6. Structure 021

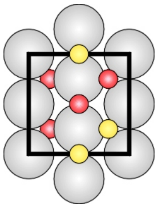

$$-4.285\,\mathrm{eV} = E^0_{\mathrm{O,hol}} + E^0_{\mathrm{O,br}} + E^0_{\mathrm{CO,hol}} + E^0_{\mathrm{CO,br}} + 2V_{\mathrm{O-O,br-hol}} + 2V_{\mathrm{CO-CO,br-hol}} + 4V_{\mathrm{O-CO,hol-hol}} + 4V_{\mathrm{O-CO,br-br}} + 2V_{\mathrm{O-CO,br-hol}} + 2V_{\mathrm{O-CO,hol-br}}$$

7. Structure 025

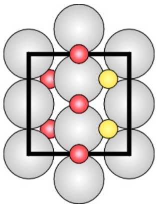

$$-2.947\,\mathrm{eV} = 2E^0_{\mathrm{O,br}} + 2E^0_{\mathrm{CO,hol}} + 4V_{\mathrm{O-O,br-br}} + 4V_{\mathrm{CO-CO,hol-hol}} + 8V_{\mathrm{O-CO,br-hol}}$$

8. Structure 028

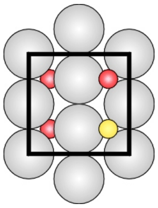

$$-3.277\,\mathrm{eV} = E^0_{\mathrm{O,hol}} + E^0_{\mathrm{CO,hol}} + 4V_{\mathrm{O-CO,hol-hol}}$$

9. Structure 029

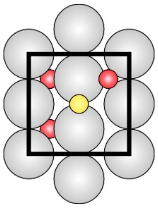

$$-3.080\,\mathrm{eV} = E^0_{\mathrm{O,hol}} + E^0_{\mathrm{CO,br}} + 2V_{\mathrm{O-CO,hol-br}}$$

10. Structure 040

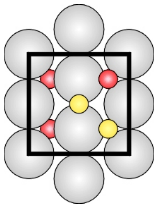

$$-4.210\,\mathrm{eV} = E^0_{\mathrm{O,hol}} + E^0_{\mathrm{CO,hol}} + E^0_{\mathrm{CO,br}} + 2V_{\mathrm{CO-CO,br-hol}} + 4V_{\mathrm{O-CO,hol-hol}} + 2V_{\mathrm{O-CO,hol-br}}$$

11. Structure 044

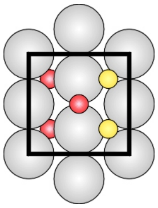

$$-3.263\,\text{eV} = E^0_{\text{O,br}} + 2E^0_{\text{CO,hol}} + 4V_{\text{CO-CO,hol-hol}} + 4V_{\text{O-CO,br-hol}}$$

12. Structure 047

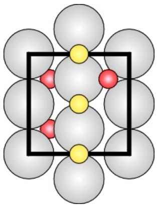

$$-3.888\,\text{eV} = E^0_{\text{O,hol}} + 2E^0_{\text{CO,br}} + 4V_{\text{CO-CO,br-br}} + 4V_{\text{O-CO,hol-br}}$$

13. Structure 050

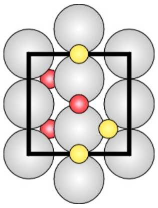

$$\begin{aligned}-2.958\,\text{eV} = {} & E^0_{\text{O,br}} + E^0_{\text{CO,hol}} + E^0_{\text{CO,br}} \\ & +2V_{\text{CO-CO,br-hol}} + 4V_{\text{O-CO,br-br}} + 2V_{\text{O-CO,br-hol}}\end{aligned}$$

14. Structure 054

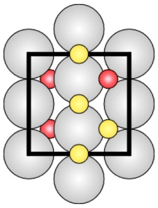

$$\begin{aligned}-4.861\,\text{eV} = {} & E^0_{\text{O,hol}} + E^0_{\text{CO,hol}} + 2E^0_{\text{CO,br}} \\ & +4V_{\text{CO-CO,br-br}} + 4V_{\text{CO-CO,br-hol}} \\ & +4V_{\text{O-CO,hol-hol}} + 4V_{\text{O-CO,hol-br}}\end{aligned}$$

15. Structure 057

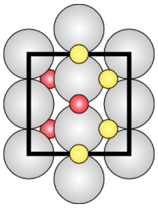

$$\begin{aligned}-3.927\,\text{eV} = {} & E^0_{\text{O,br}} + 2E^0_{\text{CO,hol}} + E^0_{\text{CO,br}} \\ & +4V_{\text{CO-CO,hol-hol}} + 4V_{\text{CO-CO,br-hol}} \\ & +4V_{\text{O-CO,br-br}} + 4V_{\text{O-CO,br-hol}}\end{aligned}$$

16. Structure 060

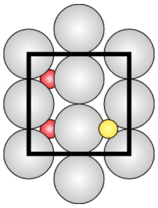

$$-1.922\,\mathrm{eV} = E^{0}_{\mathrm{CO,hol}}$$

17. Structure 064

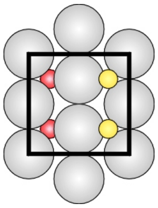

$$-3.397\,\mathrm{eV} = 2E^{0}_{\mathrm{CO,hol}} + 4V_{\mathrm{CO-CO,hol-hol}}$$

18. Structure 065

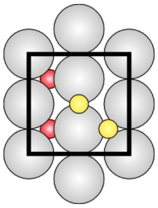

$$-3.206\,\mathrm{eV} = E^{0}_{\mathrm{CO,hol}} + E^{0}_{\mathrm{CO,br}} + 2V_{\mathrm{CO-CO,br-hol}}$$

19. Structure 072

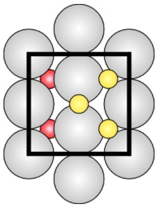

$$-4.126\,\mathrm{eV} = 2E^{0}_{\mathrm{CO,hol}} + E^{0}_{\mathrm{CO,br}} + 4V_{\mathrm{CO-CO,hol-hol}} + 4V_{\mathrm{CO-CO,br-hol}}$$

20. Structure 075

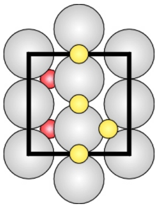

$$-3.962\,\mathrm{eV} = E^{0}_{\mathrm{CO,hol}} + 2E^{0}_{\mathrm{CO,br}} + 4V_{\mathrm{CO-CO,br-br}} + 4V_{\mathrm{CO-CO,br-hol}}$$

21. Structure 078

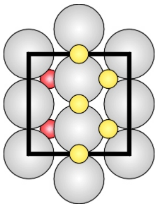

$$\begin{aligned}-4.637\,\mathrm{eV} &= 2E^0_{\mathrm{CO,hol}} + 2E^0_{\mathrm{CO,br}}\\ &\quad +4V_{\mathrm{CO-CO,hol-hol}} + 4V_{\mathrm{CO-CO,br-br}} + 8V_{\mathrm{CO-CO,br-hol}}\end{aligned}$$

22. Structure 081

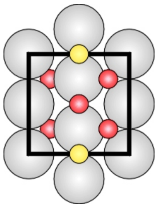

$$\begin{aligned}-4.474\,\mathrm{eV} &= 2E^0_{\mathrm{O,hol}} + E^0_{\mathrm{O,br}} + E^0_{\mathrm{CO,br}}\\ &\quad +4V_{\mathrm{O-O,hol-hol}} + 4V_{\mathrm{O-O,br-hol}}\\ &\quad +4V_{\mathrm{O-CO,br-br}} + 4V_{\mathrm{O-CO,hol-br}}\end{aligned}$$

23. Structure 090

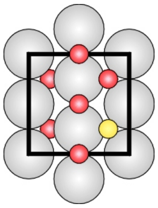

$$\begin{aligned}-3.394\,\mathrm{eV} &= E^0_{\mathrm{O,hol}} + 2E^0_{\mathrm{O,br}} + E^0_{\mathrm{CO,hol}}\\ &\quad +4V_{\mathrm{O-O,br-br}} + 4V_{\mathrm{O-O,br-hol}}\\ &\quad +4V_{\mathrm{O-CO,hol-hol}} + 4V_{\mathrm{O-CO,br-hol}}\end{aligned}$$

24. Structure 093

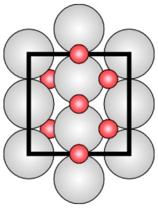

$$\begin{aligned}-3.561\,\mathrm{eV} &= 2E^0_{\mathrm{O,hol}} + 2E^0_{\mathrm{O,br}}\\ &\quad +4V_{\mathrm{O-O,hol-hol}} + 4V_{\mathrm{O-O,br-br}} + 8V_{\mathrm{O-O,br-hol}}\end{aligned}$$

25. Structure 099

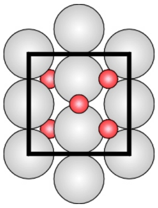

$$-3.845\,\mathrm{eV} = 2E^0_{\mathrm{O,hol}} + E^0_{\mathrm{O,br}} + 4V_{\mathrm{O-O,hol-hol}} + 4V_{\mathrm{O-O,br-hol}}$$

26. Structure 102

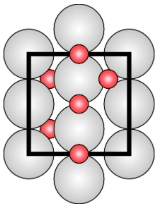

$$-2.428\,\mathrm{eV} = E^0_{\mathrm{O,hol}} + 2E^0_{\mathrm{O,br}} + 4V_{\mathrm{O-O,br-br}} + 4V_{\mathrm{O-O,br-hol}}$$

27. Structure 105

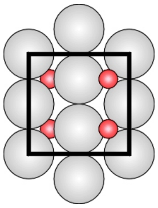

$$-3.714\,\mathrm{eV} = 2E^0_{\mathrm{O,hol}} + 4V_{\mathrm{O-O,hol-hol}}$$

28. Structure 106

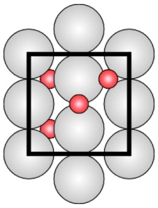

$$-2.445\,\mathrm{eV} = E^0_{\mathrm{O,hol}} + E^0_{\mathrm{O,br}} + 2V_{\mathrm{O-O,br-hol}}$$

29. Structure 113

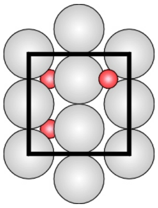

$$-1.825\,\mathrm{eV} = E^0_{\mathrm{O,hol}}$$

Bibliography

[1] R. A. VanSanten [Ed.], P. W. N. M. van Leeuwen [Ed.], J. Moulijn [Ed.], B. A. Averill [Ed.], *Catalysis: an integrated approach*, Elsevier, Amsterdam, 2nd edition, 1999.

[2] I. E. Maxwell, *Nature* **394**, 325 (1998).

[3] S. M. Senkan, *Nature* **394**, 350 (1998).

[4] H. I. Lee, J. M. White, *J. Catal.* **63**, 261 (1980).

[5] N. W. Cant, P. C. Hicks, B. S. Lennon, *J. Catal.* **54**, 372 (1978).

[6] H. Over, Y. Kimm, A. Seitsonen, S. Wendt, E. Lundgren, M. Schmid, P. Varga, A. Morgante, G. Ertl, *Science* **287**, 1474 (2000).

[7] A. Böttcher, H. Niehus, *Phys. Rev. B* **60**, 14396 (1999).

[8] K. Reuter, M. Scheffler, *Phys. Rev. Lett.* **90**, 046103 (2003).

[9] K. Reuter, M. Scheffler, *Phys. Rev. B* **68**, 045407 (2003).

[10] K. Reuter, D. Frenkel, M. Scheffler, *Phys. Rev. Lett.* **93**, 116105 (2004).

[11] D. R. Lide [Ed.], H. P. R. Frederikse [Ed.], *CRC handbook of chemistry and physics: a ready-reference book of chemical and physical data*, CRC Press, 76th edition, 1995.

[12] G. V. Samsonov [Ed.], *The Oxide Handbook*, IFI/Plenum, New York, 1973.

[13] G. Rovida, F. Pratesi, M. Maglietta, E. Ferroni, *J. Vac. Sci. Technol.* **9**, 796 (1972).

[14] G. Rovida, F. Pratesi, M. Maglietta, E. Ferroni, *Surf. Sci.* **43**, 230 (1974).

[15] J. Schnadt, A. Michaelides, J. Knudsen, R. T. Vang, K. Reuter, E. Lægsgaard, M. Scheffler, F. Besenbacher, *Phys. Rev. Lett.* **96**, 146101 (2006).

[16] W. X. Li, L. Österlund, E. K. Vestergaard, R. T. Vang, J. Matthiesen, T. M. Pedersen, E. Lægsgaard, B. Hammer, F. Besenbacher, *Phys. Rev. Lett.* **93**, 146104 (2004).

[17] E. Lundgren, G. Kresse, C. Klein, M. Borg, J. N. Andersen, M. De Santis, Y. Gauthier, C. Konvicka, M. Schmid, and P. Varga, *Phys. Rev. Lett.* **88**, 246103 (2002).

[18] M. Todorova, E. Lundgren, V. Blum, A. Mikkelsen, S. Gray, J. Gustafson, M. Borg, J. Rogal, K. Reuter, J. N. Andersen, M. Scheffler, *Surf. Sci.* **541**, 101 (2003).

[19] E. Lægsgaard, L. Österlund, P. Thostrup, P. B. Rasmussen, I. Stensgaard, F. Besenbacher, *Rev. Sci. Instrum.* **72**, 3537 (2001).

[20] B. L. M. Hendriksen, J. W. M. Frenken, *Phys. Rev. Lett.* **89**, 046101 (2002).

[21] C. Quiros, O. Robach, H. Isern, P. Ordejón, S. Ferrer, *Surf. Sci.* **522**, 161 (2003).

[22] A. Stierle, N. Kasper, H. Dosch , E. Lundgren, J. Gustafson, A. Mikkelsen, J. N. Andersen , *J. Chem. Phys.* **122**, 044706 (2005).

[23] E. Lundgren, J. Gustafson, A. Mikkelsen, J.N. Andersen, A. Stierle, H. Dosch, M. Todorova, J. Rogal, K. Reuter, M. Scheffler, *Phys. Rev. Lett.* **92**, 046101 (2004).

[24] M. Ackermann, O. Robach, C. Walker, C. Quiros, H. Isern, S. Ferrer, *Surf. Sci.* **557**, 21 (2004).

[25] S. Helveg, C. López-Cartes, J. Sehested, P. L. Hansen, B. S. Clausen, J. R. Rostrup-Nielsen, F. Abild-Pedersen, J. K. Nørskov, *Nature* **427**, 426 (2004).

[26] H. Bluhm, M. Hävecker, E. Kleimenov, A. Knop-Gericke, A. Liskowski, R. Schlögl, D. S. Su, *Top. Catal.* **23**, 99 (2003).

[27] K. Reuter, C. Stampfl, and M. Scheffler, *Ab initio atomistic thermodynamics and statistical mechanics of surface properties and functions* In: *Handbook of Maerials Modeling, Part A. Mehtods*, Springer, Berlin, 2005.

[28] R. M. Nieminen, *J. Phys.: Condens. Matter* **14**, 2859 (2002).

[29] B. L. M. Hendriksen, S. C. Bobaru, J. W. M. Frenken, *Surf. Sci.* **552**, 229 (2004).

[30] B. L. M. Hendriksen, S. C. Bobaru, J. W. M. Frenken, *Catal. Today* **105**, 234 (2005).

[31] B. L. M. Hendriksen, *Model Catalysts in Action: High-Pressure Scanning Tunneling Microscopy*, PhD thesis, Leiden University, 2003.

[32] A. Szabo, N. Ostlund, *Modern Quantum Chemistry*, Dover Publications, Inc., Mineola, New York, 1989.

[33] I. Levine, *Quantum Chemistry*, Prentice-Hall, Inc., New Jersey, 2000.

[34] M. Born, and J. R. Oppenheimer, *Ann. Phys.* **84**, 457 (1927).

[35] D. R. Hartree, *Proc. Camb. Phil. Soc.* **24**, 328 (1928).

[36] V. A. Fock, *Z. Phys.* **61**, 126 (1930).

[37] C. Møller, and M. S. Plesset, *Phys. Rev.* **46**, 618 (1934).

[38] B. O. Roos, and P. R. Taylor, *Chem. Phys.* **48**, 157 (1980).

[39] R. J. Bartlett, *J. Chem. Phys.* **93**, 1697 (1989).

[40] R.G. Parr, W. Yang, *Density Functional Theory of Atoms and Molecules*, Oxford University Press, New York, 1989.

[41] R.M. Dreizler, E.K.U. Gross, *Density Functional Theory*, Springer Verlag, Berlin, Heidelberg, 1990.

[42] W. Koch, and M. C. Holthausen, *A Chemist's Guide to Density Functional Theory*, Wiley-VCH, Weinheim, 2001.

[43] L. H. Thomas, *Proc. Camb. Phil. Soc.* **23**, 542 (1927).

[44] E. Fermi, *Rend. Accad. Lincei* **6**, 602 (1927).

[45] P. Hohenberg, and W. Kohn, *Phys. Rev. B* **136**, 864 (1964).

[46] W. Kohn, and L. J. Sham, *Phys. Rev. A* **140**, 1133 (1965).

[47] D. M. Ceperley, and B. J. Alder, *Phys. Rev. Lett.* **45**, 566 (1980).

[48] S. J. Vosko, L. Wilk, and M. Nusair, *Can. J. Phys.* **58**, 1200 (1980).

[49] J.P. Perdew, Y. Wang, *Phys. Rev. B* **45**, 13244 (1992).

[50] J.P. Perdew, K. Burke, M. Ernzerhof, *Phys. Rev. Lett.* **77**, 3865 (1996).

[51] B. Hammer, L. B. Hansen, and J. Nørskov, *Phys. Rev. B* **59**, 7413 (1999).

[52] W. E. Pickett, *Comp. Phys. Rep.* **9**, 115 (1989).

[53] D.J. Singh, L. Nordström, *Planewaves, Pseudopotentials and the LAPW Method*, Springer, New York, 2nd edition, 2006.

[54] J. C. Slater, *Phys. Rev.* **51**, 846 (1937).

[55] E. Sjöstedt, *Augmented Planewaves, Developments and Applications to Magnetism*, PhD thesis, Uppsala University, 2002.

[56] O. Andersen, *Phys. Rev. B* **12**, 3060 (1975).

[57] E. Sjöstedt, L. Nordström, and D. J. Singh, *Solid State Comm.* **114**, 15 (2000).

[58] G. K. H. Madsen, P. Blaha, K. Schwarz, E. Sjöstedt, and L. Nordström, *Phys. Rev. B* **64**, 195134 (2001).

[59] P. Blaha, private communication.

[60] J. Rath, A. Freeman, *Phys. Rev. B* **11**, 2109 (1975).

[61] H. Monkhorst, J. Pack, *Phys. Rev. B* **13**, 5188 (1976).

[62] D. Spanjaard, C. Guillot, M. C. Desjonqueres, G. Treglia, J. Lecante, *Surf. Sci. Rep.* **5**, 1 (1985).

[63] W. F. Egelhoff, *Surf. Sci. Rep.* **6**, 253 (1987).

[64] B. Johansson, N. Mårtensson, *Phys. Rev. B* **21**, 4427 (1980).

[65] J. F. Janak, *Phys. Rev. B* **18**, 7165 (1978).

[66] S. Lizzit, A. Baraldi, A. Groso, K. Reuter, M. Ganduglia-Pirovano, c. Stampfl, M. Scheffler, M. Stichler, C. Keller, W. Wurth, D. Menzel, *Phys. Rev. B* **63**, 205419 (2001).

[67] P. Blaha, K. Schwarz, G. K. H. Madsen, D. Kvasnicka and J. Luitz,, *WIEN2k, An Augmented Plane Wave + Local Orbitals Program for Calculating Crystal Properties*, K. Schwarz, Techn. Universität Wien, Austria, 2001, ISBN 3-9501031-1-2.

[68] J. Behler, *Dissociation of Oxygen Molecules on the Al(111) Surface*, PhD thesis, Techn. Universität Berlin, 2004, cf. Appendix A.

[69] R. Dohmen, J. Pichlmeier, M. Petersen, F. Wagner, M. Scheffler, *Comp. in Sci. & Eng.* **3**, 18 (2001).

[70] E. Kaxiras, Y. BarYam, J. D. Joannopoulos and K. C. Pandey, *Phys. Rev. B* **35**, 9625 (1987).

[71] M. Scheffler, In: *Physics of solid surfaces - 1987*, Elsevier, Amsterdam, 1988.

[72] M. Scheffler and J. Dabrowski, *Phil. Mag. A* **58**, 107 (1988).

[73] G.-X. Qian, R. M. Martin, D. J. Chadi, *Phys. Rev. B* **38**, 7649 (1988).

[74] X.-G. Wang, W. Weiss, Sh. Shaikhutdinov, M. Ritter, M. Petersen, F. Wagner, R. Schlögel, M. Scheffler, *Phys. Rev. Lett.* **81**, 1038 (1998).

[75] X.-G. Wang, A. Chaka, M. Scheffler, *Phys. Rev. Lett.* **84**, 3650 (2000).

[76] K. Reuter, M. Scheffler, *Phys. Rev. B* **65**, 035406 (2001).

[77] Z. Lodzianan, J. K. Nørskov, *J. Chem. Phys* **118**, 11179 (2003).

[78] A. Zangwill, *Physics at Surfaces*, Cambridge University Press, Cambridge, 1988.

[79] P. W. Atkins, *Physical Chemistry*, Oxford University Press, Oxford, 4th edition, 1990.

[80] N.W. Ashcroft, N.D. Mermin, *Solid State Physics*, CBS Publishing, Asia Ltd, 1976.

[81] J. McBride, K. Hass, W. Weber, *Phys. Rev. B* **44**, 5016 (1991).

[82] K. Reuter, M. Scheffler, *Appl. Phys. A* **78**, 793 (2004).

[83] D. R. Stull [Ed.], H. Prophet [Ed.], *JANAF thermochemical tables*, U.S. Governm. Print. Off., Washington, D.C., 2nd edition, 1971.

[84] J. Rogal, K. Reuter, *Ab initio atomistic thermodynamics for surfaces: A primer* In: *Experiment, modeling and simulation of gas-surface interactions for reactive flows in hypersonic flights*, RTO-AVT-142, VKI Lecture Series, Belgium, 2006.

[85] M. P. Allen, D. J. Tildesley, *Computer simulation of liquids*, Oxford University Press, Oxford, 2000.

[86] D. Frenkel, B. Smit, *Understanding Molecular Simulation*, Academic Press, San Diego, 2nd edition, 2002.

[87] A. Gross, *Surf. Sci. Rep.* **32**, 293 (1998).

[88] D. P. Landau, K. Binder, *A Guide to Monte Carlo Simulations in Statistical Physics*, Cambridge University Press, Cambridge, 2000.

[89] A. B. Bortz, M. H. Kalos, J. L. Lebowitz, *J. Comp. Phys.* **17**, 10 (1975).

[90] D. T. Gillespie, *J. Comp. Phys.* **22**, 403 (1976).

[91] A. F. Voter, *Phys. Rev. B* **34**, 6819 (1986).

[92] H. C. Kang, W. H. Weinberg, *J. Chem. Phys.* **90**, 2824 (1989).

[93] K. A. Fichthorn, W. H. Weinberg, *J. Chem. Phys.* **95**, 1090 (1991).

[94] P. Ruggerone, C. Ratsch, M. Scheffler, *Density-functional theory of epitaxial growth of metals.* In: *Growth and Properties of Ultrathin Epitaxial Layers*, volume 8 of *The Chemical Physics of Solid Surfaces*, Elsevier, Amsterdam, 1997.

[95] D. De Fontaine, In: *Statistics and dynamics of alloy phase transformations*, NATO ASI Series, Plenum Press, New York, 1994.

[96] J. M. Sanchez, F. Ducastelle, D. Gratias, *Physica A* **128**, 334 (1984).

[97] A. Zunger, *First principles statistical mechanics of semiconductor alloys and intermetallic compounds.* In: *Statistics and dynamics of alloy phase transformations*, NATO ASI Series, Plenum Press, New York, 1994.

[98] C. Stampfl, H.J. Kreuzer, S.H. Payne, H. Pfnür, M. Scheffler, *Phys. Rev. Lett.* **83**, 2993 (1999).

[99] K. Reuter, M. Scheffler, *Phys. Rev. B* **73**, 045433 (2006).

[100] G. H. Vineyard, *J. Phys. Chem. Solids* **3**, 121 (1957).

[101] P. Hänggi, P. Talkner, M. Borkovec, *Rev. Mod. Phys.* **62**, 251 (1990).

[102] G. R. Darling, S. Holloway, *Rep. Prog. Phys.* **58**, 1595 (1995).

[103] M. Karikorpi, S. Holloway, N. Henriksen, J. K. Norskøv, *Surf. Sci.* **179**, L41 (1987).

[104] G. Henkelman, G. Jóhannesson, H. Jónsson, *Methods for finding saddle points and minimum energy paths.* In: *Progress on Theoretical Chemistry and Physics*, Kluwar Academic Publishers, Dordrecht, 2000.

[105] G. Henkelman, H. Jónsson, *J. Chem. Phys.* **115**, 9657 (2001).

[106] G. Henkelman, H. Jónsson, *J. Chem. Phys.* **111**, 7010 (1999).

[107] A. F. Voter, F. Montalenti, T. C. Germann, *Ann. Rev. Mater. Res.* **32**, 321 (2002).

[108] R. A. Miron, K. A. Fichthorn, *J. Chem. Phys.* **119**, 6210 (2003).

[109] T. W. Orent, S. D. Bader, *Surf. Sci.* **115**, 323 (1982).

[110] E. M. Stuve, R. J. Madix, C. R. Brundle, *Surf. Sci.* **146**, 155 (1984).

[111] S.-L. Chang, P. A. Thiel, *J. Chem. Phys.* **88**, 2071 (1988).

[112] S.-L. Chang, P. A. Thiel, J. W. Evans, *Surf. Sci.* **205**, 117 (1988).

[113] G. Zheng, E. I. Altman, *Surf. Sci.* **504**, 253 (2002).

[114] D. Rogers, R. Shannon, J. Gillson, *J. Solid State Chem.* **3**, 314 (1971).

[115] J. Rogal, Elektronenstruktur und Stabilität von Pd und PdO (Dichtefunktionaltheorierechnungen), Diplomarbeit, Freie Universität Berlin, 2002.

[116] C. Nyberg, C. G. Tengstål, *Surf. Sci.* **126**, 163 (1983).

[117] G. Herzberg, *Molecular spectra and molecular structure, I: Spectra of diatomic molecules*, Van Nostrand Reinhold, New Yorck, 2nd edition, 1950.

[118] A. P. Miller, B. N. Brockhouse, *Can. J. Phys.* **49**, 704 (1971).

[119] P. W. Tasker, *J. Phys. C* **12**, 4977 (1979).

[120] C. Noguera, *J. Phys.: Condens. Matter* **12**, R367 (2000).

[121] R. Pentcheva, F. Wendler, H. L. Meyerheim, W. Moritz, N. Jedrecy, M. Scheffler, *Phys. Rev. Lett.* **94**, 126101 (2005).

[122] G. Wulff, *Z. Kristallogr.* **34**, 449 (1901).

[123] J. H. Holland, *Adaption in Natural and Artificial Systems*, The MIT Press, 1992.

[124] R. L. Johnston, *Dalton Trans.* **22**, 4193 (2003).

[125] M. I. J. Probert, private communication.

[126] D. Ciuparu, E. Altman, L. Pfefferle, *J. Catal.* **203**, 64 (2001).

[127] A. M. Bradshaw, F. M. Hoffmann, *Surf. Sci.* **72**, 513 (1978).

[128] F. M. Hoffmann, *Surf. Sci. Rep.* **3**, 107 (1983).

[129] R. J. Behm, K. Christmann, G. Ertl, M. A. Van Hove, P. A. Thiel, W. H. Weinberg, *Surf. Sci. Lett.* **88**, L59 (1979).

[130] R. J. Behm, K. Christmann, G. Ertl, M. A. Van Hove, *J. Chem. Phys* **73**, 2984 (1980).

[131] P. Uvdal, P.-A. Karlsson, C. Nyberg, S. Andersson, N. V. Richardson, *Surf. Sci.* **202**, 167 (1988).

[132] K. Yoshioka, F. Kitamura, M. Takeda, M. Takahashi, M. Ito, *Surf. Sci.* **227**, 90 (1990).

[133] J. N. Andersen, M. Qvarford, R. Nyholm, S. L. Sorensen, C. Wigren, *Phys. Rev. Lett.* **67**, 2822 (1991).

[134] W. Berndt, A. M. Bradshaw, *Surf. Sci. Lett.* **279**, L165 (1992).

[135] P. J. Feibelman, B. Hammer, J. K. Nørskov, F. Wagner, M. Scheffler, R. Stumpf, R. Watwe, J. Dumesic, *J. Phys. Chem. B* **105**, 4018 (2001).

[136] A. Eichler, J. Hafner, *Phys. Rev. B* **57**, 10110 (1998).

[137] C. J. Zhang, P. Hu, *J. Am. Chem. Soc.* **123**, 1166 (2001).

[138] A. Eichler, *Surf. Sci.* **498**, 314 (2002).

[139] H. Conrad, G. Ertl, J. Küppers, *Surf. Sci.* **76**, 323 (1978).

[140] A. P. Seitsonen, Y.D. Kim, S. Schwegmann, H. Over, *Surf. Sci.* **468**, 176 (2000).

[141] H. Over, *Prog. Surf. Sci.* **58**, 249 (1998).

[142] J. N. Andersen, private communication.

[143] O. Gunnarsson, K. Schönhammer, *Surf. Sci.* **80**, 471 (1979).

[144] M. Todorova, *Oxidation of Palladium Surfaces*, PhD thesis, Techn. Universität Berlin, 2004.

Danksagung

Zuerst möchte ich Matthias Scheffler danken für die Möglichkeit diese Arbeit am Fritz-Haber-Institut anzufertigen, sowie für seine Unterstützung und kritische Begutachtung dieses Projektes. Auch dafür, dass ich an zahlreichen Konferenzen teilnehmen und dort, sowie in Berlin, viele interessante Leute kennen lernen konnte.

Ganz besonders möchte ich mich bei Karsten Reuter bedanken für die ausführlichen Diskussionen und seine ausgezeichnete Betreuung, die sehr zum Gelingen dieser Arbeit beigetragen haben. DANKE!

Mein Dank geht auch an Jörg Behler und Mira Todorova, die mir einen guten Start und auch eine gute Zeit hier am Institut ermöglicht haben, an Patrick Rinke, Thomas Hammerschmidt, Mahbube Hortamani, Ralf Gehrke und Yongsheng Zhang für die nette Atmosphäre im Institut, auf Konferenzen und auch anderswo. Also thanks to all the other people in the theory department, it is really a great and inspiring environment.

Des Weiteren danke ich Prof. Dr. E.K.U. Gross für seine Bereitschaft als Zweitgutachter an der Freien Universität zu fungieren, sowie allen Mitgliedern des Prüfungsausschusses für ihre Zeit diese Arbeit zu lesen.

Ein besonderer Dank der ganz anderen Art geht an meine Eltern. Ich danke euch für euer Vertrauen und eure Zuversicht, dass der Weg, den ich versuche zu finden, schon der richtige sein wird.

Ich danke Henrik für die wundervolle Zeit. Ohne dich ist das alles kein Spaß.

Lebenslauf

Jutta Rogal
geboren am 06.06.1977 in Oberhausen

Studium

2002 – 2006	Promotion am Fritz-Haber-Institut der Max-Planck-Gesellschaft
2002	Diplom
2001 – 2002	Diplomarbeit am Fritz-Haber-Institut der Max-Planck-Gesellschaft Thema: ”Elektronenstruktur und Stabilität von Pd und PdO (Dichtefunktionaltheorierechnungen)”
1998 – 2002	Studium der Chemie (Diplom) an der Freien Universität Berlin mit Physik als 4. Fach im Diplom
1998	Diplomvorprüfung Chemie an der Universität Hamburg
1996 – 1998	Studium der Chemie (Diplom) an der Universität Hamburg

Schulausbildung

1996	Abitur
1994 – 1996	Heinrich-Heine-Gymnasium, Bottrop
1993 – 1994	Ryle High School (Schüleraustausch), Kentucky USA
1987 – 1993	Heinrich-Heine-Gymnasium, Bottrop

Publications

- M. Todorova, E. Lundgren, V. Blum, A. Mikkelsen, S. Gray, J. Gustafson, M. Borg, J. Rogal, K. Reuter, J.N. Andersen, and M. Scheffler, *The Pd(100)-*$(\sqrt{5} \times \sqrt{5})R27^\circ$*-O surface oxide revisited.* Surf. Sci. **541**, 101-112 (2003).
- J. Rogal, K. Reuter, and M. Scheffler, *Thermodynamic stability of PdO surfaces.* Phys. Rev. B **69**, 075421 (2004).
- E. Lundgren, J. Gustafson, A. Mikkelsen, J.N. Andersen, A. Stierle, H. Dosch, M. Todorova, J. Rogal, K. Reuter, and M. Scheffler, *Kinetic hindrance during the initial oxidation of Pd(100) at ambient pressures.* Phys. Rev. Lett. **92**, 046101 (2004).
- J. Rogal and K. Reuter, *Ab initio atomistic thermodynamics for surfaces: A primer.* Appeared in: RTO-AVT-142, VKI Lecture Series on "Experiment, modeling and simulation of gas-surface interactions for reactive flows in hypersonic flights", Rhode-St-Gense, Belgium (2006).
- A. Kiejna, G. Kresse, J. Rogal, A. De Sarkar, K. Reuter, and M. Scheffler, *Comparison of the full-potential and frozen-core approximation approaches to density-functional calculations of surfaces.* Phys. Rev. B **73**, 035404 (2006).
- Y. Zhang, J. Rogal, and K. Reuter, *Density-functional theory investigation of oxygen adsorption at Pd(11N) vicinal surfaces (N=3,5,7): Influence of neighboring steps.* Phys. Rev. B **74**, 125414 (2006).
- J. Rogal, K. Reuter, and M. Scheffler, *First-principles statistical mechanics study of the stability of a sub-nanometer thin surface oxide in reactive environments: CO oxidation at Pd(100)*, submitted to Phys. Rev. Lett.